Universidad de Jaén

**Tesis Doctoral**

# IMPLICACIÓN DE LAS INTERACCIONES INTERFACIALES EN LA ESTRUCTURA Y COHESIÓN DEL SUELO.

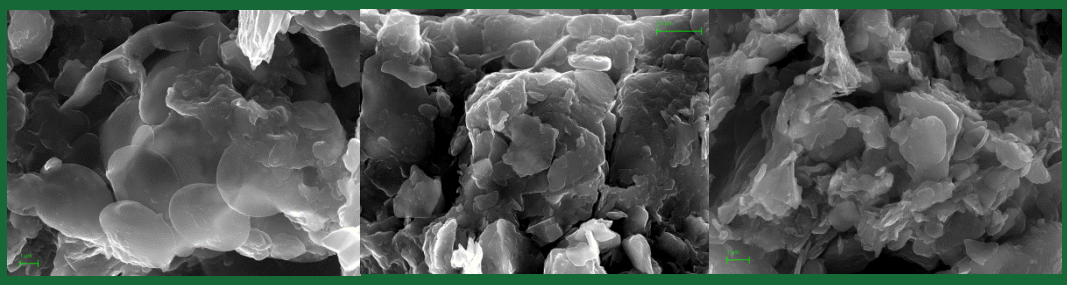

**Iván Plaza Félix**

**Jaén, 2017**

**UNIVERSIDAD DE JAEN**

**DEPARTAMENTO DE FÍSICA**

**TESIS DOCTORAL**

# Implicación de las interacciones interfaciales en la estructura y cohesión del suelo.

PRESENTADA POR:

**IVÁN PLAZA FELIX**

DIRIGIDA POR:

**DR. ALFONSO ONTIVEROS ORTEGA**

**DR. JULIO CALERO GONZÁLEZ**

**DR. VICTOR ARANDA SANJUÁN**

**JAÉN, JULIO DE 2017**


Universidad de Jaén

# Implicación de las interacciones interfaciales en la estructura y cohesión del suelo.

Memoria presentada para optar al grado de

**"Doctor por la Universidad de Jaén"**

Programa de Doctorado en Ciencias

**JAÉN, JULIO DE 2017**

# UNIVERSIDAD DE JAÉN

## DEPARTAMENTO DE FISICA

**D. Alfonso Ontiveros Ortega, Profesor Titular de Universidad de Jaén, adscrito al Departamento de Física, hace constar:**

**Que la presente memoria titulada: "Implicación de las interacciones interfaciales en la estructura y cohesión del suelo." ha sido realizada bajo su dirección por el doctorando D. Iván Plaza Félix y cumple los requisitos necesarios para que su autor pueda optar al grado de Doctor por la Universidad de Jaén.**

**VºBº del Director**

**Fdo. Iván Plaza** **Fdo. Prof. Alfonso Ontiveros**

# UNIVERSIDAD DE JAÉN

## DEPARTAMENTO DE GEOLOGIA

**D. Julio Calero González y D. Víctor Aranda Sanjuán, Profesores de Universidad de Jaén, adscritos al Departamento de Geología, hace constar:**

**Que la presente memoria titulada: "Implicación de las interacciones interfaciales en la estructura y cohesión del suelo" ha sido realizada bajo su dirección por el doctorando D. Iván Plaza Félix y cumple los requisitos necesarios para que su autor pueda optar al grado de Doctor por la Universidad de Jaén.**

**Fdo. Iván Plaza**

**VºBº del Directores**

**Fdo. Prof. Julio Calero** **Fdo. Prof. Víctor Aranda**

“EL ÉXITO DE LA VIDA NO ESTÁ

EN VENCER SIEMPRE,

SINO EN NO DARSE POR VENCIDO

NUNCA.”

“ANÓNIMO”

A mis padres,

***Francisco y Francisca***

POR TODO VUESTROS APOYO

POR HACER POSIBLE LO IMPOSIBLE

A mi hermana

***Laura***,

Mi pequeñina,

Por trasmitirme toda tu fuerza,

Por apoyarme en mi decisiones,

Por estar cuando siempre

que te he necesitado

# AGRADECIMIENTOS

Es tanta gente la que me ha apoyado en este camino que no quiero olvidarme de ninguno de ellos. En especial deseo recordar aquellos que ya no están a mi lado, pero que desde arriba han cuidado de mí.

Quiero mostrar mi más profundo agradecimiento a todos aquellos que durante estos intensos años me han brindado su ayuda, apoyo, y cariño, para conseguir llevar a buen término esta memoria que es, sin duda, resumen de una de las etapas más importantes de mi modesta aportación a la investigación.

No puedo evitar acordarme, con especial cariño de mis tres directores, a los que quiero agradecer su tesón, trabajo y apoyo. Agradezco en particular a Alfonso Ontiveros Ortega su sabia tutela, el trato amable y la paciencia que siempre me dispensó; A Julio Calero González por sus claras y concisas explicaciones que tantas ocasiones me han ayudado a comprender difíciles resultados; por su tesón y palabras de apoyo en los momentos duros. A Víctor Aranda

Sanjuán, por su apoyo técnico y logístico y por su búsqueda incasable de todo aquello que necesitaba.

Una mención especial merece el Departamento de Física de la Universidad de Jaén, y en especial al Grupo de Investigacion Física de Interfases. Tecnología Textil (TEP-145); por su disposición ayudarme en cualquier momento y bríndame su apoyo y experiencia.

A mis queridos compañeros de laboratorio, en el que tanto tiempo hemos estado: Dña. Elena Giménez Martín y D. José Alberto Moleón Baca; por su desinteresado esfuerzo que han puesto cuando he requerido su cooperación; por acogerme desde el primer momento y confiar en mí, por sus sabios consejos, por estar siempre ahí y por preocuparse de mi bienestar.

Por ultimo quiero agradecer a todas aquellas personas que han contribuido de forma desinteresada en la realización de esta memoria, debo hacer una mención especial a aquellas personas que han cedido sus fotografías para esta publicación.

**"Gracias a todos por realizar este sueño posible"**

# RESUMEN

La caracterización eléctrica y termodinámica de una interfase sólido-líquido es importante en una amplia gama de problemas, tanto desde punto de vista fundamental como por sus aplicaciones tecnológicas. Muchos de los fenómenos que tienen lugar en la interfase sólido-líquido, incluyendo humectabilidad, adsorción o fenómenos de adhesión, dependen en gran medida de los cambios en la energía libre superficial de dicha interfase.

Aunque este estudio es a menudo complejo, se ha demostrado en repetidas ocasiones que el análisis combinado de la carga superficial y las propiedades termodinámicas puede proporcionar una amplia información acerca de las interacciones que tienen lugar en la interfase sólido-líquido. Estas energías de interacción entre la fracción más fina del suelo son las responsables de su cohesión y, por tanto, de su microestructura,

determinando además fenómenos como la fijación de carbono, la erosionabilidad del mismo, la retención de agua y contaminantes.

En nuestro estudio, tres tipos de interacciones interfaciales serán consideradas, Lifshitz-van der Waals (LW), electrostática (EL), y ácido-base (AB). El modelo teórico que explica dichas interacciones es modelo de Van Oss (TEORIA DLVO-Extendida); según este modelo las tres contribuciones dependen de la naturaleza de las interfases involucradas (potencial zeta y las componentes de la energía libre superficial), lo que nos exigirá una caracterización eléctrica y termodinámica de todos los materiales a estudiar.

El objetivo del trabajo de investigación será analizar desde el punto de vista de las interacciones interfaciales, fenómenos importantes que afectan la calidad de suelos agrícolas y naturales, tales como fijación de carbono, la estabilidad de la estructura y la resistencia a la erosión superficial y en masa.

# ABSTRACT

The electrical and thermodynamic characterization of a solid-liquid interface is important in a wide range of problems, both from a fundamental point of view and its technological applications. Many of the phenomena occurring at the solid-liquid interface, including wettability, adsorption or adhesion phenomena, are largely dependent on changes in the free surface energy of the interface.

Although this study is often complex, it has been repeatedly demonstrated that the combined analysis of surface charge and thermodynamic properties can provide ample information about the interactions taking place at the solid-liquid interface. These energies of interaction between the finer fraction of the soil are responsible for their cohesion and, therefore, their microstructure, determining also phenomena such as carbon fixation, erosionability of the same, retention of water and pollutants, etc.

In our study, three types of interfacial interactions will be considered, Lifshitz-van der Waals (LW), electrostatic (EL), and acid-base (AB). The theoretical model that explains these interactions is Van Oss model (DLVO-Extended Theory); According to this model the three contributions depend on the nature of the interfaces involved (zeta potential and the components of free surface energy), which will require an electrical and thermodynamic characterization of all the materials to be studied.

The objective of the research work will be to analyze from the point of view of interfacial interactions, important phenomena that affect the quality of agricultural and natural soils, such as carbon fixation, structure stability and resistance to surface erosion and mass.

# Índice

# Capítulo 1
# Introducción

## 1.1. Introducción general.

Los suelos tienen como principales funciones la sustentación de nuestra agricultura, producción de biomasa, regulación de los ciclos de carbono y nitrógeno (entre otros), la base sobre la que construimos, sobre la que nos desplazamos y en el que obtenemos una amplia variedad de materias primas. La importancia de los mismos es clara, y las políticas de la Unión Europea están destinadas a proteger este recurso **(**Parlamento Europeo, Abril y Septiembre 2006**)** y a su investigación a través del Séptimo Programa Marco de investigación y desarrollo tecnológico (2007-2013) que incluye un capítulo para apoyar las acciones de investigación sobre la protección y las funciones del suelo.

En los últimos años el interés científico y comercial por los suelos, ha dado lugar a numerosos estudios con distintos fines y en el marco de nuevas normativas europeas que apoyan su investigación (Joint Research Centre). El European Soil Data Centre (ESDAC) es el centro temático de datos sobre el suelo en Europa. Su ambición es ser el único punto de referencia y recibir todos los datos e información sobre el suelo pertinentes a nivel europeo. Contiene una serie de recursos que se organizan y presentan de varias maneras: conjuntos de datos, servicios/aplicaciones, mapas, documentos, eventos, proyectos y enlaces externos ha puesto de manifestado en detalle cuales son las amenazas para el suelo, y se han identificado las estrategias temáticas de este en la comunicación del Parlamento Europeo de 2006.

En este comunicado las amenazas se clasifican en ocho apartados:

- ✓ Erosión del suelo (Erosion by water or wind).
- ✓ Contenido de carbono orgánico (Organic Matter decline).
- ✓ Compactación del suelo (Soil Compaction).
- ✓ Salinización del suelo (Soil Salinisation).
- ✓ El sellado y encostramiento del suelo (Soil Sealing and Crusting).
- ✓ La contaminación del suelo (Soil Contamination).
- ✓ La biodiversidad del suelo (Soil Biodiversity).
- ✓ Los deslizamientos de tierra (Landslides).

En este sentido nuestra investigación se centra principalmente en tres de estas estrategias europeas para la investigación (ver figura 1.1.):

- ✓ Estudios microscópicos relacionados con la pérdida de carbono orgánico del suelo (Organic matter decline).
- ✓ Estudios microscópicos cuyo objetivo es la compresión de los factores que determinan la microestructura de los suelos (Soil Compaction), determinante en su uso para la agricultura y que a su vez determinan comportamientos macroscópicos relacionados con procesos de erosión y transporte en masa de estos (Soil erosion and Landslides). Pero que además tienen implicaciones en otras directrices como la salinidad, la biodiversidad o la contaminación de este.

El análisis de la microestructura del suelo y de los parámetros que la determinan será el objetivo principal de esta memoria. En este sentido, analizaremos las interacciones entre las partículas más finas del suelo para lo cual realizaremos una completa caracterización de este: química, mineralógica, morfológica, eléctrica y termodinámica, con el objeto de interpretar los procesos de adsorción-absorción de materia orgánica y coagulación-agregación y retención de agua.

La caracterización eléctrica y termodinámica de una interfase sólido líquido ha sido estudiada en una amplia gama de campos científicos, tanto desde el punto de vista fundamental como por sus aplicaciones tecnológicas. No obstante, son menos los estudios que han aplicado este tratamiento teórico a la comprensión de los procesos edafológicos.

En este contexto se centra esta tesis doctoral, en la caracterización eléctrica y termodinámica de diferentes tipos suelos y como se modifican estas propiedades en presencia de diferentes electrolitos, materia orgánica y distintos valores de pH. Esta caracterización nos permitirá el cálculo de las energías de interacción entre las partículas más finas que forman los suelos objeto de estudio, y que nos permitirán interpretar muchas de sus propiedades.

## 1.2. Estado actual de las investigaciones.

El estudio de las propiedades superficiales de distintos materiales a través de la caracterización eléctrica y termodinámica de una interfase solido-liquido es importante en una amplia gama de materiales, tanto desde el punto de vista fundamental como por sus aplicaciones tecnológicas en los fenómenos de adhesión, adsorción y absorción (Moleon et al., 2015). Las implicaciones que estas propiedades tienen en distintos campos de la ciencia y la tecnología son hoy uno de los campos de mayor interés en la comunidad científica (Manuel-Espinosa et al., 2003; Ontiveros et al, 1996; Ontiveros et al., 1998; Bagshaw et al., 2011; Cockell et al., 2010; Plaza et al., 2014; Ontiveros et al., 2012; Ontiveros-Ortega et al., 2015; Aranda et al., 2015). El interés se justifica debido a que el comportamiento macroscópico de la mayoría de los sistemas naturales, puede ser explicado en gran medida mediante las propiedades microscópicas de estos.

Aunque el análisis de la interfase solido-líquido es a menudo complejo, se ha demostrado en repetidas ocasiones que el estudio combinado de las propiedades eléctricas y termodinámicas superficiales, puede proporcionar una amplia información acerca de las interacciones que tienen lugar en estas interfases (Dexter 1975; Chiristensen et al. 1985; Paul et al. 1985). De acuerdo con la teoría clásica de estabilidad coloidal DLVO (Derjaguin, Landau, Verwey y Overbeek) de 1940 el computo de interacciones eléctricas de doble capa y dispersivas Lifshitz-Van de Waal dan repuesta a un gran número de situaciones experimentales observadas, aunque son otras muchas las que no quedan adecuadamente descritas en el contexto de la teoría clásica DLVO, principalmente aquellas en la los materiales presentan alto grado de hidrofobicidad. Posteriormente en la década de los 80, con el objeto de subsanar las deficiencias de la teoría clásica, aparecieron sus versiones más actualizadas DLVO-extendida (van Oss et al., 1984; van Oss et al., 1994; Israelachvili et al., 1992), que considera además una forma de abordar las interacciones no dispersivas o estructurales.

De acuerdo con la teoría de van Oss, además de la interacción eléctrostática (EL) y dispersiva Lifshitz-Van de Waals (LW), se considera la interacción ácido bases (AB). Las tres contribuciones dependen de la naturaleza de las interfases involucradas (potencial zeta), las componentes de la energía libre superficial, y de la distancia de separación entre superficies (van Oss et al., 1994).

***Figura 1.1.*** En la composición fotográfica se muestran las distintas amenazas del suelo (de arriba abajo y de izquierda a derecha tenemos: organic matter decline, soil salinisation, soil compaction, soil erosion and soil contamination.

Fuente: @Katharina Helming, @Holger Casselmann, @Volker Prasuhn, @ Roger469 And @ Tomas Castelazo. [CC BY-SA LICENCE FREE 3.0 http://creativecommons.org/]

Esta memoria interpreta los fenómenos estudiados y relacionados con la estructura del suelo y la adsorción de materia orgánica en los términos de la teoría DLVO extendida.

En la bibliografía podemos encontrar actualmente sobre esta forma de interpretar los fenómenos edafológicos a diversos autores: Hwang et al. (2010) que han caracterizado la adhesión bacteriana a las partículas minerales, Zhu et al. (2014), Li & Chen (2012) y Sequaris et al. (2010) han comprobado los efectos de la adición de HA en la retención coloidal, Zhang et al. (2010), Kumahor et al. (2015) y Sharma et al. (2008) han estudiado el transporte de coloides por flujos de agua, etc. Por lo tanto, es un método ampliamente probado en la literatura.

### 1.3. Objetivos marcados.

El presente estudio se marca como objetivo principal estudiar como las interacciones interfaciales pueden justificar la estabilidad estructural y la adsorción de carbono por parte del suelo, así como las implicaciones agronómicas y ambientales que se derivan de estos procesos.

Más detalladamente podemos dividir en dos el objetivo principal:

- ✓ Primero, el cálculo de las interacciones interfaciales, contempladas en la teoría DLVO-Extendida, para conocer el papel que estas juegan en la estructura del suelo y como afectan a sus propiedades físicas (infiltración, reserva de agua, porosidad, hidrofobicidad) y físico-químicas (fijación y adsorción de carbono).

Para ello se procederá a una caracterización eléctrica y termodinámica de la interfase suelo-agua de cada una de las muestras objeto de estudio.

- ✓ Segundo, el estudio de las implicaciones que las interacciones interfaciales tienen en la cohesión del suelo y determinar qué condiciones son de mayor estabilidad para aquellos depósitos susceptibles de generar movimientos de masas gravitacionales.

Estos objetivos prioritarios se pueden dividir en varios objetivos secundarios:

- ✓ Interpretar el efecto que distintos cationes tienen en los distintos sistemas estudiados; ver sus efectos en la carga superficial así como en sus propiedades termodinámicas.
- ✓ Analizaremos la importancia que en estas propiedades superficiales tienen en la adsorción de materia orgánica y sus efectos en la calidad del suelo.
- ✓ Determinar si la presencia de compost y materia orgánica artificial pueden provocar hidrofobicidad/hidroficilidad en el suelo.
- ✓ Pretendemos poner en valor la importancia de las interacciones interfaciales en la estabilidad de laderas, para ello analizaremos la energía total de interacción y su relación con el factor de cohesión de los depósitos en términos cualitativos.

Para logar alcanzar estos objetivos se partió de la siguiente hipótesis de trabajo: considerar la importancia de las interacciones interfaciales en

todos los fenómenos edafológicos, y como el conocimiento de las propiedades superficiales del material que compone el suelo nos permite interpretar su calidad.

### 1.4. Contenidos de la investigación.

El presente documento se encuentra dividido en VI capítulos y cinco apéndices, donde se recogen las investigaciones realizadas desde comienzos de 2013 hasta las últimas investigaciones en julio de 2017.

En el Capítulo I, se presenta el estado del arte, antecedentes y objetivos de la investigación. En el Capítulo II, se introduce brevemente los antecedentes teóricos y modelos utilizados para la interpretación de los datos obtenidos en nuestra investigación: teoría de DVLO Clásica y Extenida. También, se hace en dicho Capítulo una explicación de las interacciones interfaciales según la teoría DLVO extendida, contemplada en el modelo de van Oss destacando el modelo propuesto por van Oss y et al. (1987, 1988).

En el Capítulo posterior, III, se describen las principales características de los suelos utilizados en esta investigación. La metodología utilizada para desarrollar nuestro trabajo es explicada en el Capítulo IV.

En los Capítulos V, se presentan los resultados obtenidos sobre los suelos estudiados y estructurados por artículos. Donde se hace un recorrido por distintos tipos de suelo, y se muestra como el análisis de las

interacciones interfaciales pueden dar respuesta a algunos procesos que ocurren en los suelos.

El Capítulo VI, estará dedicado a recapitulación de los resultados obtenidos de las investigaciones, la obtención de conclusiones y las aportaciones que se ha hecho en este campo.

En último lugar, aparecen los apéndices donde figuran un listado de tablas, figuras y derechos de autor de las mismas.

**1.5. Grado de innovación que se pretende.**

Como ya se ha dicho anteriormente, hasta el momento presente son muchos los trabajos publicados sobre la interpretación de la fenomenología coloidal y sus aplicaciones tecnológicas considerando la teoría DVLO y DLVO extendida, área en la cual el grupo al que pertenezco tiene gran bagaje y experiencia. La aportación principal de este trabajo es la aplicación de estos conocimientos al área de la Edafología.

Con este trabajo se pretende llevar a cabo un estudio riguroso y completo de cómo los fenómenos de superficie condicionan la estructura del suelo y por ende las funciones que estos desempeñan en los ecosistemas y en la economía humana, enfatizando el estudio del papel que juegan los suelos como sumidero de carbono de la atmósfera y como elemento clave de la producción agrícola, aspecto relevante en el entorno socioeconómico de la provincia de Jaén.

A continuación se muestra la relevancia que se espera de esta investigación:

i) La generación de la estructura del suelo es clave para la su calidad, pero es a la vez un proceso multifactorial y complejo, muy difícil de abordar con modelos basados en la DLVO tradicional, que tratan las interacciones electrostáticas y dispersivas como principales agentes de estabilidad de los coloides edáficos. Estos modelos nos explican muchos procesos como, por ejemplo, el hecho de que algunos suelos de poca carga presenten una elevadísima estabilidad estructural. La teoría DLVO-extendida, al incorporar el efecto de interacciones ácido-base pretende explicar de una forma más completa este proceso. El análisis de las propiedades de distintos suelos, entre las que se encuentran las hidrofóbicas, sobre distintos tipos de materiales geológicos y distintos de uso, que nos permitirá determinar cuáles son las propiedades que los caracterizan y como estas evolucionan justificando el comportamiento que los diferencia y caracteriza. Los aspectos aplicados de este estudio en el campo agroambiental serían significativos, por ejemplo, en su incorporación a los protocolos de la agricultura ecológica.

ii) Además de los fenómenos de estabilidad de las suspensiones, el estudio de las propiedades superficiales aporta un avance en el estudio de los mecanismos de adsorción de carbono (Sangil et al., 2013).

iii) Por último, los suelos no siempre constituyen superficies horizontales en las cuales la componente del peso es normal a estas superficies, por el contrario, es común, suelos sometidos a pendientes importantes cuya estabilidad se ve comprometida dependiendo de la pendiente, la cohesión del suelo, y de la capacidad de retener agua. Estas situaciones actualmente crean problemas de ingeniería de difícil tratamiento. El conocimiento de la cohesión de estos depósitos y los factores que la determinan aportan a esta tesis una pincelada interesante y abre nuevas vías de estudio y continuidad al trabajo realizado.

# Capítulo 2
# Aspectos teóricos

## 2.1. Interacción electrostática. La doble capa eléctrica.

### *2.1.1. Introducción.*

El conocimiento de la distribución de carga y potencial en las proximidades de una partícula inmersa en un medio líquido iónico es fundamental para abordar el estudio de fenómenos tales como la agregación entre partículas coloidales del mismo tipo (homo-coagulación), o diferentes (hetero-coagulación), o bien, en los procesos de adhesión entre partículas coloidales y un substrato sólido. Todos ellos son muy dependientes de la energía de interacción entre los materiales sólidos inmersos en la fase liquida de dispersión y, como dijimos anteriormente, una de las contribuciones fundamentes a esta energía de interacción es la electrostática (EL).

Cuando dos fases entrar en contacto, (por ejemplo, cuando se dispersa un sólido en un medio líquido polar) se crea una diferencia de potencial eléctrico entre ellas. La interfase se caracteriza por una distribución desigual de carga, de forma que en la superficie de una de las fases existe un exceso de carga eléctrica de un signo, mientras que la carga necesaria para neutralizarla se distribuye en la zona adyacente en la otra fase. En consecuencia, cuando una partícula solida se encuentra en el seno de un líquido, estará rodeada por una doble capa eléctrica (d.c.e). Una parte de la d.c.e está formada por la carga distribuida uniformemente sobre la particula, lo que determina la existencia de una densidad de carga superficial. Siendo estrictos, la suposición de que la carga se reparte uniformente no es muy correcta, a causa de la existencia de huecos, sitios de adsorción preferente, grupos químicos ionizables, etc. Sin embargo en general, la distancia media entre grupos cargados sobre la superficie es pequeña y la aproximación se puede considerar valida.

La distribución desigual de la carga a través de la interfase y, por tanto, en la d.c.e. puede originarse por varias causas:

i. ionización de grupos ionogénicos superficiales, que pueden dar lugar a una carga neta sobre la superficie de la partícula,
ii. la desigual adsorción de iones del medio sobre la superficie de las partículas,
iii. la distinta tendencia a disolverse de los iones que forman la red cristalina y

iv. la adsorción y orientación de moléculas dipolares sobre la fase sólida.

La otra parte de la doble capa está formada por el exceso de contraiones (y déficit de coiones) en el medio de dispersión, distribuidos de forma que neutralicen el exceso de carga eléctrica de la superficie. Debido a la difusión térmica, esta capa de iones se extiende desde la superficie de la partícula hacia el seno del medio de dispersión.

Se suele admitir que la d.c.e está compuesta por dos zonas: una región interna, que puede incluir los iones adsorbidos y por tanto, ligados a la superficie, y una región difusa en la cual los iones se distribuyen bajo la influencia de las fuerzas eléctricas y del movimiento browniano. Analicemos ambas partes con objeto de caracterizar la distribución de potencial eléctrico existente en ellas.

### *2.1.2. Parte difusa de la doble capa eléctrica*

Una primera aproximación teórica a la d.c.e se debe a Gouy y Chapman (Hunter et al., 1981), tratamiento que se basa en las siguientes hipótesis:

i. La superficie se supone plana, de extensión infinita y uniformemente cargada.
ii. Se considera que los iones situados en la parte difusa de la d.c.e son cargas puntuales distribuidas de acuerdo con la distribución de Boltzmann.

iii. La estructura de disolvente no influye en la configuración de d.c.e, puesto que se toma para la constante dieléctrica en esta región difusa el valor que posee la del disolvente (véase, sin embargo, la discusión al respecto en Hunter, 1966 , & James, 1979).

Llamemos $\Psi_0$ al potencial eléctrico en la superficie plana y $\Psi$ el potencial a una distancia x desde la superficie hacia el medio de dispersión. Si suponemos la superficie cargada positivamente hacia el medio de dispersión de iones en la que aparece un exceso de aniones (respecto del medio de dispersión), debido a la atracción eléctrica de la superficie cargada, frente a un defecto de cationes (ver figura 2.1).

La fuerza eléctrica entre iones debe competir con la correspondiente componente difusiva, de forma que en el equilibrio, el potencial electroquímico de los iones debe ser constante en cualquier punto, es decir $\nabla \mu_i = - z_i e \nabla\Psi$, donde $z_i$ es la valencia del ion i. Utilizando la aproximación del potencial químico para disoluciones diluidas: $\mu_i = \mu_i^0 + k T \ln n_i$ ; donde $n_i$ es el número de iones del tipo i por unidad de volumen, tenemos que:

$$\ln n_i = -\frac{z_i e}{kt}\nabla\psi \quad [1].$$

Integrando esta ecuación desde un punto en el seno de la disolución donde $\Psi=0$ y $n_i = n_{i,}^{\ 0}$, obtenemos la ecuación de Boltzmann:

$$n_i = n_i^0 \exp\left(-\frac{z_i e \psi}{KT}\right) \quad [2].$$

La densidad de carga por unidad de volumen, ρ, en los puntos donde el potencial es Ψ viene dada por la expresión:

$$\rho = \sum_{i=1}^{N} n_i z_i e \ [3],$$

donde N es el número de especies iónicas.

Por otro lado, existe una relación entre Ψ y ρ a través de la ecuación de Poisson, que para una doble capa plana toma la forma

$$\frac{d^2\psi}{dx^2} = -\frac{\rho}{\varepsilon} \quad [4],$$

donde ε es la permitividad del medio .

Combinando las expresiones [2] y [4] se obtiene:

$$\frac{\mathbf{d^2\psi}}{\mathbf{dx^2}} = -\frac{e}{\varepsilon}\sum_{i=1}^{N} z_i n_i^0 \exp\left[\frac{-z_i e \psi}{KT}\right] [5],$$

Para pequeños valores de Ψ, tales que $z_i e\Psi < kT$, para los que es válida la aproximación $e^{-x} = 1 - x$, tenemos que:

$$\frac{d^2\psi}{dx^2} = k^2\psi \ [6],$$

donde

$$k = \left(\frac{e^2 \sum_{i=1}^{N} z_i^2 n_i^0}{\varepsilon kT}\right)^{1/2} \quad [7].$$

Para lo que se ha tenido en cuenta la condición de electroneutralidad en el medio líquido $\sum_{i=1}^{N} z_i n_i^0 = 0$. Esta aproximación, propuesta por Debye en 1921, proporciona la siguiente solución para la dependencia del potencial con la distancia.

$$\psi = \psi_0 e^{-kx} \text{ [8].}$$

con las condiciones de contorno $\mathbf{\Psi = \Psi_0}$ para $\mathbf{x = 0}$ y $\mathbf{\Psi = 0, d\Psi / dx = 0}$ para $x \rightarrow \infty$.

En el caso de un electrolito simétrico la ecuación diferencial [5] se puede expresar como:

$$\frac{d^2\psi}{dx^2} = \frac{2\, n^0 ze}{\varepsilon} \operatorname{sen} h\left(\frac{ze\psi}{kt}\right) \text{ [9],}$$

donde $n_0 = n_0^{(+)} = n_0^{(-)}$ y $z = z^{(+)} = -z^{(-)}$. Su solución viene dada por:

$$\tan h\left(\frac{ze\psi}{kt}\right) = \tan h\left(\frac{ze\psi_0}{kt}\right) \exp(-kt) \text{ [10],}$$

$k^{-1}$ suele denominarse longitud de Debye-Hückel, puesto que representa el espesor de la d.c.e, o la distancia para la cual el potencial ha disminuido un factor $1/e$ del valor que presenta en la superficie ($\Psi_0$). Un aumento en la concentración de electrolito origina una disminución de $k^{-1}$, es decir una compresión de la d.c.e.

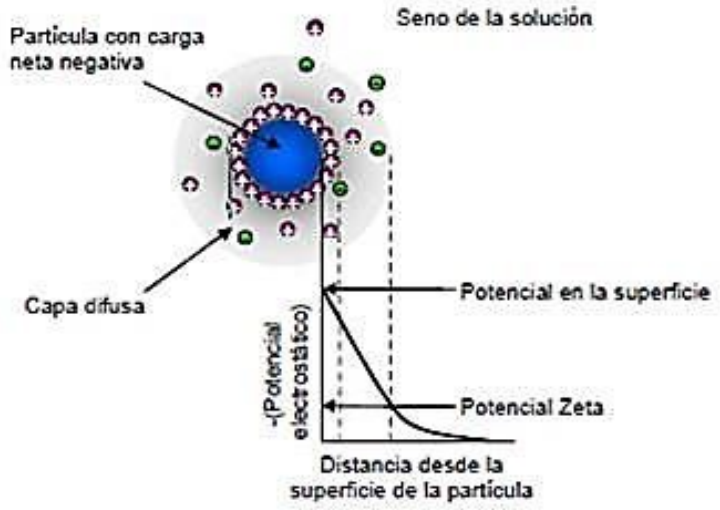


***Figura 2.1.*** Distribución de potencial de la superficie y concentración de iones para una doble capa esférica.

Fuente: Karina Estefanial Leiva Tirado, monografias.com [CC BY-SA LICENCE FREE 3.0 http://creativecommons.org/]

Una vez obtenida la variación del potencial, se puede conocer la distribución de iones a partir de la expresión [2]. Si se considera la aproximación de Debye-Hückel anteriormente mencionada, la distribución de iones positivos y negativos vendrá dada por

$$n_+ = n^0 \left(1 - \frac{ze\psi}{kt}\right) \qquad n_\mp = n^0 \left(1 + \frac{ze\psi}{kt}\right) \qquad [11],$$

donde se observa que los dos tipos de iones experimentan variaciones simétricas de concentración para potenciales bajos. Sin embargo, para potenciales elevados se produce una acumulación de contra-iones y expulsión de co-iones en la d.c.e.. Los contra-iones juegan, por tanto, un papel más importante que los co-iones y por este motivo es posible tratar un

electrolito asimétrico como si fuera simétrico, con valencia igual a la de los contra-iones, sin incurrir en demasiado error (Verwy & Overbeek, 1948) (ver figura 2.2).

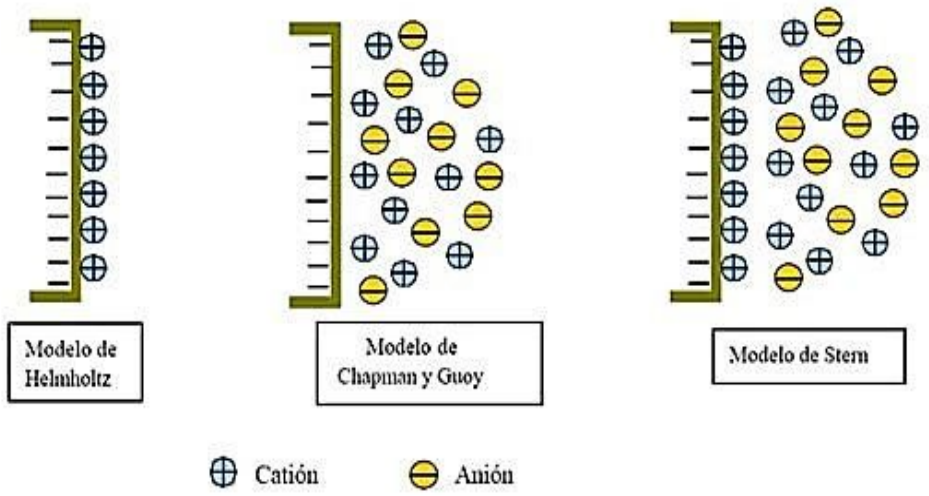


***Figura 2.2***. Modelo de acumulaciones de contraiones y expulsión de coiones: Modelo De Helmholtz, Modelo De Chapman Y Guay Y Modelo De Stern.



La magnitud que da idea del valor de expulsión o acumulación de iones en la d.c.e. es la densidad de iones de tipo i, por unidad de área. Se puede obtener mediante la expresión:

$$r_i = \int_0^{\infty}(n_i - n_i^0)dx = -\frac{2n^0}{k}\left[1 - \exp\left(-\frac{z_i e\psi_0}{2kt}\right)\right] [62],$$

válida para el caso de un electrolito simétrico.

Por otra parte, la densidad de carga sobre la superficie, $\sigma_o$, debe ser igual y de signo contrario a la almacenada en la d.c.e. , para que se cumpla la condición de electro-neutralidad del sistema completo:

$$\sigma_o+\sigma_d=0,$$

en el caso de una superficie plana, existe una expresión analítica para $\sigma_o$:

$$\sigma_0 + \sigma_d = 0 \ [\ 7],$$

que para electrolitos simétricos se reduce a:

$$\sigma_0 = -\int_0^\infty \rho dx = \ -\varepsilon(\frac{d\psi}{dx})_{x=0} \ [\ 8],$$

y para pequeños potenciales

$$\sigma_0 = \ \varepsilon k \psi_0 [15].$$

Es decir, en estas condiciones una d.c.e. tiene una capacidad igual a la de un condensador de placas plano-paralelas con separación $k^{-1}$ entre las mismas.

### *2.1.3. Parte interna de la doble capa eléctrica*

La teoría de Gouy-Chapman presenta algunas limitaciones debido fundamentalmente a que considera los iones del medio como cargas puntuales. El tamaño finito de los iones limita necesariamente la distancia de máxima aproximación a la superficie, que puede ser del orden de un radio iónico hidratado si no hay adsorción específica de iones en la

superficie.En disoluciones diluidas, donde la extensión de la d.c.e. es considerable, no tener en cuenta el tamaño de los iones no introduce demasiado error pero a concentraciones más elevadas las expresiones nos llevan a resultados incorrectos.

Stern propuso en 1924 un modelo en el cual consideraba adsorción especifica de iones y una d.c.e. dividida en dos partes separadas por el llamado plano Stern, localizado a una distancia de aproximación un radio de ion hidratado de la superficie. La parte interna de la d.c.e. está formada por una capa de iones adsorbidos sobre la superficie cargada y se representa en la teoría por una capa superficial concentrada en un plano a pequeña distancia de la superficie, $\delta$, aproximadamente $10^{-8}$ cm, que coincide con los centros de los iones adsorbidos específicamente. La parte externa al plano de Stern constituye la parte difusa de la doble capa, que se extiende desde $x = \delta$ hasta $x \rightarrow \infty$. Por tanto, el tratamiento anterior de Gouy-Chapman es válido con solo reemplazar $\Psi_0$ (potencial superficial) por $\Psi_\delta$ (potencial de Stern).

El decrecimiento del potencial eléctrico en la doble capa de acuerdo con este modelo se presenta en la figura 2.3.

Entre $X=0$ y $X=\delta$ el potencial eléctrico decrece linealmente, y se puede tratar la capa de Stern como un condesado molecular de espesor $\delta$, donde:

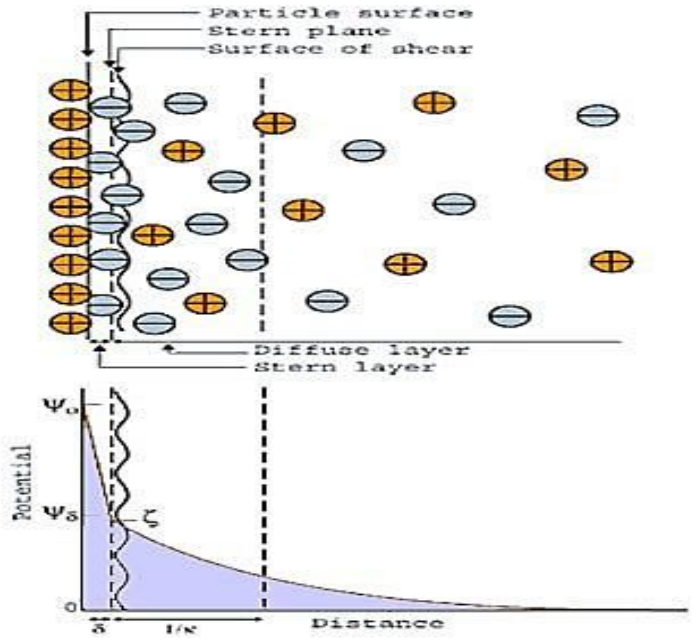


***Figura 2.3***. Representación esquemática de la doble capa eléctrica según la Teoría de Stern.

Fuente: Karina Estefanial Leiva Tirado, monografias.com [CC BY-SA LICENCE FREE 3.0 http://creativecommons.org/]

$$\sigma_d = \frac{\varepsilon'}{\delta} (\psi_0 - \psi_\delta) \text{ [16].}$$

Para describir el equilibrio entre los iones adsorbidos en la capa de Stern y los de la parte difusa de la d.c.e., Stern usa una isoterma de tipo Langmuir. Considerando solamente la adsorción de contra-iones, la densidad de carga superficial $\sigma_\delta$, responde a la expresión:

$$\sigma_\delta = \frac{\sigma_m}{1+\frac{N_a}{n^0 V_m}\exp\left[\frac{ze\psi_\delta+\varphi}{kT}\right]} \text{ [17],}$$

siendo $\sigma_m$ la densidad de carga superficial en el plano de Stern correspondiente a una mono-capa de contra-iones y $V_m$ el volumen molar del disolvente. La energía de adsorción está dividida en dos términos: uno eléctrico ($ze\Psi^0$) y otro de van de Waals ($\phi$). Al aplicar la condición de electro-neutralidad se tendrá:

$$\sigma_o + \sigma_\delta + \sigma_d = 0 \text{ [18]},$$

donde $\sigma_d$ es la densidad de carga de la parte difusa de la d.c.e y viene dada por la ecuación [15] reemplazando $\Psi_0$ por $\Psi_\delta$.

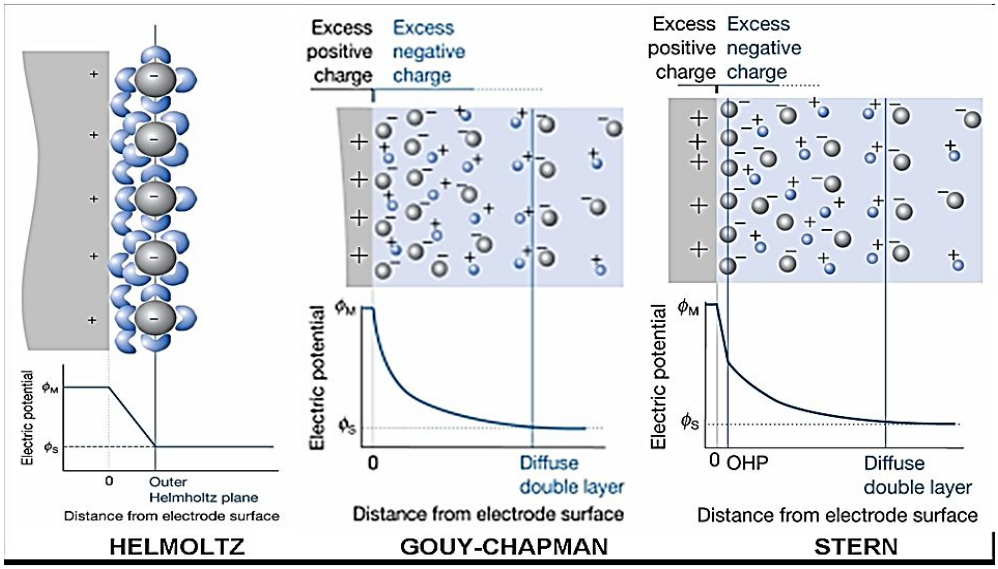


***Figura 2.4***. Doble capa eléctrica según el modelo de Helmoltz, Gouy-Chapman y Stern en la que se representa el Plano Interior de Helmholtz (HP) , El Plano Exterior de Helmholtz (OHP) y el límite de la doble capa difusa.

Fuente: @ Cloelffp www.userscontent2.emaze.com [CC BY-SA LICENCE FREE 3.0 http://creativecommons.org/]

En una versión más moderna de la teoría de Stern, propuesta por Grahame en 1947, la parte difusa de la d.c.e. comienza a una distancia $\delta_2$ desde superficie, donde se sitúa el llamado plano exterior de Helmholtz (OHP), definido por los centros de los iones hidratados en contacto con la superficie. Para distancias $X > \delta_2$ las fuerzas de interacción específicas se consideran despreciables. La distancia mínima de acercamiento de un ion a la superficie $\delta_1$ , definiendo los iones situados a esa distancia un plano llamado plano de Helmholtz (IHP), donde estaría específicamente unidos a la superficie por enlaces covalentes o de van de Waals. Estos iones adsorbidos específicamente están probamente deshidratados al menos en la dirección de la superficie, lo cual les permitirá un mayor acercamiento a esta que en el modelo de Stern clásico. (Ver figura 2.4). Podemos ver un esquema de la doble capa según la versión modificada de la teoría de Stern.

### *2.1.4. Parte interna de la doble capa electrica con simetría esférica.*

Para este tipo de simetría, el potencial eléctrico es función únicamente de la coordenada radial r, distancia al centro de la partícula. La ecuación de Poisson- Boltzmann para este caso toma la forma

$$\frac{1}{r^2}\frac{d}{dr}\left[r^2\frac{d\psi}{dr}\right] = -\frac{e}{\varepsilon}\sum_{i=1}^{N} n_i^0 z_i \exp\left[-\frac{z_i e\psi}{kT}\right] [9],$$

En la aproximación de Debye-Hückel para potenciales pequeños, la Ecuación [19] se reduce a:

$$\frac{1}{r^2}\frac{d}{dr}\left[r^2\frac{d\psi}{dr}\right] = k^2\psi \ [20],$$

que con las condiciones de contorno $\Psi = \Psi_0$ ( r = a, radio de la partícula) y $\Psi = 0$, $d\Psi/dr = 0$ para $r \rightarrow \infty$, se puede integrar para obtener:

$$\psi = \psi_0 a\, r^{-1} \exp[k\,(a - r)] \quad [10].$$

La carga Q sobre la partícula será igual y de signo contrario a la situada en la doble capa:

$$q = -\int_a^{\infty} 4\pi\, r^2 \rho dr = -4\pi\, a^2 \varepsilon \left[\frac{d\psi}{dr}\right]_{r=a} \quad [22],$$

Que en la aproximación de Debye-Hückel puede escribirse:

$$Q = 4\,\pi\,\varepsilon\,a\,(1 + ka)\psi_0 \quad [11].$$

Para partículas tales que el espesor de su doble capa sea pequeño en comparación con el radio de la partícula, estas deben aproximarse a las obtenidas para pequeños potenciales en dobles capas planas. Nótese si a es muy grande frente al espesor de la capa difusa, a/r tenderá a 1 en dicha capa y ka >> 1, por tanto:

$$q = 4\,\pi\,\varepsilon\,k\,a^2\,\psi_0 \quad [12]$$

De donde $\sigma_o = K\,\varepsilon\,\Psi_o$, expresión coincidente con la ecuación [16] para dobles capas planas.

Para potenciales eléctricos elevados, la aproximación de Debye-Hückel no es válida. Müller (Hunter 1981) resolvió numéricamente la ecuación de Poisson-Boltzmann para simetría esférica y sus resultados se encuentran tabulados en la bibliografía (Verwey & Overbeek, 1948).

### *2.1.5. Fenómenos electro-cinéticos. Potencial zeta.*

Cuando se intenta separar la parte móvil de la d.c.e. y la superficie cargada con los contra iones adheridos a ella (que forman parte de la doble capa), se produce los llamados fenómenos electro-cinéticos. En efecto, cuando se aplica un campo eléctrico tiene lugar un proceso de transporte de la fase dispersión, o, al contrario, se produce un campo eléctrico como resultado del movimiento de una fase respecto de la otra. Se conocen cuatros tipos principales de fenómenos electo-cinéticos: electroósmosis, electroforesis, potencial de flujo y potencial de sedimentación (Hunter et al., 1981).

Consideramos con mayor detalle el fenómeno del electro-foresis. Aunque se trata de una propiedad muy general de suspensiones y dispersiones, es sin duda en el estudio de los coloides donde ha encontrado sus principales aplicaciones. La electro-foresis de partículas coloidales es muy similar a la migración iónica en un campo eléctrico, no solo en lo que se refiere a la naturaleza y mecanismos del fenómeno, sino también en cuanto al orden de magnitud de las velocidades alcanzadas: $\approx 1 \mu m s^{-1}$ cuando el campo eléctrico es $\approx 1$ $Vcm^{-1}$ (Overbeek, 1952; Sheldko, 1966). Incluso, algunos métodos de medida de la velocidad electro-forética recuerdan a los utilizados en determinación de numero de transporte de los iones.

Las investigaciones iniciales, realizadas por Quinke hacia mediados de Siglo XIX, llevaron ponto a la idea de que los fenómenos electro-cinéticos y su causa, la presencia de cargas eléctricas en la región límite

entre el líquido y el sólido, no eran excepción sino regla; prácticamente todas las sustancias, tanto orgánicas, como inorgánicas, mostraban movilidad al aplicar un campo eléctrico a las suspensiones, especialmente en agua. La determinación del signo de la carga es trivial, y pronto se pudo comprobar que en la mayoría de los casos la carga superficial de la partícula era negativa. El problema principal radica en determinar cuanta carga lleva la partícula, como está distribuida, como se relaciona con la velocidad medida y el potencial aplicado, etc.

Para poder responder a cualquiera de estas preguntas necesitamos en primer lugar poder medir la velocidad de desplazamiento de las partículas. El método de medida, a parte de estar condicionado por las características de la suspensión (tamaño, concentración de las partículas, estabilidad), esta también muy ligado a las aplicaciones concretas que se vayan a dar a los resultados. Puede decirse que son dos los objetivos principales de los estudios electro-foréticos (Hjerten, 1969; Jirgensonsos & Straumanis, 1965), a saber, la obtención de información acerca de la carga superficial y el potencial zeta de las partículas coloidales, o bien, el análisis y/o separación de los constituyentes de una mezcla de sustancias en disolución, particularmente macro-moléculas.

Las aplicaciones de la técnica de electro-foresis son múltiples en campos científicos muy diversos, en Biología y Bioquímica, en la industria convencional e incluso en tecnologías avanzadas (Ploix et al., 1979).

El comportamiento electro-cinético depende del potencial en la superficie de separación entre la parte de la doble capa rígidamente unida a la partícula y la parte móvil. Este potencial se denomina electro-cinético o potencial zeta ($\zeta$), aunque de los iones de la capa de Stern, una cierta cantidad de disolvente será solidaria con la superficie carada y formará parte de una unidad electro-cinética compacta; es razonable suponer que el plano de deslizamiento pueda localizarse una distancia algo mayor de la superficie que el plano de Stern, y que el potencial $\zeta$ sea en general más pequeño en valor absoluto que $\Psi^{\delta}$ (Kihira & Matijevic, 1992).

Habitualmente se supone la identidad de $\Psi^{\delta}$ y $\zeta$, dada la imposibilidad de determinar experimentalmente el valor de $\Psi^{\delta}$. La diferencia entre ambos potenciales será tanto más pronunciada cuanto más alto sean los valores del potencial y la concentración del electrolito, puesto que la compresión de la parte difusa de la d.c.e. provocará que en el plano de deslizamiento tenga lugar una mayor caída de potencial de $\Psi^{\delta}$ a cero.

El potencial $\zeta$ no se puede determinar por medidas directas, sino que se debe calcular a partir de medidas electro-cinéticas tales como potencial de flujo, potencial de sedimentación, electro-ósmosis o electro-foresis, basadas en los llamados fenómenos electro-cinéticos, que implican el desplazamiento relativo entre las fases sólido/ líquido. En este trabajo se ha llevado a cabo la caracterización electro-cinética de las suspensiones a partir de medias de movilidad electro-forético ($\mu_e$), como describiremos a continuación.

*2.1.5.1. Electro-foresis: determinación experimental de $\mu_e$ y cálculo del potencial zeta.*

Se puede observar que cuando se aplica un campo eléctrico a una suspensión coloidal, se produce una migración de las partículas coloidales hacia uno de los electrodos. Este fenómeno se conoce con el nombre de electro-foresis. En general, todos los fenómenos electro-cinéticos, están directamente relacionados con la naturaleza de la parte móvil de la doble capa y, por tanto, pueden interpretarse en términos de potencial zeta o de la densidad de carga en el plano de deslizamiento, ya que estas magnitudes caracterizan a la movilidad electro-cinética.

La movilidad electro-cinética, ($\mu_e$), velocidad de las partículas por unidad de campo eléctrico aplicado, se relaciona, a través de distintos modelos teóricos, con el potencial ( $\zeta$).

Para una partícula esférica y campos eléctricos débiles, si v es la velocidad de la partícula y E el campo eléctrico aplicado, la relación entre ambas magnitudes es lineal y toma forma:

$$v = \mu_e E \quad [25].$$

Para partículas no esféricas la relación no ha de ser necesariamente lineal, porque la velocidad puede dePENder de la orientación de la partícula respecto al carácter aplicado E.

Es importante conocer el valor de potencial ($\zeta$), tanto para interpretar el comportamiento dinámico de las partículas en presencia de campos eléctricos, como para calcular la energía de interacción electrostática entre

dobles capas eléctricas, que influyen de forma decisiva en la estabilidad de los sistemas dispersos y en los fenómenos de adhesión entre partículas coloides y colectores sólidos. Por ello pasamos a exponer, en síntesis, la teoría más relevante a la dependencia entre $\mu_e$ y el potencial $\zeta$.

*2.1.5.2. Ecuación de Helholtz-Smoluchowski.*

Históricamente, la primera ecuación que relaciono la movilidad observada de una partícula coloidal con el potencial $\zeta$ se debe a Helmholtz e, independientemente, a Smoluchowski. Las hipótesis empleadas por estos autores, pueden resumirse como sigue:

Una partícula en suspensión adquiere carga. La partícula es rígida y de forma arbitraria. La superficie de la partícula o esta con una capa de líquido que se mueve solidaria a ella, posee un potencial $\zeta$ respecto al líquido lejano a la superficie.

Las dimensiones de la partícula son tan grandes que el radio de curvatura en cualquier punto es mucho mayor que el espesor de la doble capa en dicho punto. Además:

- ✓ Se supone que la partícula es no conductora.
- ✓ La conductividad eléctrica del líquido es la misma en la doble capa que fuera de ella.
- ✓ La constante dieléctrica del líquido y su viscosidad son las mismas en todos los puntos.

- ✓ El movimiento de la partícula es lineal y suficientemente lento para que se puedan despreciar los términos inerciales en las ecuaciones hidrodinámicas.
- ✓ El campo eléctrico aplicado, aunque puede distorsionarse por la presencia de la partícula, se suma vectorialmente al campo local de la doble capa.

Con estas hipótesis se obtiene una expresión para la movilidad electro-forética, dada por:

$$\mu_e = \frac{\varepsilon}{\eta}\zeta \quad [13]$$

*2.1.5.3. Ecuación de Debye-Huckel.*

Debye y Hückel propusieron una ecuación de la forma:

$$\mu = C\,\frac{\varepsilon}{\eta}\zeta \quad [27],$$

en la cual la constante C varía con la forma de la partícula y cuyo cálculo requiere un detallado análisis hidrodinámico del sistema. Hückel realizo tal análisis para una partícula esférica encontrando un valor de C=2/3. El modelo basado en la ecuación anterior, aun asumiendo la hipótesis de los modelos de Smoluchowski, no necesita sin embargo la restricción (iii) de dicho modelo. De hecho, solo es válido si la partícula pequeña, $ka \ll 1$.

***2.1.6. Energía potencial de interacción electrostática.***

La energía de interacción entre dobles capas eléctricas $V^{EL}$, puede calcularse como diferencia entre la energía libre del sistema cuando las superficies cargadas están a distancias arbitrarias, H y la energía libre cuando están a distancia infinita:

$$V^{EL} = \Delta G = G(H) - G(\infty)\ [148].$$

G puede calcularse a partir de la densidad de carga y el potencial superficial ( Verwey & Overbeek, 1948):

$$G = -\frac{1}{2}\Sigma\Psi_0\ [29].$$

O, para el caso de dos dobles capas:

$$G = -\frac{1}{2}(\Sigma_1\Psi_{01} + (\Sigma_2\Psi_{02})\ [30].$$

Teniendo en cuenta la relación entre σ y Ψ [Ecuación 14], y la expresión de Hogg et al., 1966 se obtiene:

$$\psi(x) = \psi_{01}\mathrm{Ch}\ kx + \left(\frac{\psi_{01} - \psi_{02}\mathrm{Ch}\ 2kH}{\mathrm{Sh}\ 2\ kH}\right)\mathrm{Shkx}\ [31]$$

Se encuentra

$$\sigma_1 = -\varepsilon\ k\ [\psi_{01}\mathrm{Ch}\ 2\ kH - \psi_{01}\mathrm{Ch}\ 2\ kH]\ [15]$$

$$\sigma_2 = -\varepsilon\ k\ [\psi_{02}\mathrm{Ch}\ 2\ kH - \psi_{02}\mathrm{Ch}\ 2\ kH]\ [163]$$

Y por tanto

$$G(H) = +\frac{\varepsilon k}{2}[2\,\psi_{01}\psi_{02}\,\text{Cosech}\,2kH - (\psi_{01}^2 + \psi_{02}^2)\text{Coth}\,kH]\ [174]$$

Que para H→∞ se transforman en:

$$g(\infty) = -\frac{\varepsilon k}{2}\,(\psi_{01}^2 + \psi_{02}^2)\ [185].$$

Y sustituyendo [34] y [35] en [28], llegamos a:

$$V(H) = -\frac{\varepsilon k}{2}\left[\begin{matrix}(\psi_{01}^2 + \psi_{02}^2)(1 - \text{Cosech}\,2kH) + \\ 2\,\psi_{01}\psi_{02}\text{Cosech}\,2kH\end{matrix}\right]\ [36].$$

Expresión de la energía de interacción electrostática entre dos doble capas plano-paralelas, en función de los potenciales superficiales y de la distancia de separación H.

Con objeto de calcular la energía de interacción entre las dobles capas eléctricas de dos partículas esféricas. Derjaguin (Derjaguin, 1939) introdujo la aproximación de que el espesor de la doble capa es mucho menor que el radio de las partículas; y realizo el cálculo como suma de iteraciones entre planos infinitesimales. Considerando que la energía potencial de interacción entre las dos doble capas se pueden expresar como:

$$V_R = \int_0^{-} 2\pi h v^{EL} dh\ [19],$$

donde $V^{EL}$ viene dado por la expresión [37], y h es la distancia entre particulas.

Atendiendo a la geometría del sistema podemos escribir que:

$$H - H_0 = r_1 + r_2 - \sqrt{r_1^2 - h^2} - \sqrt{r_2^2 - h^2}\ [208].$$

Diferenciado esta expresión tenemos:

$$dH = \left( \frac{1}{r_1 \sqrt{\frac{1-h^2}{r_1^2}}} + \frac{1}{r_2 \sqrt{\frac{1-h^2}{r_2^2}}} \right) h\, dh\ [219].$$

Si consideramos $h << r_1, r_2$ tenemos:

$$h\, dh \sim \left(\frac{r_1 r_2}{r_2 + r_1}\right) dh\ [40].$$

Y sustituyendo en la ecuación 36 obtenemos:

$$V_R = \frac{2\pi r_1 r_2}{r_2 + r_1} \int_{h_0}^{\infty} V^{EL}(H) dH\ [41].$$

La integral se puede resolver analíticamente y se obtiene:

$$V_R = \frac{\pi \varepsilon_r \varepsilon_0 r_{12} r_2 (\psi_{01}^2 + \psi_{02}^2)}{4(r_1 + r_2)}$$

$$\left[\frac{2\psi_{01}\psi_{02}}{(\psi_{01}^2 \psi_{02}^2)} \operatorname{Ln}\left(\frac{1+\exp(-kH)}{1-\exp(-kH)}\right) + 1(1 - \exp(-2kH))\right]\ [42].$$

Ecuación validad cuando $\Psi_{01}$ y/o $\Psi_{02}$ sean del orden de 25 mV, y para condiciones en las cuales el espesor de la doble capa es pequeño comparado con el tamaño de las partículas, aunque proporciona una buen aproximación para valores de $\Psi_{01}$ y $\Psi_0$ del orden de hasta 50-60 mV (Hogg

et al., 1966) e incluso de hasta 100 mV cuando $\Psi_{01}$ y/o $\Psi_{02}$ son suficientemente diferentes (Kihira et al., 1992).

Si en la expresión 36 consideramos $r_2 \rightarrow \infty$ se obtiene (Nelligan et al., 1981):

$$V_R = \pi\varepsilon_r\varepsilon_0 r_1$$
$$\left[(\psi_{01}^2 + \psi_{02}^2)^2 \,\mathrm{Ln}\,(1 + e^{-kH} + (\psi_{01} + \psi_{02})^2 \mathrm{Ln}\,(1 - e^{-kH})\right] [43]$$

corresponde a la energía de interacción entre la doble capa esférica y otra plana.

## 2.2. Interacción Lifshitzvan der Waals.

### *2.2.1. Entre átomos o molécula en el vacío.*

La existencia de una interacción atractiva entre moléculas o entre átomos se propuso inicialmente por van de Waals para interpretar las propiedades de los gases y líquidos no ideales. Esta interacción, de naturaleza distinta de la covalente y de la electrostática, se conoce como interacción de van de Waals.

El estudio de la naturaleza de este tipo de interacción se llevó a cabo en una serie de trabajos de Keesom, Debye y London, publicados en el primer tercio de este siglo (Keesom, 1921; Debye, 1921; London, 1930). Según estos autores, cuando dos átomos o moléculas se encuentran en el vacío, se puede considerar tres distribuciones diferentes en la interacción de van de Waals:

- Interacción entre dipolos permanentes o fuerzas de orientación descritas por Keesom;
- Interacción entre dipolos permanentes y dipolos inducidos en otros átomos o moléculas (fuerzas de inducción de Debye);
- Interacción que se produce entre dipolos instantáneos originados por fluctuaciones de carga eléctrica y dipolos inducidos ( fuerza de dispersión de London)

Obviamente, las interaccionas de Keesom y Debye aparecen cuando intervienen moléculas o átomos de carácter dipolar permanente. Por el contrario, las de tipo London son universales y están presentes en todas las interacciones átomo-átomo o molécula-molécula, siendo por ello las más importante en la descripción de las interacciones entre cuerpos macroscópicos en fase condensada (Fowkes, 1983). Se ha demostrado (Chaudhury, 1986) que las interacciones entre cuerpos macroscópicos en fase condensada son principalmente de dispersión (London- van de Waals), siendo la contribución neta de los otros dos tipos, del orden de 2-3%.

Las tres contribuciones citadas a la energía de van de Waals decrecen con sexta potencia de la distancia H que separa al par de átomos o moléculas (Overbeek, 1952).

$$V_{Keeson} = -\frac{\mu^4}{kTH^6}\,[22].$$

$$V_{Debye} = -\frac{\alpha\mu^2}{H^6}\,[45].$$

$$V_{London} = -\frac{3}{4}\frac{h\upsilon\alpha^2}{H^6}[46].$$

donde k es la constante de Boltzmann y T es la temperatura absoluta. En estas expresiones, μ es el momento dipolar del átomo, α su polarizabilidad, h la constante de Plank y ν la frecuencia de dispersión. Es frecuente rescribir ecuación 3 en la forma:

$$V_{ii} = -\frac{\beta_{ii}}{H^6} \text{ [47]},$$

con $\beta_{ii}=3/4\ \alpha^2 h\nu$ esta constante suele escribirse en función de la denominada de Hamaker, $A_{ii}$ como:

$$A_{ii} = \pi^2 q_I^2 \beta_{ii} \text{ [48]},$$

donde $q_i$ es el número de átomos por unidad de volumen.

Para dos materiales i y j, la constante $\beta_{ij}$ puede expresarse como la media geométrica de las que corresponden a las fases individuales:

$$\beta_{ij} = \sqrt{\beta_{ii}\beta_{jj}} \text{ [23]}.$$

O usando la ecuación 49,

$$A_{ij} = \sqrt{A_{ii}A_{jj}} \text{ [5024]}.$$

Que nos da la constante de Hamaker para un sistema formado por dos fases a partir de las propiedades individuales de cada una de las fases constituyente.

***2.2.2. Entre fases condesadas.***

Hamaker (Hamaker, 1936) fue el primero en calcular la energía de interacción dispersiva para cuerpos macroscópicos como suma de las propiedades individuales de las moléculas (suponiendo que estas propiedades son aditivas y no retardadas). Utilizando esta aproximación, la energía total de dispersión de London para un sistema formado por fases distintas de un mismo material, con interfases planas, infinitas y paralelas separadas una distancia *H*, en aire o en vacío (siendo H del orden de unos diámetros atómicos), toma la forma:

$$V^{LW} = -\frac{A}{12\,\pi H^2}\,[51],$$

donde, como hemos dicho anteriormente, A es la constante de Hamake.

Se admite que cuando una material 1 se encuentra inmerso en un medio 3, o cuando dos materiales distintos de 1 y 2 están separados por un tercer medio, 3 se puede escribir (Visser, 1972).

$$A_{131} = A_{11} + A_{33} - A_{13}\,[52],$$

$$A_{132} = A_{12} + A_{33} - A_{13} - A_{23}[53],$$

Partiendo de la ecuación 51, podemos escribir las ecuaciones 53 de la forma:

$$A_{131} = \left(\sqrt{A_{11}} - \sqrt{A_{33}}\right)^2\,[54],$$

$$A_{132} = \left(\sqrt{A_{11}} - \sqrt{A_{33}}\right)^2\left(\sqrt{A_{22}} - \sqrt{A_{33}}\right)^2\,[25],$$

donde podemos observar que $A_{131}$ puede ser positivo o nulo, mientas que $A_{132}$ puede tomar valores negativos si (Viseer, 1972):

$$A_{11} > A_{33} > A_{22} \text{ [266]}$$

$$A_{11} < A_{33} < A_{22} \text{ [277]}$$

Puede ocurrir, por tanto, que la energía de London- van der Waals sea repulsiva, posibilidad que ya fue contemplada por Hamaker en 1938 y por Derjaguin en 1954.

Podemos concluir, diciendo que la interacción Liifshitz-van der Waals entre dos moléculas iguales es siempre atractiva o nula y que lo mismo ocurre entre dos moléculas o partículas iguales inmersas en un líquido (véanse ecuaciones 56 y 57). Pero cuando dos materiales diferentes 1 y 2 interaccionan inmersos en un líquido 3, con $A_{11}$ diferente $A_{22}$, las ecuaciones 56 y 57 predicen situaciones en las que energía de interacción dispersiva puede ser repulsiva.

Si admitimos la ditivadad propuesta por Hamaker (Hamaker, 1937), para el caso de dos esferas idénticas de radio R separadas una distancia H, en una primera aproximación (R<<H), la energía de interacción dispersiva se puede expresar como:

$$V^{LW} = -\frac{AR}{12H} \text{ [288].}$$

Mientras que la fuerza entre ambas esferas sería:

$$F^{LW} = \frac{AR}{6H^2}\ [299].$$

Para dos planos infinitos y paralelos se obtiene (Nir 1976):

$$\Delta V = -\frac{A}{12\pi H^2}\ [6030].$$

Y la correspondiente expresión para la fuerza:

$$F = \frac{A}{6\pi H^3}\ [311].$$

La situación experimental que nos interesa en esta Memoria es la adhesión de partículas coloidales de forma esférica y tamaño controlado sobre diferentes sustratos. Estos se presentaran ante las partículas como planos semi-infinitos, en cuyo caso la energía potencial de van de Waals toma la forma (Visser & Matijevic, 1976)

$$V^{LW} = \frac{A_{132}}{6}\left[\mathrm{Ln}\left(\frac{H+2a}{H} - \frac{2a\ (a+H)}{H(H+2a)}\right)\right]\ [62]$$

Siendo a radio de la esfera y H la distancia de separación entre la superficie de esta y el plano. Haciendo en ecuación 62 la aproximación H >>a se obtiene:

$$V^{LW} = -\frac{A_{132}a}{6H}\ [323].$$

La tabla 2.1 muestra de forma resumida las expresiones de $V^{LW}$ para las diferentes configuraciones geométricas (van Oss et al., 1994)

**Tabla 2.1.** Expresiones de $V^{LW}$ para diferentes configuraciones geométricas.

| **Configuración** | $\boldsymbol{V^{LW}}$**(H)** | $\boldsymbol{F^{LW}}$ **(H)** |
|---|---|---|
| Planos semi-infinitos paralelos | $\frac{A}{12\pi H^2}$ | $\frac{A}{12\pi H^3}$ |
| Esferas de radio a y un plano | $-\frac{A_{132}a}{6H}$ | $\frac{A_{132}a}{6H^2}$ |
| Dos esferas de radio a | $\frac{A_{132}a}{12H}$ | $\frac{A_{132}a}{12H^2}$ |

## 2.3. Interacciones entre superficies en medio acuoso: las fuerzas de solvatación.

El objetivo de este apartado de nuestra Memoria es analizar la situación actual de los conocimientos sobre las denominadas fuerzas no-DLVO (diferentes de las electrostáticas entre dobles capas eléctricas y de las de van der Waals). Entre estas fuerzas cabe incluir las denominas "de hidratación", enlaces de hidrógeno, enlaces π, las llamadas interacciones "hidrofóbicas", o la presión osmótica en suspensiones muy concentradas de polímeros. De este conjunto, las que han sido estudiadas en mayor profundidad, tanto desde su origen en la solvatación de las superficies (por ello se ha denominado "estructurales"), siendo atractivas en unos casos (efecto "hidrofóbico") y repulsivas en otros ("presión de hidratación"). Existen estudios rigurosos sobre las mismas desarrolladas durante las últimas decadas, llevados a cabo fundamentalmente por el grupo de J. Israelachvili (Israelachvili, 1992 &1995). y van Oss y cols. (van Oss et al., 1993 y 1994) basado en criterios termodinámicos. Según estos últimos, es

posible englobar todo este tipo de interacciones bajo la denominación general de interacciones electrón-receptor electrón-donante, o ácido-base (en el sentido de Lewis).

Muchas dispersiones coloidales de partículas hidrofílicas (tales como algunas arcillas o sílice) y la mayoría de las superficies biológicas y de macromoléculas, pueden permanecer estables (las interfases se mantiene separadas) en el seno de un medio de dispersión acuoso, incluso cuando existe una elevada concentración salina o ausencia de carga neta superficial. Este hecho se ha explicado convencionalmente como consecuencia de una "hidratación repulsiva" o "fuerza estructural" debida a la ordenación de las moléculas de agua en torno a la superficie. Si se tienen en cuenta los resultados experimentales se pueden enunciar una interpretación según la cual estas fuerzas aunque, en este caso, se denominan "hidrofílicas" o de hidratación pueden ser monótonamente repulsivas, atractivas e incluso oscilatorias. La repulsión hidrofílicas estaría originada (Israelacvili, 1992; Israelacvili, 1995; Pashley, 1992), por interacciones de carácter entrópico de corto alcance, aunque ambos aspectos son aún hoy materia de controversia y en continuo desarrollo, por el avance de las técnicas utilizada para su estudio.

El agua, usualmente utilizada como medio de dispersión tiene propiedades, que son poco comunes si no únicas. Su complejidad deriva de la combinación de factores, su pequeño tamaño y la distribución tetraédrica de la carga en la molécula de agua, lo que da lugar a intensas interacciones por enlaces de hidrógeno con un alto grado de direccionalidad. Del mismo

modo se pueden producir enlaces fuertes con otros disolventes polares y con compuestos "hidrofílicos" lo que le confiere excelentes propiedades como disolvente de una amplia gama de moléculas de iones, y como medio de suspensión de partículas coloidades, micelas, vesículas, y estructuras biológicas tales como proteínas y células. Incluso se encuentra con frecuencia que moléculas o partículas no cargadas son miscibles son agua (observación que llevo a Langmuir y Derjaguin a postular la existencia de una fuerza repulsiva que parecía de "hidratación" era originada por agua). Se creyó, en principio, que esta fuerza de "hidratación" era originada por una primera capa de moléculas de agua fuertemente unidas y orientadas sobre superficies hidrofílicas en contacto con ella, de tal modo que impediría la aproximación entre dos superficies a distancias menores de aproximadamente 5 Å (la longitud de dos moléculas de agua). Existirían evidencias fiables, tanto teóricas como experimentales, de la existencia de esta capa "primaria" de hidratación. Además, es relativamente común encontrar fuertes interacciones soluto-disolvente en muchos sistemas binarios. Sin embargo, para explicar una fuerza de repulsión que supera a la de atracción de van der Waals, tanto en magnitud como en alcance, es necesario que esta fuerza se propague más allá de dos capas moleculares, y aquí es donde surge el problema.

Parece lógico que la primera capa de moléculas enlazadas y orientadas origine la aparición de una segunda capa de manera similar, y esta a su vez, la de una tercera y así sucesivamente. De este modo, tendríamos la imagen de unas superficies recubiertas por moléculas de agua estructurada, que presentan una fuerte oposición a ser desordenadas o

"deshidratadas", dando lugar a una fuerza repulsiva entre dos superficies que tienden a aproximarse en un medio acuosos. Se ha sugerido que el alcance de esta interacción puede variar en el intervalo entre el nanómetro y la micra (Israelacvili, 1992; Skavarla & Kmet, 1991; van Oss et al., 1994). Y se han propuesto varias teorías fenomenológicas basadas sobre las peculiaridades de las interacciones agua-agua. En todo caso, hace solo veinte años que se ha propuesto una explicación cuantitativa coherente sobre la naturaleza de estas interacciones ácido-base de Lewis en el seno de la suspensión acuosa.

Durante los últimos cuarenta años se ha desarrollado algunas técnicas de media directa de las fuerzas entre superficies en este tipo de sistemas (particularmente con el "aparato de fuerza superficial" desarrollado por el grupo de Israelacvili, entre superficies de mica o de sílice, v. Israelacvili et al., 1992), y parece demostrado que la teoría clásica DLVO no permite explicar muchos de los resultados obtenidos. Pero el hecho sorprendente fue el hallazgo de que estas fuerzas adicionales (no-DLVO) no son siempre repulsivas; sino que pueden ser atractivas (como es el caso de las denominadas interacciones hidrofóbicas) e incluso oscilatorias.

Una posibilidad alternativa (Israelacvili, 1994), sobre el origen de las repulsiones observadas, consiste en analizar no solo la propiedades especiales del agua o de las interacciones agua-agua, sino también el papel que juega la naturaleza físico-química e la superficies presentes. Esto es, considerar cuidadosamente las fuerzas que pueden aparecer entre los grupos moleculares específicos de las partículas en suspensión y/o orientados hacia

la fase liquida, tales como las bicapas de tensioactivos adsorbidos o los grupos moleculares, resulta sorprendente como su presencia puede aumentar sustancialmente el alcance de las fuerzas repulsivas. Bajo este punto de vista, el origen de estas fuerzas, y la explicación de muchos de los fenómenos gobernados por interacciones entre partículas coloidales o macromoléculas biológicas, en una suspensión acuosa adquiere un enfoque completamente diferente. Si este enfoque es correcto, ya que no deberíamos considerar que las fuerzas repulsivas, que evitan el contacto entre grupos hidrofílicos superficiales, como es el caso de las proteínas, tengan su origen en la oposición que presentan las capas de moléculas a ser "desplazadas" o "desordenadas". Por el contrario, la presencia de "grupos superficiales" les hace participar activamente en la interacción con las moléculas de agua produciéndose, como resultado final, (una situación en la que la fase dispersa es la configuración termodinámicamente más favorecida). En conclusión, como sugiere ISRAELACVILI en sus primeros trabajos (Israelacvili, 1994), para controlar los efectos de este tipo de fuerzas, deberíamos fijar nuestra atención más sobre las modificaciones de la naturaleza físico-química de las superficies que sobe las posibles alteraciones en la configuración del disolvente. Podremos así actuar en la forma deseada tanto en problemas de homo y heterocoagulación de dispersiones coloidales, como en otros importantes campos de aplicación técnica (p.ej. deslizamientos de suelos cohesivos, recuperación de suelos.

La determinación directa de los valores que alcanza este tipo de fuerzas exige disponer de dispositivos capaces de medir fuerzas a distancias de separación del orden del nanómetro, para superficie muy pulidas (mica).

No obstante para superficies rugosas de partículas de tamaño coloidal dispersas en medio acuosos, no existen, que nosotros sepamos, dispositivos capaces de detectar directamente la fuerza en juego. En consecuencia, como por otra parte también se hace para las fuerzas electrostáticas y de van de Waals, será necesario utilizar modelos que permitan determinarlas indirectamente. Entre estos modelos cabe citar el modelo termodinámico enunciado por van Oss y cols. (van Oss et al., 1994). Según este modelo, las fuerzas de hidratación pueden considerarse como una subclase de las interacciones ácido-base de Lewis, en las que las relaciones entre grupo electrón-donantes (base de Lewis) y electrón-receptor (ácido Lewis) determinan el efecto repulsivo considerado. A ello dedicaremos el siguiente apartado.

## 2.4. Estimación de las energías de interacción Lifshitz-van der Waals y ácido base.

### *2.4.1. Tensión superficial y tensión interfacial.*

Nos hemos referido ya en los apartados anteriores a los aspectos más sobresalientes y al origen físico de las fuerzas interfaciales que pueden influir en los procesos de adhesión. Lo que nos interesa ahora es que, de la misma manera que la caracterización eléctrica superficial nos da idea del alcance e intensidad de la repulsión eléctrica entre las interfases, es posible obtener el de las restantes interacciones interfaciales (Lisfshitz van der Waals, LW, y ácido-base, AB) si se lleva a cabo una caracterización termodinámica completa de las superficies.

Partiremos para ello del siguiente razonamiento: Consideremos el proceso reversible de acercamiento entre dos cilindros de un sólido o líquido, 1, hasta formar una fase continua (ambos cilindros tienen bases de área unidad). Supondremos que inicialmente las superficies que se destruyen en el proceso, están en el vacío (Good, 1993). Llamaremos energía libre de cohesión, $\Delta G_{1,c}$ , a la variación de energía libre que tiene lugar en el proceso, y trabajo de cohesión, $W_{1,c}$ , al opuesto de esta magnitud; a partir de ella se puede definir la tensión superficial del material 1, $\gamma^1$, como:

$$\Delta G_1^C = -W_1^C = -2\,\gamma_1\ [64],$$

donde el factor 2 obedece a que al unir los dos cilindros desaparecen dos interfases.

Si ahora imaginamos un proceso reversible similar con cilindros de dos materiales distintos, 1 y 2, hablaremos de energía libre de adhesión (Ver figura 11 b), $\Delta G_{12,a}$ , mientras que su opuesto recibe el nombre de trabajo de adhesión, $W_{12c}$ ; en este caso se destruyen las interfases 1-vacio y 2-vacio, pero se crea la 1-2. Definimos entonces la tensión superficial, $\gamma^{12}$, mediante:

$$\Delta G_{12}^{\alpha} = -W_{12}^{a} = \gamma_{12} - \gamma_1 - \gamma_2\,[335],$$

que es la conocida ecuación de Dupré (Adamson, 1982).

Supongamos que el proceso consiste en unir dos cilindros como descritos, de materiales 1 y 2 en un medio líquido 3; desaparecerán dos interfases 1-3 y 3-2 creándose en cambio la 1-2, con lo que la ecuación de Dupre se escribirá:

$$\Delta G_{132} = \gamma_{12} - \gamma_{13} - \gamma_{23}\,[346].$$

Esta variación de energía libre nos dará una medida de la energía de interacción no electrostática entre los materiales 1 y 2 en el medio 3. Si se trata de dos cilindros idénticos de material 1, entonces

$$\Delta G_{131} = -2\gamma_{13}\ [357],$$

y estaremos en el caso de interacción entre, por ejemplo partículas idénticas en suspensión en medio líquido.

La tensión interfacial está relacionada con las fuerzas de interacción que las superficie de las fases 1 y 2 se ejercen entre sí (cohesión) o con las de la otra fase (adhesión). Si encontramos un método de determinación de $\gamma_1$ y $\gamma_2$, es decir, si caracterizamos termodinámicamente los materiales implicados o, mejor, sus superficies, obtendremos información acerca de la interacciones presentes en la interfase, del mismo modo que el potencial $\zeta$ ( o las magnitudes con él relacionadas) nos permiten evaluar las interacciones de naturaleza electrostática.

### *2.4.2. Modelo de van Oss, Goog y Chaudhury*

*2.4.2.1. Antecedentes.*

La ecuación de Dupre que no da la energía libre de adhesión entre dos materiales diferentes, aunque confirmada ampliamente por la experiencia, solo es válida cuando la interacción existente entre un material 1 y otro 2 o del primero consigo mismo es de tipo dispersivo (no polar). Esto representa una restricción importante, puesto que tenemos que estimar la interacción interfacial completa, y no solo su componente dispersiva, utilizando parámetros individuales de las fases en contacto.

Fowke, en 1963, relaciono la tensión superficial con los distintos tipos de interacciones intermoleculares que tiene lugar en la interfase. Sugirió la descomposición de esta magnitud en varias componentes, cada una de las cuales se correspondía a un tipo de interacción intermolecular:

$$\gamma_i = \sum_j \gamma_i^j \ [68],$$

donde el superíndice j se refiere a los distintos tipos de interacciones: dispersión (London), dipolo-dipolo, dipolo-dipolo inducido, y a todo un conjunto de interacciones que no presentan el mismo carácter que las anteriores, tales como puentes de hidrógeno, enlaces $\tau$ o enlace metálico. La necesidad de evaluar la contribución a la tensión superficial de estas interacciones no dispersivas, ha llevado a algunos autores a definir una componente, $\gamma^n$, de la tensión superficial, que reuniría estas contribuciones, llamadas de no-dispersión por unos, y polares por otros. Podríamos escribir la componente como:

$$\gamma^{n} = \gamma - \gamma^{d}\ [69],$$

donde en $\gamma^{d}$ se incluyen las contribuciones de carácter dispersivo. De la misma manera forma par ale trabajo de adhesión tendremos:

$$W_A^n = W_A - W_A^d\ [70].$$

Basándose en la Ec. [69], (Owens & Wendt, 1969; Kaelbe, 1970; Kaelbe & Cirlin, 1971 y Wu, 1970, 1971) propusieron sucesivamente tres modelos, en los que se expresaba la tensión interfacial, $\gamma^{12}$, en función de las tensiones superficiales de las fases individuales, y de sus componentes de dispersión y no dispersión, $\gamma_d$ y $\gamma_n$. estos modelos se pueden considerar como una extensión del de Fowkes. En ellos se expresan la componentes no dispersiva del trabajo de adhesión, $W^{An}$, en función de las componentes de no dispersión de las tensiones superficiales de las dos fases. Utilizando para ello medias geométricas o armónicas.

Sin embargo, Fowkes nunca expresó los términos de no dispersión del trabajo de adhesión como función de las componentes de la tensión superficial de las fases en contacto. Por el contrario, siempre mantuvo que tal expresión era imposible, por no ser aditivas dichas interacciones. A pesar de ello, todas las propuestas mencionadas se han utilizado ampliamente durante los últimos cuarenta años. Las objeciones y críticas empíricas no han sido justificadas teóricamente hasta los últimos años (Fowkes et at., 1990).

Good y Girifalco, que consideraban errónea la descomposición antedicha de la tensión superficial, presentaron a principios de los años sesenta otro modelo alternativo (Grifalco & Good, 1957b; Good, 1953). El punto de partida consiste en relacionar la energía libre de adhesión de dos sustancias inmiscibles 1 y 2, $\Delta G_{A12}$, con la media geométrica de las energías libres de cohesión de cada una de ellas, según:

$$\Delta G_{A,12} = \sqrt{\Delta G_{C,1}\,\Delta G_{C,2}} = 2\sqrt{\gamma_1\gamma_{21}}\,[71].$$

Ya que la tensión superficial de una fase i se define también como la mitad del cambio de energía libre de cohesión del material en el vacío (Good, 1967):

$$\Delta G_{C,I} = -2\,\Gamma_I\,[31] \text{ y}$$

$$\gamma_{12} = \gamma_1 + \gamma_2 - 2\sqrt{\gamma_1\gamma_2} = [\sqrt{\gamma_1} - \sqrt{\gamma_2}]^2\,[72].$$

Ecuación que permite la predicción de la tensión interfacial a partir de las tensiones superficiales individuales. Al ensayar está ecuación se comprobó que las predicciones eran adecuadas cuando las parejas de líquidos eran ambos, o bien muy polares, o completamente no-polares, es decir, cuando las fuerzas intermoleculares de cada fase fuesen del mismo tipo. Examinando las teorías de London y Keesom sobre intermoleculares, se comprobó que, para estos sistemas, la componente dominante de las fuerzas entre pares de moléculas semejantes. Parecía razonable pensar que lo mismo ocurrirá entre moléculas a través de la interfase Goody Girifalco propusieron llamar a las interfases en los sistemas en los cuales las fuerzas

dominantes cohesivas y adhesivas son del mismo tipo, "interfases regulares".

Para el resto de los sistemas "no regulares", como por ejemplo agua-hidrocarburo, parecía razonable introducir en la Ec.[31] un coeficiente empírico, característico de la interfase, definido como:

$$\Phi \equiv \frac{\gamma_1+\gamma_2+\gamma_3}{2\sqrt{\gamma_1\gamma_2}} \equiv -\frac{\Delta G_{A,12}}{\sqrt{\Delta G_{C,1}\,\Delta G_{C,2}}} \text{ [73].}$$

Con lo que resulta:

$$\gamma_{12} = \gamma_1 + \gamma_2 - 2\Phi\sqrt{\gamma_1\gamma_2} \text{ [74].}$$

Naturalmente, las ecs.[73] y [74] no tiene más contenido físico que el de las definiciones de energía libre de adhesión y de cohesión. Lo que dio cierto interés a esta ecuación fue el valor predictivo del parámetro Φ. En efecto, para todas las interfases regulares, Φ=1. Para el resto de los sistemas, se valuó Φ haciendo uso de la Ec.[74] y de las energías de adhesión y cohesión, calculadas mediante suma de las energías de interacción existentes a través de una interfase plana, considerando potenciales de interacción tipo Lennard-Jones. De esta forma, es posible calcular Φ mediante expresiones que contienen propiedades moleculares, como el momento dipolar, μ, la polarizabilidad molecular, y la energía de ionización, I, aparte de otros coeficientes geométricos. La expresión de Φ en función de estos parámetros, presentada por Good & Elbing (1970), es la siguiente:

$$\Phi = \frac{\frac{3}{4}\alpha_1\alpha_2\frac{2I_1I_2}{I_1+I_2}+\frac{\alpha_1\mu_2^2+\alpha_2\mu_1^2}{2}+\frac{\mu_1^2\mu_2^2}{3kT}}{\sqrt{\left(\frac{3}{4}\mu\alpha_1^2I_1+\alpha_1\mu_1^2+\frac{\mu_1^4}{3kT}\right)\left(\frac{3}{4}\mu\alpha_2^2I_2+\alpha_2\mu_2^2+\frac{\mu_2^4}{3KT}\right)}} [75]$$

donde T la temperatura y k la constante de Boltzmann.

Las predicciones de esta teoría no son muy correctas en el caso de que las moléculas de alguna de las fases no generen campos de fuerzas con simetría esférica. Es el caso de los compuestos nitro-aromáticos cuando interaccionan con moléculas como, por ejemplo, agua. Para el sistema nitro-benceno/agua y otros compuestos nitro-aromáticos, el valor experimental de $\Phi$ es aproximadamente 0.80, mientras que los valores que se predicen están en el rango 0.91-0.96. con todo, el modelo es de aplicabilidad bastante general y, cuando se dispone de información relativa a las propiedades moleculares, puede estimarse $\Phi$, y obtenerse valores de $\gamma^{ij}$ mediante la ecuación [74], que concuerdan muy bien con los valores experimentales.

Neumann y col. (Neumann et al., 1974; Ward & Neumann, 1974), basadose en los datos experimentales de Zisman y col. (Bernett & Zisman, 1962; Ellison & Zisman, 1954; Fox & Zisman 1952; Shafrin & Zisman, 1962) encontraron la existencia de una relación lineal entre $\Phi$ y $\gamma_{12}$:

$$\Phi = -\alpha\gamma_{12} + \beta \qquad [7636],$$

donde $\alpha$ y $\beta$ son constantes empíricas, cuyos valores eran próximos a 0.0075 y 1, respectivamente. Con ello se confirmaba la validez de la ecuación empírica (denominada “de estado” por Neumann y col.) propuesta por Shell y Neuman, que expresaba $\gamma_{12}$ únicamente en función de $\gamma_1$ y $\gamma_2$ :

$$\gamma_{12} = \frac{[\sqrt{\gamma_1}-\sqrt{\gamma_2}]^2}{1-0.0015\sqrt{\gamma_2\gamma_1}}\,[77].$$

La ecuación de estado de Neumann ha sido muy criticada en los últimos años. Según Fowkes et al., (1990) su punto más débil es que se ignora cualquier contribución química a la tensión superficial o interfacial, y trata estas propiedades como resultado de interacciones tipo van der Waals. En términos simples, puede afirmarse que la Ec.[76] predice resultados correctos cuando se refiere a sólidos o líquidos en los que no existe contribuciones polares a la energía de cohesión. Cuando interviene el agua o alcoholes, por ejemplo, a los resultados se alejan totalmente de la realidad, ya que se ignoran las contribuciones de los puentes de hidrógeno a las energías de cohesión de los líquidos.

*2.4.2.2. Modelo de van Oss, Good y Chaudhury*

Las aportaciones más recientes sobre la interpretación de la tensión superficial y sus componentes se deben a van Oss y Good y a Fowkes. Ambos tratamientos tienen en común que contemplan dos clases de interacciones en el estado condensado: las de van de Waals y las interacciones ácido-base de Lewis o interacciones electrón-receptor/electrón-donante. La principal aportación de ambos grupos consiste en la interpretación de lo que hasta entonces se venía llamando componente "polar" de las interacciones interfaciales, así como en la propuesta de procedimientos experimentales para estimar los parámetros que caracterizan dicha interacción.

A continuación expondremos en síntesis el modelo de van Oss y cols. (van Oss et al., 1994).

La componente LW de la tensión interfacial, $\gamma_{12}{}^{LW}$, puede expresarse mediante la regla de Good-Girifalco:

$$\gamma_{12}^{LW} = \left[\sqrt{\gamma_1^{LW}} - \sqrt{\gamma_2^{LW}}\right]^2 = \gamma_1^{LW} + \gamma_2^{LW} - 2\sqrt{\gamma_1^{LW}} - \sqrt{\gamma_2^{LW}} \text{ [78].}$$

Donde $\gamma_1{}^{LW}$ y $\gamma_2{}^{LW}$ son las componentes Lifshitz-van der Waals de las tensiones superficiales de las fases 1 y 2, respectivamente.

Aunque las interacciones entre las sustancias apolares pueden ser exclusivamente de tipo LW, no ocurre así en el caso de sustancias polares, que siempre sitios polares y apolares. Así, para dos sustancias polares 1 y 2, la energía libre total de adhesión se puede expresar como:

$$\Delta G_{A,12}^{TOT} = \Delta_{A,12}^{LW} + \Delta_{A,12}^{AB} \text{ [79].}$$

El término de adhesión LW se expresa, al igual que en el modelo de Good :

$$\Delta G_{A,12}^{LW} = -2\sqrt{\gamma_1^{LW} + \gamma_2^{LW}} \text{ [80]}$$

De forma similar, la energía de cohesión de cualquier ab material en el estado condensado, es:

$$\Delta G_C{}^{TOT} = \Delta G_C{}^{LW} + \Delta G_C{}^{AB} \text{ [81].}$$

O lo que es lo mismo, pero considerando la Ec.[64]:

$$\gamma^{TOT} = \gamma^{LW} + \gamma^{AB} \text{ [82]}.$$

Es decir, ambas componentes de la tensión superficial son aditivas.

La principal contribución del modelo de van et al., consiste en expresar la componente ácido-base (AB) de $\Delta_{A,12}^{TOT}$ como función de dos parámetros, $\gamma^+$ y $\gamma^-$, caracterísitcos, respectivamente, de la capacidad de cada sustancia para ser receptora de electrones (ácidos de Lewis) o donante de electrones (base de Lewis). Ambas contribuciones son intrisecamente asimétricas y, por tanto, no aditivas. En la mayoría de los casos, $\gamma^+ = \gamma^-$.

La componente AB de la energía libre de adhesión entre dos sustancias en el estado condesado se define como (van Oss, 1987b):

$$\Delta G_{A,12}^{AB} = -2\sqrt{\gamma_1^+\gamma_2^-} - 2\sqrt{\gamma_1^-\gamma_2^+} \text{ [83]}.$$

La contribución polar a la energía de cohesion de un material es por tanto:

$$\Delta G_C^{AB} = -2\sqrt{\gamma^+\gamma^-} - 2\sqrt{\gamma^-\gamma^+} - 4\sqrt{\gamma^-\gamma^+} \text{ [84]}.$$

O bien, teniendo en cuenta la Ec. [51] del apartado II:

$$\gamma^{AB} = 2\sqrt{\gamma^+ + \gamma^-} \text{ [85]}.$$

Teniendo en cuenta la Ec. [50], la Ec. [51] del aparatado II, se escribe:

$$\gamma^{TOT} = \gamma^{LW} + 2\sqrt{\gamma^{+} + \gamma^{-}}\ [86].$$

La ecuación base del modelo de van Oss et al., es:

$$\gamma^{TOT}{}_{12} = \gamma^{LW}{}_{1} + \gamma^{LW}{}_{2} - 2\sqrt{\gamma^{LW}{}_{1}\gamma^{LW}{}_{2}} + 2\sqrt{\gamma^{+}{}_{1} + \gamma^{-}{}_{1}} +$$

$$2\sqrt{\gamma^{+}{}_{2} + \gamma^{-}{}_{2}} - 2\sqrt{\gamma_1^{+}\gamma_2^{-}}\,2\sqrt{\gamma_1^{-}\gamma_2^{+}}\ [87].$$

O lo que es lo mismo:

$$\gamma^{TOT}{}_{12} = \gamma_1 + \gamma_2 - 2\sqrt{\gamma^{LW}{}_{1}\gamma^{LW}{}_{2}} - 2\sqrt{\gamma_1^{+}\gamma_2^{-}}\,2\sqrt{\gamma_1^{-}\gamma_2^{+}}\ [88].$$

Que expresa la tensión superficial del material 1 inmerso en un líquido 2.

En el caso de dos materiales 1 y 2 inmersos en un líquido 3, usando la ecuación de Dupre en la forma:

$$\Delta G_{132} = \gamma_{12} - \gamma_{13} - \gamma_{23}\ [89].$$

Podemos obtener la energía de interacción entre los materiales 1 y 2 inmersos en un líquido 3, como suma de sus componentes LW y AB:

$$\frac{\Delta G_{132}}{2} = \sqrt{\gamma^{LW}{}_{1}\gamma^{LW}{}_{3}} + \sqrt{\gamma^{LW}{}_{2}\gamma^{LW}{}_{3}} -$$

$$\sqrt{\gamma^{LW}{}_{1}\gamma^{LW}{}_{2}} - \gamma^{LW}{}_{3} + \gamma^{+}{}_{3}\left(\sqrt{\gamma^{-}{}_{1}} + \sqrt{\gamma^{-}{}_{2}} - \sqrt{\gamma^{-}{}_{3}}\right)$$

$$+\gamma^{-}{}_{3}\left(\sqrt{\gamma^{+}{}_{1}} + \sqrt{\gamma^{+}{}_{2}} - \sqrt{\gamma^{+}{}_{3}}\right) - \sqrt{\gamma_1^{+}\gamma_2^{-}} - \sqrt{\gamma_1^{-}\gamma_2^{+}}\ [90].$$

Análogamente, para describir la interacción entre moléculas o partículas de una sustancia 1 en un medio 3 tendríamos:

$$\Delta G_{A131} = -2\gamma_{13} = -2\left(\sqrt{\gamma_1^{LW}} - \sqrt{\gamma_3^{LW}}\right)^2$$

$$-4\left(\sqrt{\gamma_1^+\gamma_1^-} + \sqrt{\gamma_3^+\gamma_3^-} - \sqrt{\gamma_1^+\gamma_3^-} + \sqrt{\gamma_1^-\gamma_3^+}\right) [91].$$

De acuerdo con esta expresión, un valor negativo de $\Delta G_{131}$ implicaría una repulsión neta entre las superficies (1) (presión de hidratación). Teniendo en cuenta que $\Delta G_{131}{}^{LW}$ es siempre negativo, el carácter atractivo o repulsivo de la interacción, representado por l valor de $\Delta G_{131}$, dependerá de la contribución ácido-base, $\Delta G_{131}{}^{AB}$.

En medio acuoso, la componente AB de la energía de cohesión del agua es 102 $mJm^{-2}$, valor lo suficientemente elevado como para imponer un efecto atractivo neto entre superficies de partículas apolares o débilmente polares (efecto hidrofóbico). En otras ocasiones, como sucede en especial con las superficies "monopolares" (van Oss, 1988a) ($\gamma=\gamma^{lw}$; $\gamma AB=0$; usualmente $\gamma^+\cong 0$ Y $\gamma\neq 0$), el elevado valor del carácter básico de estas superficies les hace muy hidrofílicas, existiendo fuertes interacciones repulsivas ("presión de hidratación") por el elevado valor de $[(\gamma^-_1\ \gamma^+_3)1/2]$, y por tanto el signo positivo de $\Delta G_{131}{}^{AB}$ ($/\Delta G_{131}{}^{AB}/) > /\Delta G_{131}{}^{LW}$ /. Desde este punto de vista, el modelos de van Oss propone una interpretación de las interacciones " de solvatación", descritas en el apartado 2.3 de esta Memoria, según la cual dichas interacciones tiene su origen en intercambios AB, ácido-base de Lewis, entre las superficies dispersas y el medio ( agua,

generalmente) de dispersión. En ambos casos, la componente AB del cambio de energía libre de Gibbs asociado a dicha interacción, sería la fuerza termodinámica responsable de la misma.

Finalmente, podemos deducir para interacción de un material 1 con un material 2 en el vacío (imponiendo $\gamma_3 = 0$):

$$\Delta G_{A12} = -2\sqrt{(\gamma_1^{LW}\gamma_2^{LW})} + \sqrt{\gamma_1^{+}\gamma_2^{-}} + \sqrt{\gamma_1^{-}\gamma_2^{+}} \quad [9237]$$

Nótese que la Ec. [91] indica que la interacción entre dos sustancias 1 y 2 en el vacio siempre es atractiva, ya que $\Delta G_{12}$ es negativa en todos los casos. Esta ecuación justifica la existencia de una interacción atractiva entre sustancias apolares (hidrocarburos alifáticos, por ejemplo) y el agua, siendo esta atracción debida a interacciones LW. Por completar la nomenclatura, diremos de acuerdo con lo anterior, que un líquido apolar es aquel en el que la componente AB de la energía libre de cohesión, $\Delta G_c^{AB}$, así como de la energía libre de adhesión con cualquier otro material, $\Delta G_A^{AB}$, es cero. En otras palabras, las moléculas de un líquido apolar no tienen (o son despreciables) interacciones ácido-base o con otras moléculas de su entorno exterior. En opinión de Fowkes, líquidos polares son aquellos que se auto asocian a través de enlaces químicos específicos (interacciones ácido-base de Lewis, incluyendo enlaces de hidrógeno), que tienen una contribución ácido-base a su energía de cohesión y tensión superficial, y por lo tanto, tiene una tensión superficial. De acuerdo con esta definición, los líquidos polares deben tener a la vez sitios ácidos y básicos, y son fácilmente

identificables por su insolubilidad en los alcanos superiores, especialmente el escualeno. Los líquidos que os nacidos o básicos (según el criterio de Lewis), pero que no poseen ambas cualidades en sus moléculas, son bastantes miscibles en el alcanos superiores, ya que o están auto-asociados; estos líquidos se denominan monopolares.

Como se indicó en el párrafo anterior, los compuestos monopolares tienen valores altos de $\gamma^+$ o $\gamma^-$, pero en ausencia del parámetro de signo opuesto, no existe contribución alguna a la energía libre de cohesión; es decir, $\Delta G_c^{Ab}=0$, de acuerdo con la Ec. [84]. sin embargo, paradójicamente, aunque la tensión superficial total de los compuestos monopolares es igual a su componente LW, pueden interaccionar fuertemente con líquidos bipolares, tales como agua, a través de su parámetro polar (p.e., su $\gamma^-$) y el opuesto del agua. Por ello, uno de los términos de la Ec. [84] siempre permanece distinto de cero, incluso si uno de los componentes es monopolar.

En la clase I, las interacciones polares están lógicamente ausentes. En las clases II, IIIA y IV, las propiedades polares no contribuyen a la iteración a través de la interfase, bien porque los sólidos polares no interaccionan a través de la interfase, bien porque los sólidos polares no interaccionan en este sentido con los líquidos apolares (II y IIIA) o porque se trata de interacciones entre mono-polos del mismo signo (IV). En otras palabras, en el estudio de los sistemas I, II, IIIA y IV, la ec. [80] se reduce a:

$$\Delta G_{A,12}^{TOT} = \Delta G_{A,12}^{LW} = -2\sqrt{(\gamma_1^{LW}\gamma_2^{LW})} \quad [93]$$

Hay ejemplos de estos sistemas (van Oss, 1988b) como: hexadecano sobre teflón (clase I), agua sobre teflón (clase IIIB) y dimetilsulfóxido sobre acetato de celulosa (clase IV).

La situación existente en IIIB es parecida a las anteriores; de hecho la contribución de las interacciones ácido-base a la energía libre de adhesión es nula. En este caso, la polaridad del líquido influye solo sobre su cohesión, y no en relación con la adhesión al sólido. Un ejemplo es el sistema agua-teflón. Para las clases V y VIa, se aplica la Ec. [83], con la ligera modificación de que ahora, $\gamma_1^{TOT}=\gamma_1^{LW}$. Un ejemplo de clase V es diodometano sobre DNA, y de la clase VIa, diodometano sobre varias tipos de proteínas hidratadas (van Oss, 1988b). Para el estudio de la clase VIb se tiene presente que uno de so dos términos polares es cero, dependiendo del signo de la monopolaridad del sólido.

Ejemplo de este tipo de sistemas es agua, glicerol sobre superficies de DNA, de numerosas proteínas o bien de acetato de celulosa o poli-metil-metacrilato. Finalmente, para el estudio de los sistemas de la clase VII, se tienen que considerar todas las posibilidades de interacción, y de las ecuaciones presentadas anteriormente se utilizan en toda su extensión (ver figura 2.5).

***2.4.3. Dependencia con la distancia de la componente ácido-base.***

Se ha demostrado, incluso experimentalmente, que las fuerzas de interacción AB decrece exponencialmente con la distancia H entre las superficies (Parsegian et al. 1985), de acuerdo con una expresión de la forma:

$$F_H = F_{H_0} \exp\left[\frac{(H_0 - H)}{\lambda}\right] [94],$$

donde $H_0$ es la distancia crítica (de equilibrio) entre las interfases, y cuyo valor suele tomarse como 1.58±0.08 Å (van Oss, 1988). Como ya mencionamos anteriormente (v. apartado II.4.) el parámetro $\lambda$=1nm, (van Oss et al., 1994 ; Israelachvili, 1992).

Mediante la integración de la expresión anterior se puede obtener la expresión del potencial (van Oss et al., 1986). La Tabla 2.2 muestra como depende la energía de interacción ácido-base con la distancia entre las fases sólidas, H, para distintas configuraciones geométricas. En esta tabla el factor $\Delta GH_o^{AB}$ se calculará de forma diferente según se trate de un sistema 132 (material 1-medio de dispersión 3- material 2) o bien 121, de acuerdo con las ecuaciones [90] o [91], respectivamente en función de la distancia.

**Tabla 2.2.** Expresiones donde se relacionan la energía de interacción ácido-base con la distancia entre las fases sólidas, H, para distintas configuraciones geométricas

| **Configuración geométrica** | $\Delta G^{AB}$ |
|---|---|
| Planos semi-infinitos paralelos | $\Delta G_{H_0}^{AB} \exp\left[\frac{(H_0 - H)}{\lambda}\right]$ |
| Esferas de radio a y un plano | $2\,\pi\,a\,\lambda\,\Delta G_{H_0}^{AB} \exp\left[\frac{(H_0 - H)}{\lambda}\right]$ |
| Dos esferas de radio a | $\pi\,a\,\lambda\,\Delta G_{H_0}^{AB} \exp\left[\frac{(H_0 - H)}{\lambda}\right]$ |

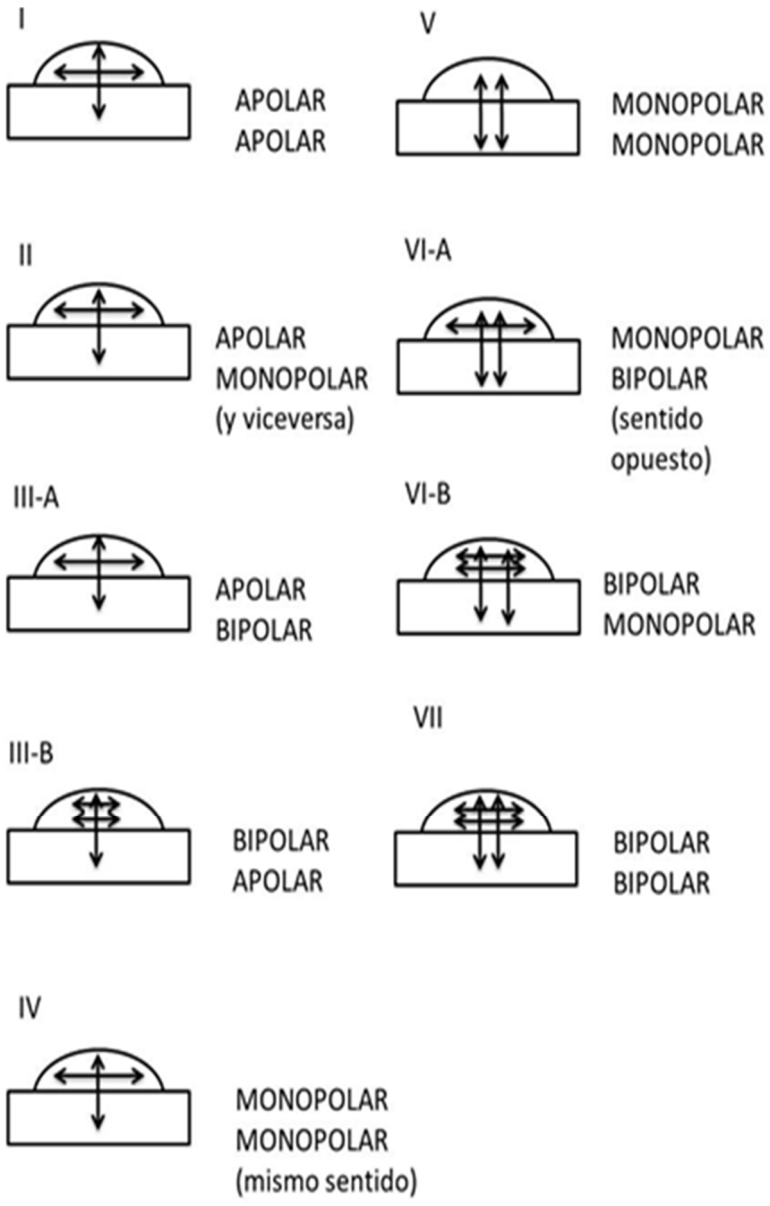


***Figura 2.5.*** Descripción de diferentes clases de sistemas solido- líquido.
Fuente: adaptación del libro de van Oss, C. J. (2006). Interfacial forces in aqueous media. Crc Press.

# Capítulo 3
# Materiales

## 3.1. Consideraciones previas.

El material edáfico es un material complejo y de gran variabilidad, lo que hace que sea de vital importancia elegirlo correctamente. El método de trabajo que vamos a utilizar es extremadamente sensible a las condiciones en las que se encuentren las muestras, por este motivo se han tomado en cuenta las siguientes consideraciones en el manejo de estas:

- Se han evitado muestrear en zonas de alteración antrópica (vertidos de fertilizantes, pesticidas, residuos orgánicos) ya que estas situaciones podrían modificar los resultados obtenidos en este estudio.
- La toma de muestras se realizó en los 5 cm más superficiales del perfil de suelo.

- Las muestras se han cogido por triplicado,
- La cantidad de muestra recogida ha sido siempre duplicada del mínimo necesarios para poder replicarla en caso de necesidad.
- Todas las muestras fueron identificadas y registrada la situación geográfica (GPS) en las que se tomaron las muestras.
- La toma de muestra se ha realizado siempre con el uso de guantes, para evitar que entre en contacto nuestras manos con él (la grasa humana altera las medidas de energía superficial).
- Durante el análisis de las medidas es obligatorio el uso de guantes para su manejo.
- Los frascos de recolección fueron desprecintados en el momento de efectuar la toma de la muestras.

Una vez el material en el laboratorio, se eliminaron manualmente los restos orgánicos y clastos inorgánicos superiores a 2 mm de grosor a través de un tamizador.

### 3.2. Suelos seleccionados para el estudio.

Para el análisis de las propiedades interfaciales del material edáfico se han seleccionado muestras de diferente naturaleza y con diferente grado de evolución edafogenética. Con esta selección de material, pretendemos ver la eficacia de las propiedades interfaciales en diferentes tipos de suelo, con diferente evolución y cómo estas se modifican bajo la acción de

hombre (cultivo tradicional *vs*. cultivo ecológico). A continuación abordaremos las características generales de cada uno de ellos.

En primer lugar se han escogido estos dos tipos de materiales fuente: de origen silíceo (material volcánico de diversas procedencias) y calcáreo (caliza Jurásica); para poder tener un patrón de comportamiento de las propiedades superficiales en estos depósitos con mínima actividad edafológica.

En segundo lugar, se seleccionan distintos perfiles edáficos en los que se tuvieron en cuenta dos tipos de cultivos de olivar (convencional y ecológico) para dos tipos de materiales parentales (silíceos y carbonatados). Con esta selección de material se pretende ver si el efecto de la técnica de laboreo utilizada influye en las propiedades superficiales del suelo, y el grado en que esta relación se ve modificada en función del tipo de material original del suelo.

Una consideración importante que hemos tenido en cuenta en este estudio, es la aportación antrópica de material fertilizante a estos, ya sea de origen orgánico (compost). En el caso de agricultura ecológica, donde los habituales aportes de abonos minerales están muy limitados, los materiales edáficos se someten a un aporte anual de materia orgánica para poder mantener su producción. Es por ello que el análisis de los efectos que su presencia tiene en el suelo y el efecto que produce en las propiedades superficiales, y por ende, sobre la estructura de este, será objeto primordial de este trabajo. Para ello se han seleccionado cuatro parcelas (2 silíceas y 2

calcáreas), dichas parcelas durante los últimos 15 años han estado abonadas por un compost orgánico (Ver Capitulo 5 para ver sus propiedades). El efecto del compost en las propiedades superficiales del suelo es un campo de gran interés por su aplicación en el control de erosión, infiltración, retención de agua, etc., además desde el punto de vista de la fijación de carbono, un proceso clave en la modelización del cambio climático. En este sentido hemos analizado la capacidad de adsorción que poseen los suelos objeto de estudio y su comportamiento en presencia y ausencia de ácidos húmicos.

Por último, se ha extendido el estudio a dos suelos bajo bosque natural, no sometidos a explotación agrícola. Estos últimos materiales servirán de nivel de referencia para comprobar el efecto del cultivo en las propiedades edáficas de los suelos estudiados.

A continuación se muestran una clasificación de los suelos de cultivo estudiados atendiendo a los criterios expuestos anteriormente y la denominación que reciben estos según la clasificación taxonómica de suelos de la FAO (FAO, 2006):

(i) Sª Mágina: Estos suelos, se encuentran sobre sobre calizas coluviales y margas, se clasificaron respectivamente como Cutanic Luvisol y Haplic Regosol. Por otra parte, junto a los suelos de cultivo, se muestreo un suelos bajo vegetación (bosque mediterráneo), clasificado como Haplic Cambisol (Aranda et al., 2011).

(ii) Andújar: Los suelos calcáreos y silíceos son los materiales dominantes provenientes de material calcarenítico y cuarcítico, respectivamente. Los suelos dominantes en el área calcárea fueron Eutric Regosol y en el área silícica Dystric Leptosol, respectivamente (Aranda et al., 2016).

(iii) Sª Morena: Suelos desarrollados sobre granitos: Suelo con manejo convencional (Dystric Regosol), y bajo cultivo ecológico y bosque natural (Dystric Cambisol).

A continuación, se van a detallar las principales características geológicas, tectónicas y vulcanológicas de los depósitos volcánicos a teniendo a su ubicación geográfica del volcán. En segundo lugar se describirán las características geológicas, climatológicas y edafológicas de los demás materiales ubicados en la provincia de Jaén y Córdoba.

### *3.2.1 Depósitos volcánicos.*

Los suelos volcánicos pueden tomar varias denominaciones según el tipo de clasificación que se utiliza, por lo general suelen recibir el nombre genérico de "Andosoles" según la clasificación FAO (FAO, 2006). Un Andosoles o suelo volcánico típico según la FAO son aquellos "que se desarrollan en eyecciones de vidrios volcánicos bajo diferentes climas (excepto bajo condiciones climáticas hiperáridas)".

Los materiales estudiados en este documento no poseen las características suficientes para denominarse Andosoles, de hecho ni siquiera

se pueden considerar suelos, pero si suponen el estado primigenio del suelo, el blanco a partir del cual se obtienen distintos suelos. Las características identificativas de un Andosol según la FAO son poseer un horizonte tipo "Vítrico" ("vidrio volcánico" en abundancia dentro de los 25 cm desde la superficie del suelo) y un perfil en profundidad de al menos de 25 cm, encontrándose la roca madre en ese intervalo de profundidad (Horizonte C).

El término que recibe nuestros materiales de forma genérica es el de "Regosol" (manto de alteración que cubre la tierra) según la FAO. Los Regosoles se desarrollan sobre materiales no consolidados, alterados y de textura fina. Suelen aparecer en cualquier zona climática sin permafrost y a cualquier altitud. La evolución del perfil es mínima como consecuencia de su juventud, su perfil es de tipo AC.

A pesar de su juventud en términos edafológicos (0-500 años), dichos suelos poseen bastantes características similares a los Andosoles. Como son: intercambio catiónico muy dependiente del pH del suelo; la fracción total de poros aumenta conforme avanza la alteración bioquímica (intemperización) de los Regosoles, llegando hasta el 50% y más del 75%; poseen un excelente drenaje interno y poseen una alta permeabilidad al agua lo que hace que sean suelos relativamente resistentes a la erosión hídrica (FAO, 2006).

A continuación se describen las principales características geológicas y ambientales que han determinado las características de los Regosoles que

han sido objeto de estudio en esta tesis, clasificados según su ubicación geográfica (Ver Tabla 3.1).

**Tabla 1.1.** Coordenadas geográficas donde se han extraído las muestras utilizadas en esta memoria.

| NOMBRE | COORDENADAS GEOGRAFICAS | | UBICACIÓN |
|---|---|---|---|
| *Decepción* | *62º54'53.21''S* | *60º33'41.70''O* | *Antártida* |
| *Fogos* | *14º50'58.60''N* | *24º43'7.90''O* | *Cabo verde* |
| *Estromboli* | *38º47'42.44''N* | *15º12'59.68''E* | *Italia* |
| *Etna* | *37º44'41.70''N* | *14º59'58.01''E* | *Italia* |
| *Vulcano* | *38º23'47.81''N* | *14º58'9.20''E* | *Italia* |
| *El Hierro* | *27º42'31.37''N* | *18º3'8.32''O* | *Isla Canarias, España* |
| *Tenerife* | *28º12'48.77''N* | *16º38'36.21''O* | |
| *Sierra Morena* | *38º22'12.00''N* | *4º52'55.20''O* | *Córdoba, España* |
| *Espeluy* | *38º52'11.29''N* | *3º52'11.29''O* | *Jaén, España* |
| *Sierra Mágina* | *37º46'43.61''N* | *3º20'40.75''O* | *Jaén, España* |

*3.2.1.1. Volcanes en Italia.*

La Italia insular ha sido la región elegida para nuestro estudio. Un área de 200 $km^2$, en el que podemos encontrar volcanes con características vulcanológicas, petrológicas y tectónicas muy diferentes para la corta distancia que los separa (origen asociado a punto calientes y a procesos subducción), en estos volcanes en la actualidad siguen habiendo una cierta controversia acerca de sus orígenes como muestran los últimos estudios (Francalanci et al., 1999).

Los volcanes seleccionados son Monte Vulcano, Monte Estrómboli y Monte Etna (ver figura 3.1.); volcanes con un amplio historial en cuanto a datos científicos.

*A) Vulcano, isla de Vulcano, Italia.*

Monte Vulcano situado en las islas Eólicas, al Norte de la isla de Sicilia, con una superficie de 22 $km^2$ y una altura de 500 metros sobre el nivel de mar; se asienta sobre una corteza continental que evoluciona al este. En este contexto tectónico el origen de dicho volcán se ha asociado a un proceso de subducción (Astis et al., 1997), pero otros autores (Barberi et al., 1994) y (Ventura, 1994) se asocia el origen del mismo a una estructura tipo graben, con composiciones magmáticas variables.

La actividad volcánica empezó hace unos 35 ka hasta la actualidad, con la emisión de rocas traquiandesíticas, con composiciones shoshoníticas y latíticas. La muestra seleccionada proviene de la erupción de 1984, se trata de una muestra de color grisáceo, de tamaño muy variable limos-gravas (Ver figura 3.2.-a). Se asocia a esta erupción de tipo III (Vulcaniana) con emisión de nube de cenizas. Prueba de este vulcanismo explosivo es la topografía de vulcano, con multitud de cicatrices, huella de los deslizamientos pasados como el deslizamiento del 20 de Abril de 1988 (Rasà & Villari, 1991), en el flanco noreste del cono con un volumen de material afectado de 200,000 $m^3$. Pero los recientes estudios submarinos ponen de manifiesto cicatrices de deslizamientos antiguos y sus depósitos asociados (Romagnoli et al., 2012).

*B) Isla de Estromboli, Italia.*

La pequeña isla de Estromboli situada al Norte la región de las islas de Eólicas posee una elevación sobre el nivel del mar de 924 m y más de 2000 metros sobre el fondo oceánico. Esta isla se encuentra ubicada en la corteza compleja (transición a oceánica) sobre un punto caliente con emisiones de magma basáltico, cuya característica principal es la ausencia de gases, con 45-55% de fenocristales y altos contenido en potasio (Francalanci et al., 1999).

Con una actividad volcánica casi permanente (Rosi et al., 2013), de ahí su nombre "Río de Fuego", desde su origen hasta la actualidad a través de su cono central. La actividad volcánica está divida en dos etapas: una más tranquila y otra más explosiva. La etapa tranquila está marcada por emisiones de lava a alturas de 100-200 metros y ausencia de explosiones, los productos típicos de esta actividad son escorias negras y salpicaduras de clastos piroclásticos (Bertagnini et al., 2008). Este periodo de calma es interrumpido por fuertes explosiones de pequeña duración (Rosi et al., 2013) con depósitos de piroclastos asociados a nubes piroclásticas pequeñas.

La muestra de estudio, proviene de erupción del año 2014, de los alrededores del cono central correspondientes con la etapa vulcanológica más tranquila. La muestra estudio tienen como características principales a simple vista color gris oscuro, tamaño arena, (Ver figura 3.2.-b).

*C) Etna, isla de Silicia, Italia.*

Sicilia es una isla situada a 3 Km de la península Italiana y separada por el estrecho de Mesina. Tectónicamente es una región muy activa, situada por encima del margen de placa convergente entre la placa africana y la placa euroasiática. En este contexto clásicamente se asociaba al Monte Etna con un origen de tipo convergente. Las primeras investigaciones sitúan el volcán en medio de tres placas tectónicas: Hyblean Placa, la corteza oceánica (Lentini, 1982; Cristofolini et al., 1979; Ben Abraham & Grasso, 1990), actualmente, existen otras teorías acerca del origen tectónico de este volcán.

El monte Etna es un estratovolcán con una altura de 3222 m, cubre un área de 1190 $km^2$ con una circunferencia basal de 140 $km^2$. Es un volcán muy activo, con erupciones constantes, cuya primera erupción datada históricamente es del siglo I. Geológicamente su actividad comenzó hace unos 500 ka (Gillot et al., 1994; Branca et al., 2008). Analizando la topografía del Monte Etna se observa que su edificio volcánico presenta distintas fisuras y son evidentes deslizamientos a lo largo de sus laderas.

La muestra seleccionada se corresponde con la erupción de 2014, una erupción estromboliana con emisión de piroclastos en los alrededores del cono, se trata de clastos muy angulosos, de color oscuro, muy poroso, muy ligero y de composición basáltica (Ver figura 3.2.-c).

Panorámica del Monte Vulcano, Italia

Panorámica del Monte Estromboli, Italia

Panorámica del Monte Etnai, Italia

***Figura 3.1.*** *Composición fotográfica donde se pueden observar una panorámica de volcanes seleccionados en la península de Italia.*

*Fuentes: de arriba abajo los autores son: Brisk G, Simon, Benaveling bajo licencia CC BY-SA LICENCE FREE 3.0 http://creativecommons.org*

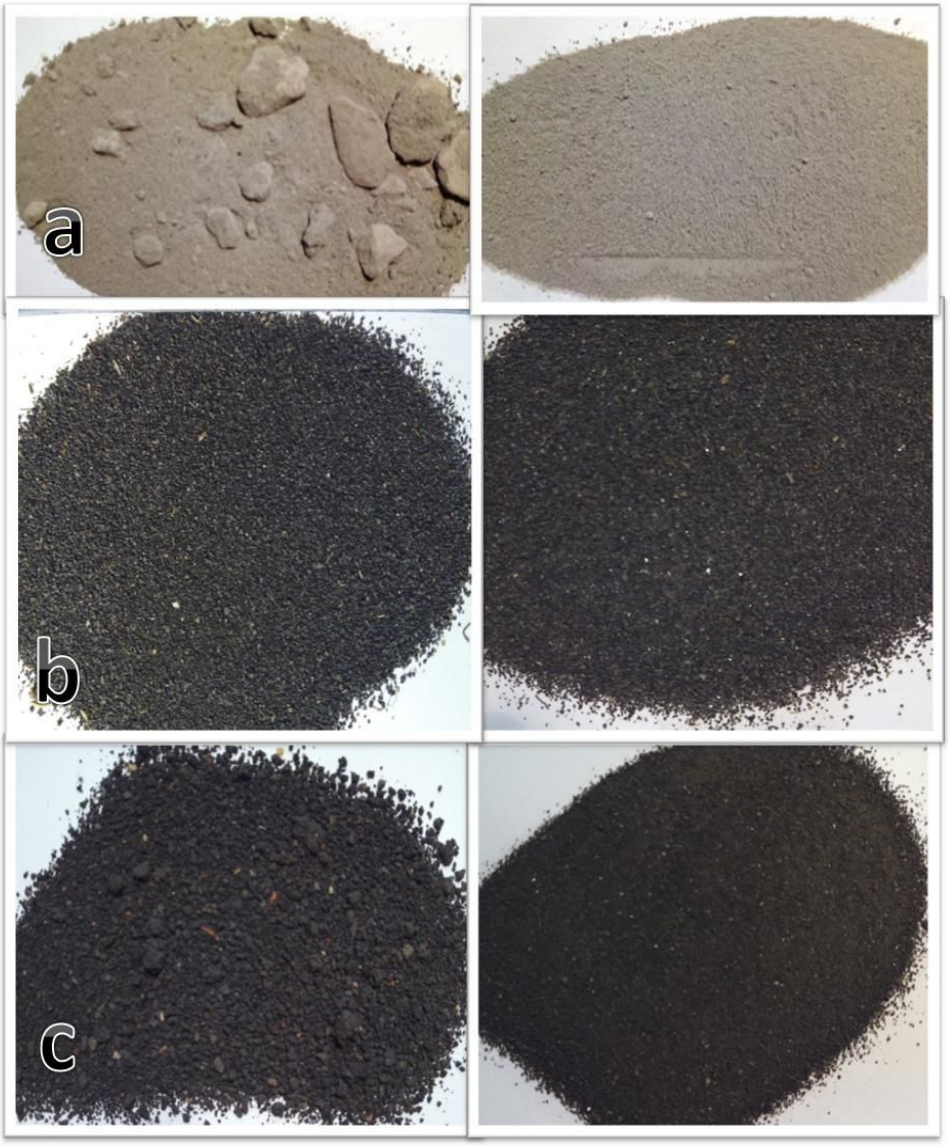


***Figura 3.2.*** *Composición fotográfica donde se pueden observar las muestras estudias de los diferentes volcanes: Vulcano (a), Estromboli (b) y Etna (c). Cenizas antes de pretamientos (fotografía de la izquierda) y después del tratamiento con el mortero de ágata (fotografía de la derecha). De arriba a abajo encontramos las cenizas de Vulcano, Estromboli y Etna respectivamente.*

*3.2.1.2. Volcanes en las Islas Canarias e Islas de Fogos.*

Las Islas Canarias (Ver figura 3.3.-a & b) ubicadas geográficamente sobre el océano Atlántico frente a las costas de Marruecos y tectónicamente sobre un una corteza continental transicional, su origen está asociada a un punto caliente y al movimiento de dicha placa oceánica. Concretamente este estudio se centrará en las Islas del Hierro y Tenerife (Hausen et al., 1995).

Las Isla de Fogo (Ver figura 3.3.-c), ubicadas geográficamente más sur de las Islas Canarias y tectónicamente situadas sobre la placa oceánica atlántica. Su origen también está asociado a un punto caliente, pero esta isla se encuentra dentro de la placa oceánica como puede verse en las características tectónicas, no son iguales para ambas islas siendo este el motivo de la elección de dichas islas para el estudio (Courtney & White, 1986).

*A) El Teide, islas Canarias, España.*

La isla del Teide ubicada en la placa oceánica africana, se enmarca dentro de un complejo de estratovolcanes asociados a un punto caliente y al movimiento de la placa oceánica africana sobre este. Se trata de un complejo volcánico que se eleva alrededor de 5000 metros sobre el fondo oceánico, con una edad de 11,9 millones de años. La historia geológica de este volcán ha sido estudiada en numerosos investigaciones (e.g., Hausen, 1955; Fúster et al., 1968; Ridley, 1970; Abdel-Monem et al., 1971; Carracedo, 1975; Schmincke, 1982; Wolff, 1983; Ancochea et al., 1999;).

Otro aspecto destacable es la presencia de grandes deslizamientos, de edades diferentes, asociados a la etapa sub-área y área. Pero sin duda una de las características geomorfológicas más importantes de esta isla es la presencia de grandes y pequeños barrancos en todo su relieve que es visible desde imagen aérea.

La muestra de este volcán se encuentra ubicada en el área geográfica del edificio de Las Cañadas II. Posee un color rojizo muy característico fruto de la meteorización de los componentes férricos, posee una granulometría tamaño arena y el espesor de la capa es unos 50-100 cm (Ver figura 3.4.-a) La historia geológica de este material, ha sido compleja y difícil, se encuentra en medio de dos complejos basales, siendo la deposición del material superior basáltico, el responsable del metamorfismo térmico local sobre el estrato estudiado.

*B) El Hierro, islas Canarias, España.*

Ubicada en el área suroccidental del Archipiélago Canario, y una edad de sólo 1,2 millones de años (Gillou et al., 1996) es la isla más joven y la más pequeña con una extensión de soló 271 $km^2$. Su historia geológica está caracterizada por la sucesión de tres ciclos volcánicos vinculados al desarrollo de varios edificios volcánicos (Guillou et al., 1996; Balcells & Gómez, 1997a) la actividad volcánica inicial está asociada a la formación del Edificio Tiñor, ubicado en el área nororiental de la isla y con edades de entre 1.12–0.88 Ma. El colapso lateral de la parte norte de este edificio en 888 ka fue posteriormente colmatado por las lavas del edificio de El Golfo-Las Playas (545–176 ka), afectado luego por grandes deslizamientos entre

130-80 ka (Longpré et al., 2011). En torno a los 158 ka se produce el inicio del volcanismo de los Rifts WNW, NE y SSE (Guillou et al., 1996), que continúa, sin grandes interrupciones (Pérez Torrado et al., 2011) hasta nuestros días.

La mayor parte del volcanismo de los Riffs corresponde a erupciones máficas de naturaleza basáltica, caracterizadas por la construcción de uno o varios edificios volcánicos constituidos por escorias y lapillis y la emisión de abundantes flujos lávicos.

La muestra fue recogida en un depósito de piroclastos basálticos de dispersión constituido por dos paquetes de lapilli bien diferenciados, separados por un nivel erosivo, con una edad aproximada de 100 ka.

La muestra fue recogida de un nivel cinerítico localizado hacia el muro del depósito, de color negro, aspecto fresco y muy poco consolidado (Ver figura 3.4.-b). Algunos autores, (Balcells et al., 1977 b), asocian la presencia de estos niveles de grano muy fino a pulsos o fases freatomagmáticas vinculadas a erupciones monogenéticas puramente magmáticas desarrolladas en el área de cumbres de la dorsal NW de la isla.

*C) Pico de Fogos, Cabo Verde.*

La isla de Fogo situada en la parte suroeste del Archipiélago de Cabo Verde a unos 800 km de la costa africana. Ubicada sobre la corteza oceánica africana, su formación es debida al ascenso de un penacho de manto hace unos 200 ka (Courtney & White, 1986). Su altura es superior a los 3-4 km

sobre el nivel de fondo oceánico y unos 200-300 metros sobre el nivel del mar.

La estructura de cráter es de tipo central resultado de numerosos colapsos y explosiones, aunque también posee erupciones fisurares laterales.

Wallenstein et al. (2007) describe los peligros volcánicos indirectos del volcán Pico de Fogo; estos riesgos se producen por la interacción entre el edificio volcánico, los procesos sísmicos, hidrotermales, la gravedad y el agua.

Debido a estas interacciones, son frecuentes los deslizamientos en sus flancos ocasionados por la alta pendiente de sus flancos. Paris et al. (2011) describe la formación de posibles tsunamis debido a estos deslizamientos. Otra característica de esta zona volcánica son las altas emisiones de $CO_2$ y $SO_3$ (Paris et al., 2011).

La muestra fue recogida de la zona conocida como "Cha das Caldeiras fogo", se trata de una muestra poco compacta, de color oscuro, con gran cantidad de vesículas y de clastos anguloso (Ver figura 3.4.-c).

Panorámica del Monte Teide, Tenerife

Isla del Hierro vista desde Arenas Blancas

Panorámica del Monte Pico de Fogo, Islas de Cabo Verde.

***Figura 3.3.*** Composición fotográfica donde se pueden observar fotografías de los volcanes: Tenerife (a), El Hierro (b) y Pico de Fogo (c).

Fuente: de arriba abajo los autores son: @Philippn, @Carlos Teixidor Cadenas Y @Pascal Givry bajo licencia CC BY-SA LICENCE FREE 3.0 HTTP://CREATIVECOMMONS.ORG/


***Figura 3.4.*** Composición fotográfica donde se pueden observar fotografías de los volcanes: Tenerife (a), El Hierro (b) Y Pico de Fogo (c) y Decepción (d), cenizas antes (fotografía de la izquierda) y después del tratamiento con el mortero de Ágata (fotografía de la derecha), de arriba a abajo encontramos las cenizas de Tenerife (a), El Hierro (b), Pico de Fogo (c) y Decepción (d).

*3.2.1.3. Volcán de la Isla Decepción (Antártida).*

La Isla de Decepción (Ver figura 3.5) ubicada en la península Antártida en el estrecho de Bransfield, se sitúa en el riff que recibe el mismo nombre. Más concretamente se encuentra ubicada en la intersección entre el eje de la cuenca Bransfield y la extensión de la zona de fractura Hero. Dicho límite se ha descrito una actividad hidrotermal asociada (Han y Suess 1987).

Isla Decepción es una isla resultado del colapso de la estructura central del volcán, provocando una inmensa caldera volcánica. Su origen de tipo tectónico es debido a la subducción de la Placa Phoenix debajo de la Placa Antártica (González-Ferrán, 1985). La construcción de la isla según los autores Smellie (2001) y Martí et al. (2013) se produce en tres fases: pre-, sin- y post-caldera. En la primera fase se construyó el escudo submarino (Hawkes, 1961), la segunda la Formación Outer Coast Tuff se depositó discordantemente sobre las unidades escudo (Smelli, 2001; Gale, 2014) y la última fase posterior a la caldera, en el que se incluye las erupciones históricas recientes y estás consisten en episodios eruptivos diseminados por toda la isla (Martí et al., 2013).

El vulcanismo reciente de la isla ha venido asociado con peligros indirectos derivados de la erupción: lahares e inundaciones (Smellie, 2002b). La muestra seleccionada recibe denominada tefra volcánica: castos redondeados de obsidiana (Ver figura 3.4.-d.) Una de las características principales de este materiales es material es su aspecto elipsoidal recubierto de una película superficial de material orgánico tal y como Ontiveros (Ontiver et al., 2014).

***Figura 3.5.*** Composición fotográfica donde se pueden observar panorámicas de la Isla Decepción (Antártida).

Fuente: de arriba abajo los autores son @Andrew Shivae Y @Arcibel Bajo LICENCIA CC BY-SA LICENCE FREE 3.0 HTTP://CREATIVECOMMONS.ORG/

### *3.2.2. Suelos de la provincia de Jaén y Córdoba.*

#### *3.2.2.1. Introducción.*

Los materiales seleccionados para elaborar este estudio, cubren en su gran parte los suelos ocupados y destinados al cultivo del Olivar en Andalucía y en especial en la Provincia de Jaén. La importancia del estudio de estos suelos para la provincia es clara, la economía de Jaén depende casi en exclusiva del cultivo del Olivo, siendo esta zona una de las mayoras productoras de aceite a nivel mundial.

La provincia de Jaén se encuentra ubicada en un contexto geológico en los materiales Jurásico y Cretácicos de las Zona Subbética, Unidades Intermedias y Zona Prebética de las Zonas Externas de las Cordilleras Béticas, rodeado al norte por los materiales Cuaternarios de la ribera del río Guadalquivir y los Paleozoicos del basamento. En ellas el material predominante es la roca sedimentaria carbonatada (calizas, dolomías, margas y materiales coluviales de todas ellas), aunque también es posible encontrar materiales de tipo silíceo (granitos y materiales coluviales de él), en zonas de norte de la provincia y en las terrazas fluviales de los ríos que nacen allí.

Para este estudio se han elegido muestras superficiales (0-5 cm) de suelos con diferente grado de evolución. El grado de evolución de un suelo puede ser evaluado por muy diversos parámetros, uno de ellos es su mineralogía (Ruhe, 1956), para ello se compara la mineralogía de la roca madre y la del suelo. Los minerales alterados o secundarios están más

desarrollados en la parte superior del perfil edáfico y disminuye a medida que aumentamos la profundidad.

Los suelos de la provincia de Jaén están destinados al monocultivo del olivar en una gran extensión, prácticamente el 50% del territorio. Son suelos típicos mediterráneos, caracterizados por su bajo contenido de materia orgánica (≤1%), por el clima semiárido en el que se desarrollan y con alta degradación, debida fundamentalmente la agricultura intensiva (Nieto et al., 2012).

*3.2.2.2. Sierra Mágina (suelos carbonatados).*

El Parque Natural de Sierra Mágina está situado en el Centro-Sur de la provincia de Jaén, a pocos kilómetros de la capital en dirección Sureste. Geográficamente está limitada por la depresión del Guadalquivir al Norte, la depresión del Guadiana Menor al este, el valle del río Guadalbullón al oeste y las estribaciones más septentrionales de la Hoya de Guadix al Sur. La zona elegida para la toma de muestras se encuentra en el Barranco de Atanor, al sur de la localidad de Jódar (Jaén), concretamente en las proximidades de la Balsa del Atanor 37 46058.810'N 3 19054.610'W.

Los suelos agrícolas seleccionados están ubicados en una zona mediterránea con características semiáridas. Los valores totales de precipitación oscilan entre los 527 mm/año en la estación de Huelma (situada a una altitud de 1084 m). La dinámica de las temperaturas es la típica del régimen Mediterráneo: máximos en verano, disminución significativa de la temperatura a partir del mes de octubre que se prolonga

de forma gradual hasta el mes de Enero en el que de nuevo se inicia el ascenso.

Geológicamente se enmarca en el contexto montañoso de las cordilleras Béticas. Los materiales elegidos se encuentran sobre terrenos Jurásicos de margas. La roca madre de los suelos la constituyen rocas sedimentarias carbonatadas (calizas, dolomías, margas y materiales coluviales de todas ellas) y en menor medida, rocas sedimentarias no carbonatadas (arcillas y arcillas con yesos); todas ellas de edades Jurásica y Cretácica. Estructuralmente estos materiales pertenecen a la Zona Subbética, Unidades Intermedias y Zona Prebética de las Zonas Externas de las Cordilleras Béticas.

Existe un fuerte control litológico sobre el relieve (geomorfología) de la zona, apareciendo grandes escarpes sobre materiales compactos de caliza y dolomía, que contrastan con las suaves lomas de pendientes moderadas sobre rocas deleznables tipo marga y arcilla expuestos a procesos de degradación progresiva a través de los procesos de erosión.

Estos suelos de Sierra Mágina, descrito con anterioridad por Liebanas, 2002 y Aranda et al., 2011, los hemos analizado según la siguiente clasificación (ver figura 3.6):

1. Suelo sobre margas: Haplic Regosol (FAO, 2006).
2. Suelo sobre depósitos calcáreos (coluvios de ladera): Cutanic Luvisol (FAO, 2006) conocidos más comúnmente como Suelo Rojo Mediterráneo.

3. El suelo bajo cubierta vegetal natural desarrollado sobre coluvios calizos junto a margas: Haplic Cambisol (FAO, 2006).

*(a) Regosoles.*

Estos suelos margosos han recibido la denominación de OEM2 y OCM2, según la clasificación de la FAO son Regosoles (FAO, 2006), con un perfil A-C. Son suelos constituidos sobre materiales originales sueltos, con muy baja evolución, con presencia de marcas de erosión superficial.

*(b) Luvisoles.*

Los suelos desarrollados sobre coluvios de calizas (OEM1 y OCM1) son los que presentan mayor evolución edáfica. Se trata de Luvisoles (FAO, 2006), con perfil A-Bt- C, una gran evolución, más rubefactados (coloración más rojiza), mayor ilimerización y parcial decarbonatación, comparados con los suelos sobre margas. El porcentaje de las formas de Fe libre en la tierra fina es superior al de los suelos sobre margas, lo que concuerda con que son suelos rojizos (7.5YR Munsell colour).

Son suelos con un perfil típico estratificado A-C-Ab-C-Ab-C-Ab-C, originados a partir de materiales fluviales recientes en las cercanías de los ríos. La materia orgánica no se encuentra distribuida de forma aleatoria, por el contrario presentan una cierta tendencia a encontrarse en niveles profundos.

Desde un punto de vista edafológico, es de esperar un suelo con mayor estructura y grado de formación que el anterior.

*(c) Cambisoles.*

Dicho suelo se ha desarrollado sobre margas mezcladas con coluvios de calizas (SM), es un Haplic Cambisol (FAO, 2006). Muestra una secuencia de horizontes A-AB-Bw, una meteorización similar a los Luvisoles en cuanto a contenido en formas de hierro libre, coloración parda, y un alto contenido en carbonatos. Los similares contenidos en Fe libre con los suelos coluviales demuestran su proximidad desde el punto de vista del material formador.

*3.2.2.3. Suelos de la zona de Andújar.*

La zona de muestreos se encuentra en la localidad de Villanueva de la Reina (Jaén) cerca de la finca de la almazara "Hermejor de la Reina" cuyas coordenadas son 38.033401 N, -4.065017 E. En la finca afloran materiales del Cuaternario (depósitos de arenas, conglomerados y limos) y materiales del Paleozoico Inferior, concretamente del Carbonífero inferior: cuarcitas, grauvacas y pizarras. Ambos materiales son el origen de los suelos margosos y silíceos estudiados. Se encuentran en los depósitos Cuartanarios del rio Guadalquivir. Los materiales silícicos provienen de cuarcitas. Los suelos que se han encontrado y descrito en la zona de estudio son: en la zona calcárea del tipo Eutric Regosol (FAO, 2006) y en la zona silícea Dystric Leptosol(FAO 2006).

El olivar cultivado tiene una edad aproximada de 40 años y una densidad de plantaciones de 90 a 100 árboles/ha. Las prácticas de manejo convencional en estas parcelas fueron las que se utilizan más comúnmente

en la zona. Dos de estas parcelas han sido sometidas durante 17 años a un proceso fertilización que consistía en añadir un compost elaborado mezclando productos de desecho de la extracción del aceite (alperujo), restos de la poda del olivar, y excrementos de aves de corral, mezcla que se sometía a un proceso de co-compostaje.

Se eligieron cuatros parcelas de olivares, dos con suelos calcáreos (con y sin aplicación co-compost) y otras dos con suelos silíceos de cuarcitas una con co-compost y otra sin compostaje). Las explotaciones de olivar que recibieron co-compostaje fueron comparables a los que no recibieron el co-compost (suelos de control) en términos de clima, pendiente, orientación, tipo de suelo, densidad de plantación y edad de la planta.

El muestreo en cada parcela (Ver figura 3.7.) consistió en la selección al azar de tres lugares, y tomando al azar una muestra de suelo compuesta de cuatro sub-muestras (de la capa superficial 0-10 cm) dentro de un radio de 5 m en cada lugar.

*3.2.2.4. Sierra Morena (suelos silíceos).*

El muestreo se ha llevado a cabo al NE de la Provincia de Córdoba, en el término municipal de Obejo, en las inmediaciones de la carretera CP-165 que une ésta localidad con Pozoblanco (coordenadas 38.37° - 38.13° N; 4.88° - 4.72° W) a una altitud que varía desde los 500 hasta los 958 metros. Se trata de un área de pendientes moderadas (max. 20%, elevación media de 530 m s.n.m.), perteneciente geológicamente al Batolito de los Pedroches (complejos granitoides de origen postcinemático) y de litología

granodiorítica. El clima dominante es el mediterráneo, con una precipitación media anual de 500 mm y una temperatura media de 15ºC. Estos suelos fueron estudiados con anterioridad (Álvarez et al., 2007) parcelas convencionales sometidas a labranza y parcelas ecológicas.

Desde el punto de vista del uso, en la zona predomina un olivar de baja intensidad (secano) en el que se alternan se seleccionaron cuatro parcelas (ver figura 3.8):

- *Olivar convencional sin cubierta (SCG).* Olivar ecológico con cubierta. Se optó por muestrear dos parcelas de olivar ecológico, debido a las claras diferencias de desarrollo del perfil que mostraban estos suelos en función de su orientación.
- *Con orientación de ladera hacia SE (CUG*). Mostraban mayores signos de erosión y menor incorporación de materia orgánica que en la orientación norte.
- *Suelo natural (BNG).* Se trata de pequeñas manchas forestales de encinar y matorral alto (*Quercus coccifera*, *Myrtus communis*, *Rhamnus sp*., *Viburnun tinus*, *Arbutus unedo*, etc.) presentes en el área de muestreo, con suelo bien conservado sobre la misma granodiorita que las parcelas de olivar.

La parcela de estudio está formada por una penillanura que incluye la zona de los Pedroches, extenso territorio principalmente granítico conocido como "Batolito de los Pedroches", y que se extiende entre los ríos Zújar y Guadiato, formada en gran parte por arrastres coluviales y aportes fluviales de terrenos pizarrosos, cuarcíticos y conglomerados de gravas.

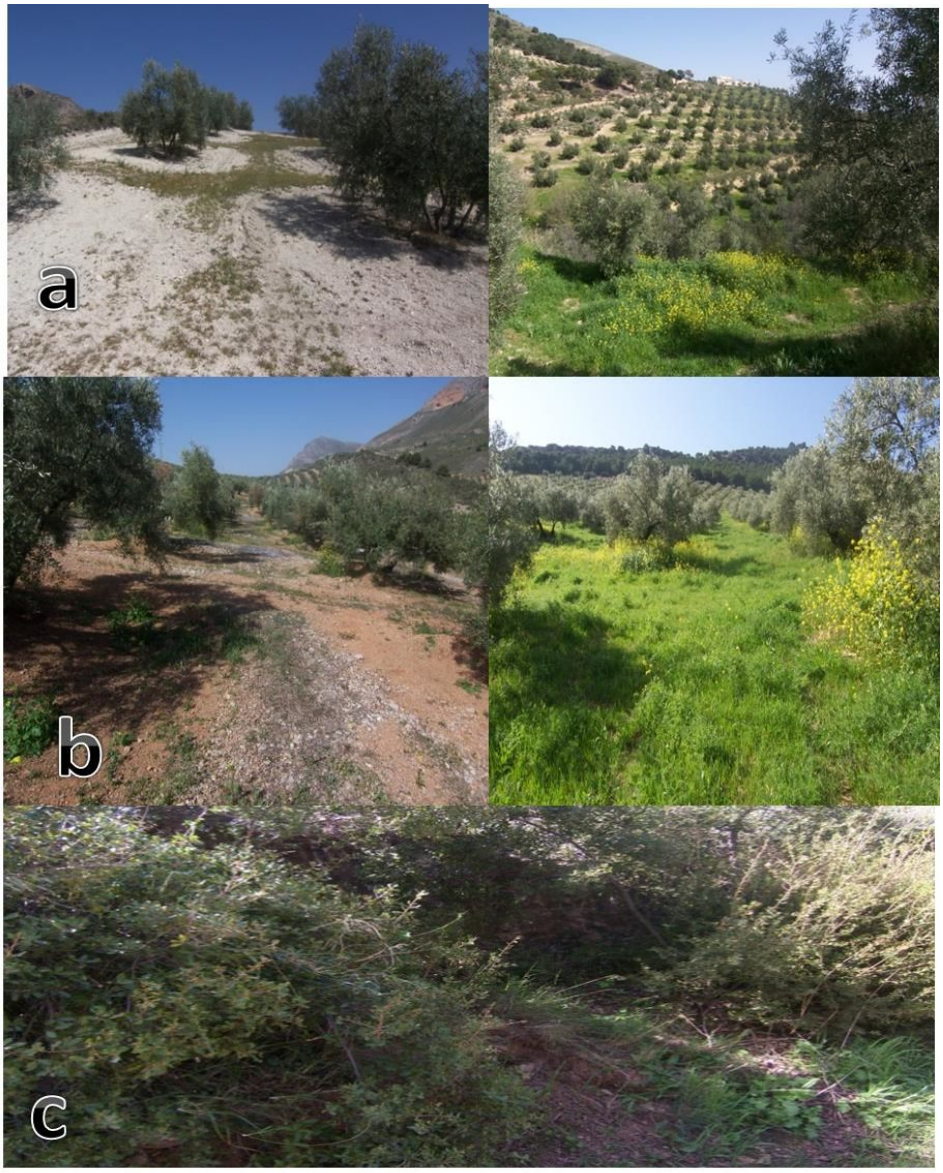


***Figura 3.6.*** Composición fotográfica donde se puede ver los distintos suelos estudiados en Sierra Mágina. De arriba a abajo tenemos suelos margosos (a) (convencional derecha y ecológico izquierda), suelos coluviales (b) (convencional derecha y ecológico izquierda y suelo en estado natural (c).

Fuente: autores de la fotografías Julio Calero y Víctor Aranda.


***Figura 3.7.*** Las dos imágenes superiores corresponden al suelo carbonatado (a su izquierda sus fotos del perfil de correspondientes a la zona de extracción) y las dos inferiores al suelo silíceo (a su izquierda sus fotos del perfil de correspondientes a la zona de extracción).

Fuente: autores de la fotografías Julio Calero y Víctor Aranda.

***Figura 3.8.*** Composición fotográfica donde se puede ver los distintos suelos estudiados en Sierra Morena. De arriba a abajo tenemos dos fotografías del olivar ecológico CUG, olivar convencional SCG y suelo en estado natural BNG.

Fuente: autores de la fotografías Julio Calero y Víctor Aranda.

Los suelos estudiados en esta área son: Dystric Regosol (suelo de olivar con manejo convencional) y un Dystric Cambisol (con cultivo de olivar con manejo ecológico y vegetación natural). Se trata de suelos ácidos (pH < 7), sin carbonatos, de composición mineralógica rica en cuarzo y texturas de francas a arenosas (relativamente poca arcilla, que es de tipo vermiculita-clorita-illita).

La diferencia más significativa entre las distintas muestras de Sierra Morena, es su contenido de materia orgánica, que depende en gran medida del cultivo que desarrollan. Tenemos el suelo natural (BNG) bajo un matorral-encinar bajo, muy rico en materia orgánica; el suelo de olivar convencional (SCG), bastante erosionado y sin materia orgánica (material tipo regolito: capa de alteración de la granodiorita) y los suelos ecológicos (CUG).

El suelo BNG puede ser considerado como representativo y con el mayor grado de evolución en la zona, aunque no corresponde a un suelo inalterado ya que probablemente se trate de suelo cultivado antiguamente (hace 50 o 100 años) que fue recolonizado por el matorral y el encinar que se ha regenerado parcialmente, sin llegar a su estado climácico.

# Capítulo 4
# Metodología

El acceso a los datos experimentales, su valor y reproducibilidad, depende en gran parte de la rigurosidad en el uso de los métodos utilizados para su obtención. Es por ello que se ha mostrado especial atención a la metodología utilizada en esta memoria, y que a continuación describimos.

En la figura 4.1. se puede observar un resumen esquematizado de los tratamientos y procesos que se han seguido en esta investigación. A continuación pasaremos a describir cada apartado en una sección correspondiente.

### 4.1. Análisis general de los suelos.

Los datos analíticos generales fueron obtenidos a partir de muestras replicadas en la fracción de tierra fina (<2 mm) de todos los suelo

estudiados. Los procedimientos analíticos utilizados son los descritos por Page et al. (1982) y Klute (1986). A continuación se muestra un sumario de los análisis realizados a la fracción de tierra fina:

- La textura de suelos se obtuvo mediante tamizado y sedimentación utilizando el método de la pipeta de Robinson.
- El carbono orgánico se determinó por el método en húmedo (oxidación con dicromato potásico).
- El nitrógeno total de la muestra se estableció por el método Kjeldahl.
- La cuantificación de $CaCO_3$ equivalente se realizó por el método del Calcímetro de Bernard.
- La capacidad de intercambio catiónico (CEC) se calculó a través del método del acetato de amonio (pH 7).
- La cantidad de fósforo disponible (P) se extrajo con la ayuda de una solución de bicarbonato de sodio y se determinó su % por colorimetría (método Olsen).
- El potasio (K) presente en las muestra se determinó por el método de acetato de amonio (pH 7) y por fotometría de llama;
- El pH de las suspensiones (en $H_2O$) en una proporción 1:2.5 (w/v) se determinó por potenciometría.
- Las formas de óxidos de hierro por el método citrato de sodio ditionito (Mehra & Jackson, 1960).

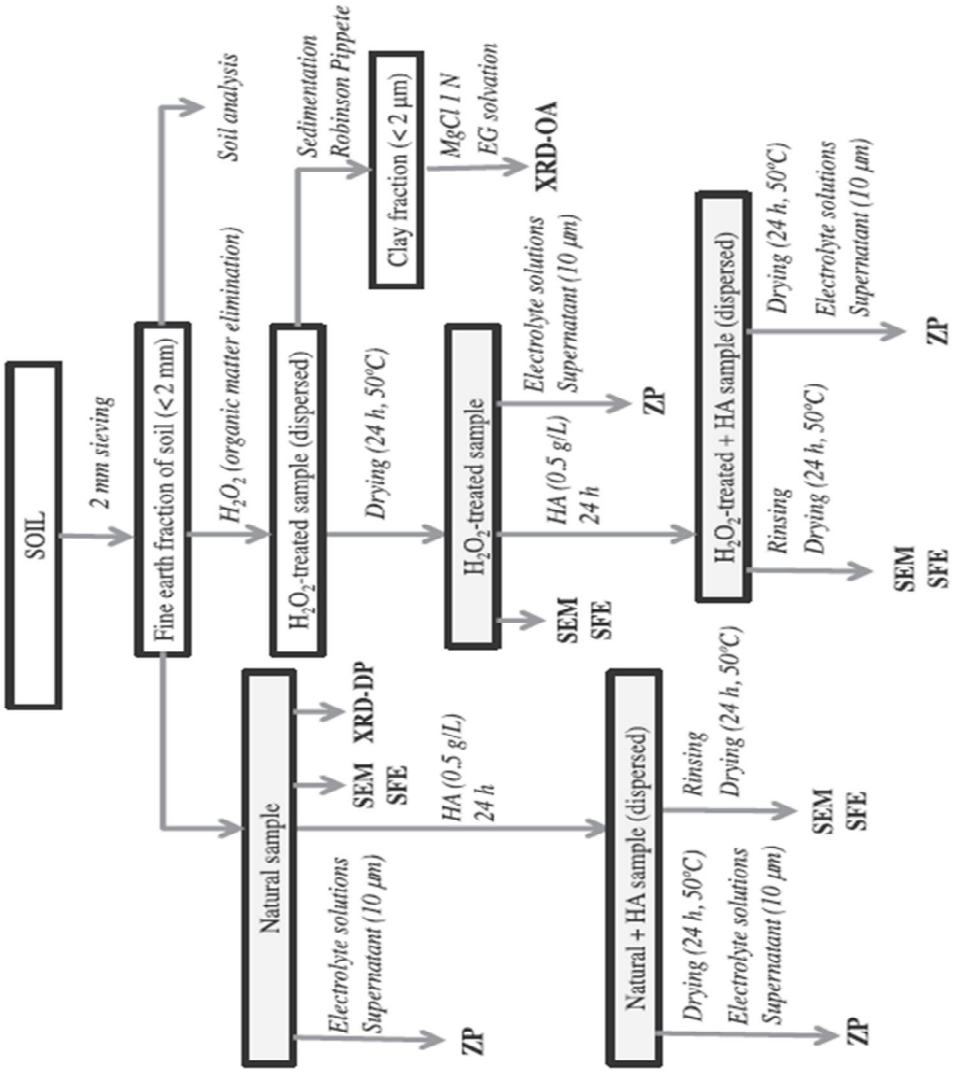


***Figura 4.1.*** En esta figura se muestran esquema de los pasos metodológicos seguidos para los tratamientos de la muestra. ZP: Potencial Zeta; SEM y TEM: Microscopía Electrónica de Barrido; SFE: Energía libre de superficie; XRD-DP: Rayos X Difracción (polvo cristalino desorientado); XRD-OA: Difracción de rayos X (agregado orientado); EG: Etilenglicol; HA: ácido húmico.

Por último, se determinó el índice de estabilidad estructural del suelo de Kemper & Rosenau (1986), densidad aparente, macroporosidad y conductividad hidráulica saturada y no saturada.

**4.2. Mineralogía del suelo.**

Para el estudio de la difracción de rayos X (XRD), se analizó la tierra fina de la muestra sin tratamientos mediante la técnica del polvo desorientado, empleando un difractómetro D5000 de rayos X. El difractómetro D5000 tenía las siguientes condiciones de funcionamiento: radiación Cu Kα (l = 0,15406 nm) a 35 kV y 15 mA, rango angular de 2-30º 2θ, y velocidad de exploración 0.05º 2θ.

Los porcentajes de las diversas fracciones minerales fueron establecidos por el método de los poderes reflectantes, empleando los factores expuestos en Martín-García et al. (1997) y Calero et al. (2009).

La mineralogía de las arcillas se hizo con la técnica del agregado orientado. Para esta técnica se llevó a cabo sobre las fracciones finas del suelo: limo (fracción 0.05 – 0.002 mm) y arcilla (fracción > 0.002 mm). Los agregados orientados se preparó a partir de muestras saturadas en Mg y K (cloruros magnésico y potásico 1N, respectivamente), añadiendo una suspensión de ≈ 50 mg de arcilla/limo en una placa de vidrio y procediendo a su secado al aire a temperatura y humedad ambiental (Whitting and Allardice, 1986). Los análisis de las placas se realizaron en las condiciones especificadas por estos autores: 1) secas al aire, 2) saturadas en vapor de etilenglicol (solo muestras Mg), 3) solvatadas en glicerol (solo muestras

Mg), y 4) calentadas durante una hora a 550º C (solo muestras potásicas). Los análisis de agregado orientado se harán en el difractómetro Siemens D5000 (radiación Cu Kα, 35 kV y 15 mA) en un rango angular de 2-30 º2θ, una velocidad angular de 0.2 º2θs-1 y una constante de tiempo de 2 s.

Para la identificación exacta de los filosilicatos se hizo una descomposición en la zona 3–10 º2θ de los patrones de difracción de las muestras secas al aire y saturadas en Mg-etilenglicol, mediante el programa DecompRX (Lanson, 1997), siguiendo las recomendaciones de Barré et al. (2008). Una vez realizada la deconvolución e identificados los filosilicatos, se estimará el porcentaje de cada fase según el área relativa de cada pico identificativo (Velde and Barré, 2010).

### 4.3. Estructura microscópica del suelo (SEM)

Con el objetivo de esta técnica es analizar la estructura del suelo a escala microscópica (Calero et. al, 2009). Para ello se empleó el microscopio electrónico de barrido (SEM). Las muestras fueron montadas en el soporte de muestras de plata coloidal y metalizada con oro depositado en dos orientaciones (20-30º). Se utilizó un microscopio de barrido con un voltaje de 25 kV (S-510; Hitachi Ltd., Tokio, Japón) equipado con un detector de rayos X de energía dispersiva (EDAX; Rontec GmbH, Berlín, Alemania). La imagen de SEM se realizó a tres escalas: baja (3200x), media (11200x) y altas (46000x). De esta forma se obtuvieron las características de la fábrica donde se podían analizar la existencia y orientación de las tres unidades más características de la fábrica del suelo: los macroagregados (>

250 μm), microagregados y cúmulos de arcilla (250-10 μm) y dominios de arcilla (> 10 μm).

#### *4.3.1. Protocolo de estudio de la fábrica SEM del suelo.*

Hasta la fecha, no existen protocolos universales para la descripción sistemática de la estructura del suelo mediante microscopía electrónica de barrido, denominada también fábrica SEM. Por esta razón, expondremos un breve desarrollo y justificación del protocolo que hemos aplicado al estudio de la fábrica SEM de nuestras muestras, justificando los procedimientos, parámetros y términos empleados con estudios previos de Calero et al., (2009).

El protocolo descriptivo que emplearemos en la descripción de las fotografías SEM incluye seis propiedades básicas de la fábrica y tres escalas de estudio. Se trata de una simplificación del estudio morfológico exhaustivo propuesto por Calero (2005).

**1) Grado:** se trata, probablemente, del parámetro más importante en la descripción de la fábrica. A nivel macroscópico, coincide con la propiedad "grado de estructura" en las descripciones visuales de campo de la FAO (FAO, 2006, pg. 45) y el USDA (Schoeneberger et al. 2012, pg. 62), en este caso a las distintas escalas del microscopio electrónico. Se define como la visibilidad y grado de individualización de los agregados del suelo, a cualquier escala de tamaño, en función de las superficies de rotura que los delimitan entre sí. Emplearemos los descriptores: a) sin estructura (estructuras macizas o masivas), b) débil, c) moderada, d) fuerte. Los materiales arenosos, propios de suelos con menos del 5-10% de limo o

arcilla y con consistencias sueltas o blandas, tampoco desarrollan ningún tipo de estructura, debido a la carencia de material cohesivo. Se considera suelos sin estructura, aunque conviene diferenciarlos de los suelos masivos, de consistencias muy firmes y duras.

**2) Forma.** Los agregados suelen presentar alguna de estas morfologías: a) discoidal, b) alargada, c) equidimensional. A la morfología se le puede añadir el grado de redondeamiento de la superficie, resaltando una mayor o menor angulosidad y/o rugosidad. El microscopio electrónico de barrido, en razón de su elevada profundidad de campo, es muy indicado para resolver los parámetros de forma.

**3) Empaquetamiento.** Este parámetro alude a la densidad de la estructura a unos determinados aumentos, y se relaciona inversamente con la porosidad. Así, podemos distinguir: a) fábricas laxas, y b) fábricas densas. Las primeras suelen ser propias de materiales recién depositados por sedimentación, antes de sufrir ningún proceso de consolidación. Las estructuras laxas suelen ser poco comunes en suelos, ya que estos suelen desarrollarse a partir de materiales previamente consolidados, aunque podemos encontrar numerosas excepciones: suelos sobre cenizas volcánicas, suelos ricos en arcillas expansibles (esmectitas), etc.

**4) Floculación**. La floculación es una propiedad aplicable principalmente en la escala coloidal, pues se refiere a la agregación mediante fuerzas fisicoquímicas de las partículas individuales de limo fino y arcilla para formar clusters y dominios de arcilla. Como las partículas de arcilla están constituidas básicamente por filosilicatos laminares, la floculación puede

implicar uniones cara-cara, cara-borde y borde-borde. Dado que la naturaleza de caras y bordes puede ser diferente a nivel eléctrico y energético (i.e. dominancia de repulsión eléctrica entre caras, mientras que atracción entre caras y bordes), la predominancia de uno u otro de estas uniones puede suponer diferencias importantes de estabilidad estructural (a nivel coloidal). A este nivel podemos distinguir: 1) fábricas floculadas: predominancia de uniones cara-borde y borde-borde; 2) fábricas en dominios: predominancia de uniones cara-cara que conforman las mínimas unidades estructurales del suelo: los dominios de arcilla. Este nivel ha sido estudiado principalmente en el campo de la física de coloides y la ingeniería (van Olphen, 1977, Yong y Warketin, 1983).

**5) Cementación**. Esta propiedad alude a la presencia de precipitados químicos que actúan fijando y endureciendo las unidades estructurales, a cualquier escala espacial. Mientras que las unidades estructurales se conforman por uniones débiles de tipo físico-químico entre partículas, como la cohesión (puentes de hidrógeno) y la adhesión (fuerzas electrostáticas, fuerzas de van deer Waals, interacciones hidrofóbicas), la cementación implica enlaces fuertes de tipo covalente, como los generados por la precipitación de sales (carbonatos, yeso) u óxidos de hierro. Podemos describir la cementación según su extensión: 1) sin cementación, 2) escasa, 3) moderada, 4) intensa; así como según la naturaleza del agente cementante (i.e. carbonatos, óxidos, etc.), en este caso son útiles las técnicas microanalíticas de las que dispone el SEM, como el EDX. Cuando la cementación es muy extensa, los agregados estructurales desaparecen y el grado se hace masivo.

**6) Anisotropía.** Esta propiedad describe la orientación espacial de las unidades de fábrica (desde la plaqueta de arcilla hasta los macroagregados), y se relaciona con la actuación de esfuerzos preferenciales sobre la masa del suelo, como pueden ser la compactación por el tráfico o la deposición de partículas de arcilla sobre las superficies internas de los poros del suelo (iluviación de arcilla). Podemos distinguir fábricas desordenadas y fábricas anisotrópicas.

Junto con las propiedades descritas arriba, nos centraremos en tres escalas espaciales, definidas en base a las unidades estructurales propias de cada una de ellas. En la definición de las escalas y las unidades estructurales, nos hemos basado principalmente en el trabajo de Dexter (1987), que incluye los macroagregados y microagregados, junto con los clusters y dominios de arcilla. Cada escala de tamaños se estudia convenientemente a un cierto nivel de aumentos:

*i) Escala de macroagregados (desde simple vista, 1x, hasta 500x).* El nivel de aumentos de esta escala permite caracterizar los macroagregados, que son las unidades de estructura convencionales en las descripciones de campo, y cuyo estudio, normalmente, se efectúa a simple vista o con lupa. La ventaja del microscopio electrónico es que permite apreciar mejor la relación de los macroagregados con unidades estructurales de menor tamaño, como los microagregados, algo que difícilmente puede hacerse a simple vista. Los procesos responsables de la macroagregación tienden a ser de tipo mecánico, tales como las fuerzas derivadas de la contracción y expansión debida al secado-humectación (coincidiendo con verano e invierno, respectivamente), el laboreo, o las fuerzas derivadas del

crecimiento de las raíces (Peng et al., 2008). La importancia fundamental de esta escala es la generación y el mantenimiento de la macroporosidad (poros > 30 μm según Lal and Shukcla, 2004). Un suelo con desagregado o con bajo grado de agregación a este nivel va a presentar, seguramente, problemas para el drenaje y la aireación.

*ii) Escala de microagregados (desde 500x, hasta 3000x).* Existe un amplio consenso en la definición de los microagregados, tanto a nivel de tamaño (agregados de menos de 250 μm) como de su funcionalidad. Al contrario de los macroagregados, que normalmente sufren ciclos anuales de destrucción-regeneración naturales, los microagregados tienden a preservar su integridad durante todo el año, a no ser que sufran procesos de degradación importantes (Bronick y Lal, 2005). Los microagregados son, probablemente, las unidades estructurales más dependientes de la actividad biogénica: crecimiento de radículas e hifas de hongos, actividad de lombrices y otros invertebrados, exudación de compuestos mucosos, etc., y por lo mismo, la escala donde mejor se percibe la calidad biológica del suelo (Six et al., 2004; Lutzow et al., 2006).

*iii) Escala de clusters y dominios de arcilla (más de 3000x, hasta 50.000 e incluso 80.000x).* Este último nivel de estudio ve determinado principalmente por los procesos coloidales, abiogénicos, que provocan la agregación (floculación) de las partículas de arcilla y limo fino (> 10 μm), por lo que la caracterización de las fuerzas de superficie mediante modelos de tipo DLVO es muy importante para una comprensión cabal del mismo. Siguiendo a Dexter (1987), podemos diferenciar entre clusters y dominios

de arcilla. Los clusters son agregados más o menos irregulares de hasta 50 μm, constituidos por partículas individuales limo fino y de dominios de arcilla, y en los que podemos encontrar uniones cara-cara, cara-borde y borde-borde. Por último, los dominios son agregados cara-cara de partículas de arcilla de formas laminares, que constituyen apilamientos que pueden llegar hasta las 10-15 μm de espesor.

Por último, las muestras fueron sometidas a microscopia electrónica de transmisión (TEM) con un JEOL JEM-1010 que opera a 80.000 kV, para obtener información sobre los procesos de floculación y la morfología de las partículas, en tres ampliaciones: 5000; 10000 y 60,000x.

**4.4. Potencial zeta (ζ).**

La movilidad electroforética del sistema estudiado se analizarán con un Zetasizer 3000HS (Ver figura 4.3. Malvern Instruments, Worchestershire, UK). Para determinar el potencial zeta (ζ) del sistema se empleará material natural en polvo (fracciones limo y arcilla) molida en un mortero de ágata hasta obtener un tamaño de partícula adecuado (aprox. 30 μm). Para cada tratamiento, el polvo se mantuvo en una disolución de 1000 ml de electrolitos con la concentración requerida durante 24 horas. Para las medidas de movilidad electroforética, la suspensión se agitó y se dejó en reposo durante 10 minutos, tomando el sobrenadante para el estudio.

En primer lugar se prepararon soluciones homo-iónicas 10, 1 y 0.1 mM de iones monovalentes (NaCl), divalentes ($CaCl_2$) y trivalentes ($FeCl_3$ y

$AlCl_3$), donde se dispersará las cantidades necesarias de sólidos (tierra fina, limo y arcilla) para llevar a cabo las medidas electrocinéticas de las muestras.

En segundo lugar se prepararon disoluciones mono-iónicas de sodio a 1mM, con las distintas muestras de la provincia de Jaén; a la que previamente se han sometido a la eliminación de la materia orgánica natural con $H_2O_2$ y posteriormente a saturación de ácidos húmicos comerciales (HA).

La caracterización eléctrica, se realizó mediante el potencial zeta ($\zeta$), calculado bajo la aproximación de Smoluchowski tal y como se explica en el Capítulo 2 de esta memoria.

**4.5. Energía libre de superficie (SFE).**

Para estimar la energía libre de superficie de las muestras, se usaron dos métodos diferentes en función de las propiedades de compactación que presenten las muestras.

El primer método que se utilizara en muestras que presente un buen nivel de compactación, por ejemplo arcillas. Con dicho método la energía libre superficial se determinó mediante la medida de los ángulos de contacto de tres líquidos (didodometano, agua y formamida) con tensiones superficiales conocidas (ver Tabla 4.1), empleando un goniómetro NRL C.A. (Ver figura 4.3) (Ramé–Hart Inc., New Jersey, USA).

Los ángulos de contacto se midieron en pastillas del sólido en las distintas condiciones de estudio. Las pastillas se obtuvieron comprimiendo el polvo seco bajo 1.5x104 kg/cm$^2$ durante 10 min. Sólo se emplearán las pastillas con una superficie lisa y reflectante a nivel microscópico.

Una descripción detallada de la metodología seguida aparece en Young et al. 1990; y van Oss et al. 1988. Considerando la formulación de estos autores, la relación entre el ángulo de contacto θ y los componentes Lifshitz-van der Waals (LW) y Ácido-Base (AB) de la energía libre superficial del sólido (subíndice 1) y la tensión superficial del líquido ) Se puede escribir como:

$$2\sqrt{\gamma_1^{LW}\gamma_{Li}^{LW}} + 2\sqrt{\gamma_1^{+}\gamma_{Li}^{-}} + 2\sqrt{\gamma_1^{-}\gamma_{Li}^{+}} = \gamma_{Li}(1+\cos\theta) \qquad [1]$$

$\gamma_{Li}$ es la tensión superficial del líquido i que forma un ángulo de contacto θ sobre el sólido y $\gamma^{LW}_{Li}$, $\gamma^{+}_{Li}$ y $\gamma^{-}_{Li}$ son los componentes de tensión superficial del líquido.

Por lo tanto, midiendo los ángulos de contacto de los tres líquidos mencionados, se puede resolver un sistema de tres ecuaciones del tipo [1] para obtener las tres variables desconocidas, $\gamma_1^{LW}$, $\gamma_1^{+}$ y $\gamma_1^{-}$. Los componentes de energía libre de superficie de los líquidos utilizados se muestran en la tabla 3.

El segundo método utilizado para determinación de la energía libre superficial de los materiales estudiados, es la penetración de líquidos en capa fina, este método se presenta especialmente idóneo, cuando los sólidos problemas no permiten el grado de compactación que requiere la técnica de ángulos de contacto.

Para la aplicación de la técnica de penetración de líquidos en capa fina, se usaron portas de microscopio sobre las que se depositó una fina capa del material a estudiar, y se midió el tiempo de avance se distintos líquidos (agua, Diodometano y formamida) de propiedades conocidas con un cronometro de precisión,

Con estas medidas de tiempo se representan en un gráfico la distancia penetrada al cuadrado en el eje x y en el eje y el tiempo en segundos. La pendiente de la recta de ajuste se relaciona con las componentes de la energías libre superficial del sólido, mediante la ecuación de Washburn (Washburn, 1921, Chibowski et al., 1992.

$$x^2 = \frac{rt}{2\eta}\Delta G \qquad [2]$$

donde ΔG es el cambio en la energía libre asociado con el reemplazo de una interfase sólido/aire, por otra sólido/líquido en el proceso de penetración. En la Ec. [2], *r* es el radio del poro medio efectivo que forma la capa delgada de sólido. En esta notación, el proceso de mojado ocurre si ΔG> 0. Se ha demostrado que ΔG en la Ec. [2] se relaciona con los componentes de energía libre superficial del sólido, dependiendo de las condiciones experimentales consideradas en el proceso de mojado.

La tensión superficial y las componentes de los líquidos se tomaron de (Chibowski et al., 1992) y se muestran en la Tabla 4.1. El tiempo requerido para que los líquidos penetren en una distancia dada de ambas placas desnudas se determinara en laboratorio.

Tabla 4.1. Componentes de energía de superficie (mJ/m²) de los líquidos usadas para la medida de ángulos de contacto.

| Líquidos | $\gamma^{TOT}$ | $\gamma^{LW}$ | $\gamma^{+}$ | $\gamma^{-}$ |
|---|---|---|---|---|
| Agua | 72,8 | 21,8 | 25,5 | 25,5 |
| Formamida | 58,0 | 39,0 | 39,6 | 2,28 |
| Diodometano | 50,8 | 50,8 | 0,0 | 0,0 |

**4.6. Adsorciones de sales húmicas: isotermas de adsorción.**

La cantidad de ácidos húmicos (HA) adsorbido sobre la tierra fina de los diferentes suelos fueron calculadas por diferencia entre las concentraciones inicial y final en solución.

Las isotermas de adsorción de los HA en cada muestra se obtuvieron preparando, en primer lugar, suspensiones en agua de humato sódico (39,03% C) a distintas concentraciones, entre 1 mg/L y 1000 mg/L. Se tomaron distintas alícuotas de 30mL de estas soluciones en tubos de centrífuga de 80 mL, en las que se añadió una cantidad fija de sólido hasta obtener la saturación completa de las superficies (como valores orientativos: 0.03 g en el caso de arcilla, 0.5 g en el caso del limo y 1.0 g en el caso de la tierra fina). En el proceso, se ajustó con HCl y NaOH el pH de las soluciones igualándolo al pH del suelo de donde procede la muestra, con el

objetivo de realizar la adsorción en condiciones de pH similares al medio edáfico natural.

En cada caso, se realizaron cinéticas de adsorción de HA en las muestras para estimar el tiempo que la superficie tarda en saturarse con el adsorbato, alcanzando la condición de equilibrio (ver figura 4.2. y 4.3.). Durante todo el proceso de adsorción, la suspensión se agitó suavemente de forma mecánica, controlando la temperatura en un baño termostatizado. De esta forma se obtuvo isotermas de 20, 30 y 40 ºC, cuya comparación nos permitió obtener información acerca de los tipos de adsorciones predominantes (fisiadsorción o quimiadsorción) (Lyklema et al., 1995).

La cantidad de HA adsorbida se determinó mediante las variaciones de absorbancia óptica en la disolución de HA. Para la medida de la absorbancia se empleó un Hitachi Spectrophotometer (U-2000 model) a una longitud de onda de 554 nm, calibrando mediante soluciones de HA de concentraciones conocidas a través de la ley de Beer. Una vez obtenidas las isotermas a las distintas temperaturas de estudio, se analizaron teniendo en cuenta los modelos de de Langmuir y de Freundleich.

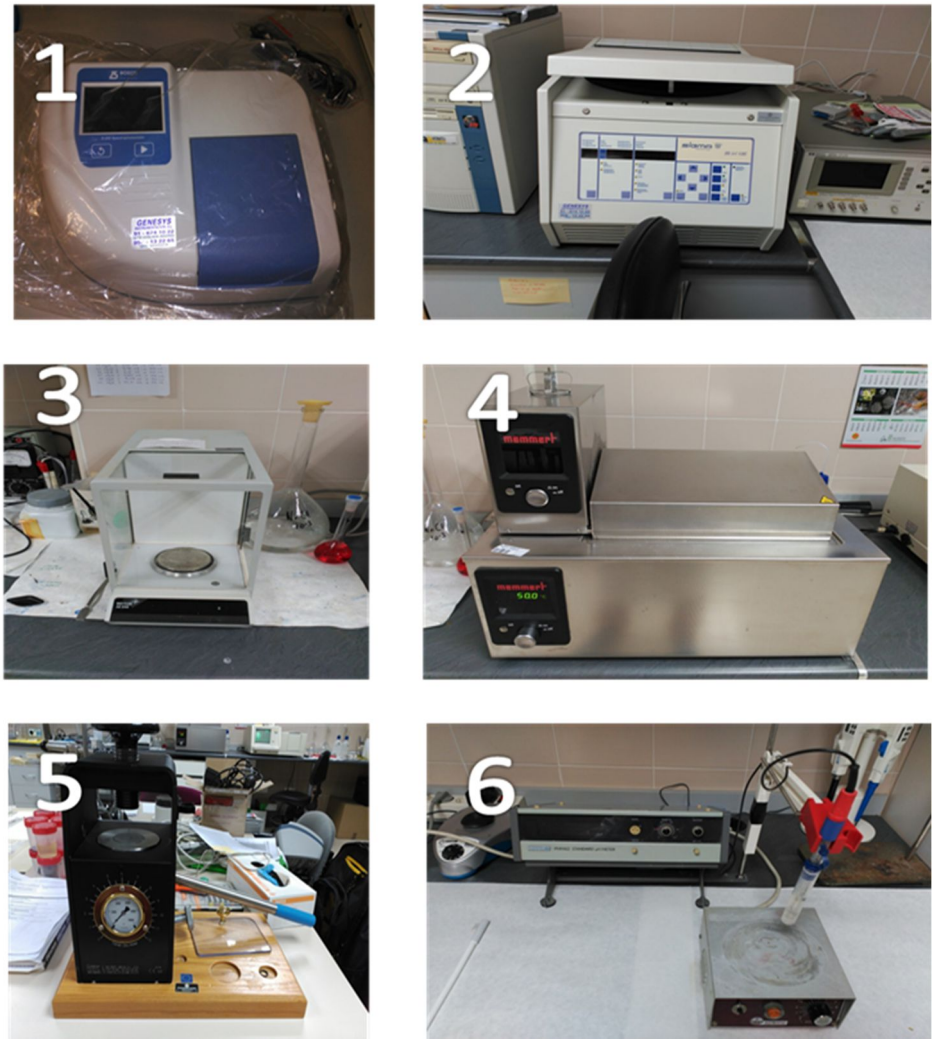


Figura 4.2. En esta figura se muestran los aparatos de medición empleados para elaborar este documento. Imagen 1. The Boeco S-220 (UV/VIS) and S-200 (VIS). Imagen 2. Used Sigma 2K15 refrigerated heated laboratory benchtop centrifuge W/ Rotor 12145. Imagen 3. Balanza analítica AE 240 balanza de dos campos. Imagen 4. Baño Memmert WNB7 Termorregulado 7 LTS. PDF. BASIC WNB 7 /7 Lts/Amb+5ºc A 95ºc. Imagen 5. The model 30 and model 40 feature the same patented lightweight and ergonomic unibody design as the 12 ton and 20 ton models. Imagen 6. London company PHM 62 - PHM62 - standard pH meter in business & industrial, healthcare, lab & life science, lab equipment.

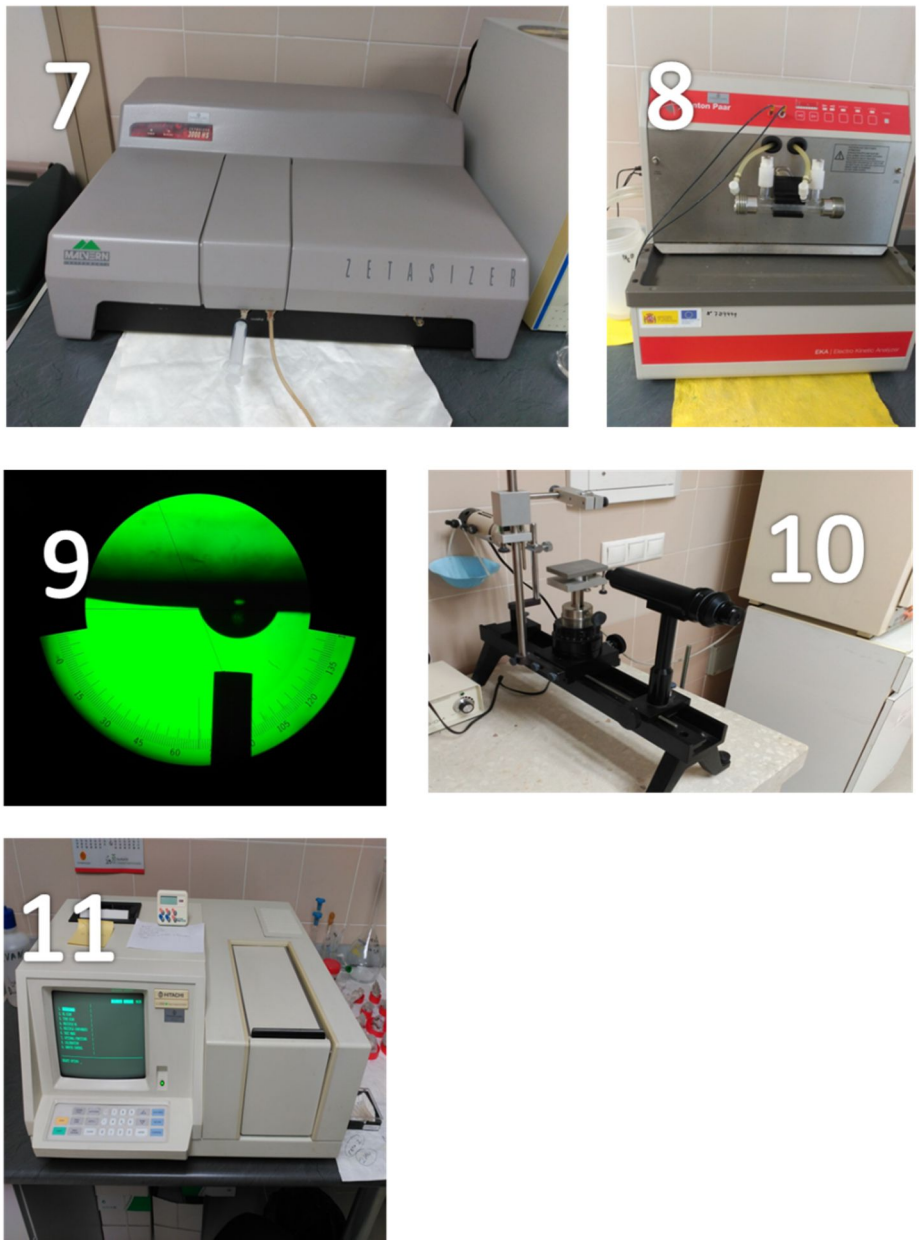


***Figura 4.3.*** Continuación de la figura 4.2. Imagen 7. Malvern Instruments Zetasizer 3000 Titrator Unit HSA Particle Size 09636, for sale surplus used equipment from hitechtrader price mt holly nj. Imagen 8. Anton Paar Instrument Eka (Electro Kinetic Analyer). Imagen 9. Imagen obtenida de la cámara video del goniómetro. Imagen 10. Gonimetro. Imagen 11. Hitachi u200 Spectrophotometer

# Capítulo 5
# Resultados

## 5.1. Introducción.

En este capítulo se van a exponer los trabajos obtenidos tras estos cuatro años de investigaciones. Los artículos han sido publicados en revistas internacionales de impacto indexadas en la base de datos JCR y de 1º cuartil, además el trabajo se ha enriquecido sustancialmente por las aportaciones y sugerencias realizadas en distintos ámbitos nacionales e internacionales a través de poster y Abstract.

El capítulo 5, empieza con el primer artículo publicado titulado **"Effect of interfacial properties on mechanical stability of ash deposit"**(5.2.1)**.** En este artículo se verá como se ha aplicado nuestros estudios de la Teoría DLVO-Extendida a materiales sedimentarios o escasamente edafizados. Como son los depósitos volcánicos en el estudio de estabilidad de depósitos de cenizas.

Los dos artículos siguientes de esta sección (5.2.2 y 5.2.3) se encuentran en proceso de revisión; se han enviados a revistas internacionales. Estos artículos son: "**Electrical and termodynamic characterizations of volcanic ashes**" and "**Interpretation of the volcano landslides in terms of zeta potencial and surface free energy**". En ellos se estudian diferentes depósitos volcánicos de distintos volcanes, con el fin de analizar las propiedades superficiales de los depósitos volcánicos. Analizamos diferentes volcanes activos como el Monte Etna, el Monte Vulcano, el Monte Stromboli, el Hierro, el Teide, el Pico de Fuego y la Isla Decepción. Se calculó esta energía de interacción para saber qué depósito podría producir deslizamiento de tierra tipo soil-type y cuales pudieran ser a factores externos como la presencia de una capa hidráulica.

El capítulo 5.3 empieza con el segundo artículo publicado, se denomina: "**Implication of zeta potential and surface free energy in the description of agricultural soil quality: effect of different cations and humic acids on degraded soils"**. Este artículo supone la primera toma de contacto en el estudio de la calidad del suelo a través del análisis de sus propiedades eléctricas y termodinámicas.

El siguiente artículo (tercero publicado) se denomina: **"Humic acid adsorption and its role in the aggregation processes at colloidal scale in organic olive grove soils, studied by zeta potential, surface free energy and the extended-DLVO theory"** se encuentra aún en fase de pre-impresión, aunque aquí podrán encontrar la última versión de él. Se ha estudiado los procesos de agregación del suelo a nivel de coloidal a través

del estudio de la Teoría DLVO-Extendida. En este artículo científico también se ha estudiado la adsorción de ácidos húmicos comerciales sobre el suelo, para determinar el mecanismo de adsorción de este.

El cuarto artículo de este capítulo en fase pre-print, se ha denominado genéricamente **"Improvement of the structural stability at the colloidal scale in marginal olive grove soils by organic agriculture, characterized by the extended-DLVO model".** En este estudio se ha aplicado la metodología utilizada en el artículo numero 3 pero a suelos de tipo silíceo. Destacar que esta última investigación ha sido posible gracias al proyecto del Instituto de Estudios Giennenses") project no. RFC/IEG 2015 *Capacidad de adsorción y estabilización de materia orgánica en los suelos del olivar: factores ambientales y de manejo, y mecanismos fisicoquímicos implicados.*

Por último, también podemos ver el último artículo publicado denominado: **"Long-term effects of olive mill pomace co-compost on wettability and soil quality in olive groves".** En él se fijó el objetivo de estudiar el efecto que produce la adicción de compost sobre la estructura, porosidad, permeabilidad y humectabilidad del suelo.

Estos proyectos han sido financiados por la Universidad de Jaén con el número de proyecto **UJA2015/06/13** con la colaboración de la fundación **Caja Rural de Jaén.**

## 5.2. Aplicación de la DLVO-Extendida al estudio de suelos y depósitos volcánicos. Caracterización y estabilidad de los depósitos.

### *5.2.1. Artículo: Effect of interfacial properties on mechanical stability of ash deposit.*

Resumen

Los suelos volcánicos se encuentran en multitud de países de todo el mundo. La geología de superficie en estas zonas de islas volcánicas está dominada por ellos. En estas zonas geográficas suelen encontrase una alta densidad de población en las faldas de los volcanes principales o secundarios. Los suelos volcánicos se apoyan en laderas con planos muy inclinados, que a menudo están totalmente desprovistas de vegetación, y son susceptibles a sufrir deslizamientos.

La investigación de tixotropía en suelos de origen volcánico es relevante para una mayor comprensión de comportamiento mecánico, por ejemplo, para la comprensión de procesos dinámicos tales como deslizamientos de tierra. Los procesos tectónicos que dan lugar a la actividad volcánica y a la formación de los volcanes y sus depósitos tienden a producirse acompañados de una actividad sísmica. La isla de El Hierro, Islas Canarias en España, es una de las regiones donde los deslizamientos de tierra son frecuentes y algunos de ellos son inducidos por los terremotos de origen volcánico, por lo que estos constituyen un peligro natural muy significativo para la población residente de la isla.

González de Vallejo et al. (1981) presentaron un estudio de un suelo volcánico de la isla, en él se mostraba una tendencia general a formar agregados de partículas de arcilla, que por lo general muestra diferentes estructuras y niveles de cementación. Dichas partículas y sus relaciones entre ellas, determinaran la cohesión de los depósitos volcánicos.

En este trabajo se estudia la cohesión de las partículas de dos muestras de cenizas volcánicas, utilizando para dicho fin, los análisis de energía libre superficial y del potencial zeta. Los resultados se presentarán en términos de energía total de interacción entre las partículas dispersas, calculado a partir de la teoría DLVO extendida. Se presta especial atención al papel de las interacciones interfaciales y a los procesos de agregación que dependerá en gran medida en el valor de pH y la fuerza iónica del medio acuoso, similar al efecto que diversos cationes tienen en la cohesión de los depósitos.

Se pudo observar que: (1) El pH del medio determina la cohesión de los depósitos de ceniza. (2) El efecto del electrolito $Na^{+}$ en los depósitos de ceniza es totalmente diferente en los dos tipos de cenizas, cenizas blancas inestabilidad y cenizas negras estabilidad. (3) Por su parte el $Ca^{2+}$ provoca una mayor estabilidad en los dos tipos de cenizas. (4) El efecto de $Fe^{3+}$ mostró que las condiciones óptimas de estabilidad aparecieron en valores de pH neutros.

# Artículo científico:

# EFFECT OF INTERFACIAL PROPERTIES ON MECHANICAL STABILITY OF ASH DEPOSIT.

# Revista científica:

# Journal of Rock Mechanics and Geotechnical Engineering,

Journal of Rock Mechanics and Geotechnical Engineering 8 (2016) 187–197

Contents lists available at ScienceDirect

Journal of Rock Mechanics and Geotechnical Engineering

journal homepage: www.rockgeotech.org

Full length article

# Effect of interfacial properties on mechanical stability of ash deposit

A. Ontiveros-Ortega [a,b,*], J.A. Moleon [a], I. Plaza [a], C. Guillén [c]

[a] Department of Physics, Campus Universitario de las Lagunillas s/n, Edificio A-3, University of Jaén, Jaén, 23071, Spain
[b] Instituto Andaluz de Geofísica, University of Granada, Granada, 18071, Spain
[c] Department of Geography, Campus Universitario de Guajara s/n, University of La Laguna, Islas Canarias, 38071, Spain

ARTICLE INFO

*Article history:*
Received 30 July 2015
Received in revised form
14 October 2015
Accepted 26 October 2015
Available online 27 January 2016

*Keywords:*
Zeta potential
Surface free energy
Volcanic ash
Deposits stability
El Hierro Island

ABSTRACT

The paper presents a study on the cohesion of volcanic ash particles using surface free energy determination and zeta potential analyses. This is a subject of great interest in physical volcanology, as many researches on volcanic particle aggregation are frequently reported. In this case, special attention is paid to the role of structural or hydration forces between hydrophilic surfaces, which are a consequence of the electron-donor/electron-acceptor character of the interface. From this point of view, the results are potentially interesting as they could give valuable insights into this process. The results are presented in terms of the total energy of interaction between dispersed particles, computed from the extended DLVO theory. Contributions to the total free energy of interaction were determined from the zeta potential and surface free energy of ash, measured under different experimental conditions. Two samples of basaltic volcanic ash (black and white) with silica contents of 44% and 63% respectively are studied. The surface free energy and zeta potential were analysed for ashes immersed in different electrolytes (NaCl, $CaCl_2$, $FeCl_3$). The presence of electrolytes changes the surface properties of the solid materials. The analysis of total interaction energy between the ash particles in aqueous medium shows that soil cohesion strongly depends on ash surface properties, chemical nature, the adsorbed cation on the surface, and pH value.


## 1. Introduction

Volcanic soils are encountered in many countries around the world and dominate the surface geology in several areas of high population density. Furthermore, many of the areas where volcanic soils are predominant are within tropical regions with high annual rainfalls and frequently intense precipitation. Volcanic soils support near-vertical slopes, which are often totally denuded of vegetation, are susceptible to sudden and catastrophic failure (Bommer et al., 2002). The El Hierro Island is one of the regions where earthquake-induced landslides constitute significant natural hazards. Mitigation of landslide hazards in regions such as Canary Island first requires a thorough understanding of the behaviour of these volcanic soils under static and dynamic conditions.

Gonzalez de Vallejo et al. (1981) presented a study of a volcanic soil located in Tenerife, Canary Island, Spain. The soil shows a general tendency to form aggregations of clay particles, usually showing different fabrics and levels of cementation. The cohesion of ash deposits depends on several factors. Rheological properties in aqueous media are influenced by the interactions between particles. The control of flocculation phenomena, adsorption, wetting and rheological properties of dispersion depends on the particle interactions (Plaza et al., 1998; Bailey et al., 2009; Cockell et al., 2010; Gimmi and Kosakowski, 2011; Baumgarten et al., 2012, 2013; Kadar et al., 2014; Ontiveros-Ortega et al., 2014). Much of the scientific and technological interest in clay minerals derives from their interfacial interactions with colloidal particles (clays and other minerals) in the presence of a liquid, most often water. Andosols are highly sensitive to any mechanical disturbance, but they have the potential to recover their structure after a certain rest time (Rao, 1995). However, the mechanism of thixotropy in these soils on the particle-to-particle scale is still not well understood. The investigation of thixotropy in volcanic ash soils is relevant to greater comprehension of mechanical behaviour at various scales as induced by trampling or remoulding, for example, for understanding dynamic processes such as landslides (Li et al., 1997; Baumgarten et al., 2013).

Surface thermodynamic theory can describe the interactions between condensed-phase materials across an interface and therefore provides a basis for a natural and quantitative definition of cohesion of volcanic ash deposits, and for total interaction energy in the form of the free energy of interfacial interaction between particles in an aqueous environment (van Oss and Good, 1989; Duran et al., 1998). Such a definition can reveal which properties

* Corresponding author. Tel.: +34 953 212830.
*E-mail address:* aontiver@ujaen.es (A. Ontiveros-Ortega).
Peer review under responsibility of Institute of Rock and Soil Mechanics, Chinese Academy of Sciences.
1674-7755 © 2016 Institute of Rock and Soil Mechanics, Chinese Academy of Sciences. Production and hosting by Elsevier B.V. All rights reserved.
http://dx.doi.org/10.1016/j.jrmge.2015.10.008

of the materials and of the liquid medium are responsible for the interfacial behaviour and therefore soil cohesion.

This work deals with the total energy of interactions between colloidal ash particles in different experimental conditions. Special attention is paid to the role of interfacial interactions, not only electrostatic and van der Waals but also structural or hydration forces between hydrophilic surfaces, which are a consequence of the electron-donor/electron-acceptor character of the interface (van Oss, 1994). A similar approach has been used to explain bacteria adhesion on volcanic glass (Ontiveros-Ortega et al., 2014), zinc sulfide on silicon (Duran et al., 1998), or calcium carbonate on glass (Ontiveros et al., 1996a). We also focus our interest on the fact that aggregation processes depend strongly on pH value and ionic strength of the aqueous medium, similar to the effect that various cations have on the cohesion of deposits.

The tectonic processes that give rise to the volcanism responsible for the formation of these deposits tend to occur in areas of high seismic hazards. The El Hierro Island is one region where volcanic soils are abundant and earthquake-induced landslides constitute significant natural hazards (Masson et al., 2006). The submarine eruption of "El Mar de las Calmas" at the El Hierro Island (Perez et al., 2015) developed on a submarine slope about 2 km from the southern tip of the island, between October 2011 and March 2012. This eruption revealed the need to characterise in detail the most recent eruptive history of the island, in order to know and minimise the effects of probable future eruptive episodes.

In the southwestern part of the Canary Islands with the area of 268.7 $km^2$ (Instituto Canario de Estadística), volcanism emerged only 1.2 million years ago (Guillou et al., 1996) on the El Hierro Island. It has the smallest surface area and the youngest geological age of all the Canary Islands. Its geological history is characterised by a succession of three volcanic cycles linked with the development of several volcanic edifices (Guillou et al., 1996; Balcells and Gomez, 1997a, b, c, d). The initial volcanic activity is associated with formation of the Tiñor Edifice in the northeast of the island, with the age of 1.12–0.88 million years. The collapse of the north side of this edifice at 888 thousand years ago was subsequently silted up by the lava edifice "El golfo-Las playas" (545–176 thousand years), and then affected by large landslides over 130–80 thousand years (Longpre et al., 2011).

Around 158 thousand years ago, volcanism of the northwest, northeast and south-southeast rifts started (Guillou et al., 1996), which has continued without major interruption (Pérez Torrado et al., 2011) to the present day. Volcanic activity of the rifts largely coincides with the intermediate series (Coello, 1971; Pellicer, 1977), undifferentiated series and cliff- and platform-forming formations (Carracedo et al., 2001). El Hierro has a total of 179 monogenetic eruptive centres, 78 of which are developed in the northeast rift, 62 in the west, and 39 in the south (Becerril et al., 2013).

The Holocene period has only five datings, and some of them are unassociated with accurate emission centres: (1) Emission centre without precise location, in the southwest rift, dated at 8.3 thousand years (Pérez Torrado et al., 2011); (2) Tanganasoga Volcano in the southwest rift, dated at 6.74 thousand years (Pellicer, 1977); (3) Humilladero Mountain in the southwest rift, dated at 5.1 thousand years (Pérez Torrado et al., 2011); (4) Emission centre without precise location in the west-southwest rift, dated at 3.5 thousand years (Pérez Torrado et al., 2011); and (5) Chamuscada Mountain in the northeast rift, dated at 2.5 thousand years (Carracedo et al., 2001).

Following its conquest by the Spanish, there were references to possible volcanic activities on the island. Controversy surrounding these references can be found in Bravo (1968), Hernández Pacheco (1982), and Romero (1991). Nonetheless, the submarine eruption of Mar de las Calmas is the first eruptive event observed on the island in the last 500 years.

Most volcanism of rifts corresponds to mafic eruptions of basaltic nature, characterised by the construction of one or more volcanic edifices. These edifices are constituted by slag, lapilli, and abundant emission of lava flows. Eruptive mechanisms involved are mainly of Strombolian, but also have been described as having a phreatomagmatic character.

## 2. Materials

### 2.1. Chemical

All reagents and chemicals used were of analytical grade (NaCl, $CaCl_2$ and $FeCl_3$ provided by Sigma–Aldrich Co., USA; Diiodomethane and formamide by Merck KGaA. LLC, Germany). Water for surface free energy determination was twice-distilled, and Milli-Q reagent-grade water was used for electrophoretic measurements. Solution pH value was adjusted by adding a reagent-grade solution of either NaOH or HCl both provided also by Merck.

### 2.2. Random sampling

Two samples of cinder materials with very different features were collected (see Fig. 1). The first was taken around Malpaso Peak (1502 m) at 1046 m altitude, the coordinates of 27 R 791479/3070.212. In this place, there is a level of very fine loose ash, greyish (white ash, white triangle in Fig. 1), finely laminated and a general power of ~50 cm, which is covered at the top by a black lapilli layer. This cineritic layer has been previously described by Pellicer (1977) and Balcells and Gomez (1997b). They stated that these are the only pyroclastic deposits of composition salic on the El Hierro Island. These deposits may correspond to an episode of marked explosive features, which are believed to be prior to the formation of Tanganasoga Volcano. However, Pellicer (1979) associated them to a volcanic event after the formation of this volcanic edifice.

The second sample (black ash, black triangle in Fig. 1) was collected in a reservoir of basaltic pyroclastic of dispersal (coordinates of 27 R 786848/3068.855, altitude of 1023 m). The sample was taken from a cineritic level of black colour, fresh appearance, and very little consolidation. Balcells and Gomez (1997b) associated the presence of this very fine-grained level with pulses or phreatomagmatic phases linked to purely magmatic monogenic eruptions around the northwest ridge summits of the island.

## 3. Methods

### 3.1. Scanning electron microscope images of ash

Ash morphological aspect of soil structure is properly examined by scanning electron microscope (SEM). We used a scanning microscope with acceleration voltage of 25 kV (S-510; Hitachi Ltd., Tokyo, Japan) equipped with an energy-dispersive X-ray detector (EDAX; Rontec GmbH, Berlin, Germany). Fine ash was mounted on the sample holder with colloidal silver and metallised with gold deposited in two orientations (20°–30°). Conventional SEM images at low (3200), medium (11,200) and high (46,000) magnifications were obtained.

### 3.2. X-ray fluorescence

A wavelength dispersive X-ray fluorescence spectrometer (WDXRF) S4 explorer model pioneer from Bruker is used here. The spectrometer analyses elements from carbon to uranium in a wide

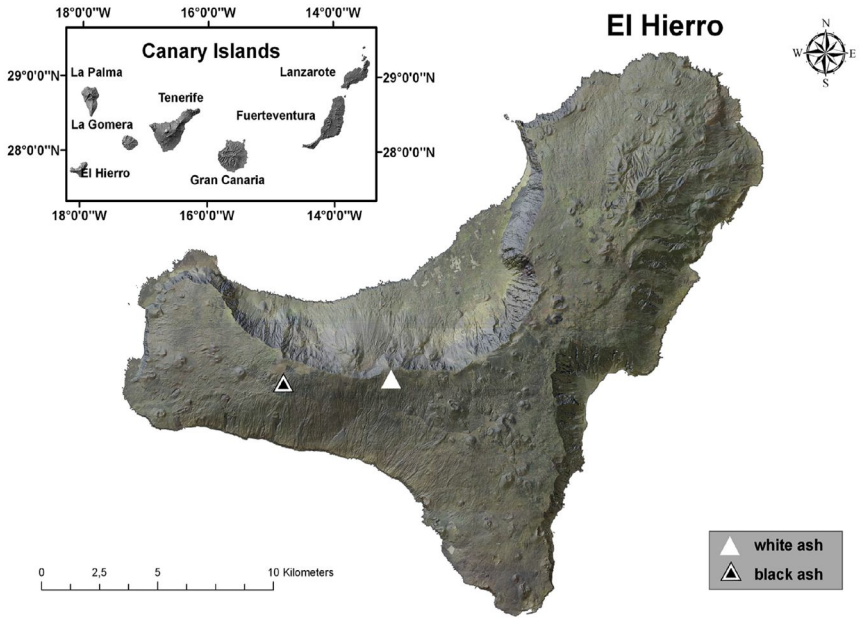


**Fig. 1.** Location of the main geological units of the El Hierro Island. Satellite image is shown for onshore part. Triangles indicate location of sample collection. Location of the island is relative to the Canary Islands.

variety of samples with accuracy and precision. The source for the excitation of the sample is an X-ray tube with Rhodium anode and Be window of 75 μm. The tube and the X-ray generator are designed to provide a maximum output of 4 kW with applicable maximum voltage and current of 60 kV and 150 mA, respectively. The device has two collimators: 0.23° and 0.46°, and five crystals analyzers: OVO-55, PET, Ge, LiF220 and LiF200. The machine is equipped with two sensors ("sealed proportional counter" and "scintillation counter") whose movement is controlled by a high precision goniometer covering. Samples were made in tablet form, using a hydraulic press, Nannetti Mignon SS model.

### 3.3. Surface free energy determination

This energy determination is based on measurement of time $t$ that a liquid of viscosity $\eta$ and surface tension $\gamma_3$ takes to penetrate a distance $x$ through a thin porous layer of the solid on a microscope glass slide. The most general description of the process is given by a generalised form of Washburn's equation (Washburn, 1921; Chibowski, 1992; Duran et al., 1998):

$$x^2 = \frac{rt}{2\eta}\Delta G \tag{1}$$

where $\Delta G$ is the change in free energy associated with replacement of a solid/air interface by a solid/liquid one in the wicking process, and $r$ is the effective mean radius of the capillary network forming the thin layer of solid. In this notation, spontaneous wicking occurs if $\Delta G > 0$. It has been shown that $\Delta G$ in Eq. (1) is related to the solid surface free energy components, dependent on experimental conditions considered in the wicking process. For brevity, we do not describe this in detail; the reader is instead directed to the main references on this topic, in association with Washburn's equation.

The experimental procedure was described as follows. Microscope glass slides covered by a thin layer of ash were prepared by spreading 2 mL of 50 g/L aqueous suspensions of ash, and drying them for 24 h at room temperature. Then, they were both oven-dried at 110 °C for 1 h and stored in a desiccator (bare plates), or put into contact with the vapour of the liquid used in the wicking experiments in a closed chamber for several hours ("precontacted" plates). Liquids used for the experiments were water, formamide, and n-decane. Surface tension and its components of the liquids were taken from the literature and are shown in Table 1. The time required for the liquids to permeate a given distance of both bare and precontacted plates was measured to obtain surface free energy components of the ash (Chibowski, 1992). This powdered ash was previously equilibrated during 24 h with electrolyte solutions at the desired concentration (1 mmol/L) at natural pH value.

### 3.4. Zeta potential

For electrical characterisation, zeta potential $\zeta$ was calculated based on the Smoluchowski relationship (Smoluchowksi, 1921) using

**Table 1**
Surface tension and its components (mJ/m$^2$) of liquids used in contact angle and thin layer wicking measurements (taken from van Oss, 1994).

| Liquid | $\gamma$ | $\gamma^{LW}$ | $\gamma^+$ | $\gamma^-$ |
|---|---|---|---|---|
| n-decane | 23.8 | 23.8 | 0 | 0 |
| Formamide | 58 | 39 | 2.28 | 39.6 |
| Water | 72.8 | 21.8 | 25.5 | 25.5 |

$$\zeta_{EP} = \frac{V\eta}{\varepsilon_0 \varepsilon_r E_x} \quad (2)$$

where $V$ is the particle velocity, $E_x$ is the axial electric field (V/m), $\varepsilon_r$ is the relative dielectric constant (assuming 80.1 for water at 20 °C), $\varepsilon_0$ is the absolute dielectric constant ($\approx 8.8541 \times 10^{-12}$ F/m), $\eta$ is the dynamic viscosity of the liquid (N s cm$^{-2}$), and $\zeta_{EP}$ is the electrophoretic zeta potential (mV).

The $\zeta$ value of ash particles was calculated from electrophoretic mobility measurements at (20 ± 0.5) °C in a Malvern Zetasizer 3000HS. To measure the mobility of ash particles, original beads were further grounded, and those with dimensions smaller than 1.5 mm were separated by sedimentation. For each treatment, the powder was conditioned by different electrolytes for 24 h in 500 mL of solution at the required concentrations.

## 4. Theory

For colloidal-sized ash particles, the transport, deposition and mechanical stability of the final deposit are strongly influenced by surface interactions between particles dispersed in water. The possibility of aggregation between particles is also of interest. According to extended DLVO theory (van Oss et al., 1988; van Oss and Good, 1989; van Oss, 1994), three kinds of interfacial interactions should be considered, i.e. Lifshitz–van der Waals (LW), electrostatic (EL), and acid–base (AB). The total interaction energy between the particles is given by

$$\Delta G_{131}^{TOT} = \Delta G_{131}^{EL} + \Delta G_{131}^{LW} + \Delta G_{131}^{AB} \quad (3)$$

where the subscript 131 refers to the phases involved. In our case, 131 refers to particle-liquid medium-particle for the aggregation process. The three contributing interactions depend on the nature of the interfaces involved and on the distance $H$ between the surfaces. Under double-layer model and for moderate potentials, the electrostatic interactions can be obtained from Duran et al. (1998):

$$\Delta G_{131}^{EL} = 2\pi\varepsilon a\zeta^2 \ln\left(1 + e^{-\kappa H}\right) \quad (4)$$

where $a$ is the particle radius, $\varepsilon$ is the dielectric constant of the liquid, $\kappa$ is the Debye screening length (double-layer thickness), and $H$ is the distance between the surfaces.

Corresponding expression for Lifshitz–van der Waals interaction (Visser, 1976; Gregory, 1981) is

$$\Delta G_{131}^{LW} = -\frac{A_{131}}{6}\left[\frac{2a^2}{H(4a+H)} + \frac{2a^2}{(2a+H)^2}\right] + \ln\frac{H(4a+H)}{(2a+H)^2} \quad (5)$$

where $A_{131}$ is the Hamaker constant for each system, and can be estimated from surface tension determination of the materials involved. We use the thermodynamic treatment proposed by van Oss (1994) for a full account of the theory. According to those authors, the surface free energy (or surface tension) $\gamma_i$ of a condensed phase consists of two additive contributions, dispersive LW and polar AB, which in turn depend on two parameters accounting for the electron-donor ($\gamma^-$) and electron-acceptor ($\gamma^+$) characters of the materials ($\gamma_i = 2(\gamma_i^+\gamma_i^-)^{1/2}$). If $\gamma_i^{LW}$ is known for all phases involved, the Hamaker constant can be obtained as

$$A_{131} = 12\pi H_0^2 \Delta G_{131,\ H_0}^{LW} \quad (6)$$

$$\Delta G_{131,\ H_0}^{LW} = -2\left(\sqrt{\gamma_1^{LW}} - \sqrt{\gamma_3^{LW}}\right)^2 \quad (7)$$

where $H_0$ is estimated at (1.58 ± 0.08) Å (van Oss et al., 1988).

Similarly, the calculation of $H$-dependence of $\Delta G_{131}^{AB}$ requires knowledge of $\gamma_i^+$ and $\gamma_i^-$ for the two phases:

$$\Delta G_{131}^{AB} = 2\pi a\lambda \Delta G_{131,\ H_0}^{AB} e^{(H_0 - H)/\lambda} \quad (8)$$

where $\lambda$ is the correlation length of water molecules, approximately $\lambda = 1$ nm for hydrophilic surfaces; and $\Delta G_{131,\ H_0}^{AB}$ depends on the AB parameters of the free energy of phases 1 and 3 (van Oss, 1994; Ontiveros et al., 1996a). According to van Oss (1994), the expression for $\Delta G_{131,\ H_0}^{AB}$ is

$$\Delta G_{131,\ H_0}^{AB} = 4\left(\sqrt{\gamma_1^+\gamma_1^-} + \sqrt{\gamma_3^+\gamma_3^-} - \sqrt{\gamma_1^+\gamma_3^-} - \sqrt{\gamma_3^+\gamma_1^-}\right) \quad (9)$$

## 5. Results and discusion

### 5.1. SEM photographs

The two samples of volcanic ash showed visible differences in density and porosity. Macroscopic differences revealed that the material with higher porosity was white ash and the black ash has less porosity, with a glazed aspect. These porosity differences were more clearly appreciated using SEM at low magnification (shown in Fig. 2). Both white and black ashes were highly vesiculated, indicating that both materials had a high gas contents at the time of eruption. This would explain the explosive origin of this ash. This is normal behaviour within the parameters of mafic eruptions of the Canary Islands.

From a viewpoint of textural characterisation, it is observed that for black ash there is no internal structure, and an aggregate of micro-pores and volcanic glass can be observed without order or direction of growth.

In the case of white ash, the main difference from the black ash is its flat surface. At higher magnification, sharp edges and surface aggregation of micro-particles can be seen, which indicate a more violent eruption.

### 5.2. Soil mineralogy

A quantitative analysis of the material used via X-ray fluorescence (XRF) spectrometry was done. From the analysis (Table 2), black ash was identified as basanite. The white ash, however, presented a compositional range extending to rhyolite–trachyte (see Fig. 3), with high aluminium content (13.9% $Al_2O_3$). Basanite is a typical magma in the eruptions of the El Hierro Island and, in general, in the Canary Islands eruptions, it has 43%–45% $SiO_2$ and a volatile content of ~2%. The white ash had the $SiO_2$ content of 63.2% (trachyte) with high contents of $Al_2O_3$ (17.5%), and volatile content of 4%–5%. This would make it potentially much more explosive than basanite.

### 5.3. Surface free energy components of ash

Tables 3 and 4 show the surface free energy components of the white and black ashes for the bare and various electrolyte concentrations tested.

Surface free energy components of the ash were obtained by the thin layer wicking technique. Fig. 4 shows as an example graph in

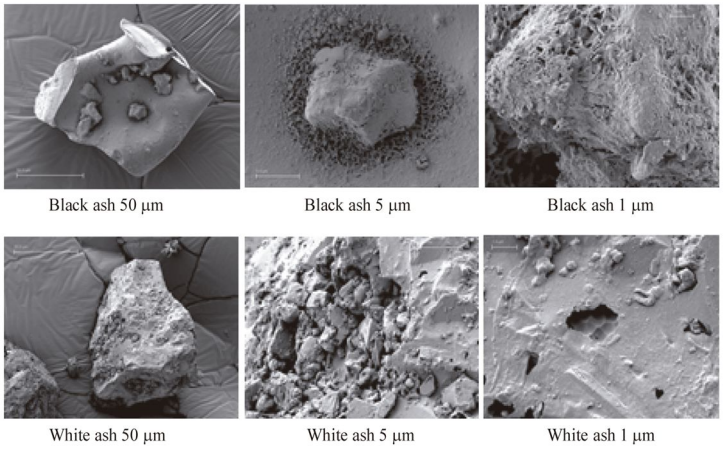


**Fig. 2.** SEM images of volcanic ash at different magnifications.

which the wicking of various liquids and experimental conditions are represented as a function of time. Substantial linearity is evident, as predicted by Washburn's equation (Eq. (1)).

The $\gamma^{LW}$ component for untreated black ash was around 35 mJ/m$^2$ and 63 mJ/m$^2$ for untreated white ash. This is likely because black ash has a more ordered structure of water molecules at the solid/liquid interface. This behaviour is modified with the presence of electrolytes in solutions. The effect of the electrolytes is generally to equilibrate the value of the dispersion component, increasing the value in the black ash and decreasing it in the white ash. In any case (except $Ca^{2+}$), the dispersive component $\gamma^{LW}$ is smaller for black ash.

Tables 3 and 4 also show the effect that different electrolytes (mono-, di- and tri-valent) had on polar components $\gamma^+$ and $\gamma^-$ for both types of ashes. This reveals that the volcanic ash can be considered as electron-donor in nature ($\gamma^+ \approx 0$, $\gamma^- > 0$). Unlike $\gamma^+$, $\gamma^-$ is very sensitive to the ash surface composition and the treatments. However, $\gamma^+$ is not different from zero within experimental error. That is, all the oxides in general (Plaza et al., 1998) and $SiO_2$ (Ontiveros-Ortega et al., 2014) in particular are essentially monopolar substances in the sense of van Oss (1994); they might have AB interactions with phases of any polarity ($\gamma^+$, $\gamma^-$ or both, different from zero).

Table 3 lists surface free energy components of white ash. It can be seen that $\gamma^{LW}$ decreases with increasing cation valence to 36.8 mJ/m$^2$ in presence of NaCl. For the polar component, it is observed that the untreated white ash was strongly monopolar ($\gamma^+ \approx 0$, $\gamma^- > 60$ mJ/m$^2$) with the electrolyte treatment, whereas black ash was moderately monopolar. This is similar to what other authors have found for different inorganic compounds (Ontiveros et al., 1996a, b; Plaza et al., 1998). White ash seems to have a Lewis base, but this behaviour is strongly modified when the cation present is $Ca^{2+}$, probably because of AB neutralisation between the ash surface and the cations (Lewis acid).

**Table 2**
X-ray fluorescence (XRF) analysis for black and white ash. The bold text corresponding to the $SiO_2$ and the cations used in our experiments.

| Compound | Concentration (%) | |
|---|---|---|
| | Black | White |
| $Na_2O$ | **2.71** | **7.27** |
| MgO | 5.71 | 0.857 |
| $Al_2O_3$ | 13.9 | 17.5 |
| $SiO_2$ | **44.3** | **63.2** |
| $P_2O_5$ | 0.98 | 0.16 |
| $K_2O$ | 1.68 | 3.72 |
| CaO | **10.37** | **2.55** |
| $TiO_2$ | 4.5 | 0.799 |
| MnO | 0.178 | 0.151 |
| $Fe_2O_3$ | **14.14** | **3.94** |
| NiO | 0.011 | 0.017 |
| ZnO | 0.03 | 0.019 |
| $Rb_2O$ | 0.023 | 0.058 |
| SrO | 0.132 | 0.108 |
| Total | 98.664 | 100 |

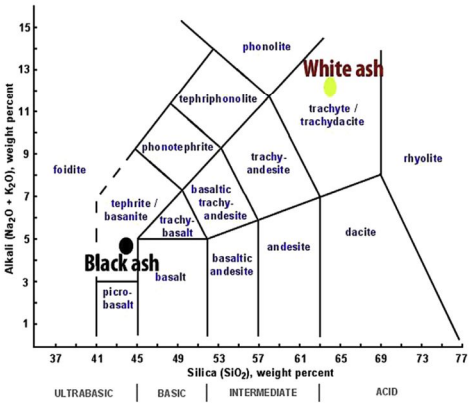


**Fig. 3.** Classification of studied ashes, black and white, according to TAS diagram.

**Table 3**
Values of LW component $\gamma^{LW}$, electron-acceptor $\gamma^+$ and electron-donor $\gamma^-$ parameters of AB component of surface free energy for white ash.

| White ash | $\gamma^{LW}$ (mJ/m$^2$) | $\gamma^+$ (mJ/m$^2$) | $\gamma^-$ (mJ/m$^2$) |
|---|---|---|---|
| Bare white | 62.8 ± 4 | 0.43 ± 0.2 | 66 ± 20 |
| + NaCl | 36.79 ± 1 | 0.35 ± 0.1 | 53.67 ± 20 |
| + $CaCl_2$ | 39.48 ± 1 | 7.23 ± 0.8 | 16.09 ± 11 |
| + $FeCl_3$ | 48.6 ± 0.7 | 1 ± 0.2 | 63 ± 0.8 |

**Table 4**
Values of LW component $\gamma^{LW}$, electron-acceptor $\gamma^+$ and electron-donor $\gamma^-$ parameters of AB component of surface free energy for black ash.

| Black ash | $\gamma^{LW}$ (mJ/m$^2$) | $\gamma^+$ (mJ/m$^2$) | $\gamma^-$ (mJ/m$^2$) |
|---|---|---|---|
| Bare black | 35.2 ± 2 | 3.78 ± 0.6 | 34.6 ± 0.3 |
| + NaCl | 33.87 ± 1.8 | 2.66 ± 0.2 | 11.4 ± 2 |
| + $CaCl_2$ | 43.44 ± 0.1 | 2.45 ± 0.6 | 34.12 ± 1 |
| + $FeCl_3$ | 45 ± 0.1 | 1 ± 0.1 | 63.07 ± 0.3 |

Table 4 shows the effect of electrolytes on the surface free energy components for black ash, which can be considered electron-donor in nature. In the case of treatment with $FeCl_3$, black ash is a strong electron-donor, with $\gamma^-$ of about 63.07 mJ/m$^2$. Similar results have been obtained for hematite (Plaza et al., 1998). Also it can be observed that with increasing cation valence, the electron-acceptor component $\gamma^+$ decreases (from 3.8 mJ/m$^2$ to 1 mJ/m$^2$) and electron-donor component $\gamma^-$ increases (from 34.6 mJ/m$^2$ to 63.1 mJ/m$^2$).

The stability of ash deposits also depends on their ability to retain water, that is, it depends on the hydrophobicity or hydrophilic nature of the ash particles. Normally, this distinction is based on wetting behaviour, but since the aim of the present study is to examine colloidal forces (exclusive of electrostatic interaction energy) between ash particles immersed in water, the most logical distinction between hydrophobic and hydrophilic properties may be the sign of the total interfacial free energy (van Oss, 1994). A negative sign of $\Delta G_{131}^{TOT}$ indicates net attraction or a hydrophobic surface; it is clear that the samples were hydrophilic in general and there should have net repulsions between particles induced solely from LW and AB interactions. If these repulsive forces in conjunction with repulsive electrostatic forces arised from electrostatic charge on the particles, then geological deposits of ash would tend to be mechanically unstable in the presence of water; the more unstable the deposit, the stronger the repulsion.

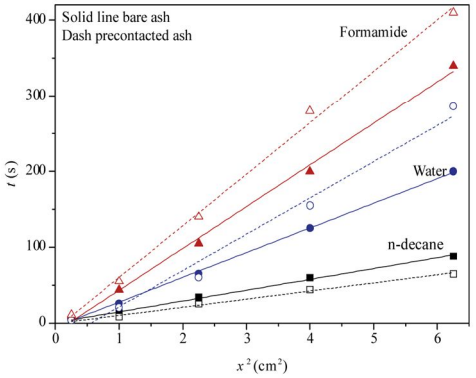


**Fig. 4.** Plot of time taken by n-decane, water and formamide to penetrate a distance $x$ in thin layers of ash samples, bare (solid) and precontacted with vapour of liquid (dash) as function of $x^2$.

**Table 5**
Free energy of interaction (LW and AB contributions) between ash particles in aqueous media at equilibrium distance $H_0$ (all quantities in mJ/m$^2$).

| Aqueous media | Ash | $\Delta G_{131}^{LW}$ | $\Delta G_{131}^{AB}$ | $\Delta G_{131}^{TOT}$ |
|---|---|---|---|---|
| Bare | Black ash | −3.19 ± 2 | 10.8 ± 0.6 | 7.59 ± 2.6 |
| | White ash | −21.2 ± 1 | 54.3 ± 02 | 33.1 ± 1.2 |
| + NaCl | Black ash | −2.65 ± 1.8 | −21.8 ± 0.2 | −24.44 ± 2 |
| | White ash | −3.9 ± 2.1 | 41.11 ± 0.8 | 37.1 ± 2.9 |
| + $CaCl_2$ | Black ash | −7.36 ± 1 | 11.6 ± 0.6 | 4.19 ± 1.6 |
| | White ash | −5.22 ± 2 | −9.14 ± 1 | −14.4 ± 3 |
| + $FeCl_3$ | Black ash | 8.32 ± 0.1 | 47.1 ± 0.1 | 3.88 ± 0.3 |
| | White ash | −9.44 ± 2 | 47 ± 0.2 | 37.6 ± 2.2 |

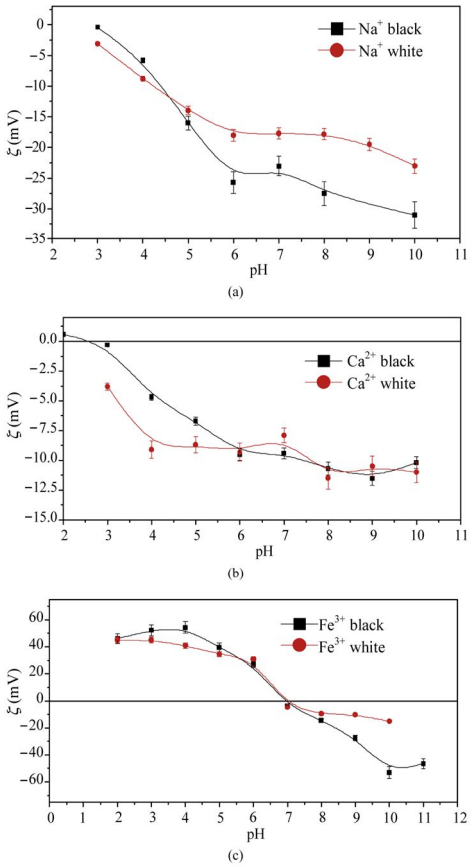


**Fig. 5.** Zeta potential ($\zeta$) of ash particles as function of pH value for 1 mmol/L concentrations of electrolytes indicated.

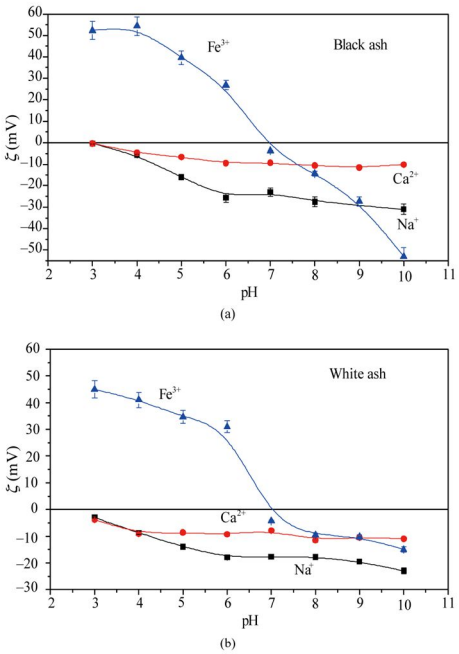


**Fig. 6.** Zeta potential (ζ) of ash particles as function of pH for 1 mmol/L concentrations of electrolytes indicated at the presence of $Na^+$, $Ca^{2+}$, and $Fe^{3+}$.

Using the data in Tables 3 and 4, calculations based on Eq. (3) can be performed for black and white ash particles. The results are shown in Table 5. The essentially negative character of LW interactions appeared systematically in all cases, although it was somewhat larger in absolute value for white ash. However, this negative interaction is, in most cases, more compensated by AB repulsions, except black ash with $Na^+$ and white ash with $Ca^{2+}$ (Table 5), thereby rendering the total interaction repulsive ($\Delta G_{131}^{TOT} > 0$ in all cases). This suggests that white ash deposits are more hydrophilic, retain more water, and are less stable than those of black ash (overall repulsion is stronger).

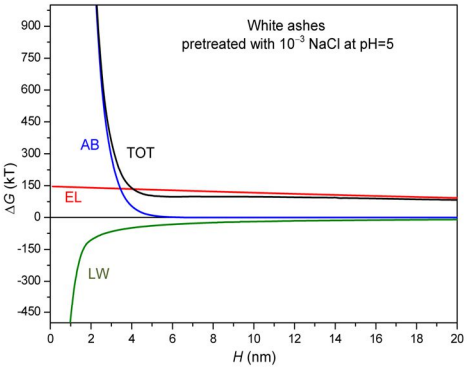


**Fig. 7.** Components of total energy of interaction (in kT) between ash particles as the function of the distance between surfaces, *H*.

### 5.4. Zeta potential of ash

Fig. 5 shows the effect of different electrolytes (mono-, di- and tri-valent) on the zeta potential. The mean ζ of ash particles in the presence of $Na^+$ at various pH conditions is shown in Fig. 5a, for which the mean values of ζ were negative in the pH range of 3–10. It was found that mean values of ζ of black and white ashes were linearly proportional to pH value of the solution when the pH value changed from 2 to 6, but had relatively constant values at higher pH value. Black ash had the highest absolute values of ζ.

Fig. 5b shows the effect of $Ca^{2+}$ on ζ of volcanic ash. It can be seen that differences between black and white ashes occurred at low pH values, with white ash having greater negative charge.

**Table 6**
Parameters used to calculate the potential energy of interaction between particles.

| Electrolyte | Parameter | White ash | | | Black ash | | |
|---|---|---|---|---|---|---|---|
| Untreated | γ (mJ/m$^2$) | $\gamma^{LW} = 62$, Hamaker constant $= -1.9 \times 10^{-20}$ | $\gamma^+ = 1$ | $\gamma^- = 65$ | $\gamma^{LW} = 37$, Hamaker constant $= -3.7 \times 10^{-21}$ | $\gamma^+ = 2$ | $\gamma^- = 37$ |
| Sodio | γ (mJ/m$^2$) | $\gamma^{LW} = 37$, Hamaker constant $= -3.7 \times 10^{-21}$ | $\gamma^+ = 0$ | $\gamma^- = 52$ | $\gamma^{LW} = 34$, Hamaker constant $= -2.5 \times 10^{-21}$ | $\gamma^+ = 2$ | $\gamma^- = 12$ |
| | ζ (mV) | pH = 3 | −3.1 | | pH = 3 | −0.4 | |
| | | pH = 5 | −14 | | pH = 5 | −16 | |
| | | pH = 7 | −17.7 | | pH = 7 | −23 | |
| | | pH = 9 | −20 | | pH = 9 | −29.5 | |
| Calcio | γ (mJ/m$^2$) | $\gamma^{LW} = 40$, Hamaker constant $= -5.1 \times 10^{-21}$ | $\gamma^+ = 8$ | $\gamma^- = 20$ | $\gamma^{LW} = 34$, Hamaker constant $= -2.5 \times 10^{-21}$ | $\gamma^+ = 0$ | $\gamma^- = 53$ |
| | ζ (mV) | pH = 3 | −3.8 | | pH = 3 | −0.3 | |
| | | pH = 5 | −8.7 | | pH = 5 | −6.7 | |
| | | pH = 7 | −7.9 | | pH = 7 | −9.5 | |
| | | pH = 9 | −10.5 | | pH = 9 | −11.2 | |
| Hierro | γ (mJ/m$^2$) | $\gamma^{LW} = 49$, Hamaker constant $= -9.8 \times 10^{-21}$ | $\gamma^+ = 0.98$ | $\gamma^- = 67.8$ | $\gamma^{LW} = 45$, Hamaker constant $= -7.7 \times 10^{-21}$ | $\gamma^+ = 1.1$ | $\gamma^- = 63.1$ |
| | ζ (mV) | pH = 3 | 45 | | pH = 3 | 52 | |
| | | pH = 5 | 35 | | pH = 5 | 39 | |
| | | pH = 7 | −4.9 | | pH = 7 | −11 | |
| | | pH = 9 | −10.5 | | pH = 9 | −27.7 | |

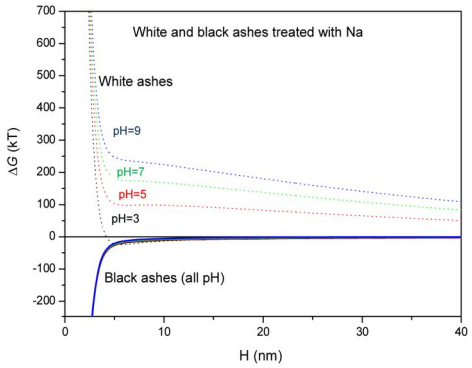


**Fig. 8.** Total energy of interaction (in kT) between ash particles as the function of the distance between surfaces, *H*, for pH values indicated when the electrolyte present in solution was $Na^{+}$.

ζ values remained constant with increasing pH value for both materials. This constancy appeared at pH value of 4 for white ash. For pH value greater than 6, there were no major ζ differences between white and black ashes.

Fig. 5c presents the behaviour of the ζ value of ash-$FeCl_3$ system versus pH value of the liquid phase. The effect of $Fe^{3+}$ in white and black ashes was analogous, although ζ had greater absolute values in the black ashes. It can be seen that ζ changed from positive to negative at pH value of 7. The positive values can be attributed to the fact that there was adsorption of $Fe^{3+}$ onto ash particles at acid conditions. ζ Value of the system decreased to −50 mV for the largest pH value, attributable to progressive adsorption of hydroxyl groups. It is found that extreme pH value resulted in the largest absolute values of ζ. In general, ζ may be controlled by adjusting pH value of the slurry. A possible explanation for this is that increasing or decreasing pH value alters the number of ions available in the slurry, which affects the charge in the double layers.

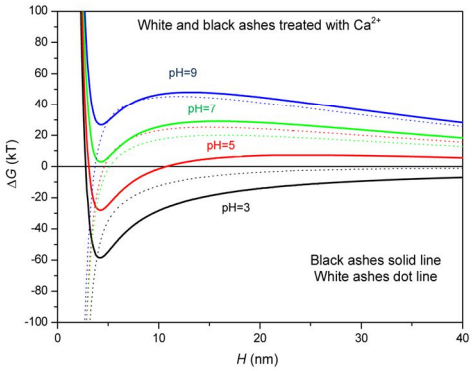


**Fig. 9.** Total energy of interaction (in kT) between ash particles as the function of the distance between surfaces, *H*, for pH values indicated when the electrolyte present in solutions was $Ca^{2+}$.

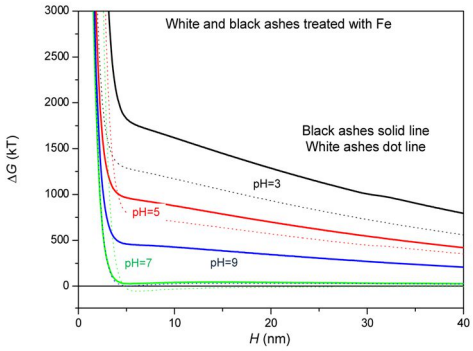


**Fig. 10.** Total energy of interaction (in kT) between ash particles as the function of the distance between surfaces, *H*, for pH values indicated when the electrolyte present in solutions was $Fe^{3+}$.

Fig. 6 compares the effect of electrolytes in the black (Fig. 6a) and white ashes (Fig. 6b). Note that the effect is similar in both materials, but the black ash is more charged. This indicates that with an equal number of ash particles, electrostatic repulsion is stronger in black ash, which suggests that black ash is less stable than white ash (overall repulsion is stronger).

This conclusion is opposite to that obtained from the analysis of surface free energy. We conclude that only a combination of the two contributions, electric and thermodynamic, can give an idea of actual stability of ash deposits.

### 5.5. Energy of interaction between particles

Qualitative explanation of soil cohesion has been given in terms of the total energy of interaction between the particles themselves, computed from the extended DLVO theory including AB interactions. As stated above, the total potential energy of interaction ($\Delta G^{TOT}$) between two colloidal particles is given by the sum of the energy of interaction of the double layers ($\Delta G^{EL}$) and of the particles themselves, caused by van der Waals ($\Delta G^{LW}$) and polar or AB ($\Delta G^{AB}$) interaction forces.

With the data shown in Table 6 and using Eqs. (4), (5) and (8), the interaction energies between ash particles are illustrated in Figs. 7–11. Fig. 7 is a typical plot of the $\Delta G^{TOT}$ between two interacting particles as a function of their separation *H*. When the surface potentials of the two particles are large and have the same sign, $\Delta G^{EL}$ is positive. Physically, this means that the particles must cross a potential barrier before coagulation can take place. When the surface potentials are very small or of opposite sign, there is no barrier and rapid coagulation may occur. The rate of coagulation somewhat depends on the magnitude of $\Delta G^{TOT}$, and it remains to express this dependence quantitatively. After obtaining ζ and surface free energy of the ash, potential energies of interaction between particles were calculated, in which the relative contributions of each interaction type (AB, LW, and EL) could be distinguished. The curves in Fig. 7 show some general features (repulsive short-range interaction, and attractive van der Waals interaction in all cases, with strength and range unaffected by the surfaces involved), but it is most interesting to focus on variations of EL contribution with pH value. Thus, Fig. 8 shows an increasing repulsion of white ash with pH value, owing to the increase of ζ observed in Fig. 5a. Also, in Fig. 8 we see the effect of $Na^{+}$ on black ash; in this case, interactions between particles become attractive, increasing soil cohesion.

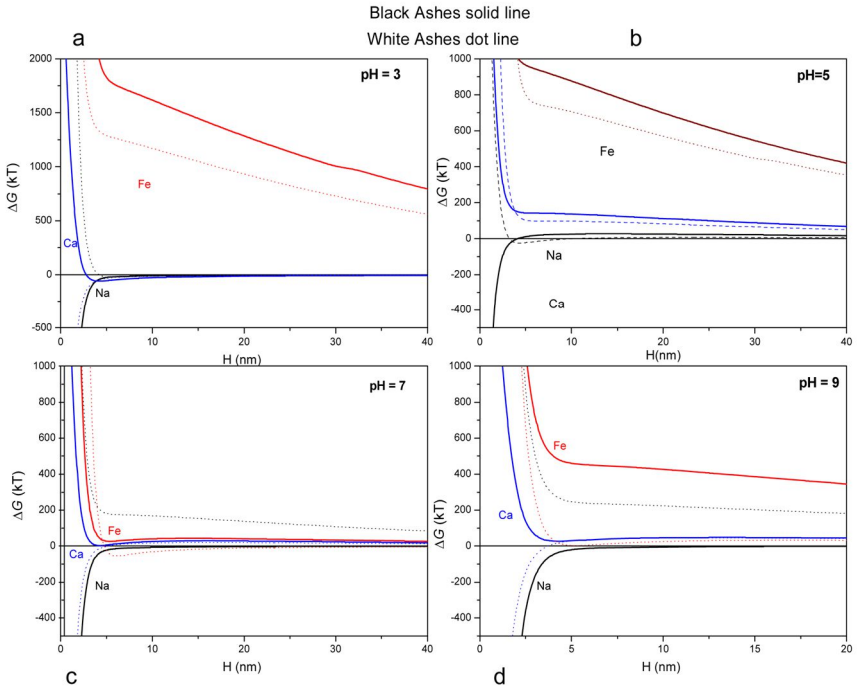


**Fig. 11.** Effect of $Na^{+}$, $Ca^{2+}$, and $Fe^{3+}$ on total energy of interaction (in kT) between ash particles as function of the distance between surfaces, *H*, for pH value indicated.

Fig. 9 displays the effect of $Ca^{2+}$ on the total energy of interaction. The behaviour is significantly different from that shown in Fig. 8 with respect to the pH effect. In all cases, the total energy of interaction between particles suggests a coagulation process, because the potential barrier can be overcome by particles that are effectively trapped by the potential well. In any case, the presence of $Ca^{2+}$ confers more stability to the white ash deposit than $Na^{+}$ presence because the potential barriers are lower.

The effect of $Fe^{3+}$ is shown in Fig. 10. In this case, we observe that the optimal conditions for particle coagulation appeared with medium pH values. Contrary to the effect produced by $Na^{+}$ and $Ca^{2+}$ ions, repulsion increased at acid conditions when the absorbed cation was $Fe^{3+}$.

Fig. 11 compares the three cations for acid, neutral and basic pH values. Fig. 11a shows the energy of interaction between particles of volcanic ash for pH = 3. It is significant that for sodium and calcium, electrostatic repulsion was overcome for the sum of LW and AB components of energy of interaction for both white and black ashes. For iron, the electrostatic repulsion was dominant, resulting in net repulsion.

Fig. 11b shows the electrolyte effect at pH = 5. Under these conditions, calcium had only attractive interaction. Sodium and iron again presented potential barriers, i.e. repulsion between ash particles. It is noteworthy that the behaviour of iron again had very repulsive interactions.

Fig. 11c shows the electrolyte effect at neutral pH. In this case, there were values close to zero potential, except sodium (for white ash) with a potential barrier of ~200 kT. The results at pH = 9 (Fig. 11d) show that only iron (black ash) and sodium (white ash) presented potential barriers, i.e. significant repulsion between ash particles.

If we consider that energies of interaction between ash particles have implications for the stability of ash deposits, Fig. 11 generally indicates the importance of pH value of the medium for deposit stability, with greater stability at neutral pH and more instability at extreme acidic or basic pH. However, as discussed above, the effect of electrolytes in solution is critical to the value and sign of these interactions. In general, calcium gives greater stability to the deposit, and iron gives the least.

Given the nature of both types of volcanic ashes, the results show that the white ash deposits are more stable than the black ones. On the contrary, in the case of other polyvalent electrolytes ($Ca^{2+}$ and $Fe^{3+}$), the black ash in the presence of sodium is the one with greater stability.

## 6. Conclusions

In this work, we described the surface properties of eruptive material (white and black ashes) from the El Hierro Island in the Canary Islands of Spain.

Two surface properties, i.e. surface free energy and ζ, were analysed for black and white ashes immersed in various electrolytes (NaCl, $CaCl_2$, and $FeCl_3$). The presence of electrolytes altered surface properties of the solid materials.

The component $\gamma^{LW}$ for bare black ash was ~35 $mJ/m^2$, and 63 $mJ/m^2$ for white ash. These values were modified by the

presence of electrolytes in solutions. In general, the effect of the electrolytes was to equilibrate the value of the dispersion component, increasing it in the black ash and decreasing it in the white ash.

Volcanic ash has a monopolar character, the electron-acceptor component being practically zero; this material was observed to have a Lewis base. The effect of the electrolyte did not change the monopolar character of the ash, but affected the value of the electron-donor component.

The ζ of black and white ashes was studied as a function of pH value of the liquid phase in the presence of various electrolytes. For NaCl and $CaCl_2$, ζ was negative, and there was no change in the surface electrical sign with pH variation. In contrast, if the ash was immersed in $FeCl_3$ solution, pH variation of the liquid phase significantly influenced ζ, changing both the value and sign of the surface electric charge.

The rate of cohesion of ash deposits was somewhat dependent on the magnitude of total potential energy of interaction between ash particles.

From these findings, we can draw the following conclusions:

(1) The pH of the medium determined cohesion of the ash deposits, with greater stability with acid pH when the electrolytes were $Na^+$ and $Ca^{2+}$. In the case of $Fe^{3+}$, greater stability occurred at neutral pH and greater instability at extreme acid or basic pH.
(2) The effect of $Na^+$ in the white ash deposits produced a repulsion that increased with pH. In contrast, in the black ash, the effect was an increase of soil stability.
(3) Regarding the effect of $Ca^{2+}$ on total interaction energy between ash particles, in all cases, that energy suggested greater stability in both black and white ashes.
(4) The effect of $Fe^{3+}$ showed that optimal stability conditions appeared at neutral pH values. With repulsion increasing at acid pH, this stability disappeared.

In conclusion, surface properties of the studied materials and similar ones in the volcanic medium are very relevant to stability. The mechanical stability of an ash deposit on variable topography is attributed to several factors, such as deposit slope, amount of water in the ash, or regional seismic activity. There was a recent volcanic eruption 2 km south of the island, beginning on 10 October 2011. This submarine eruption was preceded by various precursory signals, the most evident of which was the seismic series that began in July 2011, consisting of almost 10,000 low-magnitude earthquakes.

El Hierro Island is known as the island of landslides. It is difficult to ultimately predict whether such a deposit will remain in place or become involved in a potentially destructive debris flow or lahar. It is clear nonetheless that, given similar geological and climatological conditions, the ash deposits are mechanically more stable when the cohesive forces between particles are stronger.

## Conflict of interest

The authors wish to confirm that there are no known conflicts of interest associated with this publication and there has been no significant financial support for this work that could have influenced its outcome.

## Acknowledgements

We gratefully acknowledge the support of the institutions involved. This work was partially funded by two projects: the MED-SUV project from the European Union Seventh Framework Programme (FP7) under Grant No. 308665, and the Spanish Government (Project CGL2011-29499-C02-01).

## References

Bailey B, Templeton A, Staudigel H, Tebo BM. Utilization of substrate components during basaltic glass colonization by Pseudomonas and Shewanella isolates. Geomicrobiology Journal 2009;26(8):648–56.
Balcells R, Gomez JA. Memorias y mapas geológicos del Plan MAGNA. 1:25000. El Hierro, Hoja de Valverde: Instituto Geológico y Minero de España, España; 1997a (in Spanish).
Balcells R, Gomez JA. Memorias y mapas geológicos del Plan MAGNA. 1:25000. El Hierro, Hoja de Frontera: Instituto Geológico y Minero de España, España; 1997b (in Spanish).
Balcells R, Gomez JA. Memorias y mapas geológicos del Plan MAGNA. 1:25000. El Hierro, Hoja de Sabinosa: Instituto Geológico y Minero de España, España; 1997c (in Spanish).
Balcells R, Gomez JA. Memorias y mapas geológicos del Plan MAGNA. 1:25000. El Hierro, Hoja de La Restinga: Instituto Geológico y Minero de España, España; 1997d (in Spanish).
Baumgarten W, Dörner J, Horn R. Microstructural development in volcanic ash soils from South Chile. Soil & Tillage Research 2013;129:48–60.
Baumgarten W, Neugebauer Th, Fuchs E, Horn R. Structural stability of Marshland soils of the riparian zone of the Tidal Elbe River. Soil and Tillage Research 2012;125:80–8.
Becerril L, Cappello A, Galindo I, Neri M, Del Negro C. Spatial probability distribution of future volcanic eruptions at El Hierro Island (Canary Islands, Spain). Journal of Volcanology and Geothermal Research 2013;257:21–30.
Bommer JJ, Rolo R, Mitroulia A, Berdousis P. Geotechnical properties and seismic slope stability of volcanic soils. In: Proceedings of the 12th European Conference on Earthquake Engineering. London, UK; 2002. Paper No. 695.
Bravo T. Geografía general de las islas Canarias. Santa Cruz de Tenerife: Goya Ediciones; 1968 (in Spanish).
Carracedo JC, Badiola ER, Guillou H, de la Nuez J, Pérez Torrado FJ. Geology and volcanology of La Palma and El Hierro, Western Canaries. Estudios Geológicos 2001;57:175–273.
Chibowski E. Solid surface free energy components determination by the thin-layer wicking technique. Journal of Adhesion Science and Technology 1992;6(9):1069–90.
Cockell CS, van Calsteren P, Mosselmans JFW, Franchia IA, Gilmoura I, Kellya L, Olsson-Francisa K, Johnson D. Microbial endolithic colonization and the geochemical environment in young seafloor basalts. Chemical Geology 2010;279(1–2):17–30.
Coello J. Contribución a la tectónica de la isla de El Hierro. Estudios Geológicos 1971;27:335–40 (in Spanish).
Duran JDG, Ontiveros A, Delgado AV, Gonzalez-Caballero F. Kinetics and interfacial interactions in the adhesion of colloidal calcium carbonate to glass in a packed-bed. Applied Surface Science 1998;134(1–4):125–38.
Gimmi T, Kosakowski G. How mobile are sorbed cations in clays and clay rocks? Environmental Science and Technology 2011;45(4):1443–9.
Gonzalez de Vallejo LI, Jimenez Salas JA, Legy Jimenez S. Engineering geology of the tropical volcanic soils of La Laguna, Tenerife. Engineering Geology 1981;17(1–2):1–17.
Gregory J. Approximate expressions for retarded van der Waals interaction. Journal of Colloid and Interface Science 1981;83(1):138–45.
Guillou H, Carracedo JC, Pérez Torrado F, Rodríguez Badiola E. K-Ar ages and magnetic stratigraphy of a hotspot induced, fast grown oceanic island: El Hierro, Canary Islands. Journal of Volcanology and Geothermal Research 1996;73(1–2):141–55.
Hernández Pacheco A. Sobre una posible erupción en 1793 en la isla de El Hierro (Canarias). Estudios Geológicos 1982;38:15–25 (in Spanish).
Kadar E, Fisher A, Stolpe B, Calabrese S, Lead J, Valsami-Jones E, Shi Z. Colloidal stability of nanoparticles derived from simulated cloud-processed mineral dusts. Science of the Total Environment 2014;466–467:864–70.
Li Z, Giese RF, Wu W, Sheridan MF, van Oss CJ. The surface thermodynamic properties of some volcanic ash colloids. Journal of Dispersion Science and Technology 1997;18(3):223–41.
Longpre M, Chadwick JP, Wijbrans J, Iping R. Age of the El Golfo debris avalanche, El Hierro (Canary Islands): new constraints from laser and furnace 40Ar/39Ar dating. Journal of Volcanology and Geothermal Research 2011;203(1–2):76–80.
Masson DG, Harbitz CB, Wynn RB, Pedersen G, Løvholt F. Submarine landslides: processes, triggers and hazard prediction. Philosophical Transactions of the Royal Society A (London: Royal Society) 2006;364(1845):2009–39.
Ontiveros A, Duran J, Delgado AV, Gonzalez-Caballero F, Chibowski E. A study on the adhesion of calcium carbonate to glass. Energy balance in the deposition process. Journal of Adhesion Science and Technology 1996a;10(9):847–68.
Ontiveros A, Duran JDG, Gonzalez-Caballero F, Chibowski E. Adhesion of colloidal ZnS on silicon. Effects of ionic strength and radio frequency electric field. Journal of Adhesion Science and Technology 1996b;10(10):999–1019.
Ontiveros-Ortega A, Vidal F, Giménez E, Ibañez JM. Effect of heavy metals on the surface free energy and zeta potential of volcanic glass: implication on the adhesion and growth of microorganism. Journal of Materials Science 2014;49(9):3550–9.

Pellicer MJ. Estudio geoquímico del vulcanismo de la Isla de Hierro (A. Canario). Estudios Geológicos 1979;35:11–25 (in Spanish).
Pellicer MJ. Estudio vulcanológico de la Isla de Hierro (A. Canario). Estudios Geológicos 1977;33:181–97 (in Spanish).
Perez NM, Somoza L, Hernandez PA, de Vallejo LG, Leon R, Sagiya T, Biain A, Gonzalez FJ, Medialdea T, Barrancos J, Ibanez J, Sumino H, Nogami K, Romero C. Reply to comment from Blanco et al. (2015) on "Evidence from acoustic imaging for submarine volcanic activity in 2012 off the west coast of El Hierro (Canary Islands, Spain) by Perez, et al. [Bull. Volcanol. (2014), 76: 882–896]". Bulletin of Volcanology 2015;77(7):63–70.
Pérez Torrado FJ, Rodríguez González A, Carracedo JC, Fernández Turiel JL, Guillou H, Hansen A, Rodríguez Badiola E. Edades C-14 del rift ONO de El Hierro (Islas Canarias). In: Resums XIII Reunió Nacional de Quaternari. Andorra; 2011. p. 101–4 (in Spanish).
Plaza RC, Zurita L, Duran JDG, Gonzalez-Caballero F, Delgado AV. Surface termodynamics of Hematite/Yttrium oxide core-shell colloidal particles. Langmuir 1998;14:6850–4.
Rao SM. Mechanistic approach to the shear strength behaviour of allophanic soils. Engineering Geology 1995;40(3–4):215–21.
Romero C. Las Manifestaciones Volcánicas Históricas del Archipiélago Canario. Editorial El Cedro S.L.; Tomo I; 1991 (in Spanish).
Smoluchowksi M. Stationâre ströme. In: Graetz L, editor. Handbuch der Elektrizität und des Magnetismus II. Leipzig, Germany: Barth; 1921. p. 366–428 (in Spanish).
van Oss CJ, Chaudhury MK, Good RJ. Interfacial Lifshitz–van der Waals and polar interactions in macroscopic systems. Chemical Reviews 1988;88(6):927–41.
van Oss CJ, Good RJ. Surface tension and the solubility of polymers and biopolymers: the role of polar and apolar interracial free energy. Journal of Macromolecular Science: Part A – Chemistry 1989;26(8):1183–203.
van Oss CJ. Interfacial forces in aqueous media. New York: Marcel Dekker Inc.; 1994.
Visser J. Adhesion of colloidal particles. In: Matijević E, editor. Surface and colloid science. New York: Wiley; 1976. p. 3–28.
Washburn EW. The dynamics of capillary flow. Physical Review 1921;17(3):273–83.

### *5.2.2. Artículo: Interpretation of the volcano landslides in terms of zeta potential and surface free energy balance.*

*Resumen*

Los depósitos de Almagre ubicados en la isla de Tenerife (Gran Canaria, España) son unas capas bien conocidas por los pintores locales, ya que suelen utilizarla como pigmento de sus pinturas. Estas capas son el resultado del metamorfismo térmico de los suelos en contacto con el flujo de lava (800-1100 ° C). Estas capas de pequeño espesor con respecto a la capa basáltica son interesantes para el estudio geotécnico, ya que la estabilidad de los depósitos está determinada por el elemento más débil, en este caso Almagre, que actúa como plano deslizante.

La brisa marina sobre las laderas de las islas volcánicas aumenta el contenido de cationes en los depósitos de cenizas. Esto modifica las propiedades superficiales del material que compone el substrato. Esta modificación afecta a la retención de agua ya la cohesión del material que constituye el depósito.

Los resultados muestran que la presencia de sodio y magnesio aumentó la hidrofobicidad del material, que tenía una capacidad de retención de agua débil y una fuerte cohesión a pH básico. Cuando hay hierro en solución, la repulsión entre las partículas es mayor que la obtenida con otros electrolitos estudiados. Por lo tanto, el depósito es menos estable, y Almagre en condiciones de agua saturada constituye una capa ideal para deslizamientos de tierra.

# Artículo científico:

# INTERPRETATION OF THE VOLCANO LANDSLIDES IN TERMS OF ZETA POTENTIAL AND SURFACE FREE ENERGY BALANCE

# Revista:

# Geomorphology

# NEW APPROACH OF MECHANISM TRIGGERING VOLCANO LANDSLIDES ON BASE OF ZETA POTENTIAL AND SURFACE FREE ENERGY BALANCE

I. Plaza[1], A. Ontiveros-Ortega, [1,2] J. Calero,[3] C. Romero[4]

[1]*Department of Physics, University of Jaén, A-3, 23071-Jaén, Spain.*

[2]*Andalusian Institute of Geophysics, University of Granada, 18071-Granada, Spain.*

[3]*Department of Geology, University of Jaén, B-3, 23071-Jaén, Spain.*

[4] *Department of Geography, University of La Laguna, Spain.*

## ABSTRACT

The caps of Almagre are the result of thermal metamorphism of soils in contact with lava flow (1073–1273 °K). These caps of small thickness relative to the basaltic wash, are interesting for geotechnical study, because the stability of the deposits is determined by the weakest element, in this case Almagre, which acts as a sliding plane. The marine breeze over the hillsides of the volcanic islands increases the content of cations in ashes deposits. This modifies the superficial properties of material that composes the substratum. This modification affects the retention of water and the cohesion of material making up the deposit. The results show that the presence of sodium and magnesium increased the hydrophobicity of the material, which had a weak water retention capacity and strong cohesion at basic pH. When there is iron in solution, repulsion between the particles is greater than one obtained with other studied electrolytes. Hence, the deposit is less stable, and Almagre under saturated water conditions constitutes an ideal layer for landslides.

**Keywords**: **Almagre, potential zeta, surface free energy, volcanic ash, landside**

# 1 Introduction

The Island of Tenerife in the Canary Islands of Spain (Figure 1) has been studied by the international scientific community. This is indicated by a multitude of articles published in recent years related to the consequences of a potential slide of hillsides (e.g., tsunami, loss of life, economic losses (Broothaerts et al., 2012; BASU, 2003). These studies analyzed the topography, extent of present vegetation, and geotechnical parameters of the area (Crozier et al., 2005), and calculated hillside safety factors via simulations (Zhou et al., 2003) based on different models of the area.

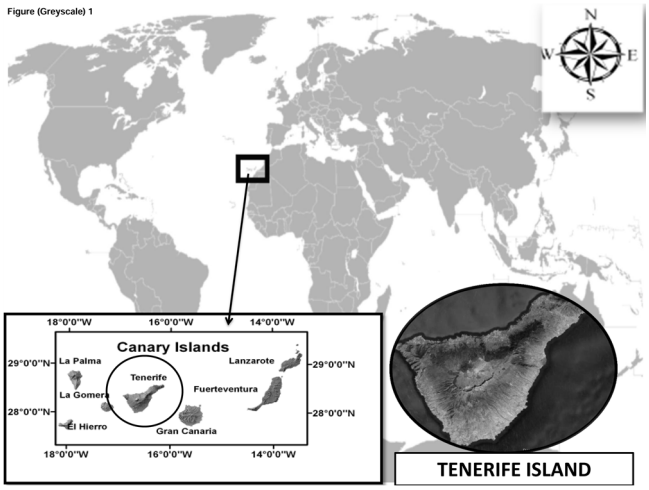


**Figure. 1**.- Location of the island is relative to the Canary Island.

Our study is based on the cap of eruptive material known as "Almagre," selected for its unique geologic history (Ancochea et al., 1990-1999) and characteristic geotechnical contacts with the low and top caps, which assume the planes of typical slides in Tenerife (Martí et al., 1997). We characterize interfacial properties of Almagre and their modification in

association with the presence of various electrolytes (Na-Mg-Fe) and different pH values.

*Geologic history and tectonic context of Tenerife*

The geologic history of the Tenerife in Canary Islands began 12 Ma ago. It has been investigated by numerous researchers ((Carracedo et al., 2007-2011a), (Longpré et al., 2009)). First it emerged I build acquaintance as “Roque de Conde” (11,6–6.4 Ma), later “Anaga” (8–3.2 Ma) and “Teno” (7.4–4.5 Ma). The geologic characteristics were investigated by Ancochea et al. (1990, 1995 & 1999), Churakov et al. (2011), Marti et al. (1994), Soto et al. (1999) and Pelipenko et al. (2013).

The origin of the volcanism is open to debate. We sampled in the complex called "Edificio de las Cañadas" (or Las Cañadas for short). This complex is in the southeastern part of the island, near the municipality of Guimaras. Nearby is a landslide with a volume of material greater than 120 $km^3$ and an approximate age of 1 Ma. It is not the only landslide; another in Las Cañadas is dated 180,000 years ago (Masson et al., 2002).

The geologic history of Las Cañadas is marked by explosive-type volcanism, with the emission of pyroclastic clouds. Between the formation of Las Cañadas I and the II was a period of erosion and relative volcanic tranquility.

Almagre is a cap of very unique origin. It formed when materials of eroded or organic soil were buried by lava flows. These deposits are rich in

iron. They are principally reddish, caused by alteration of minerals with iron, and show differential erosion in the deposit.

The above causes contact metamorphism in sedimentation of materials in previous periods and subsequent erosion, owing to layers of lava and pyroclastic expelled during this stage that buried the materials studied here. To all this must be added the effect of seawater, which in ordinary conditions contains a wide range of dissolved ions (mainly $Cl^- > Na^+ > Mg^{2+}$). Sea breezes have high moisture content, so rocks not in direct contact with seawater still experience its effects and their initial characteristics are thereby changed.

Volcanic soils support near-vertical slopes. However, these steep slopes are susceptible to sudden and catastrophic failure (Bommer et al., 2002). Thus, earthquake-induced landslides in the Canary Islands constitute significant natural hazards. Mitigation of the landslide hazard there requires thorough understanding of the behaviour of these volcanic deposits under static and dynamic conditions. The soil shows a general tendency to form aggregations of clay particles, usually showing different structures and levels of cementation. The cohesion of soils depends on several factors. Rheology properties in aqueous media are influenced by interactions between particles. The control of flocculation phenomena, adsorption, wetting, and rheological properties of dispersion depends on particle interactions (Bailey et al., 2009; Cockell et al., 2010; Churakov et al., 2011; Rošic et al., 2012; Kadar et al., 2014; Ontiveros-Ortega, 2014-2016; Plaza et al., 2015; Baumgarten et al., 2012-2013).

Much of the scientific and technological interest in clay minerals derives from their interfacial interactions with colloidal particles (clays and other minerals) in the presence of a liquid, usually water.

Almagre layers are distributed throughout the island of Tenerife. We chose a study area in the southwest part of the island of Tenerife (Mt. Teide), along local road TF-28. Samples were taken in a ravine in the nearby locality of Villa de Arico.

# 2 Methods

## 2.1 Preparation of Samples and description used materials

The samples were prepared before chemical and mineralogical analyses, they were immersed and washed by distilled water and Later they were left to dry at a temperature of 343,15 °K over 48 hours. Then, particles of diameter > 2 mm were removed by sieving. Finally, the samples were crushed by an agate mortar so all had a similar texture and particle size distribution.

All reagents and chemicals used were of analytical grade (Merck KGaA and Sigma-Aldrich Co. LLC, Germany). Water for surface free energy determination was twice-distilled, and Milli-Q reagent-grade water was used for electrokinetic measurements.

## 2.2 Chemical analysis of volcanic deposits

To characterize the samples chemically, we used fluorescence of beams-X technology. The equipment is a wavelength dispersive X-Ray fluorescence spectrometer (WDXRF) S4 EXPLORER model PIONER from

Bruker AXS Inc. (Madison, Wisconsin USA). The spectrometer analyzes elements from carbon to uranium in a wide variety of samples with accuracy and precision. The source for sample excitation was an X-ray tube with rhodium anode and Be window of 75 microns. The tube and X-ray generator are designed to provide a maximum output of 4 kW with applicable maximum voltage and current 60 KV and 150 mA, respectively. There were two collimators, 0.23° and 0.46°, and five crystal analyzers, OVO-55, PET, Ge, LiF220 and LiF200. The instrument was equipped with two sensors (sealed proportional counter and scintillation counter), whose movement is controlled by a high-precision goniometer covering the entire instrumental measurement range. Samples were made into tablet form using a hydraulic press (model MIGNON SS, Nannetti, Faenza, Italy).

## 2.3 SEM Photography

Scanning electron microscope (SEM) photography allows the definition and identification of the geometric disposition of gaseous bladders and/or volcanic glass (Holtz, 1981).

A SEM was used with voltage of acceleration 25 kV (S-510; Hitachi Ltd., Tokyo) and an energy-dispersive X-ray detector of (EDAX; Rontec GmbH, Berlin). Samples of ash under the only treatment were mounted with support of the silver and metalized by carbon deposited in two orientations (20°–30°). During the SEM photography, qualitative microanalysis was done to confirm the presence of different phases in the system.

## 2.4 Zeta Potential

The fine earth fractions of materials used in the experiments were ground in an agate mortar, and then re-dispersed in water and various solutions. For the electrophoresis experiment, we used the supernatant of the suspension obtained after sedimentation, resulting a volume fraction of 0.5 g/l. Electrokinetic properties of the studied systems were analyzed with a Malver-ZetaSizer 3000 HS, based on electrophoretic mobility measurements. For each treatment, the powder material was conditioned for 24 hours in 1 l of solution at the required concentrations, for different electrolytes.

## 2.5 Surface free energy

To estimate the surface free energy of the samples, we used a method with measurement of advancing contact angles of three probe liquids (diiodomethane, water, and formamide) of known surface-tension components onto dry soil pellets. For this purpose, a ramé-hart Instrument Co. (New Jersey, USA) NRL CA goniometer was used. Images of drops placed on the surface were captured by a video camera adapted to the goniometer, immediately after their deposition with a Gilmont (USA) micrometer syringe. Prior to contact angle measurements, the soil was dried at 343,15 °C and kept in a desiccator. Only stable drops were used to compute surface free energy components of the solids. The contact angles of water, formamide, and diiodomethane were measured on pellets of these materials. The pellets made by compressing dry powder under 5.5 × 104 $kg/cm^2$ for 10 min. Only pellets having a smooth, specular surface (at the

optical microscope level) were selected. The contact angle was recorded immediately after depositing the drop.

## 2.6 Introduction to interfacial theories

The process of adhesion between particles of colloidal size dispersed in a water medium is determined by the balance of forces between various phases that coexist in the system, namely, hydrodynamic, diffusive-type, and interfacial forces. At short distances, The interfacial forces are the responsible of interactions between particles. Three kinds of interfacial interactions should be considered, electrostatic (EL), Lifshitz–van der Waals (LW), and acid-base (AB).

### 2.6.1 Electrical characterization

For electrical characterization, zeta potential ζ was calculated based on the Smoluchowski (Smoluchowksi, 1921) relationship:

$$\xi_{EP} = \frac{V\mu}{\varepsilon E_x}, \qquad (1)$$

where $\xi_{EP}$ is the electrophoretic ζ, V is electrophoretic velocity, and μ and ε are the viscosity and permittivity of the medium, respectively. $E_x$ is the axial electric field. The Smoluchowski equation is a simplified approach; the electrostatic driving force is opposed by the frictional force and other effects are neglected. That equation is valid for solid particles with large dimensionless inverse Debye length (Wang et al., 2010). The equation gives good results only for large colloidal particles and high ionic strengths when ζ is not too high (< 120 mV). In our experiments the Smoluchowski

approximation was acceptable; specifically, particle size of a micrometer and ionic strength 1 mM, and $\zeta << 120$mV.

### 2.6.2 . Surface free-energy determination

Detailed descriptions of surface free energy formulation have been given in numerous papers (Van Oss et al., 1988-1994). Thus, the total surface free energy of a solid or liquid is described as the sum of the dispersive Lifshitz - van der Waals component $\gamma^{LW}_S$ and polar acid-base interaction $\gamma^{AB}_S$, which is in many cases due to hydrogen bonding. In general, the polar $\gamma^{AB}$ interaction is caused by electron-donor ($\gamma^-$) and electron-acceptor ($\gamma^+$) contributions. The relationship between contact angle $\theta$ and the LW and (Lewis) AB components of the surface free energy of the solid (subscript 1) and surface tension of the liquid (subscript 3) can be written as

$$2\sqrt{\gamma_1^{LW}\gamma_{Li}^{LW}} + 2\sqrt{\gamma_1^{+}\gamma_{Li}^{-}} + 2\sqrt{\gamma_1^{-}\gamma_{Li}^{+}} = \gamma_{Li}(1+\cos\theta), \quad (2)$$

where $\gamma_{Li}$ is the surface tension of liquid i forming contact angle $\theta$ on the solid, and $\gamma^{LW}_{Li}$ , $\gamma^{+}_{Li}$ , and $\gamma^{-}_{Li}$ are the surface tension components of the liquid. Thus, by measuring the contact angles of the aforementioned three liquids, a system of three equations of type (2) can be resolved to attain the three unknown variables $\gamma_1^{LW}$, $\gamma_1^{+}$ and $\gamma_1^{-}$.

## 2.7 Interfacial interactions between two similar particles in aqueous media

For colloidal-sized particles, transport, deposition and mechanical stability of the final deposit are strongly influenced by surface interactions

between particles dispersed in water. According to extended Derjaguin–Landau–Verwey–Overbeek (DLVO) theory (Van Oss et al., 1994), three types of interfacial interactions should be considered: Lifshitz-van der Waals (LW), electrostatic (EL), and acid–base (AB). The three contributions depend on the nature of the interfaces involved (i.e., the zeta potential and surface free energy components). For particles (phase 1) of the same material dispersed in water (phase 3), total interaction energy between the particles is given by

$$\Delta G_{131}^{TOT} = \Delta G_{131}^{EL} + \Delta G_{131}^{LW} + \Delta G_{131}^{AB}, \qquad [3]$$

where subscript *131* refers to the phases involved. In our case, it refers to particle - liquid medium - particle in the aggregation process. The three contributing interactions depend on the nature of the interfaces involved and on the distance H between surfaces. Under the constant potential, double-layer model for moderate potentials, the electrostatic interactions can be obtained from Duran et al. (1998):

$$\Delta G_{131}^{EL} = 2\pi\varepsilon a\xi^2 \ln(1+e^{-\kappa H}) \qquad [4]$$

where ζ is the zeta potential, a is particle radius ε the dielectric constant of the liquid, and κ is the Debye screening length (double-layer thickness).

Corresponding expressions for LW interaction are

$$\Delta G_{131}^{LW} = -\frac{A_{131}}{6}\left(\frac{2a^2}{H(4a+H)} + \frac{2a^2}{(2a+H)^2} + \ln\frac{H(4a+H)}{(2a+H)^2}\right), \qquad [5]$$

where $A_{131}$ is the Hamaker constant for each system, which can be estimated by surface tension determination of the materials involved. We used the thermodynamic treatment proposed by van Oss (1994) for a full account of the theory. According to those authors, the surface free energy (or surface tension) $\gamma_i$ of a condensed phase consists of two additive contributions, dispersive LW and polar AB, which in turn depend on two parameters accounting for the $\gamma^-$ and $\gamma^+$ characters of the materials ($\gamma i = 2(\gamma_i + \gamma_i -)^{1/2}$). If $\gamma_i^{LW}$ is known for all phases involved, the Hamaker constant can be obtained as

$$A_{131} = 12\pi H_0^2 \Delta G_{131,H_0}^{LW} \qquad [6]$$

$$\Delta G_{131,H_0}^{LW} = -2\left(\sqrt{\gamma_1^{LW}} - \sqrt{\gamma_3^{LW}}\right)^2 , \qquad [7]$$

where $H_0$ is estimated at 1.58 ± 0.08 Å (van Oss et al., 1988). Similarly, the calculation of H-dependence of $\Delta G_{AB}^{131}$ requires knowledge of $\gamma^+$ and $\gamma^-$ for the two phases.

$$\Delta G_{131}^{AB} = 2\pi a \lambda \Delta G_{131,H_0}^{AB} e^{(\frac{H_0 - H}{\lambda})} , \qquad [8]$$

where $\lambda$ is the correlation length of water molecules, approximately $\lambda$=1 nm for hydrophilic surfaces, and $\Delta G_{131}$ depends on the acid-base parameters of the free energy of phases 1 and 3 (van Oss et al., 1994; Ontiveros-Ortega et al.,, 1998).

According to van Oss, the quantity $\Delta G^{AB}{}_{131, H_0}$ is:

$$\Delta G^{AB}_{131,H_0} = 4\left(\sqrt{\gamma_1^+\gamma_1^-} + \sqrt{\gamma_3^+\gamma_3^-} - \sqrt{\gamma_1^+\gamma_3^-} - \sqrt{\gamma_3^+\gamma_1^-}\right) \quad [9]$$

# 3 Results

## 3.1 Chemical and mineralogy analyses and SEM photography

Chemical analyses of the sample indicate a typical content of silica in the rocks, if we represent the content of $Na_2O+K_2O$ with regard to $SiO_2$ (Table 1(a-b) and Figure 2). In the figure 3 we can see the content of $K_2O$ with regard to $SiO_2$, K diagram.

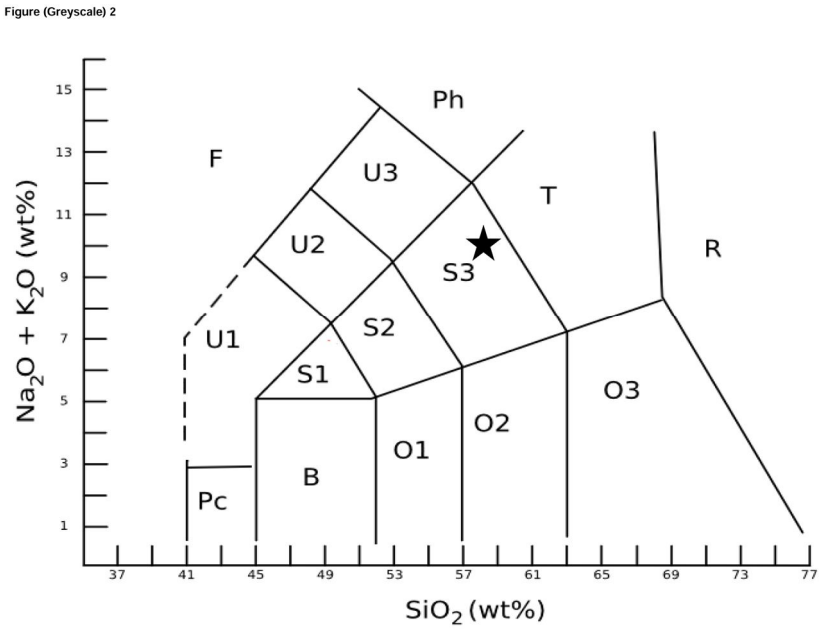


**Figure. 2**.- Classification of studied of Almagre according to total alkaline vs. $SiO_2$ (TAS) diagram.

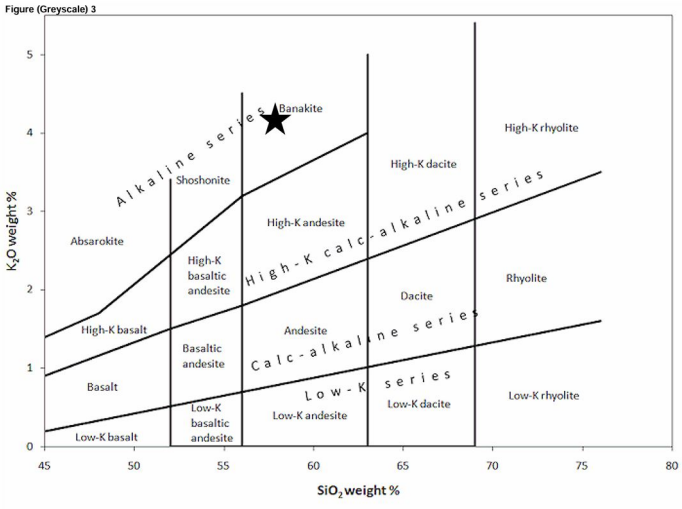


**Figure. 3.-** Classification of studied of Alamgre, according to $K_2O$ vs. $SiO_2$ diagram for rock series %K diagram.

The chemical composition of Almagre shows that the $SiO_2$ content (58.6%) corresponds to an acid rock, high in alkalis (NaO + $K_2O$). This indicates the presence of heavy elements such as Zr, Sr, and Ti. Light elements are also present as phosphates, sulfates and chlorides. However, the most striking finding is the content of organic matter (7.3%) as compared to virgin eruptive materials, indicating that the substance has been subjected to the action of edaphological processes.

It is evident that the rock is called trachyandesite, specifically banakite. It is a rock of explosive type associated with an index of volcanic explosivity III/IV. We also found a high content of Fe.

**Table 1 (a**) X-ray fluorescence (XRF) analysis for Almagre. **Table 1 (b)** Mineralogy of Almagre.

Table 1

| (a) % | Minerals | (b) % | Oxides |
|---|---|---|---|
| 5,13 | Q | 7,3 | LOI |
| | | 5,8 | Na2O |
| 1,49 | Cor | 0,83 | MgO |
| 27,65 | Ort | 17,6 | Al203 |
| 53,16 | Ab | 58,6 | SiO2 |
| | | 0,091 | P205 |
| 5,91 | An | 0,17 | SO3 |
| 2,23 | Hy | 0,21 | Cl |
| 3,9 | Hem | 4,332 | K2O |
| | | 1,22 | CaO |
| 0,09 | Ilm | 0,784 | TiO2 |
| 0,23 | Ap | 0,15 | MnO |
| 0,34 | Pv | 3,6 | Fe2O3 |
| | | 0,023 | SrO |
| 10 | %An en Pl | 0,0919 | ZrO2 |
| **91,85** | **ITT** | **100,78** | **Total** |

However, Table 1-b shows the mineralogical theoretical composition calculated from the Norm CIPW (Cross, Iddings, Pirsson and Washington) (Verma, 1993), indicating that near 60% of the rock is plagioclase, 27% pyroxene, 5% quartz, and the incidental minerals cordierite and apatite.

SEM (Fig. 4) revealed the components of the studied sample.

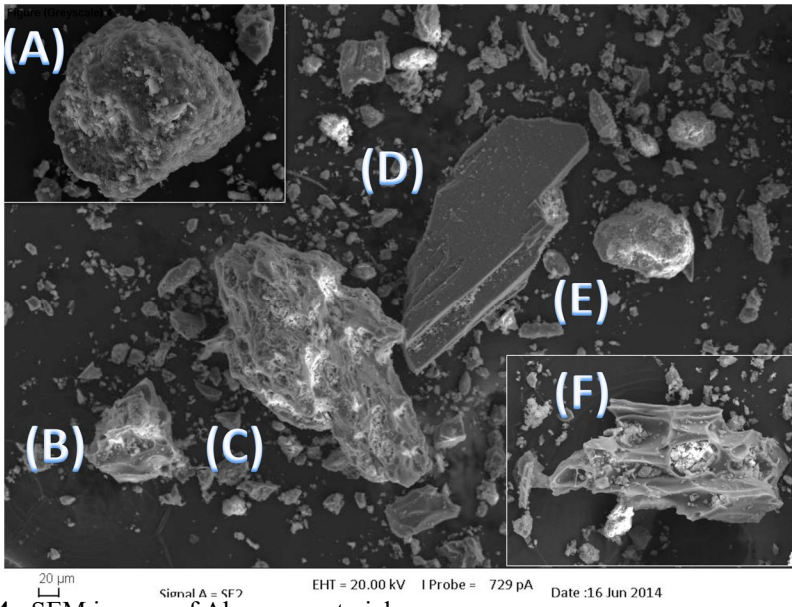


**Figure. 4.-** SEM images of Almagre material.

It is evident that the rock is constituted by various components: volcanic glasses of different forms (plane D; sphere E, chaotic B and F) and components with a soil structure (A, C, and E) with domains and micro-domains.

In the photography we observed that a structure defined in the Almagre does not exist; the components are distributed in random form within the rock. The various forms and sizes of volcanic crystal (B, D and F) and components with the structure of domains and micro-domains (A, C and E) indicate a rapid and chaotic origin.

### 3.2 Electrical Characterization of Almagre: Potential Zeta

Figures 5–7 show values of ζ as a function of pH for different electrolytes (monovalent, divalent and trivalent) and concentrations.

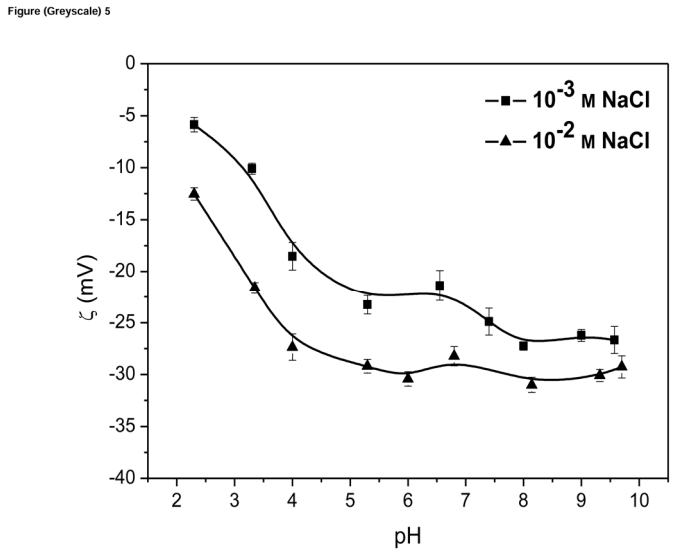


**Figure. 5.-** Zeta potential (ζ) of Almagre as function of pH value for 1 and 10 mM concentrations of NaCl.

In general, ζ values are negative for monovalent and divalent electrolytes, Almagre is considered to be ~59% $SiO_2$ (Table 1). The surface is negative because of the existence of $SiO^-$ groups. The strong decrease at basic pH (between 2 and 4) is likely attributable to the progressive adsorption of $Cl^-$ ion groups at the interface. At higher pH, the behavior can be ascribed to equilibrium between the absorption of cations at the interface and progressive adsorption of hydroxyl groups.

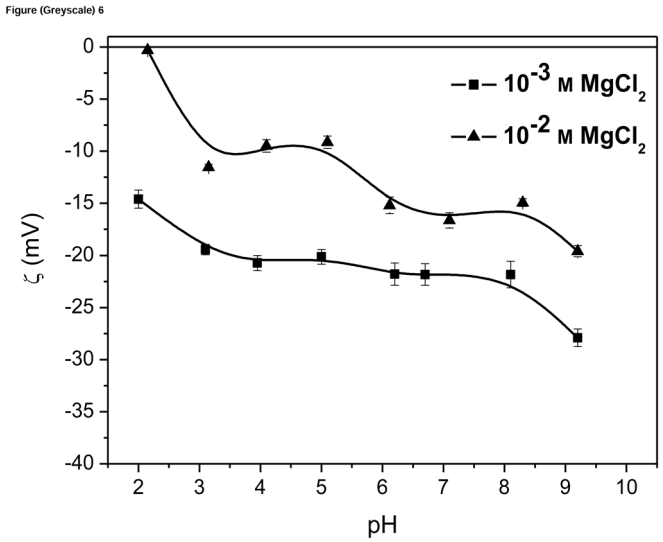


Figure. 6.- Zeta potential (ζ) of Almagre as function of pH value for 1 and 10 mM concentrations of $CaCl_2$.

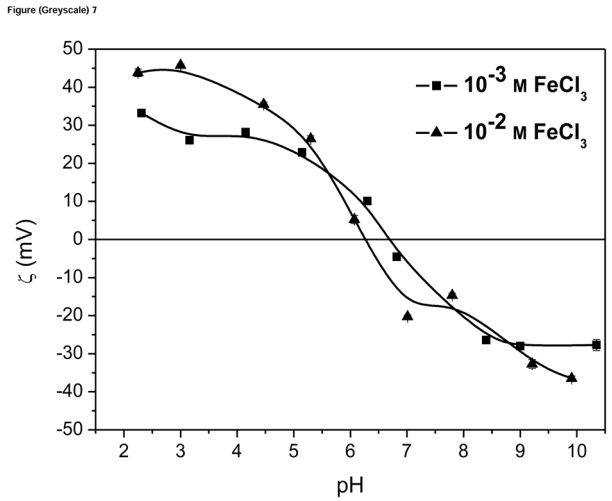


Figure. 7.- Zeta potential (ζ) of Almagre as function of pH value for 1 and 10 mM concentrations of $FeCl_3$.

The mean ζ of soil in the presence of $Na^{+}$ and in various pH conditions is shown in Figure 5. Mean ζs were negative in pH range 2–10. Mean ζ magnitudes were linearly proportional to pH in the solution for pH 2–6, but had relatively constant values at higher pH. This decrease (between 5 and 30 mV in absolute value) can be attributed to a progressive adsorption of $Cl^{-}$ ions onto soil particles. Figure 5 also shows ζ behavior for different ionic strengths of the medium. The results show that ζ for an electrolyte concentration of 0.01 M was higher than that for 0.001 M NaCl in solution. This is anomalous behavior is due probably from increased ionic strength leading to particle coagulation, which produces particles of larger radius. This in turn produces larger values of *κa* and therefore ζ (Plaza, 2015). This behavior may be also associated with an excess of electrical charge at the interface, which controls surface conductivity. In fact, the interpretation of electrophoretic mobilities of particles is complex because of such excess charge (Tejada et al., 2009) .

Figure 6 depicts the ζ behavior of soil in the presence of a divalent electrolyte $Mg^{+2}$. In this case, ζ was also negative for all pH, but its obtained values (between 0 and 15 mV in absolute value) were smaller than for the monovalent electrolytes. We see that the dependence on pH in this case is weaker, as expect from a divalent electrolyte. This behavior was explained by Lagaly et al., (2006). This process may be attributable to the behavior of the gels of alumina and allophane present in the majority of Andisols (FAO, 2006). Regarding the effect of ionic strength, we observed a decrease in ζ with increasing electrolyte concentrations, owing to compression of the double electrical layer.

In the case of trivalent electrolyte $Fe^{+3}$ (Figure 7), ζ had a double electrical nature, positive in acid medium and negative at basic pH. The zero-charge point in the case of the iron reached pH 6 to 7. $Fe^{3+}$ cations were absorbed onto particles, probably because of acid pH values. The ζ of the system decreased to +45 to 0 mV, ascribed to progressive adsorption of $Cl^-$ and hydroxyl groups with increasing pH. For the largest values of pH, the negative ζ may be attributable to the formation of coordination compounds, indicating that the iron is adsorbed in the form of $Fe(OH)^{2+}$ and $Fe(OH)^+$.

### 3.3 Surface Free Energy

Table 2 lists components of surface free energy obtained from the sample, in natural conditions and after treatments with electrolytes of Na, Mg and Fe.

**Table 2.** Values of surface free energy component: dispersive $\gamma^{LW}$, electron-donor $\gamma^-$ and electron-acceptor $\gamma^+$ for Almagre.

| | $\gamma^{LW}$(mJ/m²) | $\gamma^-$(mJ/m²) | $\gamma^+$(mJ/m²) | $\gamma^{TOT}$(mJ/m²) |
|---|---|---|---|---|
| **Almagre** | 46,941 | 36,071 | 0,57962 | 56,086 |
| **Almagre+NaCl** | 40,602 | 18,113 | 2,8704 | 55,022 |
| **Almagre+MgCL** | 44,222 | 20,885 | 1,2612 | 54,487 |
| **Almagre+FeCl** | 45,028 | 38,928 | 0,6561 | 55,135 |

The Almagre in bare conditions has a dispersive component $\gamma^{LW}$ with a value of 47 mJ/m$^2$, Analogous results have been obtained for samples rich in

silicon oxide by other authors (A. Ontiveros-Ortega et al., 2014-2016) and (Ramos-Tejada et al., 2003). The treatment with the iron electrolyte did not modify the initial characteristics of the sample under natural conditions, likely because of the high iron content in the Almagre; see in Table 2. We see that the $\gamma^{LW}$ component decreases as we move down the valence of the cation present, e.g., 6 units for the treatment with $Na^{+}$ and 3 with $Mg^{2+}$.

The results for the polar components show that in bare conditions, the sample had a monopole character ($\gamma^{+} = 0$ and $\gamma^{-} \neq 0$), and was electron-donor in nature. The treatments with electrolytes Na and Mg (both very common ions in the sea breeze) reduced $\gamma^{-}$ from 36 to 18 and 20 mJ/m$^2$, respectively, causing the sample go from hydrophilic to hydrophobic ($\gamma^{-} <$ 28 mJ/m$^2$) according to Van Oss et al. (1988). This indicates a less wettable sample (for an equal pore size).

The result for the $\gamma^{+}$ parameter shows an increase from 0.6561 ($Fe^{3+}$) to 1.26 mJ/m$^2$ ($Mg^{2+}$)) and 2.87 mJ/m$^2$ ($Na^{+}$). The effect of electrolytes conferred a slight bipolar character, and there was $\gamma^{+}$ decrease with increasing valence of the absorbed cation.

### 3.4 Energy of interaction

Figures 8–10 show curves of interaction energy, calculated from Table 3 and Equations 4,5 and 8 as a function of distance (H) between particles.

**Table 3.** Parameters used to calculate the potential energy of interaction between particles.

| | Zeta potencial (mV) without electrolytes | | | | | | SFE | | | |
|---|---|---|---|---|---|---|---|---|---|---|
| | pH 3 | | pH 6 | | pH 8 | | LW | + | - | Total |
| Sample | -6,05 | | -10,48 | | -13,88 | | 46,941 | 0,5796 | 36,071 | 56,086 |
| | pZ 0.001M | | | pZ 0.01M | | | LW | + | - | Total |
| NaCl | -8.75 | -22.17 | -26.5 | -18.5 | -29.89 | -30.4 | 40,602 | 2,8704 | 18,113 | 55,022 |
| $MgCl_2$ | -19.59 | -21.36 | -22.76 | -9.06 | -14.7 | -15.7 | 44,222 | 1,2612 | 20,885 | 54,487 |
| $FeCl_3$ | 44.6 | 6.4 | -19.15 | 28.44 | 11.96 | -22.05 | 45,028 | 0,6561 | 38,928 | 55,135 |

Figure 8 shows the obtained energy interactions between particles for the sample with $Na^+$ at different ionic strengths. These must overcome a barrier of potential that becomes greater with increasing proximity between particles, with maxima at very short distances ($H \leq 5$ nm). These barriers increase with pH. A qualitative description suggests that for pH = 3, the barrier of potential has values on the order of 50 kT. This is an approximation for the particles of Almagre, indicating a cohesive behavior. At more basic pH, the barriers strengthen, resulting in a less cohesive deposit. Because of the large $\zeta$ values shown in Fig. 5, for low ion concentrations of Na, potential barriers at lower ionic strengths are stronger than those at greater strengths.

Figure 9 shows curves obtained for Mg at different ionic strengths (0.001 and 0.01 M) and pH values (3, 6, and 8). In all cases, barriers of potential are > 75 kT, suggesting that the particles cannot approach each other and so the soil will have a low degree of compaction. For pH behavior observed in fig 9, the results show that the deposit is weakly cohesive for all

pH. It is also evident that repulsion between particles is weakest for the highest concentrations of cations in the solution.

Figure (Greyscale) 8

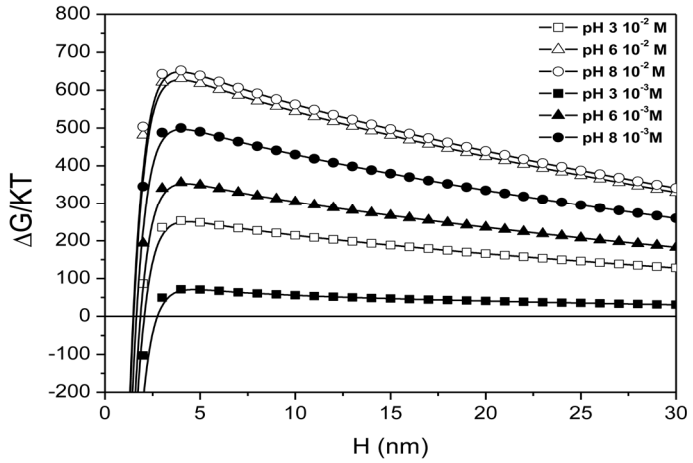


**Figure. 8.-** Total energy of interaction (in kT) between particles as the function of the distance between surfaces, H, for different pH values and ionic strength when the electrolyte present in solutions was NaCl.

Figure 10 shows curves of energy obtained for the treatment with iron. The anomalous behavior of the energy of interaction when iron is. We can observed that in acid values (pH = 3), the particles showed the maximum repulsion of all studied conditions.

This confirms that an acid contribution to deposits of Almagre drastically reduces cohesion between the particles, which would cause strong instability. In contrast, for pH = 6, the Almagre substrate was the most stable, with smaller values of potential barrier

Figure (Greyscale) 9

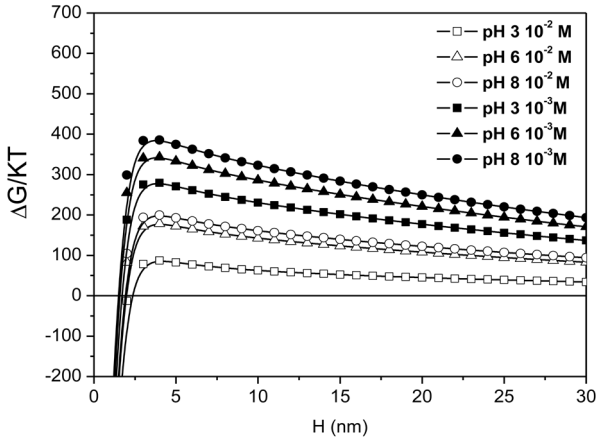


**Figure. 9.-** Total energy of interaction (in kT) between particles as the function of the distance between surfaces, H, for different pH values and ionic strength when the electrolyte present in solutions was $CaCl_2$.

Figure (Greyscale) 10

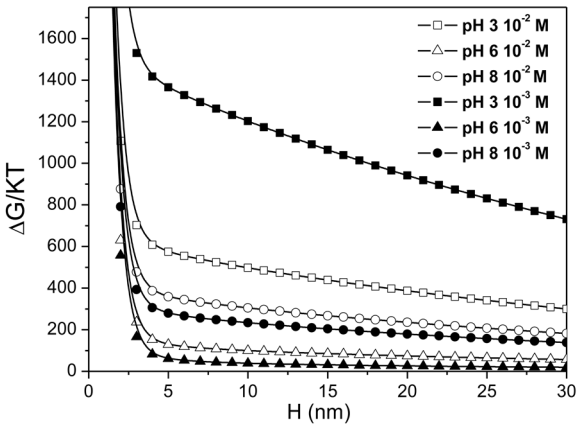


**Figure. 10.-** Total energy of interaction (in kT) between particles as the function of the distance between surfaces, H, for different pH values and ionic strength when the electrolyte present in solutions was $FeCl_3$.

## 4 Summary and Conclusions

The sea breeze over the hillsides of the volcanic islands increases the contents of sodium and magnesium of Almagre. This alters superficial properties (surface free energy and ζ) of the material composing the substratum. This alteration affects the water retention and cohesion of the material constituting the deposit. We analyzed the effects that produce sodium, magnesium, and iron through the surface free energy and superficial charge of the deposit.

We studied the effects that produce the sodium and magnesium absorbed by Almagre. The results of the surface free energy analysis show an increase in hydrophobicity of the material, which induces a weak capacity of water retention and thereby increased surface runoff. However, analysis of the energy of total interaction in the sample under very acidic (pH = 3) conditions revealed that the electrolytes of sodium and magnesium induce strong cohesion relative to a basic pH. At basic pH (remember natural pH for Almagre is 8), there is clear repulsion between the particles.

We also studied the effect of the presence of iron on our material. The results show that when there is dissolved iron, the repulsion between particles is greater than that obtained with the other electrolytes. This emphasizes that Almagre is a substratum very rich in iron that can contributed to dissolution under saturated conditions. This suggests that a saturated Almagre continues to be an ideal layer for sliding.

**Acknowledgements.**

We gratefully acknowledge the support of institutions involved. This work was partially funded by Projects, “The MED-SUV project has received funding from the European Union Seventh Framework Programme (FP7) under Grant agreement n°308665”, and, Spain government (project CGL2011-29499-C02-01). We also thank National Geographical Institute of the Spanish Ministry and the two anonymous reviewers whose constructive comments have considerably improved the quality of this work.

## 5 References.

Ancochea, E., Fuster, J., Ibarrola, E., Cendrero, A., Coello, J., Hernan, F., ... & Jamond, C. (1990). Volcanic evolution of the island of Tenerife (Canary Islands) in the light of new K-Ar data. Journal of Volcanology and Geothermal Research, 44(3-4), 231-249.

Ancochea, E., Huertas, M. J., Cantagrel, J. M., Coello, J., Fúster, J. M., Arnaud, N., & Ibarrola, E. (1999). Evolution of the Cañadas edifice and its implications for the origin of the Cañadas Caldera (Tenerife, Canary Islands). Journal of Volcanology and Geothermal Research, 88(3), 177-199.

Bailey, C., Fodor-Csorba, K., Gleeson, J. T., Sprunt, S. N., & Jákli, A. (2009). Rheological properties of bent-core liquid crystals. Soft Matter, 5(19), 3618-3622.

BASU, S. R., & DE, S. K. (2003). Causes and consequences of landslides in the Darjiling-Sikkim Himalayas, India. Geographia Polonica, 76(2), 37-52.

Baumgarten, W., Dörner, J., & Horn, R. (2013). Microstructural development in volcanic ash soils from South Chile. Soil and Tillage Research, 129, 48-60.

Baumgarten, W., Neugebauer, T., Fuchs, E., & Horn, R. (2012). Structural stability of marshland soils of the riparian zone of the tidal Elbe River. Soil and Tillage Research, 125, 80-88.

Bommer, J. J. (2002). Deterministic vs. probabilistic seismic hazard assessment: an exaggerated and obstructive dichotomy. Journal of Earthquake Engineering, 6(spec01), 43-73.

Broothaerts, N., Kissi, E., Poesen, J., Van Rompaey, A., Getahun, K., Van Ranst, E., & Diels, J. (2012). Spatial patterns, causes and consequences of landslides in the Gilgel Gibe catchment, SW Ethiopia. Catena, 97, 127-136.

Carracedo, J. C., Badiola, E. R., Guillou, H., Paterne, M., Scaillet, S., Torrado, F. P., ... & Hansen, A. (2007). Eruptive and structural history of Teide Volcano and rift zones of Tenerife, Canary Islands. Geological Society of America Bulletin, 119(9-10), 1027-1051.

Carracedo, J. C., Fernandez-Turiel, J. L., Gimeno, D., Guillou, H., Klügel, A., Krastel, S., ... & Troll, V. R. (2011). Comment on “The distribution of basaltic volcanism on Tenerife, Canary Islands: Implications on the origin and dynamics of the rift systems” by A. Geyer and J. Martí. Tectonophysics 483 (2010) 310–326. Tectonophysics, 503(3), 239-241.

Churakov, S. V., & Gimmi, T. (2011). Up-scaling of molecular diffusion coefficients in clays: A two-step approach. The Journal of Physical Chemistry C, 115(14), 6703-6714.

Cockell, C. S. (2010). Geomicrobiology beyond Earth: microbe–mineral interactions in space exploration and settlement. Trends in microbiology, 18(7), 308-314.

Crozier, M. J., & Glade, T. (2005). Landslide hazard and risk: issues, concepts and approach. Landslide hazard and risk, 1-40.

Duran, J. D. G., Ontiveros, A., Delgado, A. V., & Gonzalez-Caballero, F. (1998). Kinetics and interfacial interactions in the adhesion of colloidal calcium carbonate to glass in a packed-bed. Applied surface science, 134(1), 125-138.

Holtz, R. D., & Kovacs, W. D. (1981). An introduction to geotechnical engineering (No. Monograph).

Iuss, I. (2006). FAO, 2006. World base reference for soil resources. Report on World Soil Resources. FAO. Rome, Italy.

Kadar, E., Fisher, A., Stolpe, B., Calabrese, S., Lead, J., Valsami-Jones, E., & Shi, Z. (2014). Colloidal stability of nanoparticles derived from simulated cloud-processed mineral dusts. Science of the Total Environment, 466, 864-870.

Longpré, M. A., Troll, V. R., Walter, T. R., & Hansteen, T. H. (2009). Volcanic and geochemical evolution of the Teno massif, Tenerife, Canary Islands: Some repercussions of giant landslides on ocean island magmatism. Geochemistry, Geophysics, Geosystems, 10(12).

Martí, J. H. (1997). Vertical and lateral collapses on Tenerife (Canary Islands) and other volcanic ocean islands. . Geology, 25(10), 879-882.

Masson, D. G., Watts, A. B., Gee, M. J. R., Urgeles, R., Mitchell, N. C., Le Bas, T. P., & Canals, M. (2002). Slope failures on the flanks of the western Canary Islands. Earth-Science Reviews, 57(1), 1-35.

Ontiveros-Ortega, A., Moleon, J. A., Plaza, I., & Guillén, C. (2016). Effect of interfacial properties on mechanical stability of ash deposit. Journal of Rock Mechanics and Geotechnical Engineering, 8(2), 187-197.

Ontiveros-Ortega, A., Vidal, F., Gimenez, E., & Ibáñez, J. M. (2014). Effect of heavy metals on the surface free energy and zeta potential of volcanic glass: implications on the adhesion and growth of microorganisms. Journal of Materials Science, 49(9), 3550-3559.

Plaza, I., Ontiveros-Ortega, A., Calero, J., & Aranda, V. (2015). Implication of zeta potential and surface free energy in the description of agricultural soil quality: Effect of different cations and humic acids on degraded soils. Soil and Tillage Research, 146, 148-158.

Ramos-Tejada, M. M., Ontiveros, A., Viota, J. L., & Durán, J. D. G. (2003). Interfacial and rheological properties of humic acid/hematite suspensions. Journal of colloid and interface science, 268(1), 85-95.

Rošic, R., Pelipenko, J., Kocbek, P., Baumgartner, S., Bešter-Rogač, M., & Kristl, J. (2012). The role of rheology of polymer solutions in predicting nanofiber formation by electrospinning. European Polymer Journal, 48(8), 1374-1384.

Schmincke, H. U. (1976). The geology of the Canary Islands. In Biogeography and ecology in the Canary Islands (pp. 67-184). Springer Netherlands.

Smoluchowski, M. V. (1921). Handbook of Electricity and Magnetism. Barth, Leipzig, 366.

Soto, E. A., Coronel, M. J. H., Cantagrel, J. M., Coello, J., Casas, J. M. F., Arnaud, N., & Ibarrola, E. (1999). Evolution of the Cañadas edifice and its implications for the origin of the Cañadas Caldera (Tenerife, Canary Islands).

Tejada, M., Hernandez, M. T., & Garcia, C. (2009). Soil restoration using composted plant residues: Effects on soil properties. Soil and Tillage Research, 102(1), 109-117.

Van Oss, C. J. (1994). Polar or Lewis acid-base interactions. Interfacial forces in aqueous media, 18-46.

Van Oss, C. J., & Good, R. J. (1989). Surface tension and the solubility of polymers and biopolymers: the role of polar and apolar interfacial free energies. Journal of Macromolecular Science—Chemistry, 26(8), 1183-1203.

Van Oss, C. J., Chaudhury, M. K., & Good, R. J. (1988). Interfacial Lifshitz-van der Waals and polar interactions in macroscopic systems. Chem. Rev, 88(6), 927-941.

Verma, S. P., & Navarro de León, I. (1993). Norma CIPW–Nuevo programa de cómputo. In México, DF, Instituto de Geofísica, 3er. Congreso Nacional de Geoquímica, Memorias (pp. 117-119).

Wang, M., & Revil, A. (2010). Electrochemical charge of silica surfaces at high ionic strength in narrow channels. Journal of colloid and interface science, 343(1), 381-386.

Zhou, G., Esaki, T., Mitani, Y., Xie, M., & Mori, J. (2003). Spatial probabilistic modeling of slope failure using an integrated GIS Monte Carlo simulation approach. Engineering Geology, 68(3), 373-386.

### *5.2.3. Artículo: Electrical and thermodynamic characterizations of volcanic ashes.*

*Resumen*

La mayoría de los grandes estratovolcanes de nuestro planeta han sufrido deslizamientos en sus flancos, modificando y / o cambiando completamente el marco principal de su edificio volcánico, provocando a su vez tsunamis y tsunamis suaves asociados con ellos. Pero en una escala menor, los depósitos de cenizas volcánicas y fragmentos más gruesos también son responsables de gran cantidad de diapositivas y lahares que constituyen un riesgo geológico importante.

En los últimos años, multitud de estudios han tratado de conocer las características geotécnicas de estos depósitos para tratar de resolver los problemas geotécnicos asociados a ellos. Los edificios volcánicos presentan laderas desprovistas de vegetación, hecho que facilita las escorrentías.

Los estudios realizados tratan de analizar los factores que determinan la estabilidad de los depósitos antes mencionados son bastantes. Pero son pocos los que han analizado la cohesión de estos depósitos y los factores que lo determinan. La estabilidad de los depósitos se relaciona con la energía de interacción entre las partículas que los componen y su cálculo depende de las propiedades superficiales de éstos.

El propósito de este estudio es analizar las propiedades superficiales de los depósitos volcánicos de volcanes activos para relacionar su composición química, su índice de explosividad volcánica con la estabilidad de los mismos.

En nuestro caso, después de realizar el estudio de propiedades superficiales combinado con los análisis clásicos de cenizas volcánicas, parece indicar que en general todas las cenizas parecen tener muy bajos valores de cohesión en condiciones de pH 8. En cuanto al SFE, no existe una relación clara entre el contenido en $SiO_2$ y el gamma negativo, si podemos ver una pequeña tendencia si sólo usamos las cenizas más recientes, menor todo lo que está contenido en $SiO_2$ menor es la explosividad volcánica de los depósitos.

Recordemos que nuestros estudios se basan en condiciones de saturación de cenizas, ya que las partículas en condiciones de saturación nativas presentan altos niveles de energía (más de 100kt a 10nm de Distancia) en condiciones de pH (pH = 8). Esta característica que poseen impide que las partículas coagulen y precipiten, este es un hecho muy importante, y explicaría la rápida formación de lahares, un claro ejemplo la de Isla Decepción.

Pero enfatizando más, en las regiones sísmicas ya que es Italia, el mismo depósito (Etna, Stromboli y Vulcano) sería muy capaz de formar toboganes, debido a las descargas de energía que presentan distantemente muy cortas.

Para terminar, la isla de Fogo y El Hierro con alta emisión de Azufre. En estas islas el pH natural del suelo se encuentra modificado por la circunstancia antes mencionada siendo ligeramente inferior a 6. En estas condiciones el nivel de energía kT le corta distante es todavía bastante alto, por lo que son materiales con tendencia a sufrir diapositivas. Pero supongamos ahora que un almacén situado en un depósito volcánico y una fumarola de azufre, lógicamente el pH puede llegar a ser muy ácido en las proximidades del área, en estas condiciones la cohesión de las partículas es máxima con respecto a otro pH.

Con esta investigación trata de anunciar la importancia que puede suponer el estudio de las propiedades superficiales en los depósitos volcánicos y la infinidad de aplicaciones que poseen.

# Artículo científico:

# ELECTRICAL AND THERMODINAMYC CHARACTERIZATIONS OF VOLCANIC ASHES.

# Revista:

# Bulletin of Vulcanology

## ELECTRICAL AND THERMODYNAMIC CHARACTERIZATION OF VOLCANIC ASHES

Plaza, I[1] ; Ontiveros-Ortega, A.[1,2]; Moleón J.[1]; Calero, J.[3]

1 *Department of Physics, University of Jaén, Campus Universitario de las Lagunillas s/n, Edificio A-3, 23071 Jaén, Spain*

2 *Instituto Andaluz de Geofísica, University of Granada, 18071 Granada, Spain*

*3 Department of Geology, University of Jaen, Spain*

# ABSTRACT

This paper presents a comparative study of the surface properties of deposits of different active volcanoes that constitute a risk to the population. Stratovolcanoes have slides on their flanks, modifying and/or changing completely the main frame of their volcanic structure, in turn inducing tsunamis. There have been many studies analyzing the factors that determine the stability of volcanic deposits, but few have examined the cohesion of these deposits and their determining factors. The stability of the deposits is related to the energy of interaction between their particles, and its calculation depends on the superficial properties of the deposits. The purpose of this study is to analyze superficial properties of volcanic materials in order to relate their chemical composition, electrical and thermodynamic characteristics with cohesion. The results show that cohesion in the deposits varies with the volcano, and that this cohesion changes drastically with pH of the medium; El Hierro has the most cohesive materials, and Etna deposits the least.

**Keywords:** zeta potential, surface free energy, volcanoes, ash, cohesion

- **Introduction**

Volcanic areas are complex, where earthquake-induced landslides constitute significantly natural hazards, and where heavy rainfall can produce soil sliding (Capra et al. 2003). Mitigation of landslide hazards in such regions first requires a

thorough understanding of the behavior of soil-sliding volcanic soils under static and dynamic conditions. The cohesion of volcanic deposits and stability depend on environmental conditions of the deposits, their chemical nature, rainfall, pH or concentration of salts (Voight et al., 1997; Ontiveros-Ortega et al., 2016).
Cohesion is a determinant and depends directly on the surface properties of eruptive material from which it is formed. The analysis of surface properties of different material and solid–liquid interfaces is important within a wide range of problems in applied colloid science. Wettability, adsorption, adhesion or cohesion depend to a large extent on electrical and surface free energy changes involved in those processes (Gimmi et al 2011; Baumgarten et al, 2013; Kadar et al, 2014; Ontiveros-Ortega et al., 2016).

Charge generation and the surface properties are related by the Groups of what that the particles have on their surface. The generation of these groups depends on the chemical nature of the materials, which in the case of effusive material is related to the "cooking" of the magma. The objective of the present work was to relate the surface properties of erupted material, its chemical nature, and nature of the eruption. The behavior of flocculation phenomena, adsorption, wetting and rheological properties of dispersion depends on the interactions between particles (Plaza et al., 2015; Bailey et al., 2009; Kelly et al., 2010; Ontiveros-Ortega et al., 2014).

Given the above, we analyze the eruptive material of active volcanoes that pose a risk to the population, in order to quantify cohesion of the deposit. Once known, we determine how these properties change with environmental conditions. We also analyze electrical and thermodynamic properties of the eruptive material and, as these are modified by changes in pH of the medium, the nature of the cations and their ionic strength.

We collected samples of the following active volcanoes: Teide and El Hierro of the Canary Islands, Spain; Fogo's peak in the Cape Verde Islands; Vulcano, Stromboli and Etna in Italy; Deception Island in Antarctica.

- **Materials and Methods**

Table 1 shows characteristics of the studied volcanoes and the UTM coordinates where the sampling was done.

**Table** 1. Basic data of samples: GPS location, altitude, regional tectonics, Volcanic Explosivity Index (VEI), and type of eruption

| Volcano | UTM coordinates | | Altitude (m) | Tectonics | VEI | Type of eruption | Name of rock | Degree of magamatic differentiation |
|---|---|---|---|---|---|---|---|---|
| El Hierro Island | 27°43'22.42"N | 18° 3'45.58"O | 1046 | Interplate-C. Oceanic < 15km | I/II | Hawaiian | Tephrite | Null |
| Fogo Island | 14º56'55.36"N | 24º20'29.32"O | 2731 | Interplate-C. Intermediate 15–25km | I | Hawaiian | Tephrite | Null |
| Mt. Vulcano | 38º24'15.76"N | 14º58'0.670"E | 321 | Convection Subduction > 25 km | III | Vulcanian | Trachyandesite | High |
| Mt. Stromobli | 38º47'45.10"N | 15º13'22.17"E | 538 | Convection Subduction > 25 km | II | Strombolian | Basalt rich in K | Low |
| Mt. Etna | 37º42'21.94"N | 15º00'15.83"E | 2053 | Subduction Convección > 25 km | II | Strombolian | Basalt rich in K | Low |
| Deception Island | 62°58'4.37"S | 60°33'35.02"O | 225 | Divergent limit - Cort Continental>25km | IV | Phreatomagmatic | Andesitic basaltic | High |

Information obtained through Smithsonian Institution's Global Volcanism Program (GVP), housed in the Department of Mineral Sciences, National Museum of Natural History, Washington D.C. (http://volcano.si.edu)

*The Hierro, Spain*

Hierro Island is in the Canary Islands, 100 km from the African coast. The origin of the four islands and seven islets is linked to a hotspot in an oceanic crust transition to the African continent (Guillou et al., 1996). Hierro eruptions are classified as Volcanic Explosivity Index (VEI) type I/II (Ancochea et al., 1990). The geologic history of this island, though short at only 2 Ma, is marked by the collapse of its principal structure (Carracedo et al., 2002). Slides on both islands are frequent and of large dimension (Siebert et al., 2010). Selected deposits are in high terrain near an old crater. The color is gray ash, finely rolled to a thickness of 50 cm.

*Fogo's Peak, Cape Verde Islands*

The Cape Verde Islands are within the same tectonic context as the Canary Islands, although this location is further north and more removed from the African plate. The origin is also associated with a hotspot beneath the Atlantic oceanic crust (Dionis et. al., 2015). The eruption mechanism is type I (fissure/Hawaiian) in the VEI (Paris et al., 2011). The most recent eruption was only a few years ago (2014), in from which we can observe the basaltic character of volcanic washes and fissure eruptions with Strombolian periods rich in pyroclastic emissions (Dionis et. al., 2015). The geologic–geomorphologic history of the island is marked by large slides in its principal vent, the scars of which are visible in satellite images (Masson et al., 2008).

The deposits gathered at Fogo's peak correspond with the eruption of 2011. They are fragments of very dark color with very homogeneous dimensions (< 10 mm in length × 20 mm in width and 5–10 mm in thickness) On the island, there are frequent volcanic emissions rich in sulfur (Hernández et al., 2005).

## Volcanoes around the island of Sicily, Italy

Sicily is a tectonically complex area because of collision between the African and Eurasian plates. In the east, the volcanic context is that of arch islands (as with Mt. Vulcano). However, there is the volcano of Mt. Etna, which has been the subject of much scientific discussion because its origins are not certain (Andronico et al., 2005; Behncke et al., 2009).
The Etna Vulcano is located in the north of Sicily. It constitutes a volcanic arch that one agrees on a continental bark that reaches the ocean on the east (Beccaluva et al., 1985). Recent publications on the generation of this volcano reveals large slides on its flanks and enormous associated tsunamis (Tinti et al., 1996). Deposits of Vulcano date to 1985 (Arrighi et al., 2006) have a grayish color, very heterogeneous size, and very soft texture.

Mt. Etna, also a very active volcano, is on the eastern coast of Sicily. The geologic history of this volcano shows overlapping volcanic cones (Lentini, et al., 1982; Branca et al., 2004; Scollo et al., 2005). Recent investigations reveal large slides on the mountain (Barbano et al., 2014). The samples are very homogeneous, of size < 3 mm and dark color.

The complexity of the geographic area is great. Stromboli volcano is the result of a complex process of subduction, rifting, basin formation, and their extension (Ferrari et al., 1993). Stromboli is in the Tyrrhenian Sea, north of Sicily. This volcanic island is characterized for its regular and spectacular eruptions, 2000-2500 years ago, which were interrupted by short periods of more explosive eruptions (Bertagnini et al., 2011). The geologic history of this volcano also shows signs of several collapses on the northeast face of the cone (Hornig-Kjarsgaard et

al., 1993). The samples of quiet ash from the eruption of 2013 are very homogeneous, of size < 2 mm and very dark color.

*Deception Islands: Antarctica*

Deception Island is on the Antarctic Peninsula. It is one of the most dangerous and active volcanoes in the area, with more than 20 eruptions in the last two centuries (Pallas et al., 2001, Smellie et al., 2001).

The origin of the island is related to phreatomagmatic (explosive) eruptions of basaltic-andesite composition, with large pyroclastic quantities (Marti et. al., 1990). The morphology of the island has the mark of a great collapse across normal faults of tectonic origin (Weaver, 1979). Moreover, lahars and minor slides on the island were very frequent in the epoch of glacier thaw (Roobol et. al., 1973, 1979). The samples are of very dark color with gravel size and ellipsoidal form, and rugged. Moreover, it has been ascertained that there is diatomaceous earth glued to the surfaces (Ontiveros-Ortega et al., 2014).

- **Methods**

*Preparation of Samples and Chemical analysis*

The quiet samples had to be pre-treated before chemical and superficial property analyses, which were immersed in water and washed with distilled water.

Later, they were left to dry at a constant temperature for 48 hours. Finally, the samples were crushed by an agate mortar so they all had a similar texture.

The samples were subjected to X-ray fluorescence to determine their chemical composition. Then, fluorescent emission of a sample was measured.

*SEM Photography*

Scanning electron microscope (SEM) photography was used to describe and interpret texture (to identify the geometric disposition of gaseous bladders) and structure Holtz and Kovacs of the samples (presence of volcanic glass) (Holtz, 1981).

A SEM microscope was used with acceleration voltage 25 kV (S-510; Hitachi Ltd., Tokyo, Japan) equipped with an X-ray detector of dispersive energy (EDAX; Rontec GmbH, Berlin, Germany). The samples of volcanic material had only one treatment, by colloidal silver and metallization by carbon deposited in two orientations (20°–30°).

*Zeta potential*

To study zeta potential (ξ), dissolutions of electrolytes were prepared (sodium, calcium, iron and aluminum to make concentrations of 1 and 0.1 mm) along with a small quantity of ash sample (0.05 g). This suspension (20 ml) was mechanically agitated and pH was adjusted between 3 and 9 using NaOH and HCl additions. Upon fitting with the pH measurements, we obtained the ξ values from electrophoretic mobility at 20.0 ± 0.5 °C in a Malvern Zetasizer 3000 HS.

ξ was calculated based on the Smoluchowski approximation (Smoluchowksi, 1921).

*Surface free energy determination*

To determine surface free energy, we used the thick-layer wicking method. This is based on measurement of the time t that a liquid of viscosity η and surface tension $\gamma^3$ takes to penetrate a distance x through a thin porous layer of a solid on a

microscope glass slide. The most general description of the process is given by a generalized form of Washburn's equation (Washburn, 1921; Chibowski et al., 1992; Duran et al., 1998, Ontiveros et al., 2014):

*Calculation of Interaction Energy*

The adhesion between solid particles of colloidal size dispersed in aqueous media is determined by the balance of forces between various phases coexistent in a system, namely, hydrodynamic, diffusive-type and interfacial. The first two are used for the approximation of particles and short distances (to 100 nm).

The interfacial forces act at distances < 100 nm. These are electrical interactions between two layers, as well Lifshitz-van der Waals (LW) and acid-base (AB) interactions between condensed phases.

According to the so-called extended Derjaguin-Landau-Verwey-Overbeek or DLVO theory (van Oss et al., 1988, 1989; van Oss et al., 1994), three types of interfacial interactions should be considered, LW, electrostatic (EL), and AB. For particles *(phase 1)* of the same material dispersed in water *(phase 3),* the total interaction energy between particles is given by

$$\Delta G_{131}^{TOT} = \Delta G_{131}^{EL} + \Delta G_{131}^{LW} + \Delta G_{131}^{AB}, \qquad [1]$$

where subscript 131 refers to the phases involved. In our case, 131 in $\Delta G_{131}$ refers to particle – liquid medium – particle in the aggregation process:

$$\Delta G_{131}^{EL} = 2\pi\varepsilon a\xi^2 \ln(1+e^{-\kappa H}) \qquad [2]$$

$$\Delta G_{131}^{LW} = -\frac{A_{131}}{6}\left(\frac{2a^2}{H(4a+H)} + \frac{2a^2}{(2a+H)^2} + \ln\frac{H(4a+H)}{(2a+H)^2}\right) \quad [3]$$

where a is particle radius, ε the dielectric constant of the liquid, and κ the Debye screening length (double-layer thickness), and $A_{131}$ the Hamaker constant for each system, which can be estimated by surface tension determination for the materials involved. Using the approximations proposed by van Oss (1994), the surface free energy (or surface tension) $\gamma i$ of a condensed phase consists of two additive contributions, dispersive LW and polar AB, which in turn depend on two parameters accounting for the electron-donor ($\gamma^-$) and electron-acceptor ($\gamma^+$) characters of the materials ($\gamma_{i=2}(\gamma_i^+ \gamma_i^-)^{1/2}$). If $\gamma_i^{LW}$ is known for all phases involved, the Hamaker constant can be obtained as

$$A_{131} = 12\pi H_0^2 \Delta G_{131,H_0}^{LW} \quad [4]$$

$$\Delta G_{131,H_0}^{LW} = -2\left(\sqrt{\gamma_1^{LW}} - \sqrt{\gamma_3^{LW}}\right)^2 , \quad [5]$$

where $H_0$ is estimated at 1.58 ± 0.08 Å (van Oss et al., 1988).

Similarly, the calculation of H-dependence of $\Delta G^{AB}_{131}$ requires knowledge of $\gamma^+$ and $\gamma^-$ for the two phases.

$$\Delta G_{131}^{AB} = 2\pi a\lambda \Delta G_{131,H_0}^{AB} e^{(\frac{H_0-H}{\lambda})} , \quad [6]$$

where λ is the correlation length of water molecules, approximately λ=1 nm for hydrophilic surfaces, and $\Delta G_{131}$ depends on the AB parameters of the free energy of phases 1 and 3 (van Oss et al., 1994; Ontiveros-Ortega et al.,2016).

According to van Oss, the quantity $\Delta G^{AB}_{131,\ H_0}$ is

$$\Delta G^{AB}_{131,H_0} = 4\left(\sqrt{\gamma_1^+\gamma_1^-} + \sqrt{\gamma_3^+\gamma_3^-} - \sqrt{\gamma_1^+\gamma_3^-} - \sqrt{\gamma_3^+\gamma_1^-}\right) \quad [7]$$

- **Results**

*Chemical analyses*

The chemical analysis (Table 2) of the samples indicated a varying typical content of silica in the rocks, especially if we represent the content of $NaO+K_2O$ as a function of $SiO_2$ (Figure 1). We observe tephrite (Mt. Fogo and El Hierro Island), basalts (Mt. Stromboli, Mt. Etna), basaltic-andesite (Deception Island), and trachyandesite (Mt. Vulcano). Associated with this composition, the VEI shows that the studied volcanic materials have an index between I and IV, with an order from highest to lowest of Fogo, El Hierro, Stromboli, Etna, Deception and Vulcano.

The origin of primary magma can be determined by observing the contents of $Fe_2O_3$, MgO, $TiO_2$, CaO, NaO, and $MgO_2$. Thus, we saw three different magma: peridotite (Etna, Stromboli, Fogo and El Hierro), andesite (Deception), and rhyolite (Vulcano). Regarding KO content, it could also be classified into three groups: Series Shoshonisticas (Vulcano), high K content (Etna and Stromboli), containing (Deception) or not containing K (Fogos and El Hierro).

From the data shown in Table 3, we see that for Deception Island, the tectonic model is not adapted to the chemical nature of the erupted material. The samples have a relatively large number of heavy elements (Sr and Zr), revealing a very

important contribution from the mantle (iron-type peridotitic material). However, they showed a great amount of volatility (LOI). This suggests that there has been interaction of the magma with water. We also observed high sodium content, indicating the assimilation of box rock. The presence of water in the magmatic chamber accelerates the fractional crystallization process of Bowen. This increases acidity and therefore the volcanic hazard. Another possible cause of this apparent anomaly is the assimilation of continental rocks by the magmatic chamber. This is plausible because in the geographic zone near the volcano, there is a limit on convergent plates that contribute magmatic material. As a result, there is the formation of magma with intermediate characteristics, such as the one observed.

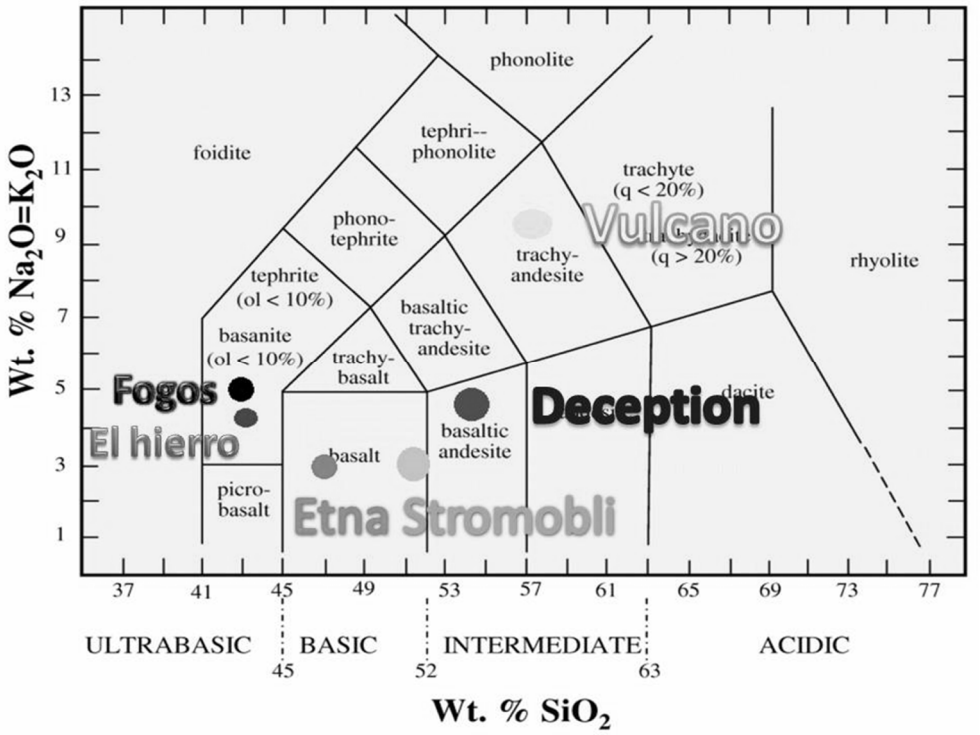


**Figure 1**. Classification of studied ashes according to TAS diagram.

Etna is a volcano with pre-arc subductive origin and Stromboli one with subductive origin of post-arc basin. The chemical data of Table 3 show that the two volcanoes have very similar characteristics. This is confirmed later using pZ data. It would be plausible (as affirmed by other authors) that both magmatic chambers are interconnected by an enormous internal fracture. In the magmatic chamber of Etna, a mixture of magma (intermediate and basic) is produced.

**Table 2**. X-ray fluorescence (XRF) analysis for various volcanic deposits (%oxide).

| Oxides\Volcano | Vulcano | Deception | Stromboli | Etna | El Hierro | Fogo |
|---|---|---|---|---|---|---|
| $SiO_2$ | 58.5 | 54.2 | 51.7 | 47.9 | 43.3 | 42.8 |
| $Al_2O_3$ | 15.6 | 15 | 13.9 | 14.1 | 14.1 | 14.6 |
| LOI* | 1.46 | 6.7 | 0.17 | 0.19 | 0.59 | 0.18 |
| $Na_2O$ | 3.38 | 4.08 | 1.4 | 1.93 | 2.72 | 2.88 |
| $K_2O$ | 4.87 | 0.686 | 2 | 1.44 | 1.58 | 2.16 |
| $Fe_2O_3$ | 5.812 | 9.488 | 9.563 | 11.17 | 12.94 | 11.49 |
| CaO | 4.93 | 7.05 | 11.6 | 12.5 | 11 | 11.4 |
| MgO | 2.86 | 3.39 | 8.85 | 8.58 | 5.55 | 6.97 |
| $TiO_2$ | 0.412 | 1.71 | 0.832 | 1.48 | 4.45 | 3.09 |
| Cl | 0.093 | - | - | - | - | - |
| $SO_3$ | 0.22 | - | - | 0.042 | 0.096 | 0.1 |
| MnO | 0.092 | 0.148 | 0.162 | 0.15 | 0.158 | 0.154 |
| $P_2O_5$ | 0.35 | 0.3 | 0.52 | 0.39 | 1 | 0.88 |
| $ZrO_2$ | - | 0.0359 | 0.02 | 0.0242 | 0.0493 | 0.00287 |
| SrO | 0.0121 | 0.0322 | 0.0633 | 0.088 | 0.107 | 0.0204 |
| Total | 98.59 | 102.82 | 100.78 | 99.98 | 97.64 | 96.72 |

As already mentioned, the explosivity index is related to silica content, which together with the % Mg determines viscosity of a lava. From the results shown in Table 3, we see that the silica/Mg ratio (Table 3) for Etna and Stromboli is large with respect to the others. Deception is very similar to Vulcano, although there is a small difference between them. The El Hierro islands and Fogo have appreciable differences in this index.

**Table 3**. Silica/mg ratio

| Volcanes | Vulcano | Deception | Stromboli | Etna | El Hierro | Fogo |
|---|---|---|---|---|---|---|
| Si (%) | 58.5 | 54.2 | 51.7 | 47.9 | 43.3 | 42.8 |
| Mg (%) | 2.86 | 3.39 | 8.85 | 8.58 | 5.55 | 6.97 |
| Mg/Si Ratio | 4.89% | 6.25% | 17.12% | 17.91% | 12.82% | 16.29% |

*SEM Photography.*

As already mentioned, the studied volcanoes correspond to different tectonic plate limits, i.e., subduction (Vulcano and Etna), between tectonic plates (Fogo and Canary Islands), and divergent borders (Stromboli and Deception). The type of volcanic eruption is demarcated by these limits, but the water content, presence of sinkholes or upheavals, assimilation of rocks by the magmas, and geochemical differentiation of these can vary substantially the type of eruption. The study of the characteristic textures using the SEM showed characteristics of eruption type I origination, and allowed confirmation of the VEI.

Photos of the samples from Fogo's peak (Figure 2) show high porosity and sphericity and great numbers of air bubbles. These characteristics classify the ash as eruptive activity of type I.

The deposit of Etna (Figure 2) also showed high porosity but with more blemishes in the form of bladders, whose size was large. This indicates that the eruption was more violent than does the ash on Fogo's peak. The ash classifies the eruptive activity as type I–II.

Stromboli's ash and El Hierro (Figure 2) revealed clasts of perfectly formed material, with a relatively long cooling time (there were neither pores nor bladders, typical of long and calm eruptions). Our sample is included in this context, and the ash qualifies as eruption type II.

Vulcano's samples were completely different (Figure 2). They also showed high porosity, but the form of the bladders was very irregular, producing interconnections between them. These characteristics are typical of material that has experienced an eruption more violent than type II. Because of this, the samples qualified as type III. The eruptions were less frequent but more violent, principally because the magma was more viscous and did not remain in liquid state for much time, on having contact with the air. Therefore, the liberation of gases was most difficult.

Finally, at Deception Island (Figure 2), we observed curved and very smooth surfaces with very irregular bladders, all of which in the same mass (without separation into clasts). The eruptions were phreatomagmatic, zone those produced by the interactions waters down (sweet or salty) - magma. This caused rapid cooling of the magma and sudden gas liberation. The irregular bladders were caused by these circumstances. Here were the most explosive eruptions of all volcanoes studied, type III/IV.

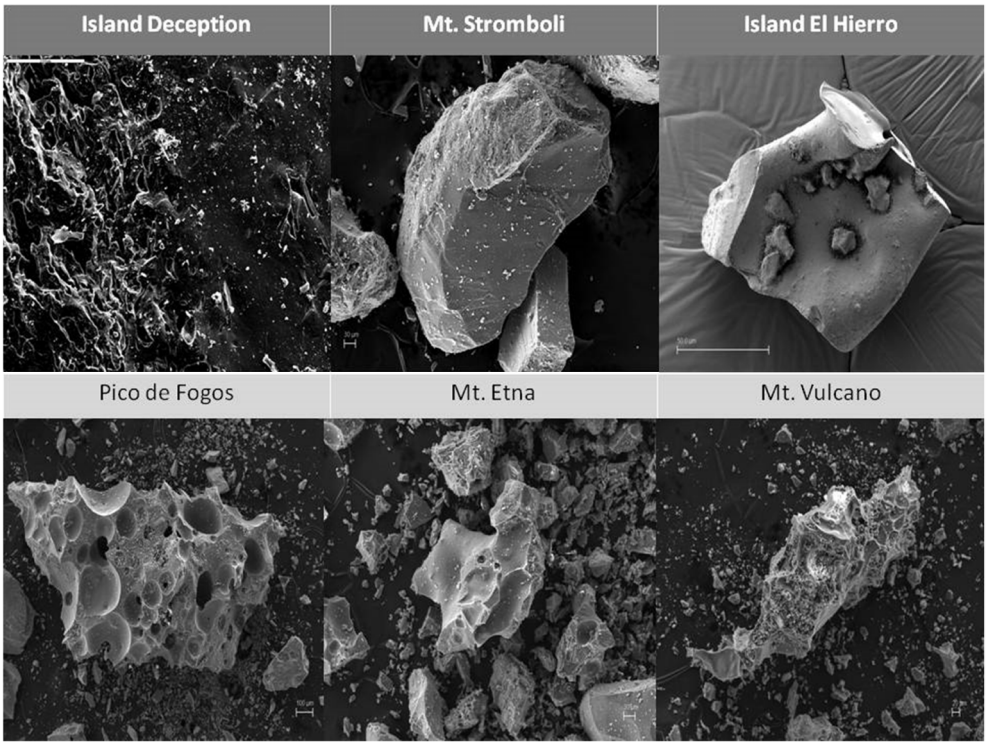


**Figure 2**. SEM images of samples.

*Zeta Potential.*

In Figure 3, we show ξ for different pH values at constant ionic strength of 1 mM of NaCl.

We see that in general, the ashes have negative charge over the entire range of pH studied. Such behavior can be attributed to the majority component $SiO_2$ with negative charge. For Fogo, ξ was positive for the smallest pH values. As pH increased, all the studied ashes showed ξ increases (in absolute value), probably because of the absorption of hydroxyl groups at the surface of the particles. The increase of ξ in absolute value was largest for Fogo (56 mV) and smallest for Deception (22.6 mV).

Although all samples increased their absolute value of electric charge with increase of pH of the medium, not all did it in the same way or in the same amount. Thus, there were steep slopes of the ξ curve for Fogo, El Hierro, Etna and Stromboli, and flatter slopes for Deception Island and Mt. Vulcano. Generally, the gentle slopes correspond with ashes that that were expelled during a more violent eruption (type III/IV, (vulcanian/phreatomagmatic) or with a more hanging discharge in eruptions I/II (Hawaiian/strombolian). If we analyze more closely the ξ data, we see that at pH 3 there is an increase of ξ with the silica concentration, confirming that the $SiO_4^{4-}$ groups conferred negative charge to the volcanic materials.

Another interesting finding that can be drawn from Figure 3 is that at basic pH, the electrostatic repulsion between particles constituting the deposit is minimal, so cohesion must be maximized.

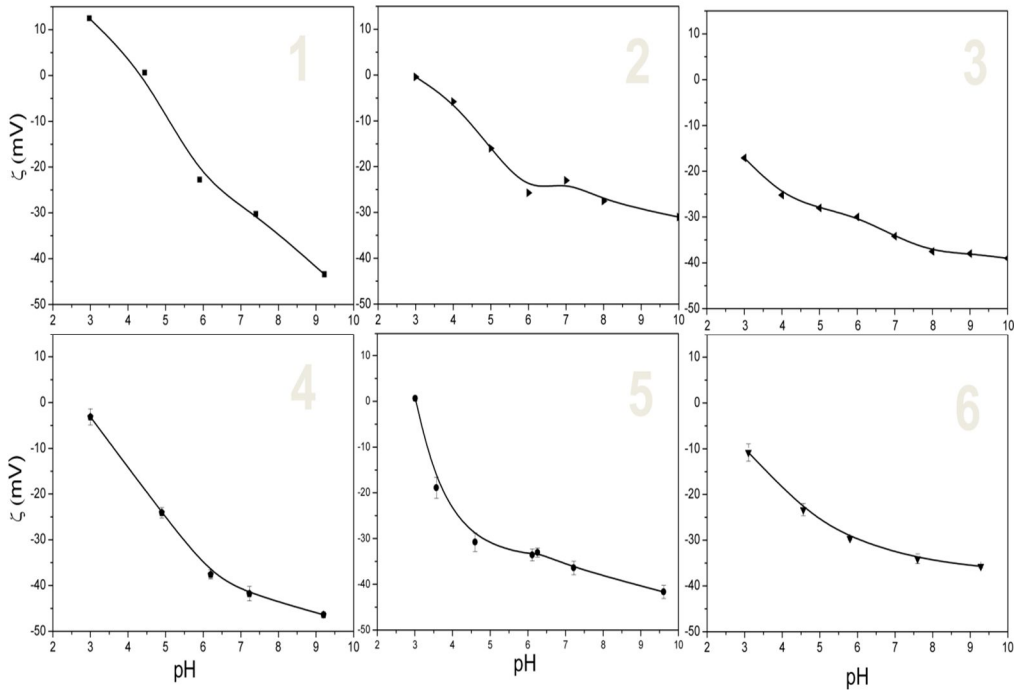


**Figure 3**. Zeta potential of samples (1=Fogo peak, 2=El Hierro, 3= Deception, 4= Etna, 5=Stromboli, 6=Vulcano) as function of pH value for 1mM concetrations of NaCl.

*Surface free energy*

Table 4 shows values of the components of surface free energy in the samples. From analysis of the dispersive component $\gamma^{LW}$, we see that the values are between those for Fogo Island (the maxima) at 71.6 ± 2 mJ/m$^2$ and those for El Hierro Island at 35.2 ± 2 mJ/m$^2$. This indicates that El Hierro material had a more ordered structure of water molecules at the solid–liquid interface.

However, from analysis of the AB components, we see that in general, the eruptive material was essentially monopolar ($\gamma^+ \approx 0$) and electron donor ($\gamma^- > 0$) in character. Given that a material is considered hydrophobic when its electron-acceptor ($\gamma^-$) component is null and its electron-donor component ($\gamma^-$) has values < 28.2 mJ/m$^2$, the samples of eruptive materials from the Stromboli, Etna and Fogo peak volcanoes had a hydrophilic character (strong water retention), because their component electron-donor had values > 50 mJ/m$^2$. However, materials from El Hierro and Vulcano had a less hydrophilic character ($\gamma^-$ < 40 mJ/m$^2$). Deception Island, with $\gamma^- = 28.8 \pm 0.7$ mJ/m$^2$, showed an essentially hydrophobic character.

**Table 4.** Values of LW component $\gamma^{LW}$, electron-acceptor $\gamma^-$ and electron-donor $\gamma^+$ parameters of AB component of surface free energy for samples

| Samples\ SFE | $\gamma^{LW}$(mJ/m$^2$) | $\gamma^-$(mJ/m$^2$) | $\gamma^+$(mJ/m$^2$) | $\gamma^{TOT}$(mJ/m$^2$) |
|---|---|---|---|---|
| **El Hierro** | 35.2±2 | 34.6±3 | 3.78±0.6 | 35.2±2 |
| **Pico do Fogo** | 71.6±2 | 52.42±3 | 1.1±0.3 | 86.987 |
| **Etna** | 52.3±2 | 62.87±3 | 0.21±0.3 | 59.674 |
| **Vulcano** | 62.847±2 | 37.85±3 | 1.0936±0.3 | 75.715 |
| **Stromoboli** | 50.213±2 | 70.072±3 | 0.002±0.3 | 51.046 |
| **Deception** | 46.2±0.3 | 28.8±0.7 | 0.326±0.003 | 52.3±0.5 |

*Energy of interaction.*

The result of interaction between the particles composing the deposit is the sum of the electric, dissipative and non-dispersive contributions.

Figures 4 and 5 show interaction energies between the ash particles composing the deposit, which are a function of the previously calculated parameters, ξ and surface free energy components. This interaction energy is presented for two opposite pH situations: one for a very acidic environment, pH = 3 (Figure 5), and the other basic one with pH = 8 (Figure 4). Figures 4–5 show the total energy between particles as a function of distance calculated from the extended DLVO theory the data from Table 5.

In Figure 4 we see that at basic pH (= 8), important barriers of potential appear, so there is net repulsion between the particles that make up the substrate, i.e., weak cohesion and therefore instability. However, if we examine the behavior from an acid perspective (Figure 5), the barriers of energy show a different situation; almost half the ashes have one value < 50 kT for 10 nm of distance (El Hierro, Stromboli and Etna), indicating greater cohesion in this group of ashes and *a priori* stable.

Finally, upon determining the difference between the values of energy between pH 8 (maximum) and pH 3 (minimal), we obtain an approximate measure of the range of variation of the samples based on the environmental pH. This information is listed in Table 5. From this, one sees that Etna and Stromboli ashes were more dependent on pH and those from the sample at El Hierro were less dependent. It appears logical to conclude that the ashes of El Hierro from the last 10,000 years had sufficient time such that the minerals were dependent on pH, whereas already weathered minerals were less dependent. In contrast, for the more recent ashes (Etna and Stromboli), this process of weathering has not been possible.

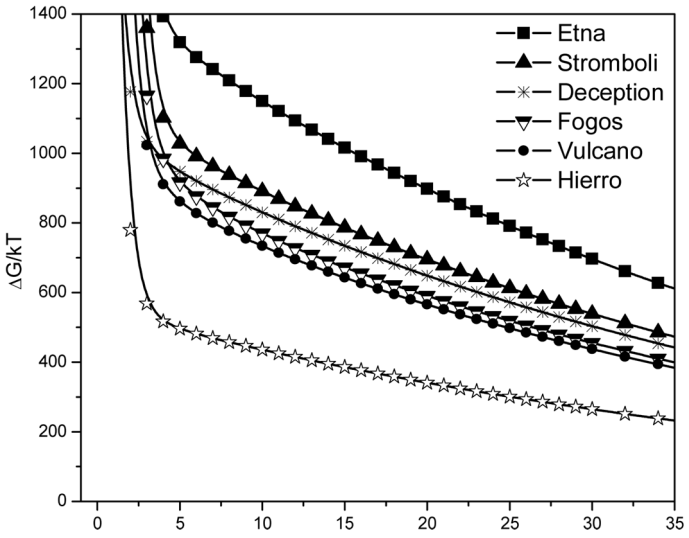


**Figure 4**. Total energy of interaction (in kT) between particles as function of distance between surfaces, H, for eight pH values and ionic strength when electrolyte present in solutions was 1 mM NaCl.

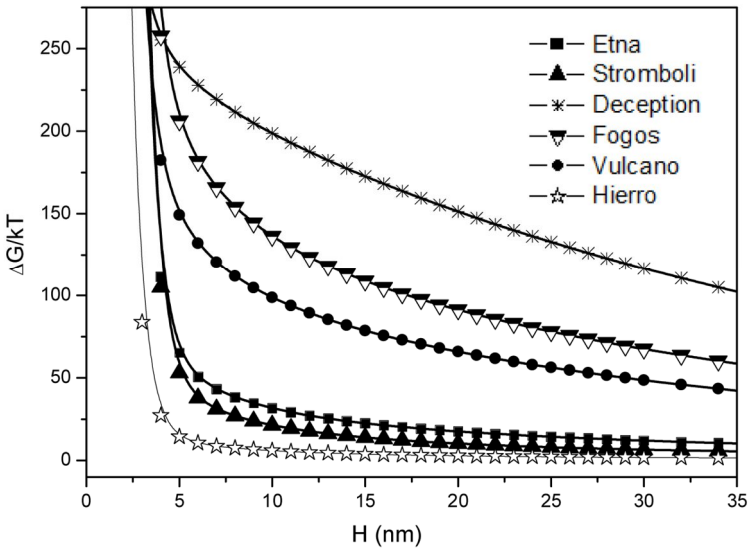


**Figure 5**. Total energy of interaction (in kT) between particles as function of distance between surfaces, H, for three pH values and ionic strength when electrolyte present in solutions was 1 mM NaCl.

**Table 5. (A)** Parameters used to calculate potential energy of interaction between particles (zeta potential is ζ)

| Volcanoes | Etna | Stromboli | Fogos | Deception | Vulcano | El hierro |
|---|---|---|---|---|---|---|
| **(ζ) pH 3** | −2.6 | +1 | +12.5 | −17.5 | −11 | −1 |
| **(ζ) pH 8** | −42.5 | −36.5 | −32.5 | −36 | −32.5 | −26 |

**Table 5. (B)** Values of energy kT at 10 nm (H) for pH 3 and pH 8 and their difference

| Volcanoes | Etna | Stromboli | Fogos | Deception | Vulcano | El Hierro |
|---|---|---|---|---|---|---|
| **Values\Age(a)** | 2014 | 2014 | 1995 | 1969-70 | 1885 | 10.000aC |
| **pH 8** | 1157 | 913 | 776 | 829 | 708 | 419 |
| **pH 3** | 33.6 | 21.1 | 134 | 200 | 98 | 4.6 |
| **(pH8−pH3)** | 1123.4 | 891.9 | 642 | 629 | 610 | 414.4 |

- **Conclusions**

- The combined study of electrical and thermodynamic properties of eruptive material facilitated determination of the cohesion of the deposits, and of how this cohesion changed with environmental conditions
- The chemical analyses and morphology of the samples revealed the type of volcanism, the eruptive character, and the eruptive episodes
- The ξ analysis showed that all the eruptive material studied had a negative charge in aqueous solution, owing to the generally large percentage of silica contained
- The surface free energy study showed that values were between those indicating a hydrophobic character of the deposit (little water retention),

such as at Deception Island, and those representing hydrophilicity as at Fogo. The hydrophilic character was the most common in our samples.

- The calculation of interaction energy showed that cohesion in the deposits varied with the volcano analyzed, and that this cohesion changed drastically with the pH of the medium.

## References

Ancochea, E., Fuster, J., Ibarrola, E., Cendrero, A., Coello, J., Hernan, F., ... & Jamond, C. (1990). Volcanic evolution of the island of Tenerife (Canary Islands) in the light of new K-Ar data. Journal of Volcanology and Geothermal Research, 44(3), 231-249.

Andronico D, Branca S, Calvari S, Burton M, Caltabiano T, Corsaro R A, Del Carlo P, Garfi G, Lodato L, Miraglia L, Mure F, Neri M, Pecora E, Pompilio M, Salerno G, Spampinato L, 2005. A multi-disciplinary study of the 2002-03 Etna eruption: insights into a complex plumbing system. Bull Volc, 67: 314-330.

Arrighi S, Tanguy J-C, Rosi M, 2006. Eruptions of the last 2200 years at Vulcano and Vulcanello (Aeolian Islands, Italy) dated by high-accuracy archeomagnetism. Phys Earth Planet Int, 159: 225-233.

Bailey, S. W., Brousseau, P. A., McGuire, K. J., & Ross, D. S. (2014). Influence of landscape position and transient water table on soil development and carbon distribution in a steep, headwater catchment. Geoderma, 226, 279-289.

Barbano, M. S., Pappalardo, G., Pirrotta, C., & Mineo, S. (2014). Landslide triggers along volcanic rock slopes in eastern Sicily (Italy). Natural Hazards, 73(3), 1587-1607.

Baumgarten, W., Dörner, J., & Horn, R. (2013). Microstructural development in volcanic ash soils from South Chile. Soil and Tillage Research, 129, 48-60.

Beccaluva, L., Civetta, L., Macciotta, G. I. A. M. P. A. O. L. O., & Ricci, C. A. (1985). Geochronology in Sardinia: results and problems. Rend. Soc. It. Min. Petr, 40, 57-72.

Beccaluva, L., Gabbianelli, G., Lucchini, F., Rossi, P. L., & Savelli, C. (1985). Petrology and K/Ar ages of volcanics dredged from the Eolian seamounts: implications for geodynamic evolution of the southern Tyrrhenian basin. Earth and Planetary Science Letters, 74(2), 187-208.

Behncke, B., Falsaperla, S., & Pecora, E. (2009). Complex magma dynamics at Mount Etna revealed by seismic, thermal, and volcanological data. *Journal of Geophysical Research: Solid Earth*, *114*(B3).

Bertagnini, A., Di Roberto, A., & Pompilio, M. (2011). Paroxysmal activity at Stromboli: lessons from the past. Bulletin of volcanology, 73(9), 1229-1243.

Branca, S., Coltelli, M., & Groppelli, G. (2004). Geological evolution of Etna volcano. Mt. Etna: volcano laboratory, 49-63.

Capra, L., Lugo-Hubp, J., & Dávila-Hernández, N. (2003). Fenómenos de remoción en masa en el poblado de Zapotitlán de Méndez, Puebla: relación entre litología y tipo de movimiento. Revista mexicana de ciencias geológicas, 20(2), 95-106.

Carracedo, J. C., Pérez Torrado, F. J., Ancochea, E., Meco, J., Hernán, F., Cubas, C. R., ... & Ahijado, A. (2002). Cenozoic volcanism II: the Canary islands. Geological Society of London.

Chibowski, E., & Holysz, L. (1992). Use of the Washburn equation for surface free energy determination. Langmuir, 8(2), 710-716.

del Potro, R., & Hürlimann, M. (2008). Geotechnical classification and characterisation of materials for stability analyses of large volcanic slopes. *Engineering Geology*, 98(1), 1-17.

Dionis, SM; Melián, G; Rodríguez, F; Hernández, PA; Padrón, E; Pérez, NM; Barrancos, J; Padilla, G; Sumino, H; Fernandes, P; Bandomo, Z; Silva, S; Pereira, J; Semedo, H, 2015, Diffuse volcanic gas emission and thermal energy release from the summit crater of Pico do Fogo, Cape Verde, 27 January 2015, Bulletin of Volcanology.

Duran, J. D. G., Ontiveros, A., Delgado, A. V., & Gonzalez-Caballero, F. (1998). Kinetics and interfacial interactions in the adhesion of colloidal calcium carbonate to glass in a packed-bed. *Applied surface science*, *134*(1), 125-138.

Ferrari, L., & Manetti, P. (1993). Geodynamic framework of the Tyrrhenian volcanism: a review. Acta Vulcanol, 3, 1-10.

Gimmi, T., & Kosakowski, G. (2011). How mobile are sorbed cations in clays and clay rocks?. Environmental science & technology, 45(4), 1443-1449.

Gregory, J. (1981). Approximate expressions for retarded van der Waals interaction. Journal of Colloid and Interface Science, 83(1), 138-145.

Guillou, H., Carracedo, J.C., Torrado, F.P., and Badiola, E.R., 1996, K-Ar ages and magnetic stratigraphy of a hotspot-induced, fast grown oceanic island: El Hierro, Canary Islands, Journal of Volcanology and Geothermal Research, v. 73, no. 1-2, pp. 141-155.

Hernández, PA; Melián, G; Dionis, SM; Barrancos, J; Padilla, G; Padrón, E; Silva, S; Fernandes, P; Cardoso, N; Pérez, NM; Rodríguez, F; Asensio-Ramos, M; Calvo, D; Semedo, H; Alfama, V, 2015, Chemical composition of volcanic gases emitted during the 2014-15 Fogo eruption, Cape Verde, EGU General Assembly 2015

Holtz, R. D., & Kovacs, W. D. (1981). An introduction to geotechnical engineering (No. Monograph).

Hornig-Kjarsgaard I, Keller J, Koberski U, Stadlbauer E, Francalanci L, Lenhart R, 1993. Geology, stratigraphy and volcanological evolution of the island of Stromboli, Aeolian arc, Italy. Acta Vulc, 3: 21-68.

Kadar, E., Fisher, A., Stolpe, B., Calabrese, S., Lead, J., Valsami-Jones, E., & Shi, Z. (2014). Colloidal stability of nanoparticles derived from simulated cloud-processed mineral dusts. Science of the Total Environment, 466, 864-870.

Kelly, L. C., Cockell, C. S., Piceno, Y. M., Andersen, G. L., Thorsteinsson, T., & Marteinsson, V. (2010). Bacterial diversity of weathered terrestrial Icelandic volcanic glasses. *Microbial ecology*, *60*(4), 740-752.

Lentini, F. (1982). The geology of the Mt. Etna basement, Mem. Soc. Geol. Ital, 23, 7-25.

Marti J, Baraldo A, 1990. Pre-caldera pyroclastic deposits of Deception Island (South Shetland Islands). Antarctic Sci, 2: 345-352.

Masson, D. G., Le Bas, T. P., Grevemeyer, I., & Weinrebe, W. (2008). Flank collapse and large-scale landsliding in the Cape Verde Islands, off West Africa. Geochemistry, Geophysics, Geosystems, 9(7).

Ontiveros-Ortega, A., Espinosa-Jiménez, M., Chibowski, E., & González-Caballero, F. (1998). Effect of tannic acid on the surface free energy of cotton fabric dyed with a cationic dye. Journal of colloid and interface science, 202(1), 189-194.

Ontiveros-Ortega, A., Moleon, J. A., Plaza, I., & Guillén, C. (2016). Effect of interfacial properties on mechanical stability of ash deposit. Journal of Rock Mechanics and Geotechnical Engineering, 8(2), 187-197.

Ontiveros-Ortega, A., Vidal, F., Gimenez, E., & Ibáñez, J. M. (2014). Effect of heavy metals on the surface free energy and zeta potential of volcanic glass: implications on the adhesion and growth of microorganisms. Journal of Materials Science, 49(9), 3550-3559.

Pallàs, R., Smellie, J. L., Casas, J. M., & Calvet, J. (2001). Using tephrochronology to date temperate ice: correlation between ice tephras on Livingston Island and eruptive units on Deception Island volcano (South Shetland Islands, Antarctica). The Holocene, 11(2), 149-160.

Paris, R., Giachetti, T., Chevalier, J., Guillou, H., & Frank, N. (2011). Tsunami deposits in Santiago Island (Cape Verde archipelago) as possible evidence of a massive flank failure of Fogos volcano. Sedimentary Geology, 239(3), 129-145.

Plaza, I., Ontiveros-Ortega, A., Calero, J., & Aranda, V. (2015). Implication of zeta potential and surface free energy in the description of agricultural soil quality: Effect of different cations and humic acids on degraded soils. *Soil and Tillage Research*, *146*, 148-158.

Roobol M J, 1973. Historic volcanic activity at Deception Island. Brit Antarctic Surv Bull, 32: 23-30.

Roobol M J, 1979. A model for the eruptive mechanism of Deception Island from 1820 to 1970. Brit Antarctic Surv Bull, 49: 137-156.

Scollo, S., Cottelli, M., Prodi, F., Folegani, M., & Natali, S. (2005). Solid Earth-L10302-Terminal settling velocity measurements of volcanic ash during the 2002-2003 Etna eruption by an X-band microwave rain gauge disdrometer (DOI 10.1029/2004GLO22100). Geophysical Research Letters, 32(10).

Siebert, L., Simkin, T., and Kimberly, P., 2010, Volcanoes of the World, Third Edition, Smithsonian Institution, Washington, D.C., and University of California Press, Berkeley, 551 pp.

Smellie, J. L. (2001). Lithostratigraphy and volcanic evolution of Deception Island, South Shetland Islands. Antarctic Science, 13(02), 188-209.

Smoluchowski, M. V. (1921). Elektroosomosis. Handbuch der Elektrizitaet und des Magnetismus, Barth Verlag, Leipzig, 366.

Thouret, J. C., Wörner, G., Gunnell, Y., Singer, B., Zhang, X., & Souriot, T. (2007). Geochronologic and stratigraphic constraints on canyon incision and Miocene uplift of the Central Andes in Peru. *Earth and Planetary Science Letters*, *263*(3), 151-166.

Tinti, S., & Piatanesi, A. (1996). Numerical simulations of the tsunami induced by the 1627 earthquake affecting Gargano, Southern Italy. *Journal of Geodynamics*, *21*(2), 141-160.

Van Oss, C. J. (1994). Polar or Lewis acid-base interactions. Interfacial forces in aqueous media, 18-46.

Van Oss, C. J. (1994). Polar or Lewis acid-base interactions. *Interfacial forces in aqueous media*, 18-46.

Van Oss, C. J., Chaudhury, M. ArrighiK., & Good, R. J. (1988). Interfacial Lifshitz-van der Waals and polar interactions in macroscopic systems. Chemical Reviews, 88(6), 927-941.

Van Oss, C. J., Ju, L., Chaudhury, M. K., & Good, R. J. (1989). Estimation of the polar parameters of the surface tension of liquids by contact angle measurements on gels. Journal of Colloid and Interface Science, 128(2), 313-319.

Visser, J. (1976). The adhesion of colloidal polystyrene particles to cellophane as a function of pH and ionic strength. Journal of Colloid and Interface Science, 55(3), 664-677.

Voight, B., & Elsworth, D. (1997). Failure of volcano slopes. Geotechnique, 47(1), 1-31.

Washburn, E. W. (1921). The dynamics of capillary flow. Physical review, 17(3), 273.

Weaver S D, Saunders A D, Pankhurst R J, Tarney J, 1979. A geochemical study of magmatism associated with the initial stages of back-arc spreading. Contr Mineral Petr, 68: 151-169.

## 5.3. Aplicación de modelos DLVO-Extendida a suelos de olivar de Andalucía con diferentes materiales originales.

### *5.3.1 Implication of zeta potential and surface free energy in the description of agricultural soil quality: effect of different cations and humic acids on degraded soils.*

*Resumen*

Los suelos se consideran la capa más activa de la superficie de la tierra, juega un papel crucial en los ciclos geoquímicos de los sistemas terrestres. La estructura del suelo es un factor clave en la calidad del suelo, ya permite que el suelo pueda desempeñar con eficacia sus funciones de regulación de los flujos de agua y gases, agua y almacenamiento de nutrientes, penetración y crecimiento de raíces, entre otros. Los suelos pueden ser vistos como una mezcla heterogénea de partículas primarias (arena, limo y arcilla), que se organizan en varios niveles jerárquicos de complejidad por medio de procesos de interfaz que enlazan estas partículas, tales como la agregación o floculación. Uno de los principales procesos de degradación de la calidad del suelo es la degradación estructural que se describe en los suelos agrícolas.

El objetivo de este trabajo fue el de analizar el comportamiento coloidal de material del suelo que afecta al desarrollo estructural de un perfil agrícola en relación con la composición del suelo y de la estructura.

De nuestro análisis mineralógico, se obtuvo que el suelo examinado tenía una textura arcillosa y su contenido de carbono orgánico muy bajo (0,40%) y que el mineral más abundante es la esmectica. Las imágenes SEM mostraban diferentes unidades estructurales a diferentes escalas (macroagregados, microagregados y cluster de arcilla y dominios). Esta estructura se dispersó y desordenó bajo tratamientos diferentes, de manera muy significativa en tratamiento $H_2O_2$ y parcialmente bajo tratamientos HA.

Los resultados de potencial zeta ($\zeta$) en soluciones de NaCl y $CaCl_2$ mostraban un valor negativo en todo el rango de pH medido. El estudio del efecto que produce el peróxido de hidrógeno en el suelo, puso de manifiesto y confirmo, la protonación de materia orgánica del suelo nativo. El aumento de $\zeta$ del suelo a pH básico, fue más significativo cuando el suelo contiene materia orgánica natural, confirma el carácter mordiente de esa materia en suelo nativo. Sin embargo, la adsorción de HAs del tipo usado en el presente trabajo puede alterar la estructura del suelo, el desarrollo estructura y el comportamiento y, por tanto, la calidad del suelo.

Los resultados de energía libre de superficie muestran que el material del suelo es esencialmente monopolar y donador de electrones en la naturaleza. Contrariamente, la adsorción de materia orgánica disminuye el carácter hidrófilo del suelo, debido a la variación principalmente debido en los componentes polares.

# Articulo Cientifico

# IMPLICATION OF ZETA POTENTIAL AND SURFACE FREE ENERGY IN THE DESCRIPTION OF AGRICULTURAL SOIL QUALITY: EFFECT OF DIFFERENT CATIONS AND HUMIC ACIDS ON DEGRADED SOILS.

## Revista científica:

## Soil and Tillage

Soil & Tillage Research 146 (2015) 148–158

Contents lists available at ScienceDirect

Soil & Tillage Research

journal homepage: www.elsevier.com/locate/still

# Implication of zeta potential and surface free energy in the description of agricultural soil quality: Effect of different cations and humic acids on degraded soils

I. Plaza [a], A. Ontiveros-Ortega [a,c,*], J. Calero [b], V. Aranda [b]

[a] Department of Physics, University of Jaén, Campus Universitario de las Lagunillas s/n, Edificio A-3, 23071 Jaén, Spain
[b] Department of Geology, University of Jaén, Campus Universitario de las Lagunillas s/n, Edificio A-3, 23071 Jaén, Spain
[c] Instituto Andaluz de Geofísica, University of Granada, 18071 Granada, Spain

ARTICLE INFO

*Article history:*
Received 24 March 2014
Received in revised form 9 October 2014
Accepted 17 October 2014

*Keywords:*
Zeta potential
Surface free energy
Smectites
Soil structure stability
Soil organic matter adsorption

ABSTRACT

Here we present results of our study about the effect of natural organic matter in the adsorptions processes of commercial humic acid (HA) on the physicochemical properties, stability, and structure of an agricultural olive soil. Our soil belongs to the loamy texture class and gives a medium-low chemical fertility. Its organic carbon content is very low (0.40%), which could be explained by the Mediterranean climate type in which the soil developed. From the fine earth mineralogy, we conclude that smectite was the most abundant mineral in our soil.

We first demonstrated that HA effectively adsorbs onto soil, mainly at basic pH. Electrophoresis measurements of soil particle suspensions as a function of pH in the presence and absence of humic acid clearly demonstrate the adsorption of negatively charged entities onto smectite in the soil. This effect is more significant when the soil contains natural organic matter, which confirms the mordant character of this matter in native soil.

Analysis of surface free energy components leads to the conclusion that humic acid molecules impart a significant electron donor character to the soil particles, which in turn decreases their hydrophilicity. All collected data were used to interpret the final soil structure. Our results are consistent with fabric images obtained by scanning electron microscopy of natural samples that present the major aggregation state. Interpretation of these results can be explained by a combination of electrical and thermodynamic interaction, electrostatic forces, double-layer repulsion, van der Waals attraction, and hydrophilic/hydrophobic repulsion/attraction.



## 1. Introduction

Soils are considered the most active layer of the earth surface, playing a crucial role in the geochemical cycles of earth systems (Bockheim and Gennadiyev, 2010), including the fixation of carbon dioxide from the atmosphere (Lal, 2007). Therefore, assuring a good quality of soil can be considered of vital importance for the future.

Soil structure is a key factor of soil quality (Kay and Grant, 1996), and permits the soil to properly carry out its ecosystem functions of regulating water and gases fluxes, water and nutrient storage, root penetration and growth, and others. Soil structure can be defined as the arrangement of primary mineral and organic particles of soil into secondary units called aggregates (Dexter, 1988). Therefore, soils can be seen as a heterogeneous mixture of primary particles (sand, silt and clay), which are organized at several hierarchical levels of complexity by means of interface processes that link these particles, such as aggregation or flocculation (Dexter, 1988). Thus, soil structure is a complex attribute with several functional (e.g., aggregate stability index of Kemper and Rosenau, 1986) and morphological (e.g., soil fabric; Holtz and Kovacs, 1981) aspects. One of the main soil quality degradation processes is the structural decay found in agricultural soils (Bronick and Lal, 2005). In many cases, this can be attributed to the colloidal dispersion of particles and rupture of aggregates (Marchuk and Rengasamy, 2011), both reflected in the loss of aggregate stability and fabric ordering (Oades and Waters, 1991).

Aggregation largely depends on soil composition. Primary soil particles differ not only in size but also in composition. Less stable

* Corresponding author at: Department of Physics, University of Jaén, Campus Universitario de las Lagunillas s/n, Edificio A-3 Dep. 414., 23071 Jaén, Spain. Tel.: +34 953212830.
*E-mail address:* aontiver@ujaen.es (A. Ontiveros-Ortega).

http://dx.doi.org/10.1016/j.still.2014.10.013
0167-1987/

minerals, as carbonates and feldspars, tend to accumulate in the larger fractions sand and silt (2–2000 μm) (Karathanasis, 2002). These are relatively inactive from a physicochemical point of view, owing to their low surface area and charge. By contrast, the clay fraction (<2 mm) concentrates the most active soil material, such as phyllosilicates, metal oxyhydroxides and humic substances. Because of its small size (2 μm to less than 100 nm nanoparticles) and larger surface area, the clay fraction can be considered the colloidal soil fraction (Jiang et al., 2012). This is a critical fraction for soil structure development (Bronick and Lal, 2005).

It is widely recognized (Tiller and O'Melia, 1993; Ramos-Tejada et al., 2003) that the physicochemical properties (mainly colloidal stability and wettability) of colloidal soil materials appear to be controlled by adsorption of natural organic matter and metal cations present in natural waters. Among the inorganic substances that constitute soils, interfacial properties are strongly determined by the adsorption of humic substances generated by decomposition of biomass (Sondi and Pravdic, 2002). Colloidal interactions between mineral particles are controlled by a variety of attractive and repulsive interparticle forces, which can be modified by the adsorption of metal cations and organic polyelectrolytes present in solution (Durán et al., 2000; Ramos-Tejada et al., 2001). The most important of these forces are electrostatic double-layer repulsion, van der Waals attraction and hydrophilic/hydrophobic repulsion/attraction. These are considered together in the so-called extended DLVO theory of colloidal stability (Israelachvili, 1991; Van Oss, 1994). The determination of interfacial interactions requires knowledge of the interface properties. Consequently, electrical and thermodynamic characterization of a soil solid–liquid interface is important with regard to flocculation processes and soil structure formation at the lower size level of aggregation (Tisdall and Oades, 1982). Surface properties, including wettability, adsorption or adhesion phenomena, depend to a large extent on the surface free energy changes involved. Although colloidal systems are often complex in nature, it has been repeatedly shown (Van Oss, 1994; Ohshima, 2002) that combined analysis of electrokinetic, adsorption and thermodynamic properties can provide extensive information about interactions at the solid–liquid interface.

The aim of this work is to analyze the colloidal behavior of soil material that affects structural development of an agricultural profile as related to soil composition and fabric, using this term to mean the spatial organization of the soil at the scanning electron microscopy (SEM) scale. For this purpose, we studied the effect of electrolyte adsorption on the electric (surface potential) and thermodynamic (surface free energy) interfacial properties of aqueous soil particle suspensions. Electrical properties were assessed by studying the zeta potential ($\zeta$) of the soil, and how this parameter changes in the presence of different ionic species in the liquid phase. Second, thermodynamic characterization of the soil–solution interface was done by comparing the surface free energy of natural soil versus samples containing absorbed cations and humic acids.

## 2. Material and methods

### 2.1. Materials

#### 2.1.1. Chemical

All the reagents and chemicals used were of analytical grade (Merck KGaA and Sigma–Aldrich Co., LLC, Germany). Water for surface free energy determination was twice-distilled, and Milli-Q

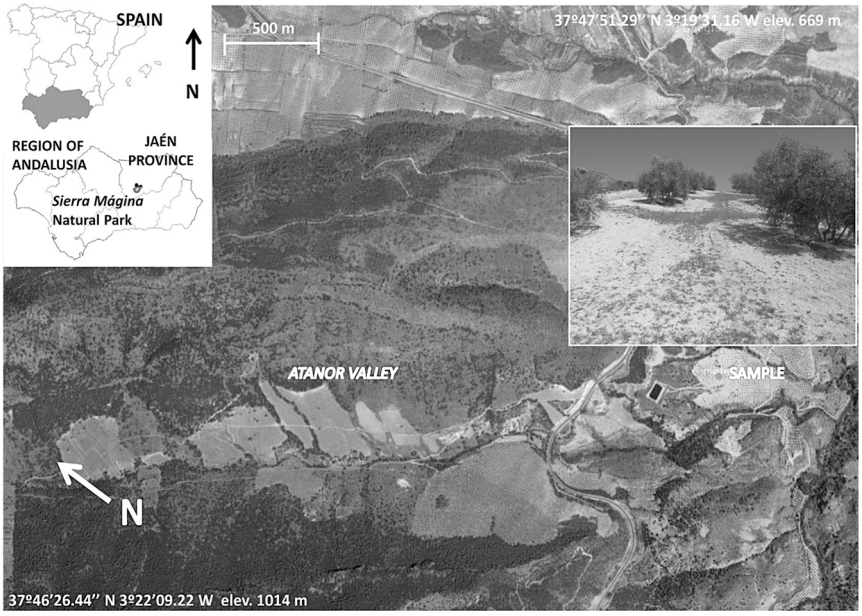


**Fig. 1.** Location of the study area. Inserted photography: olive grove and soil sampled.

reagent-grade water was used for electrokinetic measurements. Solution pH was adjusted by adding a reagent-grade solution of either NaOH or HCl. Commercial humic acid (HA) solutions were prepared by dissolving in sodium salt (Sigma–Aldrich). The chemical composition of Aldrich sodium humate was analyzed 15 years ago by Ochs et al. (1994). They found that the molecular weight distribution had two peaks, at 1000 and 5000 g/mol. These authors also reported an elementary analysis of Aldrich humic acid. Nevertheless, the chemical composition of this commercial humic material has changed over the years, and the manufacturer's present certificate of analysis specifies the following composition (in %): C: 39.03, H: 4.6, N: 0.61, S: 0.957, Na: 8.7, Ca: 1.4, Fe: 0.557; Si: 0.803; Ba, Cr, Cu, Ga, Li, Mg, Mn, K, Sr, Ti, V, Zr: <0.5. The chemical composition of humic substances depends to a large extent on origin and treatment. These components can be considered as a mixture of structural elements, but the general formula of an HA substances, bearing carboxylic and phenolic as the main ionizable groups, can be found in the literature (Jones and Bryan, 1998).

*2.1.2. Sample collection site and culture description*

Soil was collected at Atanor Valley in the province of Jaén, southern Spain (37°46′58.81″N 3°19′54.61″W; 671 m above sea level; Fig. 1). The soil had a shallow profile (20-cm thickness) with an Ap-C horizon sequence, and was classified as Haplic Regosol (FAO, 2006). The sample was taken from 0 to 5 cm depths, corresponding to the Ap horizon. The soil developed over Jurassic marls and was subject to olive cultivation for more than 30 years. Conventional soil management is characterized by plowing 3–5 times per year to depths 15–20 cm from early spring to early autumn, weed control with residual herbicides, and annual application of ammonium sulfate (300 Kg $ha^{-1}$). As many of the conventional olive grove soils in the South of Spain, they showed degradation features, as organic matter losses and erosion in the surface horizons (Fig. 1).

*2.1.3. Sample treatment with hydrogen peroxide and commercial humic acid*

The bulk sample collected in the field was dried and gently sieved through a 2-mm mesh screen, to obtain the soil fine earth fraction (<2 mm). From there, four samples were obtained (natural, $H_2O_2$-treated, natural plus HA, and $H_2O_2$-treated plus HA), following the methodological scheme shown in Fig. 2.

First, to eliminate natural organic matter for $H_2O_2$ samples, 100 ml of water was added over 10 g of fine earth, and this suspension was heated at 70–80 °C. Hydrogen peroxide was then added in 20-ml fractions at 20-min intervals. This process was repeated with continuous mechanical stirring until there was no observed release of $CO_2$, and then dried.

The adsorption of HA onto the natural and $H_2O_2$ treated samples was performed in a HA solution at 0.5 g/l concentration, equilibrated with an electrolyte solution over a 24-h period and dried.

## 3. Methods

### 3.1. Zeta potential

The fine earth fraction of soil material used in our experiments was re-dispersed in different aqueous solutions. For the electrophoresis experiment, to determine the $\zeta$ of the system, the supernatants of the suspension ($\leq$10 μm) were used. Electrokinetic properties of the studied systems were analyzed with a Zetasizer 3000HS (Malvern Instruments, Worchestershire, UK), based on electrophoretic mobility measurements. For each treatment, the samples were conditioned for 24 h in 1000 ml of solution at required concentrations for different electrolytes, as described below.

For electrical characterization, $\zeta$ was calculated based on the Smoluchowski relationship, using the following equation.

$$\xi_{EP} = \frac{V\mu}{\varepsilon E_x}, \quad (1)$$

where $\xi_{EP}$ is the electrophoretic $\zeta$ (mV), $V$ the electrophoretic velocity (Cm/s), $\mu$ and $\varepsilon$ the viscosity (Cp) and permittivity of the aqueous medium in standard conditions, respectively, and $E_x$ is the axial electric field. The Smoluchowski equation is a simplified approach in which the electrostatic driving force is opposed by the frictional force, and other effects are neglected. The Smoluchowski equation is valid for solid particles with large dimensionless inverse Debye length (Wang and Revil, 2010). This equation gives good results only for large colloidal particles and high ionic

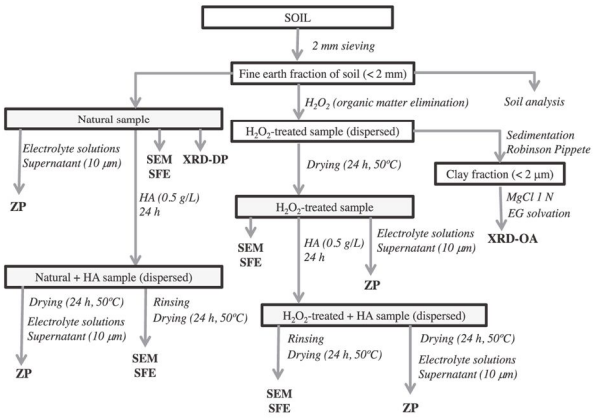


**Fig. 2.** Scheme of the methodological steps followed for the sample treatments. ZP: zeta potential; SEM: scanning electron microscopy; SFE: surface free energy; XRD-DP: X-ray diffraction (disoriented crystalline powder); XRD-OA: X-ray diffraction (oriented aggregate); EG: ethylene glycol; HA: humic acid.

strengths, when the $\zeta$ is not high. For $\zeta$ values with a practical meaning (<120 mV), the error is negligible when $\kappa a > 100$, where $a$ is the particle radius and the Debye parameter $\kappa$ is defined as

$$\kappa = \sqrt{\frac{F^2 \sum_i C_i Z_i^2}{\varepsilon RT}} \quad (2),$$

where $F$ is the Faraday constant, $C_i$ is concentration of the $i$-th ion (in mol/m$^3$), $Z$ is the valency of this ion, ε represents the dielectric permittivity, $R$ is the gas constant, and $T$ is absolute temperature. In our experiments, we worked under conditions in which the Smoluchowski approximation was acceptable, namely, particle size one micrometer and ionic strength 1 mM, a situation for which $\kappa a > 100$.

### 3.2. Surface free energy determination

To estimate the surface free energy of the studied soil samples, we measured advancing contact angles of three probe liquids (diiodomethane, water and formamide) with known surface tension components on dry pellets. An NRL C.A. goniometer (Ramé–Hart Inc.,-New Jersey, USA) was used for the measurements. Images of drops placed on the surface were captured with a video camera adapted to the goniometer, immediately after their deposition with a micrometer syringe (Gilmont Instruments, USA). Prior to contact angle measurement, the soil samples were dried at 75 °C and kept in a desiccator. Only stable drops were used to compute surface free energy components of the solids. The contact angles of water, formamide, and diiodomethane were measured on pellets made of this material. The pellets were made by compressing dried soil samples under $1.5 \times 10^4$ kg/cm$^2$ for 10 min. Only pellets having a smooth, specular surface (at the optical microscope level) were selected. The contact angle was recorded immediately after depositing the drop on the pellets.

Detailed descriptions of this approach to surface free energy formulation have been given in numerous papers (e.g., Van Oss, 1994; Van Oss et al., 1988). Thus, the total surface free energy of a solid or liquid is described as the sum of the Lifshitz-van der Waals component $\gamma^{LW}_S$ (including London dispersion—the main interaction, Debye polarization, and Keeson orientation) and acid–base interaction $\gamma^{AB}_S$, in many cases owing to hydrogen bonding. In general, the polar $\gamma^{AB}$ interaction is due to contributions of the electron donor $\gamma^-$ and electron-acceptor $\gamma^+$. The relationship between contact angle $\theta$, the Lifshitz-van der Waals (LW) and Lewis Acid–Base (AB) components of surface free energy of the solid (subscript 1), and surface tension of the liquid (subscript 3) can be written as

$$2\sqrt{\gamma_1^{LW}\gamma_{Li}^{LW}} + 2\sqrt{\gamma_1^+\gamma_{Li}^-} + 2\sqrt{\gamma_1^-\gamma_{Li}^+} = \gamma_{Li}(1+\cos\theta), \quad (3)$$

where $\gamma_{Li}$ is surface tension of liquid $i$ forming a contact angle $\theta$ on the solid; $\gamma^{LW}{}_{Li}$, $\gamma^+{}_{Li}$, and $\gamma^-{}_{Li}$ are the surface tension components of the liquid. Thus, by measuring contact angles of the three liquids, a system of three equations of type (1) can be resolved to obtain the three unknown variables $\gamma_1{}^{LW}$, $\gamma_1{}^+$, and $\gamma_1{}^-$. Surface free energy components of the liquids used are shown in Table 1.

**Table 1**
Surface free energy components (mJ m$^{-2}$) of liquids used in contact angle measurements

| Liquid | $\gamma^{TOT}$ | $\gamma^{LW}$ | $\gamma^+$ | $\gamma^-$ |
|---|---|---|---|---|
| Water | 72.80 | 21.80 | 25.50 | 25.50 |
| Formamide | 58.00 | 39.00 | 39.60 | 2.28 |
| Diiodomethane | 50.80 | 50.80 | 0.00 | 0.00 |

### 3.3. Soil analysis

The following analytical properties were obtained from the fine earth (<2 mm) fraction of the soil sample (Soil Conservation Service, 1972): texture by sieving and sedimentation (Robinson pipette); organic carbon by dichromate oxidation; total nitrogen by the Kjeldahl method; $CaCO_3$ equivalent by Bernard calcimeter; cation exchange capacity (CEC) by the ammonium acetate (pH 7) – sodium chloride method; available phosphorus (P) extracted with sodium bicarbonate solution and determined by colorimetry (Olsen method); available potassium (K) by the ammonium acetate (pH 7) method and determined by flame photometry (AAnalyst 800; PerkinElmer, Waltham, Massachusetts); pH in a 1:1 suspension of fine earth:water; and forms of free iron oxides by the sodium citrate–dithionite method (Mehra and Jackson, 1960), measured by atomic absorption spectrometry. Finally, the aggregate stability index of Kemper and Rosenau (1986) was determined (<1 signifies fewer than 50% of 0.25 mm stable aggregates in the soil).

### 3.4. SEM images of soil fabric

Soil fabric is the morphological aspect of soil structure, defined as the geometric arrangement of particles or mineral grains (Holtz and Kovacs, 1981), and is properly examined by scanning electron microscopy (SEM). We used a scanning microscope with acceleration voltage 25 kV (S-510; Hitachi Ltd., Tokyo, Japan) equipped with an energy-dispersive X-ray detector (EDAX; Rontec GmbH, Berlin, Germany). Fine earth under four treatments (natural, $H_2O_2$-treated, natural plus HA, and $H_2O_2$-treated plus HA, Fig. 2) was mounted on the sample holder with colloidal silver and metallized with gold deposited in two orientations (20°–30°). Conventional SEM images at low (320′), medium (1120′) and high (4600′) magnifications were obtained, to observe fabric features at the following scales (Dexter, 1988): macroaggregates (>250 μm), microaggregates and clay clusters (250–10 μm) and clay domains (>10 μm).

### 3.5. Soil mineralogy

X-ray diffraction (XRD) traces of the total fine earth sample were obtained using a Siemens D5000 X-ray diffractometer with Cu Kα radiation, 35 kV, 15 mA, and step size 0.2°2$\theta$. For XRD analysis, disoriented crystalline powder was used (Fig. 2), and samples prepared using a holder filled from the side. For clay fraction (<2 μm) characterization, oriented aggregates of Mg-saturated samples (1 N magnesium chloride) were prepared by sedimentation and drying on glass slides (Fig. 2), using ≈50 mg of sample (Whitting and Allardice, 1986). Analyses were done on the air-dried slides that had been treated with ethylene-glycol vapor (Brown and Brindley, 1980; Kunze and Dixon, 1986). The D5000 diffractometer had the following operating conditions: Cu Kα radiation (λ = 0.15406 nm) at 35 kV and 15 mA over angular range 2–30°2$\theta$, scan speed 0.05°2$\theta$ s$^{-1}$ and time constant 2 s. Mineral percentages for both the fine earth and clay fractions (Mg ethylene-glycol samples) were established by a mineral intensity factor approach according to previously determined factors (Martín-García et al., 1997; Calero et al., 2009). Finally, decomposition of ethylene glycol patterns of oriented aggregates in the 3–8°2$\theta$ zone was done with DecompRX software (Lanson, 1997) following published recommendations (Barré et al., 2008), and MULCALC peak simulator software (Le and Ferrer, 1996) was used to characterize decomposed peaks.

**Table 2**
Selected properties of fine earth (<2 mm) soil sample

| Granulometry (%) | Chemical properties | | | | | | | | | | |
|---|---|---|---|---|---|---|---|---|---|---|---|
| Sand | Silt | Clay | OC (%) | N (%) | pH ($H_2O$) | $CaCO_3$ (%) | FeCD (%) | P (mg $kg^{-1}$) | K (mg $kg^{-1}$) | CEC (cmol + $kg^{-1}$) | ASI[a] |
| 46 | 35 | 20 | 0.40 | 0.04 | 8.1 | 34 | 1.26 | 10 | 97 | 18 | 0.67 |

OC: total organic carbon; N: total nitrogen; FeCD: citrate-dithionite iron; P: extractable phosphorus; K: extractable potassium; CEC: cation exchange capacity.
[a] ASI: aggregate stability index = A/B × 100. A: weight of stable soil macroaggregates (≥0.25 mm), resistant to wet sieving; B: weight of unstable soil macroaggregates (≥0.25 mm) passed through the 0.25 mm grid.

## 4. Results and discussion

### 4.1. Soil analysis and mineralogy

Results of the soil sample analysis are shown in Table 2. The soil belonged to the loamy texture class, with equilibrated amounts of silt (35%) and clay (20%). However, the main soil characteristic was a very low organic carbon content (0.40%), which can be explained by the Mediterranean climate type where the soil developed. The very low organic matter content also produced low nitrogen (0.04%), phosphorus (10 mg $kg^{-1}$) and potassium (97 mg $kg^{-1}$) contents, which coupled with the high carbonate content (340 g $kg^{-1}$) gave this soil low chemical fertility despite a normal cation exchange capacity for loamy soils (18 cmol + $kg^{-1}$).

**Table 3**
Mineralogical composition of soil fine earth fraction (<2 mm, XRD analysis).

| Mineralogical composition (%) | | | | | | |
|---|---|---|---|---|---|---|
| Phyll | Q | FdK | FdNa | OxFe | Cal | Dol |
| 47 | 16 | tr. | tr. | >5 | 31 | tr. |

With respect to fine earth mineralogy (Fig. 3; Table 3), phyllosilicates (47%) and carbonates (31% of calcite, coherent with the analytical carbonates specified above) were the predominant minerals, followed by moderate amounts of quartz (16%). Feldspar and iron oxides, by contrast, had very low ratios (< 5%) in the sample.

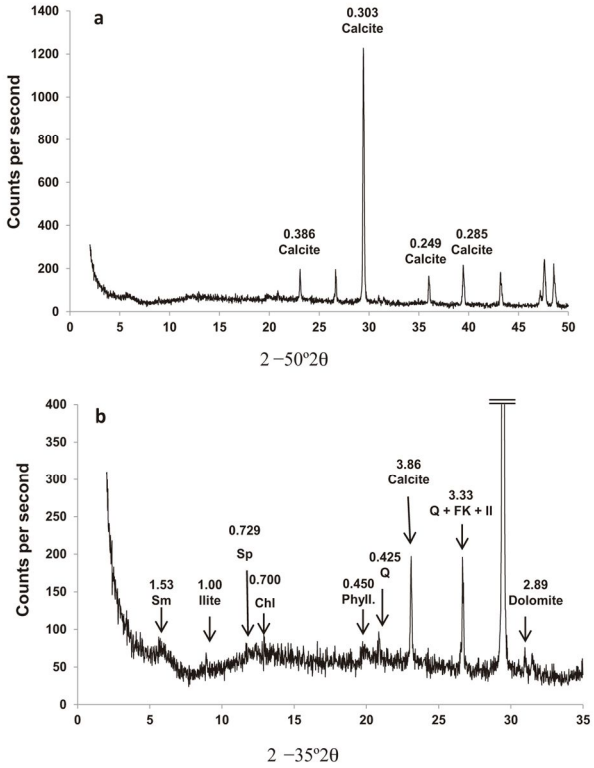


**Fig. 3.** XRD diagrams (Cu Kα) of fine earth fraction of selected soil horizons of the chronosequence: (a) region 2–50°2θ; (b) extended region 2–35°2θ. Phyll: phyllosilicates (illite, smectite, kaolinite and interstratified phases); Q: quartz; Sp = serpentine; Sm = smectite; Chl = chlorite; FK = potassium feldspar; Il = illite.

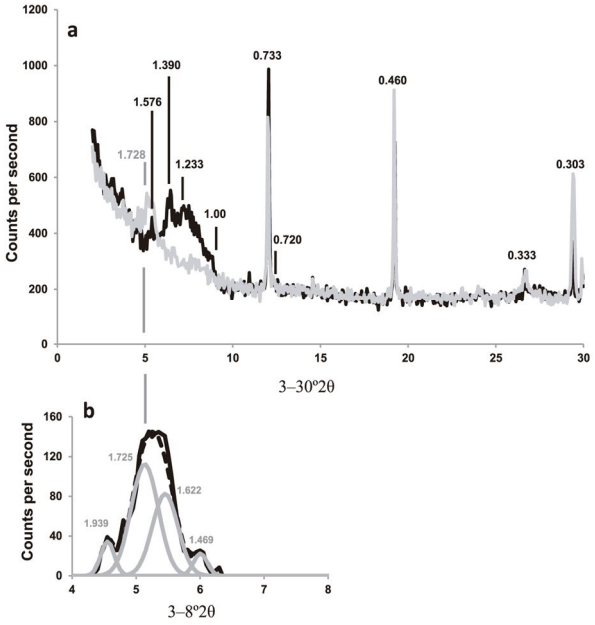


**Fig. 4.** XRD patterns of oriented aggregates from clay fraction: (a) region 3–30° 2$\theta$ with different treatments (black line: Mg saturated and air-dried; grey line: Mg saturated and solvated with ethylene glycol); (b) Decomposed XRD patterns of oriented aggregates (3–8° 2$\theta$) from clay fraction, Mg-saturated and ethylene glycol-solvated (dashed line: simulated pattern).

Phyllosilicate phases in the clay fraction (< 2 μm size fraction) were determined by the oriented aggregate XRD technique (Fig. 4a, Table 4). Smectite minerals were prevalent in the clay fraction (76%), as shown by the 1.39 nm (≈1.42 nm) peak in the Mg-air dried treatment, swelling to >1.69 nm (1.728 nm) with ethylene glycol treatment. Nevertheless, other soil phyllosilicates such as mica illite (1.00 nm), chlorite (0.700 and 0.358 nm) and kaolinite (0.720 and 0.352 nm) displayed very low contents (less than 5%). Another important peak was noted at 1.233 nm, between the smectite and illite ones. This peak is attributable to disordered smectite/illite mixed layers as demonstrated by its total swelling to 1.728 nm in the ethylene glycol treatment, leaving only small traces of illite or chlorite reflections (1.0 and 1.4 nm, respectively) in the corresponding sector of the XRD diagram.

Decomposition of the 1.728 peak (Fig. 4b) gives several elementary curves. A low-grade curve (1.939 nm) might be attributable to first-order reflection from a 2.0-nm mica polytype. Also, pure smectite (1.725 nm) and two smectite mixed layers (1.622 and 1.469 nm), which can be simulated by MULCALC (simulation parameters: 2 ethylene glycol molecules and $R = 0$), were found. The first mixed layer (1.622 nm) was dominated in its layer sequence by the swelling phase (smectite/illite, with 55% of smectite according to simulation), and the second (1.469 nm) by the non-swelling phase (chlorite/smectite, with 20% of smectite). Both mixed layer phases had a low stacking order ($R_0$) as shown by the $R$ parameter. At the base of the relative peak areas from the decomposed curves, we estimate that smectite was the most abundant mineral (52%), followed by smectite/illite (35%) and chlorite/smectite (13%).

**Table 4**
Mineralogical composition of the soil clay fraction (<2 μm; XRD analysis).

| Mineralogical composition (%) | | | | | | | |
|---|---|---|---|---|---|---|---|
| Smt. | Illite | Chlorite | Chrysotile | Kaolinite | FdK | Q | Calcite |
| 76 | tr. | tr. | 10 | >5 | tr. | >5 | 11 |

Smt.: Smectite minerals, including pure smectite and smectite mixed-layers; Q: quartz; FdK: potassium feldspar; tr: traces (<1%).

In addition to the smectite and mixed layers, only two other minerals stood out in the sample (Table 4; Fig. 4a): chrysotile (10% of the total peak areas), which clearly showed two diagnostic peaks (0 0 2 and 0 2 0, 0.733 and 0.460 nm, respectively), and calcite (11%) with peak at 104 (0.303 nm). Chrysotile, a serpentine mineral, is not an expected component of the soil parent material (marl). Its presence in the studied soil may be attributable to contamination, owing to its use as an agrochemical component (Konta, 1995). In spite of its low stability in the clay fraction, calcite was present because of its high accumulation in the sample.

Given the low amount of organic matter in the soil, the described mineralogical composition for both the total sample and soil clays is critically important to surface properties of the soil. As stated above, the prevailing mineral fraction in the sample was phyllosilicates, specifically the smectite phases (pure and/or interstratified). These are usually the main minerals in the fine clay size fraction (<0.2 μm) of soils. Smectites have a relatively high surface reactivity of polar type, owing to isomorphic substitutions in both the tetrahedral and octahedral layers (also known as permanent charges) and a high cation exchange capacity (≈100 $cmol_c\,kg^{-1}$) (Johnston and Tombácz, 2002). Despite this, given the moderate clay ratio in the fine earth (20%), the cation-exchange capacity (CEC) of the soil did not exceed normal values

(18 $cmol_c\ kg^{-1}$). Smectites can also show moderate nonpolar reactivity because of their neutral siloxane surfaces, which should be taken into account in fixing hydrophobic organic molecules.

The two most abundant minerals in the soil after phyllosilicates were calcite and quartz. Both minerals accumulated mainly in the silt and sand size fractions (as evidenced by their relative loss in the clay fraction), with low specific surface area. Both minerals showed few active sites, both polar and non-polar (Monger and Kelly, 2002). For these reasons, these are probably not significant in terms of surface properties of the soil, and thus smectite should be considered as the determinant of those properties.

### 4.2. Soil fabric SEM images

Under SEM observation, the natural sample showed a hierarchical fabric that includes macroaggregates, microaggregates, and clay clusters and domains. Thus, the aggregation process was manifest at all studied spatial scales, from the resolving power of the human eye (1′) to more than 4000′ (Fig. 5a). On the contrary, the treated samples ($H_2O_2$-treated, natural plus HA and $H_2O_2$-treated plus HA; Fig. 5b–d, respectively) were less aggregated and only the microaggregate level was clearly visible in all samples.

The natural sample showed a blocky macroaggregate (330′) with a feret diameter (the longest distance between any two points along the particle boundary) of 667 μm and subangular edges, which were composed by microaggregates of more elongated forms. Microaggregates (1120′) were also composed by fabric units of lower hierarchical level, the clay clusters. These were aggregates of rounded and spherical and/or discoidal morphologies and, at highest magnification (4600′), it was observed how they were formed by other fabric units of even smaller size. These are the clay domains, and have already been defined (Holtz and Kovacs, 1981; Aylmore and Quirk, 1960). Clay domains are face-to-face flocculated assemblages of laminar phyllosilicate particles of fine silt (<6 μm) and clay (<2 μm) sizes, which are joined by means of face-to-face and edge-to-edge interactions to form clusters. At this magnification, next to the laminar particles of phyllosilicates, we could also distinguish other idiomorphic (quartz) and granular (carbonates) crystallites, in accord with the mineral composition revealed by XRD (Table 3).

Compared with the natural sample, the $H_2O_2$-treated sample (Fig. 5b) appeared highly disaggregate or deflocculated, so it was not possible to discern macroaggregates or true clusters and domains. This may be has been due to largely eliminating the stabilizing agents of the structure, i.e., clay carbonates and organic matter (Kunze and Dixon, 1986). Deflocculation appeared particularly significant at the domain level (4600′). The dense face-to-face packing between phyllosilicate particles in the natural sample were transformed into a kind of open and loose chain, with prevalent weak edge-to-edge and edge-to-face

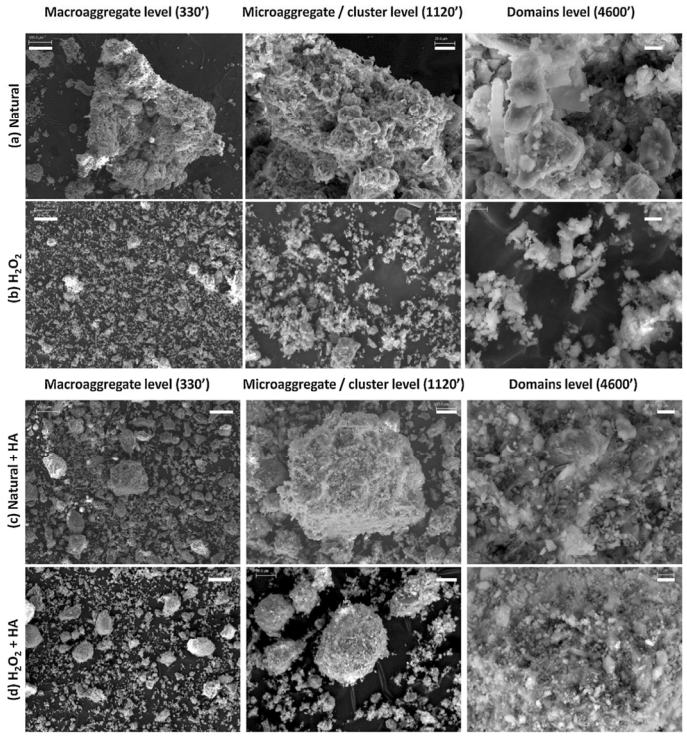


**Fig. 5.** SEM fabric images of soil samples at different spatial scales for natural and treated samples. (a) Natural sample; (b) $H_2O_2$: sample treated with hydrogen peroxide; (c) natural + HA: natural sample plus humic acid; (d); $H_2O_2$ + HA: sample treated with hydrogen peroxide plus humic acids. Scale bar represents 100 μm at macroaggregate level, 25 μm at microaggregate and cluster level, and 5 μm at domain levels.

associations, as has been described for concentrated electrolyte solutions (Van Olphen, 1991).

Compared with the above samples, those with HA added (Fig. 5c and d) appeared with spherical forms and did not show a very strong deflocculation process. This was visible mainly at the microaggregate scale. Moreover, microaggregates from the $H_2O_2$ plus HA-sample (Fig. 5d) were even more spherical than in natural plus HA sample (Fig. 5c), which might indicate a different genesis for the first or the alteration of these fabric units during the $H_2O_2$ exposition. At higher magnifications of both samples with HA added (4600′), a disordered particle flocculation was observed, in which it was not easy to recognize clay clusters and domains. All this suggests a fundamental effect of HA in soil fabric formation.

The occurrence of all hierarchical fabric levels in the natural sample proves the existence of multiple structuring forces acting in soils (Dexter, 1988). These include mechanical (contraction and retraction of soil mass from wetting and drying), biomechanical (biopores, ingestion, binding effects of roots and fungal hyphae), and physicochemical (colloid flocculation, including the biochemical mineral particle influence of organic matter) processes, such as those described in the literature (Bronick and Lal, 2005; Tisdall and Oades, 1982). According to these authors, flocculation is the dominant structuring force at cluster and domain levels, co-dominant with biomechanical processes at the microaggregate level. Flocculation is a property that affects clay particles (<2 μm) and is dependent on characteristics of the colloidal system, i.e., ionic strength, ion type, and mineral and organic surfaces (Van Olphen, 1991).

The fabrics described for the $H_2O_2$ and HA-added samples lacked macroaggregates, because these were broken down by the treatments. Also, these samples showed levels of clusters and domains tending toward full deflocculation ($H_2O_2$ sample) or disorderly flocculation that failed to constitute clay fabric units (HA samples). The presence of microaggregates of similar size and morphology in the HA samples might indicate that these flocculated under the main effect of the added HA, as described for microaggregates in natural soils with equivalent HA contents (1.64 g/100 g soil) (Sánchez-Marañón et al., 2002; Delgado et al., 2007).

### 4.3. Zeta potential

The adsorption of different cations and negatively-charged HA molecules changed the electrochemical properties of the soil/solution interface, thereby affecting the aggregation/flocculation state of soil samples. This effect has been studied by ζ measurement in suspensions, as a source of information on the electric surface potential of soil. It is of interest to first analyze the electrophoretic behavior of soil suspensions at different pH values in the absence or presence of $Na^+$, $Ca^{2+}$, $Fe^{3+}$, $Al^{3+}$ and HA, to obtain a global picture of the effect of mono-, di-, trivalent ions and polyelectrolyte adsorption.

In Fig. 6, we represent ζ as a function of pH for different salt concentrations (10, 1 and 0.1 mM NaCl). For all studied NaCl concentrations, values of ζ were negative in the pH range studied. These values were generated by the prevalence of permanent charges from smectites and smectite mixed layers (Sondi et al., 1996) and, to a lesser extent, the presence of OH groups (pH charges) on the surface and rupture edges of smectites (Sondi et al., 1997) and natural carbonates (Vdovic, 2001). The decrease in ζ observed for low pH values with ionic strength 1 mM is attributed to the protonation of soil organic matter, which is rich in phenolic and carboxylic groups. With increasing pH, ζ increased in absolute value, probably owing to the progressive decrease in acid–base neutralization and progressive adsorption of hydroxyl groups for high pH values (Vdovic, 2001). Fig. 6 also shows ζ behavior when

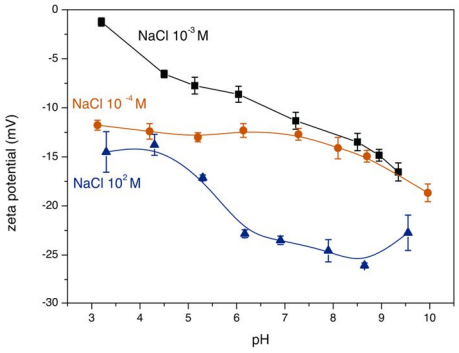


**Fig. 6.** Effect of ionic strength in zeta potential of soil in the presence of a monovalent ion.

ionic strength of the medium was varied. The results show that ζ for an electrolyte concentration of 10 mM was higher than that obtained for 1 mM NaCl in solution. When the electrolyte concentration was 0.1 mM, ζ values showed almost no increase with increasing pH. This is anomalous behavior but not unusual (Ramos-Tejada et al., 2003). This behavior may be due to the excess of electrical charge at interface, which is responsible for surface conductivity. A similar conclusion was reached by Ramos-Tejada et al. (2003) and Thomas et al. (1999). The response to ionic strength in acidic pH obtained in the present study might have been caused by the adsorbed organic matter contained in our sample.

Fig. 7 shows the effect of divalent ($CaCl_2$) ions produced in ζ of the sample. The ζ of the aforementioned material in the presence of $CaCl_2$ was negative in all pH ranges tested. The results show that the calcium cation behaves like an indifferent ion. This behavior was previously shown by Lagaly (2006), who attributed this effect to the low ratio of pH-dependent charges in smectites and strong particle aggregation caused by calcium. The results obtained for pH 10 (−35 mV) may be due to precipitated $Ca(OH)_2$ (Vdovic, 2001). We can observe a drastic reversion of the sign in ζ to pH 10, this behavior is probably due to the formation of complex ions,

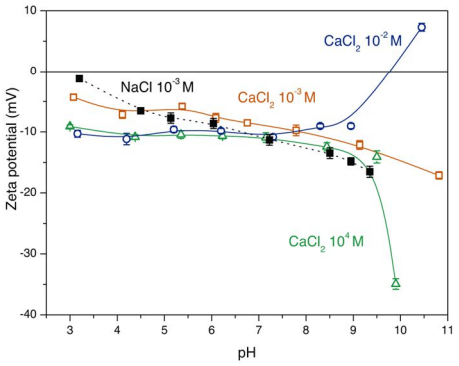


**Fig. 7.** Effect of ionic strength in zeta potential of soil in the presence of a divalent ion.

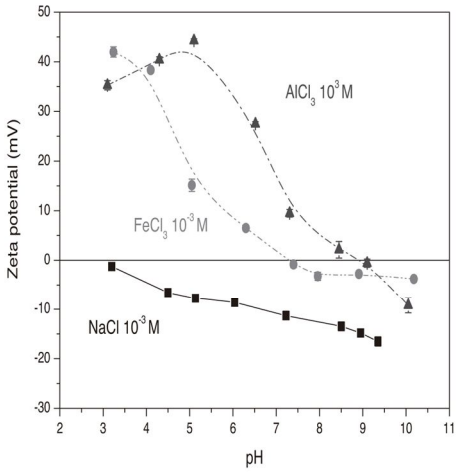


**Fig. 8.** Effect of ionic strength in zeta potential of soil in the presence of a trivalent ion.

including the formation of micelles (to high ionic strength) owed to the presence of natural organic matter.

Fig. 8 shows the effect of trivalent cations ($FeCl_3$) on $\zeta$. $Fe^{3+}$ cations were absorbed onto particles, probably owing to acid pH values. The $\zeta$ value of the system decreased from +45 mV to +0 mV for pH 7.3, attributable to progressive adsorption of hydroxyl groups. This favors formation of coordination compounds, meaning that the iron is adsorbed in the form of $Fe(OH)^{2+}$ and $Fe(OH)^{+}$. At higher pH values between 7.5 and 10, $\zeta$ was negative, probably because of saturation of the particle surfaces with coordination compounds such as $Fe(OH)_3$. For the $AlCl_3$ electrolyte, adsorption of $Al^{3+}$ and coordinating compounds between $Al^{3+}$ and $(OH)^{-}$, such as $Al(OH)^{2+}$, onto the surface effectively produced (in the range pH 3–9) an increase in the positive value of $\zeta$ of the system, up to +45 mV. For pH values higher than 5, compression of the electric double layer of the system and the formation of complex ions such as aluminate ions, $Al(OH)^{4-}$, gradually decreased the system $\zeta$ to values of −10 mV.

Fig. 9 shows $\zeta$ of soil containing natural organic matter at ionic strength 1 mM NaCl, compared with results for the same soil but with organic material removed by treatment with $H_2O_2$ (as described in the Section 3). A different behavior was found in this sample with respect to the natural (non-treated) sample. In the case of $H_2O_2$ treatment, $\zeta$ of soil colloids did not vary appreciably in the pH range 3–7. This behavior was likely due to elimination of the natural mineral-organic complex by treatment with $H_2O_2$; it was also attributable to the low concentration of soil organic matter, around 0.5%. The results also confirm the protonation of organic matter at low pH values shown in Fig. 6. The observed decrease of $\zeta$ for higher pH was probably due to the forced adsorption of OH ions at these pH values. This $\zeta$ behavior obtained by removing the organic matter is analogous to that obtained for pure smectite with low surface charge (Thomas et al., 1999).

Fig. 10 shows the effect of the adsorption of humic acids on $\zeta$ of the soil. Two different situations arose, the adsorption effect of HA on natural soil up to ionic strength 1 mM of NaCl, and a deficiency of HA adsorption on soil treated with hydrogen peroxide, hence without natural organic matter for the same ionic strength.

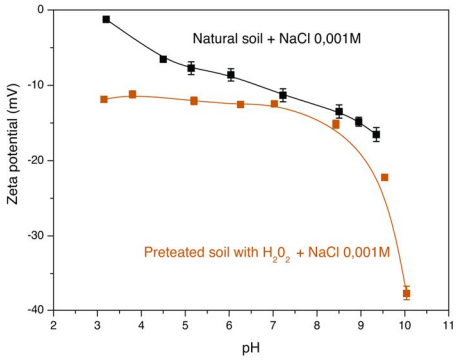


**Fig. 9.** Influence of hydrogen peroxide treatment in zeta potential of natural soil.

Considering the ionization of HA molecules at different pH values, at basic pH it is expected that the carboxyl groups (the main ionizable groups in HA) are dissociated and negatively charged. The opposite is expected at acid pH (neutral or low negative charge) (Ramos-Tejada et al., 2003). This would justify the overall increase of $\zeta$ observed with HA treatment at basic pH values.

For natural soil, HA adsorption occurred primarily at extreme pH values. The $\zeta$ increased its negative value from almost 0 mV to −10 mV at pH 3. This increase of negative charge decreased as much as 2 mV for pH values between 5 and 6. At basic pH, the HA adsorption produced in $\zeta$ progressively increased in the natural sample, as much as 20 mV at pH of 10. This behavior is probably attributable to the adsorption of HA. This adsorption of HA molecules is not favored by electrostatic interactions, because of electrostatic repulsion between HA molecules and the soil particle surfaces. However, as proposed by Ochs et al. (1994) for alumina, adsorption can also occur via coordinative interactions between positive surface sites and organic molecules, with formation of mononuclear bidentate and polynuclear surface complexes. This coordinative mechanism surely persists at acid pH, although with less intensity.

Fig. 10 also shows the effect of HA adsorption on samples treated with hydrogen peroxide, that is, clean natural organic matter. The results show no significant differences between the

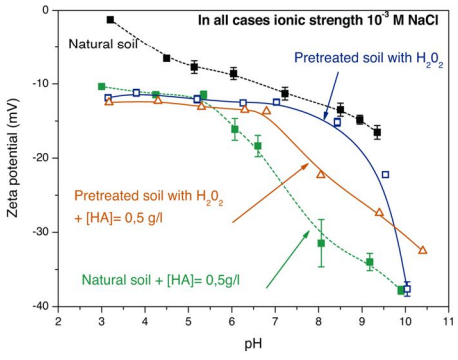


**Fig. 10.** Effect produced by absorption of humic acids on zeta potential of soil.

$H_2O_2$-treated and $H_2O_2$-treated plus HA samples at pH less than 7. This is likely due to the absence of natural organic material, which acts as a mordant. These results show that HA adsorption occurred mainly at pH greater than 7 (the natural pH of soil is around 8). $\zeta$ increased its negative charge at pH greater than 7, probably because of the ionization of HA molecules at basic pH. It is expected that the carboxyl groups are dissociated and negatively charged.

If we assume that the $\zeta$ variation is a consequence of HA adsorption and that greater charge on the particles indicates stronger electrostatic repulsion between them and thus greater dispersion of the soil, then it can be affirmed that the $\zeta$ data partially support the results shown in Fig. 5. This is especially noticeable when examining the strong aggregation in natural soil at all fabric levels, which shows a $\zeta$ under the threshold of true aggregation and sedimentation (−10 mV, according to Baumgarten et al., 2013).

However, the strong deflocculation observed in the soil sample treated with hydrogen peroxide cannot be interpreted only in terms of electrostatic interaction. Other interactions must be considered, such as the hydrophobic and hydrophilic ones.

From Fig. 10, it can be deduced that soil organic matter acts as a mordant of commercial humic acids and that this adsorption is optimal for acid and basic soils, but not for neutral soils. This is interesting because it shows the great potential of agricultural soils (degraded by intensive agricultural practices that involve little organic matter) to adsorb humic substances, although the effect may be negative from the standpoint of structure formation. From the $\zeta$ results, we can infer that $\zeta$ only reacts to natural soil pH behavior, mainly because of the acids (protonation) of natural organic matter adsorbed onto smectites. This behavior was not observed after absorption of commercial HA, and $\zeta$ at acidic pH remained unchanged, maintaining the range of $\zeta$ values because of the permanent surface charge of smectites.

### 4.4. Surface free energy

Knowledge of the surface free energy component of soil provides information about soil hydrophobic and hydrophilic character, and should thus enhance estimation of soil structure stability properties. We analyzed the surface free energy of natural soil and how these components are modified when natural organic material is removed, and we then absorbed commercial HA. Table 5 shows results of the surface free energy components obtained in our experiments.

Soil material is essentially monopolar and electron-donor in nature ($\gamma^+ = 0$ and $\gamma^- \neq 0$), according to Van Oss et al. (1988). Values of the soil dispersive component ${\gamma_1}^{LW}$, obtained here from the contact angle technique, were around 48 mJ m$^{-2}$, in the range obtained by other authors for carbonates (Durán et al., 1998). We should emphasize that the extreme values of ${\gamma_1}^{LW}$ correspond to results after treatment with HAs. There was an increase in ${\gamma_1}^{LW}$ up to 48 mJ m$^{-2}$ and of three units in ${\gamma_1}^{TOT}$ when there was HA adsorption onto the mineral components of soil versus onto natural soil (containing organic matter). From de polar components we can see a relative decrease of the electron-acceptor parameter (from 0.32 to 0.10 mJ m$^{-2}$) and the increase electron-donor parameter (from 39.6 and 48.3 mJ m$^{-2}$), respectively. These variations in the surface free components, justifying the differences in total surface free energy obtained, from 50.9 to 54.8 (Table 5).

**Table 5**
Components of surface free energy of soil material.

| Treatment | $\gamma^{LW}$(mJ m$^{-2}$) | $\gamma^-$(mJ m$^{-2}$) | $\gamma^+$(mJ m$^{-2}$) | $\gamma^{TOT}$(mJ m$^{-2}$) |
|---|---|---|---|---|
| Natural | 47.8 ± 0.3 | 39.6 ± 0.1 | 0.32 ± 0.02 | 54.9 ± 0.1 |
| Natural + HA | 46.2 ± 0.1 | 48.3 ± 0.1 | 0.10 ± 0.01 | 50.9 ± 0.1 |
| $H_2O_2$ | 47.6 ± 0.4 | 53.3 ± 0.1 | 0.21 ± 0.02 | 54.3 ± 0.1 |
| $H_2O_2$ + HA | 48.9 ± 0.2 | 47.3 ± 0.1 | 0.18 ± 0.01 | 54.8 ± 0.1 |

Natural + HA: natural sample plus humic acid (0.5 g/L); $H_2O_2$: sample treated with hydrogen peroxide; $H_2O_2$ + HA: sample treated with hydrogen peroxide plus humic acids (0.5 g/L).

Table 5 also shows results for the soil with absorbed HA. HA adsorption maintained the monopolar character of the substrate. Values obtained for both acid–base components were the same whether the substrate was $H_2O_2$-treated or natural soil. There was an increase in the electron donor component around 8 mJ m$^{-2}$ with respect to natural soil. The result of adsorption is that this material becomes more hydrophilic that natural soil.

Treatment with $H_2O_2$, thereby removing soil organic matter, gives a strong hydrophilic character (53.3 mJ m$^{-2}$), as expected in smectite surfaces cleaned of organic materials that facilitates adsorption of water. From the results of total surface free energy, there was a decrease of 4 units when HA was adsorbed in natural soil, confirming the mordant behavior of natural organic material with respect to commercial HAs. The high $\gamma^-$ may explain the intense deflocculation observed in SEM images of $H_2O_2$-treated sample. In function of this parameter, it may also account the similar level of aggregation of the samples treated with HA ($\gamma^-$ = 48 mJ m$^{-2}$), and the good aggregation state of the natural sample, which showed the lowest value ($\gamma^-$ = 39.6 mJ m$^{-2}$). Thus, a certain degree of soil hydrophobicity is important from the standpoints of maintaining aggregate soil stability, preventing soil erosion, maintaining soil fertility, and protecting soil organic matter against microbial degradation (Bachmann et al., 2006).

## 5. Conclusions

From our soil analysis and mineralogy results, the examined soil belonged to the loamy texture class and its very low organic carbon content (0.40%) is explained by the Mediterranean climate type in which it developed. From the fine earth mineralogy, we conclude that smectite was the most abundant mineral in the soil.

Our natural soil sample showed substantial fabric aggregation and flocculation from SEM images and the presence of all fabric units at various scales (macroaggregate, microaggregate and clay clusters and domains). This fabric was dispersed and disordered under varying treatments, very significantly under $H_2O_2$ treatment and partially under HA treatments (which maintained the microaggregates and clay clusters and domains, although in a much more disordered manner than in the natural sample).

In the NaCl solutions, $\zeta$ values were negative in the pH range studied. A decrease of $\zeta$ for low pH values with ionic strength 1 mM is attributed to protonation of soil organic matter. With increasing pH, $\zeta$ increased in absolute value, probably because of the progressive decrease in acid–base neutralization and progressive adsorption of hydroxyl groups at high pH values. At high ionic strength, $\zeta$ values revealed coagulation processes. Results when the soil was treated with hydrogen peroxide confirm and highlight organic matter protonation of the native soil, and reinforce the hypothesis that our soil was smectitic. The presence of HAs increased $\zeta$ of the soil to basic pH (note that the natural pH of our soil is basic). This effect was more significant when the soil contained natural organic matter, confirming the mordant character of that matter in native soil. This could be an important feature with respect to the soil's capacity to absorb organic matter in agricultural environments. However, the absorption of HAs of the type used in the present work may alter soil fabric, structure development and behavior and, thereby, soil quality.

The surface free energy results show that soil material is essentially monopolar and electron-donor in nature. Treatment with hydrogen peroxide increased hydrophilicity of the sample, as expected for smectites with no soil organic matter. Contrary,

adsorption of HAs decreases the hydrophilic character of the soil, due to mainly owing variation in the polar components. This effect seems important in explaining the state of aggregation observed under SEM. The observed deflocculation in soil samples treated with hydrogen peroxide cannot be interpreted only in terms of electrostatic interaction. In general, the soil aggregation state can be properly explained by a combination of electrical and thermodynamic interactions.

## References


Aylmore, L.A.G., Quirk, J.P., 1960. Domain or turbostratic structure of clays. Nature 187, 1046.

Bachmann, J., Marmur, A., Deurer, M., 2006. Soil hydrophobicity. In: Lal, R. (Ed.), Encyclopedia of Soil Science. Taylor & Francis, Madison, NY, pp. 1626–1629.

Barré, P., Velde, B., Fontaine, C., Catel, N., Abbadie, L., 2008. Which 2:1 clay minerals are involved in the soil potassium reservoir? Insights from potassium addition or removal experiments on three temperate grassland soil clay assemblages. Geoderma 146, 216–223.

Baumgarten, W., Dörner, J., Horn, R., 2013. Microstructural development in volcanic ash soils from South Chile. Soil Till. Res. 129, 48–60.

Bockheim, J.G., Gennadiyev, A.N., 2010. Soil-factorial models and earth-system science. A review. Geoderma 159, 243–251.

Bronick, C.J., Lal, R., 2005. Soil structure and management: a review. Geoderma 124, 3–22.

Brown, G., Brindley, G.W., 1980. X-ray diffraction procedures for clay mineral identification. In: Brindley, G.W., Brown, G. (Eds.), Crystal and X-ray Identificaction. Mineralogical Society Monograph 5, London, pp. 305–359.

Calero, J., Delgado, G., Delgado, R., Martín-García, J.M., 2009. SEM image analysis in the study of a soil chronosequence on fluvial terraces of the middle Guadalquivir (southern Spain). Eur. J. Soil Sci. 60, 465–480.

Delgado, R., Sánchez-Marañón, M., Martín-García, J.M., Aranda, V., Serrano-Bernardo, F., Rosúa, J.L., 2007. Impact of ski pistes on soil properties: a case study from mountainous area in the Mediterranean region. Soil Use Manage. 23, 269–277.

Dexter, A.R., 1988. Advances in characterization of soil structure. Soil Till. Res. 11, 199–238.

Durán, J.D.G., Ontiveros, A., Delgado, A.V., Gonzalez-Caballero, F., 1998. Kinetics and interfacial interactions in the adhesion of colloidal calcium carbonate to glass in a packed-bed. Appl. Surf. Sci. 134, 125–138.

Durán, J.D.G., Ramos-Tejada, M.M., Arroyo, F.J., González-Caballero, F., 2000. Rheological and electrokinetic properties of sodium montmorillonite suspensions: I. Rheological properties and interparticle energy of interaction. J. Colloid Interface Sci. 229, 107–117.

FAO, 2006. World Reference Base for Soil Resources. World Soil Resources Reports No. 103. FAO, Rome.

Holtz, R.D., Kovacs, W.D., 1981. An Introduction to Geotechnical Engineering. Prentice Hall, New Jersey, pp. 746.

Israelachvili, J., 1991. Intermolecular and Surface Forces. Academic Press, London, pp. 435.

Jiang, C.L., Sequaris, J.M., Vereecken, H., Klumpp, E., 2012. Effects of inorganic and organic anions on the stability of illite and quartz soil colloids in Na-, Ca- and mixed Na–Ca systems. Colloids Surf. A: Physicochem. Eng. Asp. 415, 134–141.

Johnston, C.T., Tombácz, E., 2002. Surface chemistry of soil minerals. In: Dixon, J.B., Schulze, D.G. (Eds.), Soil Mineralogy with Environmental Application. Madison, WI, pp. 37–68.

Jones, M.N., Bryan, N.D., 1998. Colloidal properties of humic substances. Adv. Colloid Interface Sci. 78 (1), 1–48.

Karathanasis, A.D., 2002. Mineral equilibria in environmental soil systems. In: Dixon, J.B., Schulze, D.G. (Eds.), Soil Mineralogy with Environmental Application. Soil Science Society of America, Inc., Madison, WI, pp. 109–149.

Kay, B.D., Grant, C.D., 1996. Structural aspects of soil quality. In: MacEwan, R.J., Carter, M.R. (Eds.), Soil Quality is in the Hands of the Land Manager. Proceedings of an International Symposium. Advances in Soil Quality for Land Management: Science, Practice and Policy, 17–19 April 1996, University of Ballarat, Ballarat, Victoria, Australia, pp. 37–41.

Kemper, W.D., Rosenau, R.C., 1986. Aggregate stability and size distribution. In: Klute, A. (Ed.), Methods of Soil Analysis, Agronomy no. 9. American Society of Agronomy and Soil Science Society of America, Madison, WI, pp. 425–442.

Konta, J., 1995. Clay and man: clay raw materials in the service of man. Appl. Clay Sci. 10, 275–335.

Kunze, G.W., Dixon, J.B., 1986. Pretreatment for Mineralogical Analysis. In: Klute, A. (Ed.), Methods of Soil Analysis, Agronomy no. 9. American Society of Agronomy and Soil Science Society of America, Madison, WI, pp. 91–99.

Lagaly, G., 2006. Colloid clay science. In: Bergaya, F., Theng, B.K.G., Lagaly, G. (Eds.), Handbook of Clay Science. Elsevier, Amsterdam, pp. 247–260.

Lal, R., 2007. Soil Science and the carbon civilization. Soil Sci. Soc. Am. J. 71, 1425–1437.

Lanson, B., 1997. Decomposition of experimental X-ray diffraction profile (profile fitting): a convenient way to study clay minerals. Clays Clay Miner. 45, 132–146.

Le, T.H., Ferrer, R., 1996. MULCALC. Department of Geology and Geophysic, E325Howe/Russell Geoscience Complex, Baton Rouge, USA.

Marchuk, A., Rengasamy, P., 2011. Clay behaviour in suspension is related to the ionicity of clay–cation bonds. Appl. Clay Sci. 53, 754–759.

Martín-García, J.M., Delgado, G., Sánchez-Marañón, M., Párraga, J.F., Delgado, R., 1997. Nature of dioctahedral micas in Spanish red soils. Clay Miner. 32, 107–121.

Mehra, O.P., Jackson, M.L., 1960. Iron oxide removal from soil and clays by a dithionite-citrate system buffered with sodium bicarbonate. Proceedings of 7th Nationall Conference on Clays and Clay Minerals, Pergamon Press, New York, pp. 317–327.

Monger, H.C., Kelly, E.F., 2002. Silica minerals. In: Dixon, J.B., Schulze, D.G. (Eds.), Soil Mineralogy with Environmental Application. Madison, WI, pp. 611–632.

Oades, J.M., Waters, A.G., 1991. Aggregate hierarchy in soils. Aust. J. Soil Res. 29, 815–828.

Ochs, M., Osovic, B., Stumm, C., 1994. Geochim. Cosmochim. Acta 58, 639.

Ohshima, H., 2002. Interfacial Electrokinetics and Electrophoresis. In: Delgado, A.V. (Ed.), Dekker, New York, pp. 123.

Ramos-Tejada, M.M., Arroyo, F.J., Perea, R., Durán, J.D.G., 2001. Scaling behavior of the rheological properties of montmorillonite suspensions: correlation between interparticle interaction and degree of flocculation. J. Colloid Interface Sci. 5, 235–251.

Ramos-Tejada, M.M., Ontiveros, A., Viota, J.L., Durán, J.D.G., 2003. Interfacial and rheological properties of humic acid/hematite suspensions. J. Colloid Interface Sci. 268, 85–95.

Sánchez-Marañón, M., Soriano, M., Delgado, G., Delgado, R., 2002. Soil quality in Mediterranean mountain environments: effects of land use change. Soil Sci. Soc. Am. J. 66, 948–958.

Soil Conservation Service, 1972. Soil Survey Laboratory Methods and Procedures for Collecting Soil Samples.. U.S. Department of Agriculture, Washington.

Sondi, I., Pravdic, V., 2002. Interfacial electrokinetics and electro-phoresis. In: Delgado, A.V. (Ed.), Interfacial Electrokinetics and Electrophoresis. Dekker, New York, pp. 7732–7734.

Sondi, I., Jasenka, B., Velimir, P., 1996. Electrokinetics of pure clay minerals revisited. J. Colloid Interface Sci. 178, 514–522.

Sondi, I., Ognjen, M., Velimir, P., 1997. Electrokinetic potentials of clay surfaces modified by polymers. J. Colloid Interface Sci. 189, 66–73.

Thomas, F., Michot, L., Vantelon, J., Montargès, D., Prélo, E., Cruchaudet, B., Delonet, M., 1999. Colloids Surf. A: Physicochem. Eng. Asp. 159, 351–358.

Tiller, C.L., O'Melia, V., 1993. Natural organic matter and colloidal stability: models and measurements. In: Tadros, T.F., Gregory, J. (Eds.), Colloids in the Aquatic Environment. Elsevier, London, pp. 89–102.

Tisdall, J.M., Oades, J.M., 1982. Organic matter and water-stable aggregates in soils. J. Soil Sci. 62, 141–163.

Van Olphen, H., 1991. An Introduction to Clay Colloid Chemistry, Reprint ed. Krieger Pub. Co., Mishawaka, IN, U.S.A.

Van Oss, C.J., 1994. Interfacial Forces in Aqueous Media. Dekker, New York.

Van Oss, C.J., Chaudhury, M.K., Good, R.J., 1988. Interfacial Lifshitz-van der Waals and polar interactions in macroscopic systems. Chem. Rev. 88, 927–941.

Vdovic, N., 2001. Electrokinetic behaviour of calcite the relationship with other calcite properties. Chem. Geol. 177, 241–248.

Wang, M., Revil, A., 2010. Electrochemical charge of silica surface at high ionic strength in narrow channels. J. Colloid Interface Sci. 343, 381–386.

Whitting, L.D., Allardice, W.R., 1986. X-ray diffraction techniques. In: Klute, A. (Ed.), Methods of Soil Analysis, Agronomy no. 9. American Society of Agronomy and Soil Science Society of America, Madison, WI, pp. 331–359.

### *5.3.2 Artículo: Humic acid adsorption and its role in the aggregation processes at colloidal scale in organic olive grove soils, studied by zeta potential, surface free energy and the Extended-DLVO theory.*

*Resumen*

El suelo es uno de los mayores sumideros de carbono en la Tierra, teniendo una función clave como regulador de los gases de efecto invernadero. Los olivares son uno de los suelos más extendidos en la región de Andalucía (sur de España) que ocupan 1,5 millones de hectáreas y, sobre todo, en la provincia de Jaén, donde supone casi la mitad de su superficie. Una de las principales preocupaciones reconocidas en la política agraria común y las leyes españolas agroambientales, es el mantenimiento de los niveles de carbono orgánico en los suelos. Sin embargo, los suelos de olivar mostraron menos del uno por ciento de carbono orgánico (0,68%), que se debe considerar niveles muy bajos en relación con estándares europeos.

Todas las formas de carbono orgánico presente en el suelo no poseen el mismo grado de estabilidad; por lo que existe una parte de carbono más móvil y otra más estable. En este artículo nos centraremos en la formación de complejos órgano-minerales: un mecanismo complejo y heterogéneo que implica interacciones físicas y químicas entre las superficies orgánicas y minerales en varias escalas espaciales. Este tipo de complejos es muy interesante ya que impiden el acceso a los microbios a la materia orgánica, debido a la formación de agregados por procesos de floculación; que protegen físicamente la materia orgánica (SOM) en su interior. Entre las

sustancias inorgánicas que constituyen los suelos, las propiedades interfaciales están fuertemente determinadas por la adsorción de las sustancias húmicas generados por descomposición de la biomasa. Las interacciones coloidales entre las partículas minerales son controladas por una variedad de fuerzas de atracción y de repulsión entre partículas, que puede ser modificado por la adsorción de cationes metálicos y polielectrolitos orgánicos presentes en la solución. Las más importantes de estas fuerzas de doble capa son las fuerzas de repulsión electrostáticas e hidrófilas, y las fuerzas de atracción de van der Waals e hidrófogas. Estas se consideran juntas en la llamada teoría DLVO-Extendida. La determinación de las interacciones interfaciales requiere la caracterización eléctrica y termodinámica de una interfaz de suelo sólido-líquido.

El objetivo del presente trabajo consiste en ver que efecto tiene el peróxido de hidrogeno en la adsorción y estabilización de moléculas de ácidos húmicos comerciales, sin olvidar el efecto que los diferentes electrolitos tienen en la estructura del suelo natural sin tratamiento previo. Por ello, hay que caracterizar el tipo mineralógico de arcilla del suelo. El tipo de arcilla del suelo viene determinada por el material original del suelo, por lo que, en última instancia, los mecanismos de estabilización dependen no solo del tipo de manejo del suelo, sino que en mayor o menor medida del material parental del que se ha formado el suelo.

Los resultados muestran que el componente donador de electrones γ- , y su implicación en la calidad física del suelo, la agregación del suelo, podrían ser vistos también como un mecanismo importante para la estabilización de la materia orgánica suelo. Esto se debe en parte a su capacidad para ocluir físicamente la materia orgánica potencialmente mineralizable dentro de los agregados. La adsorción de moléculas orgánicas en las superficies minerales también se considera por sí mismo un mecanismo de estabilización de materia orgánica.

La adsorción de carbono se caracteriza por variaciones en las curvas de potencial zeta y energías libres superficiales de las muestras naturales y de hidrógeno peróxido tratada. La adsorción de ácidos húmicos incrementó (en valor absoluto) los potenciales zeta y, al contrario que en el caso de nuestro suelo de piedra caliza, también el componente electro-donante γ-. La adsorción se verificó mediante isotermas, lo que demuestra la importancia de las interacciones débiles en el proceso. El estado natural de los suelos parece ser la condición más favorable para la estabilidad de los agregados en la escala coloidal. Una interpretación adecuada de energías superficiales totales dadas por el modelo DLVO-extendida puede ayudar a estudiar simultáneamente dos del principal mecanismo de estabilización SOM bajo diferentes condiciones de la solución del suelo (pH, tipo de iones y fuerza iónica).

# ARTÍCULO CIENTÍFICO:

# Humic Acid adsorption and its role in the aggregation processes at colloidal scale in organic olive grove soils, studied by zeta potential, surface free energy and the extended-DLVO theory.

## Revista científica:

## European Journal of Soil Science

| SPi | EJSS | ejss_12431 | B | Dispatch: May 4, 2017 | Journal: EJSS | CE: |
|---|---|---|---|---|---|---|
| | Journal Name | Manuscript No. | | Author Received: | No of pages: 13 | TS: Suresh S |

*European Journal of Soil Science*, 2017, **0**, 000–000 doi: 10.1111/ejss.12431

# Humic acid adsorption and its role in colloidal-scale aggregation determined with the zeta potential, surface free energy and the extended-DLVO theory

J. Calero[a], A. Ontiveros-Ortega[b,c], V. Aranda[a] & I. Plaza[b]

[a]*Department of Geology, University of Jaén, Campus Universitario de las Lagunillas s/n, Edificio B-3, 23071 Jaén, Spain,* [b]*Department of Physics, University of Jaén, Campus Universitario de las Lagunillas s/n, Edificio A-3, 23071 Jaén, Spain, and* [c]*Andalusian Institute of Geophysics, University of Granada, 18071 Granada, Spain*

## Summary

The effect of colloidal forces involved in the adsorption of commercial humic acids (HAs) and particle cohesion was studied in the soil of an organic olive grove with the extended Derjaguin, Landau, Verwey and Overbeek (extended-DLVO) theory. Total interaction energy was determined from the zeta potential ($\zeta$) and surface free energy, measured under different experimental conditions [natural and hydrogen peroxide ($H_2O_2$) organic matter-free mineral surfaces]. The soil was clayey, dominated by illite and vermiculite. It showed electron-donor behaviour, with negatively charged surfaces and zeta potential $< 0$ mV. Decreasing mV in the zeta potential, $\zeta$, curves and electron-donor component, $\gamma^-$, when adding HA to natural surfaces showed effective HA adsorption, but only when soil organic matter had not been removed previously. Isotherms confirmed adsorption by natural soil ($> 2.5$ mg C g$^{-1}$). Because the isotherms showed no relation with temperature, adsorption would be better attributed to weak physical interactions. On natural surfaces with HA, soil particle attraction forces increased slightly ($\approx$50 kT) through decreasing soil wettability. However, this effect on total surface energy was overcome largely by increasing electrostatic repulsive energy caused by the adsorption of negatively charged HA ($> 300$ kT). The DLVO-extended model showed that natural surfaces without $H_2O_2$ treatment or added HA seem to be the most favourable state for colloidal aggregate stability. We recommend some caution about the type and quality of organic matter added to increase organic carbon in soil.

## Highlights

- We applied the extended DLVO model to study humic acid adsorption and its effects on soil structure.
- Adsorption on soil surfaces with their natural organic matter was mostly by weak physical forces.
- Adsorption increased the total particle interaction energy through an increase in electrostatic repulsion.
- Adsorption of some types of organic matter might decrease the colloidal stability of aggregates.

## Introduction

Agriculture is probably the global activity that has the most effect on the soil carbon balance and soil organic matter (SOM) (Lal, 2013). The effect of agricultural practices on organic carbon adsorption has been studied by acquiring adsorption isotherms (Kothawala *et al*., 2008) or by assessing the effects of management on SOM pools (Aranda *et al*., 2011).

Not all soil carbon shows the same degree of stability. Soil organic matter pools can be defined according to their relative biological reactivity (Lützow *et al*., 2006). In essence, two main SOM stabilization mechanisms have been proposed (Plante *et al*., 2006), chemical recalcitrance of organic substances and formation of organo-mineral assemblages. The latter may be seen as a heterogeneous mechanism involving some physical and chemical interactions between organic molecules and mineral surfaces at several spatial scales. Once organo-mineral complexes form, they act simultaneously; they hinder access of microbes to organic substances through surface adsorption and form silt-sized assemblages (from clay domains and clusters to small microaggregates) by flocculation, which physically protect the SOM inside (Lützow *et al*., 2006; Plante *et al*., 2006). From a physicochemical point of view,

Correspondence: J. Calero. E-mail: jcalero@ujaen.es

Received 19 August 2016; revised version accepted 4 April 2017

adsorption and flocculation cannot strictly be separated because they depend on electrical and thermodynamic processes that occur between organic and mineral surfaces (Grasso *et al*., 2002; Plaza *et al*., 2015). The adsorption of organic molecules on surfaces and the tendency of a soil to flocculate and form silt-size microaggregates could reinforce each other, with consequent positive effects on the stabilization of SOM.

Surface properties of soil materials are characterized suitably by electrokinetic and thermodynamic measures (Baumgarten *et al.,* 2013; Hajnos *et al*., 2013). Soil particle behaviour can be assessed quickly by the zeta potential, which depends on both its electrical charge and composition of the medium (pH, ionic strength, etc.). Thus electrostatic interaction of soil particles could be characterized well by zeta potential (Somasundaran *et al*., 1997). Furthermore, surface free energy deals with thermodynamic and non-electrostatic forces that act on surfaces, such as van der Waals forces, hydrogen bonding, hydrophobic interactions, and so on. These forces oppose or add to the electrostatic effects that modify total interaction energy. Therefore, colloidal processes in soil are closely related to both clay mineralogy and the ionic characteristics of the soil solution (Séquaris, 2010; Barré *et al*., 2014; Plaza *et al*., 2015). The first depends mainly on the soil parent material, and the mechanisms mentioned above depend not only on soil management, but also on the geological material from which the soil formed (Aranda *et al.,* 2011). Thermodynamic and electrostatic interactions can be suitably integrated in the extended Derjaguin, Landau, Verwey and Overbeek (extended-DLVO) model (van Oss, 1994). Although the traditional DLVO model, which includes electrostatic and van der Waals forces only, has been used little to study clay particle aggregation for agricultural and environmental purposes (Li *et al*., 2013; Xu *et al*., 2015), the extended model, to the authors' knowledge, has never been used previously for this.

Olive groves are one of the most important land uses in the Andalusia Region (southern Spain). One of the main concerns of the Common Agricultural Policy and Spanish agroenvironmental laws is the maintenance of soil organic carbon contents. The soil of olive groves has less than 1% organic carbon (0.68%, according to Nieto *et al*., 2010), which is very small by European standards. Nevertheless, in previous research our group found a significant increase in soil organic carbon in organic olive groves (Aranda *et al*., 2011; Calero *et al*., 2013a; Aranda *et al*., 2016), which suggested that it could be a suitable way to improve this important soil–ecosystem service.

The purpose of this work was to characterize the adsorption of organic carbon and its role in the relative tendency of particles to flocculate in the soil of an olive grove by applying the extended-DLVO model. Experiments were carried out with a commercial humic acid as the adsorbate and the fine-earth fraction of soil (< 2 mm) as the sorbent. To understand the effects of natural organic matter on these processes, replicates were treated with $H_2O_2$ and compared with untreated samples. The electrostatic interactions were computed from electrokinetic measurements, whereas the dispersive and non-dispersive components of the extended-DLVO theory were calculated with the van Oss procedure. Finally, soil adsorption isotherms were fitted from batch experiments at several temperatures to establish qualitatively the predominant mechanism of organic carbon adsorption (physisorption or chemisorption).

## Materials and methods

### *Site description*

Soil samples were taken in the Atanor Valley, Jaén, southern Spain (37°46′58.81″N, 3°19′54.61″W; 671 m a.s.l.). The soil had a moderately deep profile (50-cm thick) with an Ah–Bt–BC horizon sequence and was classified as Cutanic Luvisol (FAO, 2006). The sample was taken from the 0–5-cm depth, corresponding to the Ah horizon. The soil, developed over Jurassic colluvial limestones, had been subjected to organic management for 16 years. Management is characterized by no-tilled soil, in which the vegetation cover is kept under control by mowing from early to late spring, animal manure is incorporated about every 4 years (approximately, 500 kg per tree) and no mineral fertilizers or pesticides are applied.

### *Soil analysis and mineralogy*

Four soil samples were taken at random in the intercanopy area of the olive grove and bulked to form a single sample. This sample was dried and gently sieved through a 2-mm mesh screen to obtain the fine-earth fraction of soil (< 2 mm). The procedures used to analyse the fine earth were as outlined by Page *et al.* (1982) and Klute (1986). The particle-size distribution was determined by the pipette method, organic carbon content by the Walkley–Black method (dichromate oxidation), pH (1:1 suspension in water) was measured by potentiometry, $CaCO_3$ equivalent was determined by the volumetric method with a Bernard calcimeter, cation exchange capacity (CEC) by the ammonium acetate-sodium acetate method (pH 7) and Fe oxides (extractable free forms) by inductively coupled plasma mass spectrometry (ICP-MS) from citrate-dithionite-bicarbonate extracts. The soil aggregate stability index (AS) was determined by wet sieving (Eijkelkamp Agrisearch Equipment, Giesbeek, the Netherlands). Mineralogical composition in the fine-earth fraction was determined by powder X-ray diffraction (XRD) with a Siemens D5000 (Siemens, Karlsruhe, Germany) diffractometer, Cu-K$\alpha$ radiation, 35 kV. Mineral percentages (phyllosilicates and other minerals) were estimated by measuring the relative area of the peaks and using the intensity factors method, which applies weighting factors on peak areas as a function of the relative absorption of X-rays by the different phases (Calero *et al.,* 2009).

The clay fraction (< 2 µm) was isolated by sedimentation, after removing organic matter with a 15% $H_2O_2$ solution and dispersing it with a 10% sodium polyphosphate solution. Nitrogen ($N_2$) surface area measurements were carried out with a Micromeritics surface area analyzer (Model Gemini 2360, Micromeritics, Norcross, USA), which calculates the specific surface area (SSA) according to the Brunauer–Emmett–Teller (BET) equation and also by the ethylene glycol monoethyl ether (EGME) method. The CEC of the clay fraction was measured by the ammonium acetate-sodium acetate method (pH 7). Clay mineralogy was determined by X-ray

diffraction (XRD), following the procedure described by Plaza *et al.* (2015). Iron oxides were removed previously with sodium citrate-dithionite bicarbonate (Page *et al.*, 1982) and later analysed by ICP-MS to obtain clay-free forms. Oriented aggregates of Mg-saturated samples (1 N magnesium chloride) were prepared by sedimentation, dried on glass slides and air-dried slides were treated with ethylene-glycol vapour. Oriented aggregates were analysed then in a Siemens D5000 diffractometer in the 3–30° $2\theta$ zone and the mineral percentages for clay fractions (Mg ethylene-glycol samples) were established by the 'relative peak area' (referred to as rpa) (Calero *et al.*, 2013b). Finally, ethylene glycol patterns of oriented aggregates in the 3–8° $2\theta$ zone were decomposed with DECOMPRX software (Lanson, 1997).

### *Surface properties*

*Sample pretreatments: removal of SOM and addition of commercial humic acids (HAs).* The fine-earth fraction of the soil (natural sample) was also subjected to three treatments, as explained in Plaza *et al.* (2015): SOM was removed with hydrogen peroxide ($H_2O_2$ sample), HA was added (HA sample) and HA was added to the soil treated previously with hydrogen peroxide ($H_2O_2$ plus HA sample). Soil organic matter was removed with a 15% $H_2O_2$ solution while heated at 70–80°C in a hot water bath. A 0.5-g $l^{-1}$ solution of commercial humic acid (sodic humate), the composition of which can be checked in Plaza *et al.* (2015), was used as the humic acid addition.

*Zeta potential and surface free energy.* To determine the zeta potential, the powdered fine earth from the natural sample was redispersed in various homogenized solutions and at different electrolyte concentrations, NaCl and $CaCl_2$ at $10^{-2}$ and $10^{-3}$ M, and $FeCl_3$ and $AlCl_3$ at $10^{-3}$ M. Dry powder for the above three treatments was also redispersed into the NaCl $10^{-3}$ M solution. After 24 hours, the solutions were agitated and the supernatant was measured with a Zetasizer 3000HS (Malvern Instruments, Malvern, UK). Zeta potential ($\zeta$) was calculated from the Smoluchowski relation with the following equation (Wang & Revil, 2010):

$$\zeta_{EP} = \frac{V\mu}{\varepsilon E_x}, \tag{1}$$

where $\zeta_{EP}$ is the electrophoretic $\zeta$, $V$ is the electrophoretic velocity, $\mu$ and $\varepsilon$ are the viscosity and permittivity of the medium, respectively, and $E_x$ is the axial electric field.

The surface free energy of samples was estimated by measuring the contact angles of three probe liquids over dry powdered pellets with a Ramé-Hart goniometer (Ramé-Hart Instrument Co., Succasunna, NJ, USA) following the procedure described in Plaza *et al.* (2015). The probe liquids were water, diiodomethane and formamide; the components $\gamma^+$, $\gamma^-$ and $\gamma^{LW}$ can be also checked in Plaza *et al.* (2015). To make the pellets, $10^{-3}$ M homoionized NaCl solutions were dried at 50°C in an oven until a dry powder was obtained, and compressed to $1.5 \times 10^4$ kg $cm^{-2}$ for 10 minutes. This procedure was also applied to the natural sample with $10^{-3}$ M solutions of $CaCl_2$, $FeCl_3$ and $AlCl_3$. According to van Oss (1994) and van Oss *et al.* (1988), the total surface free energy of solids or liquids is described as a sum of the dispersive Lifshitz–van der Waals component $\gamma^{LW}$ and the non-dispersive Lewis acid–base interaction $\gamma^{AB}$. The non-dispersive, polar $\gamma^{AB}$ interaction results from the electron-donor, $\gamma^-$, and electron-acceptor, $\gamma^+$, contributions. The relation between the contact angle $\theta$ and the components, $\gamma^{LW}$ and $\gamma^{AB}$, of the surface free energy of the solid (subscript 1), and the surface tension of the probe liquid can be written as:

$$2\sqrt{\gamma_1^{LW}\gamma_{Li}^{LW}} + 2\sqrt{\gamma_1^{+}\gamma_{Li}^{-}} + 2\sqrt{\gamma_1^{-}\gamma_{Li}^{+}} = \gamma_{Li}(1+\cos\theta), \tag{2}$$

where $\gamma_{Li}$ is the surface tension of liquid $i$, $i = 1 \ldots 3$, that forms a contact angle $\theta$ on the solid and $\gamma^{LW}{}_{Li}$, $\gamma^{+}{}_{Li}$ and $\gamma^{-}{}_{Li}$ are the surface tension components of the liquid. Thus, by measuring the contact angles $\theta$ of the three liquids mentioned, a three-equation system like Equation (2) can be solved to acquire the three unknown variables, $\gamma_1{}^{LW}$, $\gamma_1{}^{+}$ and $\gamma_1{}^{-}$. Finally, the $\gamma^{AB}$ component of the solid was found from the electron-donor and electron-acceptor parameters:

$$2\sqrt{\gamma_1^{+}\gamma_1^{-}} = \gamma^{AB}. \tag{3}$$

*Interfacial interactions between particles in aqueous media: extended-DLVO model.* Beyond the classical DLVO interactions, the electrostatic (EL) and Lifshitz–van der Waals (LW) forces, the extended-DLVO theory also considers the acid–base (AB) interactions. Therefore, for any system composed of the same type of particle (~~Equation (1)~~) dispersed in water (~~Equation (3)~~), the total interaction energy is given by:

$$\Delta G_{131}^{TOT} = \Delta G_{131}^{EL} + \Delta G_{131}^{LW} + \Delta G_{131}^{AB}, \tag{4}$$

where 131 denotes the particle–water–particle system. These three contributions depend on the nature of the surfaces and distance H (nm) away from each other. For a moderate and constant electric potential that fluctuates according to the diffuse double layer (DDL) model, the electrostatic energy can be found from (Duran *et al.*, 1998):

$$\Delta G_{131}^{EL} = 2\pi\varepsilon a\zeta^2 \ln\left(1 + e^{-\kappa H}\right), \tag{5}$$

where $\zeta$ is the zeta potential, $a$ the particle radius, $\varepsilon$ the dielectric constant of the liquid, and $\kappa$ the reciprocal of the Debye length (DDL thickness). The Lifshitz–van der Waals component is given by:

$$\Delta G_{131}^{LW} = -\frac{A_{131}}{6}\left(\frac{2a^2}{H(4a+H)} + \frac{2a^2}{(2a+H)^2}\right) + \ln\frac{H(4a+H)}{(2a+H)^2}, \tag{6}$$

where $A_{131}$ is the Hamaker constant for the system that can be calculated from the surface tension of the materials analysed. If $\gamma_i^{LW}$ is known for water and solids (particles), Hamaker's constant can be found from (van Oss, 1994):

$$A_{131} = 12\pi H_0^2 \Delta G_{131,H_0}^{LW}, \tag{7}$$

**Table 1** Selected properties of the fine-earth (< 2 mm) and clay fractions (< 2 µm) of soil

| Fine earth (< 2 mm) | | | | | | | | | Clay (< 0.002 mm) | | | |
|---|---|---|---|---|---|---|---|---|---|---|---|---|
| C.F / % | Sand / % | Clay / % | OC / % | pH $_{H2O}$ | $CaCO_3$ / % | $Fe_{CDB}$ / % | CEC / $cmol_+ kg^{-1}$ | AS* | $Fe_{CDB}$ / % | CEC / $cmol_+ kg^{-1}$ | SSA-EGME / $m^2 g^{-1}$ | SSA-BET / $m^2 g^{-1}$ |
| 59 | 18 | 48 | 3.39 | 7.8 | 12.3 | 0.863 | 25.25 | 0.99 | 6.34 | 24.02 | 215 | 24 |

CF, coarse fragments; OC, total organic carbon; $Fe_{CDB}$, citrate-dithionite-bicarbonate iron; CEC, cation exchange capacity; *AS, aggregate stability index = A/B × 100, A, weight of stable soil macroaggregates (≥ 0.25 mm) resisting wet sieving, B, weight of unstable soil macroaggregates (≥ 0.25 mm) passing through the 0.25-mm grid; SSA-EGME, specific surface area (ethylene glycol mono ethyl ether method); SSA-BET, specific surface area ($N_2$ adsorption method).

$$\Delta G^{LW}_{131,H_0} = -2\left(\sqrt{\gamma_1^{LW}} - \sqrt{\gamma_3^{LW}}\right)^2, \quad (8)$$

where $H_0$ is estimated to be $1.58 \pm 0.08$ Å (van Oss *et al*., 1988). Likewise, calculation of the relation between $H$ and $\Delta G^{AB}_{131}$ entails knowing $\gamma^-$ and $\gamma^+$ in phases 1 and 3; therefore:

$$\Delta G^{AB}_{131} = 2\pi a\lambda\Delta G^{AB}_{131,H_0} e^{\left(\frac{H_0 - H}{\lambda}\right)}, \quad (9)$$

where $\lambda$ is the correlation length of water molecules, which is approximately $\lambda = 1$ nm for hydrophilic surfaces (van Oss, 1994), and $\Delta G^{AB}_{131}$ depends on the acid–base parameters of the free energy of phases 1 and 3. According to van Oss, $\Delta G^{AB}_{131,H0}$ is given by:

$$\Delta G^{AB}_{131,H_0} = 4\left(\sqrt{\gamma_1^+\gamma_1^-} + \sqrt{\gamma_3^+\gamma_3^-} - \sqrt{\gamma_1^+\gamma_3^-} - \sqrt{\gamma_3^+\gamma_1^-}\right), \quad (10)$$

which gives the total interaction energy (Equation (4)) in the system. The relative tendency of soil to flocculate and form aggregates, or on the contrary to disperse and destroy the soil structure with the consequent release of carbon stabilized by occlusion, can be estimated using this value.

*Transmission electron microscopy*. The $10^{-3}$ M homoionized NaCl powder of the four replicates was examined by transmission electron microscopy (TEM) with a JEOL JEM-1010 (JEOL, Peabody, MA, USA) operating at 80 000 kV to obtain information on particle morphology and flocculation and at three magnifications, 5000, 10 000 and 60 000×.

*Batch experiments*. The amount of humic acid (39.03% C) adsorbed on fine earth of natural and $H_2O_2$-treated samples with different concentrations of adsorbate at different temperatures was estimated from the difference between the final and initial concentrations in solution, once the sorption equilibrium had been attained. First, 1–500 mg $l^{-1}$ aqueous solutions of humic acid were prepared. Second, 1000 mg of fine earth were added to 25-ml aliquots of solution in 50-ml centrifuge tubes to complete saturation, with the pH of solutions adjusted to the soil pH with HCl and NaOH. During the process, solutions were stirred gently in an orbital shaker while controlling temperature with a hot water bath at adsorption experiment temperatures of 283, 293 and 313 K (10, 20 and 40°C, respectively). Humic acid was removed from the solution after previously monitoring absorbance at 24-hour intervals for 6 days of incubation (293 K). No adsorption was detected after 96 hours; therefore, this was chosen as the optimum time to reach equilibrium. This also allowed us to discard any substantial desorption from samples because a steady decrease in absorbance occurred until the fourth day. The optical absorbance of the HA solutions was measured at 554 nm with a Hitachi U-2000 model (Hitachi Ltd, Tokyo, Japan) spectrophotometer (see Ramos-Tejada *et al*., 2003).

## Results and discussion

### *Soil components and properties*

The soil (Table 1) is stony (59% coarse fragments) and clayey (48% clay), the amount of carbonates (12.3% $CaCO_3$) is moderate and organic carbon content is large (3.39%) compared with soil in the Mediterranean study area under conventional tillage. Because of its clayey texture and large OC content, the soil has a large cation exchange capacity (CEC, 25.25 $cmol_+ kg^{-1}$) and a well-developed structure (aggregate stability index of 0.99). The CEC of the clay (24.02 $cmol_+ kg^{-1}$) shows that it is a high-activity clay in terms of its CEC, corresponding to vermiculite or smectite phases, or both. The results for chemical analysis of the fine earth (Table 2, Figure 1) and XRD analysis of the clay mineralogy (Table 2, Figure 2) were consistent. This supported the quantitative determination of mineral phases given in Table 2. The soil is calcareous with a large proportion of phyllosilicates (70%). Strongly-charged non-swelling phases such as illite (41% rpa) or vermiculite (23% rpa, including vermiculite-mixed layer clays) are the most abundant phyllosilicates. This explains the large CEC of the fine earth and clay fractions. Moderate smectite-mixed layers (16% rpa) and kaolinite (8% rpa) were also present. Free iron concentrates were present in the clay at a moderate-to-large percentage (6.34%) for Mediterranean soil. A considerable difference in SSA was identified by the method used: 215 $m^2 g^{-1}$ by EGME compared with 24 $m^2 g^{-1}$ by BET. This might be attributed to the smectite phases because EGME measurements can also estimate internal surfaces in phyllosilicate interlayer spaces (Wiseman & Puttmann, 2005), but both the CEC and SSA are large, regardless of the method used.

**Table 2** The XRD analysis of mineralogical composition of the fine-earth (< 2 mm) and clay fractions (< 2 µm) of soil

| Fine earth mineral composition / %[a] | | | | | | | Clay fraction/ relative peak area, %[b] | | | | | | |
|---|---|---|---|---|---|---|---|---|---|---|---|---|---|
| Q | Phy | FK | FNa | OxFe | Cal | Dol | Sm | I | V | Chl | K | Fd | Q | Cal |
| 14 | 70 | tr. | tr. | > 5 | 11 | tr. | 16 | 41 | 23 | 4 | 8 | 3 | 2 | 3 |

[a]Disoriented powder method.
[b]Mg ethylene-glycol samples, oriented aggregate method.
Phy, phyllosilicates; Q, quartz; FK, potassium feldspar; FNa, sodium feldspar; OxFe, iron oxides (goethite and haematite); Cal, calcite; Dol, dolomite; tr, traces (< 1%); Sm, including smectite and smectite-mixed layer; I, illite; V, including vermiculite and vermiculite-mixed layers; Chl, chlorite; K, kaolinite; Q, quartz; Fd, potassium feldspar + plagioclase.

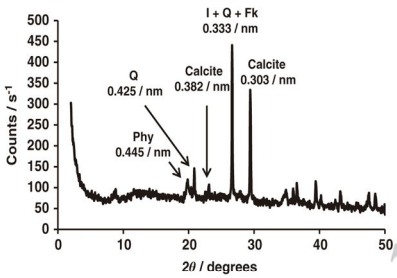


**Figure 1** The X-ray diffraction (XRD) pattern of disoriented powder for the fine-earth fraction of soil (< 2 mm). Phy, phyllosilicates; Q, quartz; FK, potassium feldspar; I, illite.

*Zeta potential*

Figure 3 shows the zeta potential for different electrolytes on the natural sample. A smooth continuous decrease in zeta potential with increasing pH in sodium solutions (Figure 3a) can be seen at both $10^{-3}$ and $10^{-2}$ M. This could be attributed to dissociation of ionizable organic and mineral groups, which cause an increase in negative pH-dependent charges. These include clay surfaces, the octahedral edges of 2:1 phyllosilicates (smectite, vermiculite and illite), kaolinite and free iron oxides, and the organic functional groups of humic acids (i.e. –COOH, –OH, and so on.). The ranges in zeta potential measured (from −5 to −35 mV) were reliable for those established for pure illite (Hussain *et al*., 1996; Sondi *et al*., 1996), which established that this phyllosilicate was the most abundant and was the main phase that controlled the electrokinetic behaviour of this soil. An anomalous, but not unusual, variation in zeta potential occurred for ionic strength in which the more concentrated solution ($10^{-2}$ M) gave larger absolute values than the more diluted ($10^{-3}$ M) (Plaza *et al*., 2015). Zeta potential in calcium solutions (Figure 3b) is pH independent at a pH below 8. This effect has been described previously by Plaza *et al.* (2015); Thomas *et al.* (1999) and Lagaly (2006) in smectites, by Duman & Tunc (2008) in vermiculites and by Martínez *et al.* (2010) in illites. Iron and aluminum salts (Figure 3c) produced positive charges related to their Lewis-acid character at acid to neutral pH (< 8.0). These pH-dependent charges neutralized the negative permanent phyllosilicate charges to give a positive soil zeta potential. For iron, the isoelectric point was reached at the pH of the natural soil (approximately 7.8, Table 3), but for aluminum it was reached at pH 9. This has been described several times for soil treated with trivalent cations (Plaza *et al*., 2015).

The combined effect of removing soil organic matter and adding HA over natural and previously $H_2O_2$-treated sodium solutions at an ionic strength of $10^{-3}$ M is shown in Figure 4. The variation in zeta potential with pH in the HA-added soil sample is similar to that of the natural soil, which decreases over the entire pH range studied (from 3 to 10). The absolute values, however, are larger after the addition of HA; their difference is up to 10 mV at a pH of about 4.0 (Figure 4). This increase must be understood as the effective adsorption of humic acid molecules on to natural soil surfaces where the zeta potential increases as a result of the dissociation of ionizable groups (i.e. –COOH) of the humic acid added. Comparable results have also been reported in samples with commercial humic acids from pure illite (Martínez *et al.*, 2010) and montmorillonite (Ramos-Tejada *et al*., 2003). The removal of soil organic matter by $H_2O_2$ involves no changes in zeta potential in the acid range; it remains at around −15 mV at pH ≈ 6.5. This might indicate the limited protonation capacity of 2:1 phyllosilicate surfaces, which are conditioned mainly by permanent negative charges. At pH > 6.5, however, deprotonation of surfaces resulted in an increase in negative charges. Humic acid added to $H_2O_2$-treated surfaces did not result in substantial changes in zeta potential, and so both curves almost overlap. Thus, it seems that no effective HA adsorption occurs over the pH range studied. These results show the positive effects of soil organic matter in the subsequent adsorption of dissolved organic carbon.

*Surface free energy*

Table 3 gives surface free energy components of soil with the different treatments (cations, $H_2O_2$ and HA). The results show that the soil is an essentially monopolar solid with a large electron-donor component ($\gamma^-$) that varies from 53.7 to 40.0 mJ m$^{-2}$ and negligible electron-acceptor component ($\gamma^+$) close to zero. The electron-donor and dispersive ($\gamma^{LW}$) components also had approximately the same weight, which is often found in mineral soil (Hajnos *et al*., 2013). Our soil has a monopolar character and might have relevant polar interactions with electron-acceptor phases ($\gamma^+$) only, which must be considered in the explanation of adsorption of humic acid molecules. Electron-donor characteristics depend on the cation used; they decrease from 53.5 mJ m$^{-2}$ in the sodium-saturated sample to 42.2 and 48.3 mJ m$^{-2}$ in calcium and aluminum samples, respectively. It remained constant in the iron solution (53.7 mJ m$^{-2}$), however. Although treatment with $H_2O_2$ did not modify $\gamma^-$ (53.3 mJ m$^{-2}$) with respect to the natural surfaces, the addition of HA decreased it considerably to 40.0 mJ m$^{-2}$,

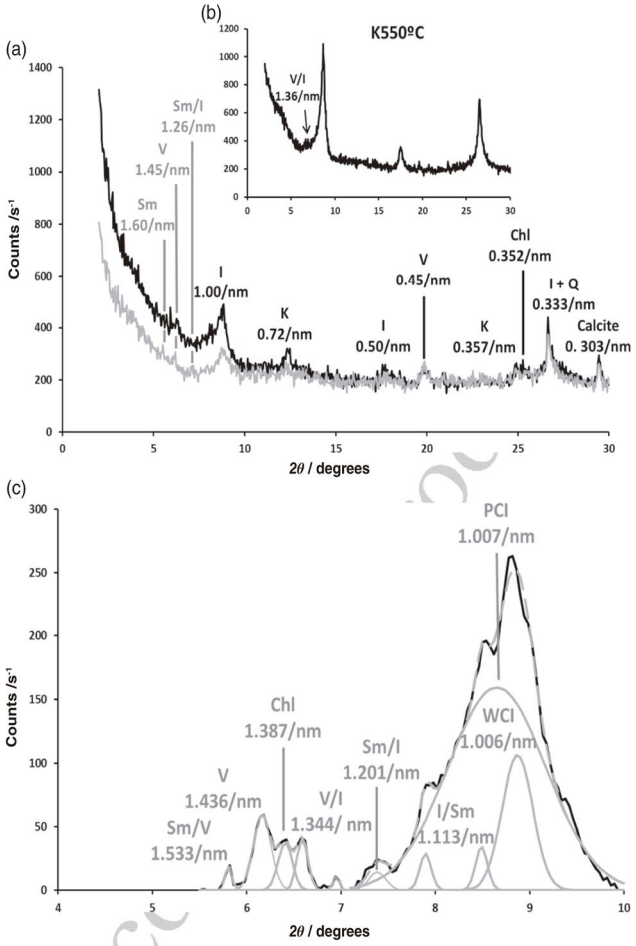


**Figure 2** The X-ray diffraction (XRD) pattern of oriented aggregates in the soil clay fraction (< 2 µm). (a) Magnesium air-dried (black line) and glycolated samples (grey line) in 3–30° 2$\theta$, (b) potassium 550°C pattern in 3–30° 2$\theta$ and (c) decomposed XRD-pattern for the magnesium glycolated samples in 4–10° 2$\theta$. Sm, smectite; V, vermiculite; Sm/V, smectite–vermiculite mixed layer; Sm/I, smectite–illite mixed layer; I/Sm, illite–smectite mixed layer; V/I, vermiculite–illite mixed layer; I, illite; WCI, well-crystallized illite; PCI, poorly crystallized illite; K, kaolinite; Chl, chlorite; Q, quartz.

which diminished its relative hydrophilicity. The addition of HA had a greater effect when the soil's natural organic matter had not been removed than after the surface had been treated with $H_2O_2$, where $\gamma^-$ decreased to 49.9 mJ m$^{-2}$ only. Like the variation in zeta potential curves with HA, divergence such as 13.3 mJ m$^{-2}$ in some components of surface free energy must be interpreted as effective adsorption of HA. Thus, unlike $\gamma^+$ and $\gamma^{LW}$, which do not vary noticeably with treatment and the cations used (range < 7 mJ m$^{-2}$), the electron-donor component $\gamma^-$ was quite sensitive to the ionic and HA treatments (range ≈ 14 mJ m$^{-2}$), and might be a good property for assessing change in surface adsorption processes. Despite these changes, all the surfaces studied were clearly hydrophilic because they were over 28.9 mJ m$^{-2}$, the van Oss & Giese (1995) threshold for clay mineral hydrophobicity.

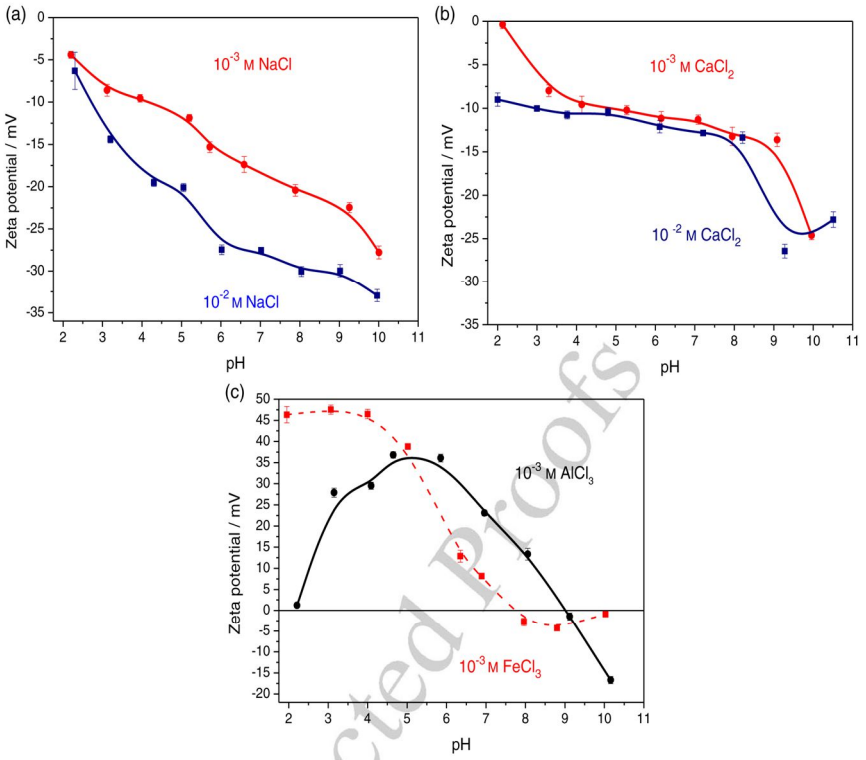


**Figure 3** Effects of ionic strength and ion type on natural soil zeta potential. (a) Monovalent ion, (b) divalent ion and (c) trivalent ion.



*Total energy of interaction between soil particles*

Humic acid adsorption changes the behaviour of soil surfaces, including electrical and thermodynamic interactions of soil particles. These changes would affect soil structure and aggregate stability, and are therefore a key factor in the physical stabilization of soil organic matter. Changes in the aggregation dynamics might be characterized by the total potential interaction energy computed from the extended DLVO theory, including acid–base interactions. Figure 5 shows typical plots of the total interaction energy $\Delta G^{TOT}_{131}$ between two identical particles (subscript 1) in a dispersion medium (subscript 3), as a function of their separation $H$ (nm) from the particle surface. A negative sign of $\Delta G^{TOT}_{131}$ indicates a primary or secondary energy minimum and an attractive force that tends to produce colloid aggregation, whereas a positive sign implies a repulsive force that hinders it. Because phyllosilicate clays modified more or less by the HA adsorbed only are considered here, the colloidal surfaces are all the same type and will always give repulsive values of the electrostatic force (EL), which were strongly related to pH: the larger is the zeta potential (absolute value), the stronger is the repulsion. In the non-dispersive (AB) polar interaction, the monopolar and hydrophilic nature of the samples also causes net repulsion between particles according to Equations (9) and (10). The AB repulsion force results from the excess in hydration pressure generated by the motion and orientation restrictions of water molecules on colloidal surfaces (hydration shells) because of hydrogen bonding (Grasso *et al.*, 2002). Finally, the dispersive component (LW) always attracts ($\Delta G^{LW}_{131}$ negative). If AB forces and the repulsive electrostatic forces together are stronger than LW attraction, the overall interaction would be repulsive and soil aggregates would tend to be mechanically unstable in water. The stronger is the repulsion, the greater is the instability.

The relative contributions of each type of interaction (AB, LW and EL) in the natural sodium samples calculated at the soil's pH of 7.8 can be evaluated in Figure 5(a). The acid–base force is relevant

**Table 3** Zeta potential ($\zeta$), Hamaker constant ($A_{131}$) and surface free energy for soil samples with several treatments (ions, hydrogen peroxide and humic acids)

| Treatment ($10^{-3}$ M) | | $\zeta$ / mV | | | $A_{131}$ / J | Surface free energy / mJ m$^{-2}$ | | |
|---|---|---|---|---|---|---|---|---|
| | | pH 7.8 | pH 6.0 | pH 4.5 | | $\gamma^{LW}$ | $\gamma^-$ | $\gamma^+$ |
| NaCl | Natural | −20.6 | −15.9 | −10.9 | $9.36\times10^{-21}$ | 47.8 ± 0.4 | 53.5 ± 0.1 | 0.02 ± 0.1 |
| | Natural + HA | −24.0 | −20.0 | −18.0 | $8.59\times10^{-21}$ | 46.5 ± 0.3 | 40.0 ± 0.3 | 0.09 ± 0.1 |
| | $H_2O_2$ | −24.9 | −15.3 | −14.0 | $8.18\times10^{-21}$ | 45.8 ± 0.2 | 53.3 ± 0.1 | 0.27 ± 0.1 |
| | $H_2O_2$ + HA | −25.7 | −15.4 | −14.0 | $9.36\times10^{-31}$ | 47.8 ± 0.2 | 49.9 ± 0.2 | 0.06 ± 0.1 |
| $CaCl_2$ | | −13.0 | −11.2 | −10.0 | $8.18\times10^{-21}$ | 45.8 ± 0.1 | 42.2 ± 0.3 | 0.41 ± 01 |
| $AlCl_3$ | | 11.6 | 35.0 | 36.6 | $5.64\times10^{-21}$ | 41.1 ± 0.2 | 48.3 ± 0.2 | 0.19 ± 0.2 |
| $FeCl_3$ | | −2.2 | 22.0 | 43.0 | $6.20\times10^{-21}$ | 42.2 ± 0.3 | 53.7 ± 0.1 | 0.19 ± 0.1 |
| NaCl ($10^{-2}$ M) | | −29.7 | −27.3 | −19.0 | $9.36\times10^{-21}$ | 47.8 ± 0.4 | 53.5 ± 0.1 | 0.02 ± 0.1 |

Natural + HA, natural sample plus humic acid; $H_2O_2$, sample treated with hydrogen peroxide; $H_2O_2$ + HA, sample treated with hydrogen peroxide plus humic acids.

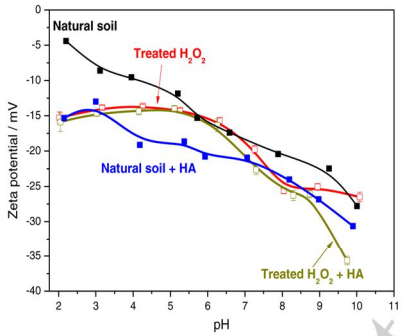


Color online, B&W in print

**Figure 4** Effects of hydrogen peroxide treatment and humic acid adsorption on soil zeta potential ($10^{-3}$ M NaCl ionic strength).

only at short range and becomes negligible above 5 nm. When the AB and LW forces are opposite they cancel each other out and the total energy is mainly from electrostatic interaction. The effects of ionic strength (Figure 5b) and cations (Figure 5c,d) on total surface energy are also shown. The $\Delta G^{LW}_{131}$ can be computed from $\gamma^{LW}$ in Table 3 by applying Equations (6–8). The acid–base component, $\Delta G^{AB}_{131}$, can be obtained from $\gamma^+$ and $\gamma^-$ from Equations (9) and (10). These equations show that the dispersive interaction is quite indifferent from the solution; it ranges from 40 to 56 kT at 3 nm for iron and calcium, respectively. Likewise, the acid–base interaction was similar for sodium and iron (380 and 370 kT at 3 nm, respectively), but smaller for calcium (290 kT at 3 nm). The above suggests that the soil $\Delta G^{TOT}_{131}$ for cations at distances > 5 nm (Figure 5c) can be explained mainly by electrostatic interaction, and ultimately by zeta potential curves at pH 7.8 (Equation (5)). The repulsive force between soil particles increases with ionic valence of the cation, and is stronger in those that are monovalent than trivalent. However, a secondary energy minimum ($\Delta G^{TOT}_{131} < 0$) occurs at $H > 100$ nm for all the cations studied at $10^{-3}$ M (Figure 5d). In spite of its small value, this might justify the colloidal aggregation described by Zhang *et al.* (2010). In $Fe^{3+}$, the strongly protonated and positively charged surfaces at pH < 5 have strong electrostatic repulsion ($\Delta G^{EL}_{131}$ over 1000 kT at 10 nm and pH 4.5, computed from the zeta potential in Table 3 with Equation (5)), reaching zero at the soil pH of ≈8, the zero charge point of soil particles in $FeCl_3$ solutions (Figure 3c). When the $\Delta G^{EL}_{131}$ force at the soil pH is added to the slightly repulsive balance between AB and LW, the total interaction energy $\Delta G^{TOT}_{131}$ for iron is < 100 kT at 10 nm (Figure 5c), which might be the most favourable aggregation state for this soil–colloidal system. Positive effects of trivalent cations on soil colloidal aggregation have been widely recognized (Lützow *et al.*, 2006). For calcium, the electrostatic forces were repulsive, but of moderate intensity, for all the pH values (Figure 3b). This resulted in $\Delta G^{EL}_{131} < 150$ kT at 10 nm, (Figure 5c); therefore, it should also be considered a favourable cation for clay particle flocculation and aggregation. On the contrary, repulsion was stronger in sodium samples ($\Delta G^{EL}_{131} > 150$ kT at 10 nm), which might also be explained by the zeta potential curves. The presence of $Ca^{2+}$ confers more stability to the soil structure than $Na^+$. According to the extended-DLVO model, the best flocculation conditions in iron solutions are with neutral to basic pH, contrary to $Na^+$ and $Ca^{2+}$ ions for which relative flocculation improves in acidic pH. The effects of ionic strength on total surface energy (sodium sample, Figure 5b) also reflect zeta potential, and at $10^{-2}$ M surface potential is larger than in the more diluted $10^{-3}$ M.

Figure 6 shows the effects of HA in the natural and $H_2O_2$-treated NaCl $10^{-3}$ M solutions at acid, neutral and basic pH. Given the relevance of electrostatic forces in total interaction energy, samples behave as expected based on their zeta potential curves (Figure 4). Small secondary energy minima also occurred for these samples at pH 7.8, 6 and 4.5 (Figure 6b,d,f, respectively). At soil pH, $\Delta G^{TOT}_{131}$ for $H_2O_2$-treated sample curves had a strong repulsive potential (> 400 kT at 10 nm) and almost overlapped. This indicates no HA adsorption on $H_2O_2$-treated surfaces, which were also less favourable for soil particle flocculation and aggregation. According to Séquaris (2010), these results could be extended to other cations such as calcium. On the contrary, in sodium solutions mineral

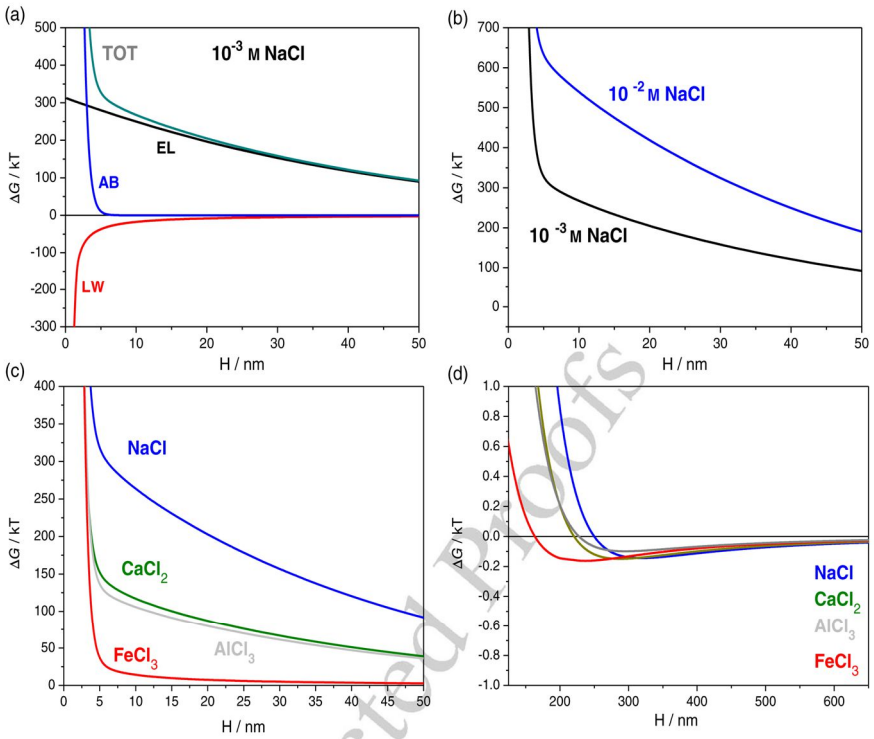


**Figure 5** Total interaction energy at the soil pH 7.8. (a) Total-energy components ($10^{-3}$ M NaCl), (b) effect of ionic strength, (c) effect of ion type ($10^{-3}$ M) and (d) secondary energy minimum for ion type ($10^{-3}$ M). TOT, total energy; EL, electrostatic component; AB, acid–base component; LW, Lifshitz–van der Waals component.

surfaces with their own organic matter provide the most favourable flocculation conditions; they had the smallest surface potentials (< 300 kT at 10 nm). Humic acids adsorbed on natural surfaces increased the electrostatic interaction $\Delta G^{EL}_{131}$ by about 100 kT, mainly from the increase in negative charge (zeta potential from −21 to −24 mV, Table 3). Séquaris (2010) reported a similar effect of more stability in soil colloid dispersion in the presence of organic carbon, which is attributed to an increase in zeta potential leading to electrostatic repulsion. Despite this, a moderate but noteworthy difference of about 50 kT in surface potentials between the natural plus HA and the two $H_2O_2$-treated samples was observed. Because their zeta potential curves almost match at pH 7.8 (in a range of ±2 mV for the three samples), this difference could be attributed to the decrease in $\gamma^-$ from about 50 mJ m$^{-2}$ on $H_2O_2$-treated surfaces to 40.0 mJ m$^{-2}$ in the natural plus HA sample (Table 3). Thus adsorption of HA contributed to a reduction in total surface potential, which made the system less repulsive because of a small increase in its relative hydrophobicity. The AB interaction implemented in the extended-DLVO model could be relevant for explaining flocculation even in fairly wettable particles such as those considered here. Surface potentials at slightly acid to neutral pH (6.0, Figure 6c) and acid pH (4.5, Figure 6e) were also closely correlated with zeta potential values. A progressive increase in particle repulsion force with an increase in pH can be observed.

### *Transmission electron microscope (TEM) images and adsorption isotherms*

Colloidal-scale soil aggregation observed under TEM (Figure 7) broadly confirms what was predicted by the total interaction energy at the soil's pH of 7.8. The smaller total surface energies correspond with larger flocculated soil fabrics (natural and natural plus HA, Figure 7a,b, respectively), whereas the $H_2O_2$-treated samples (without and with HA, Figure 7c,d, respectively) show

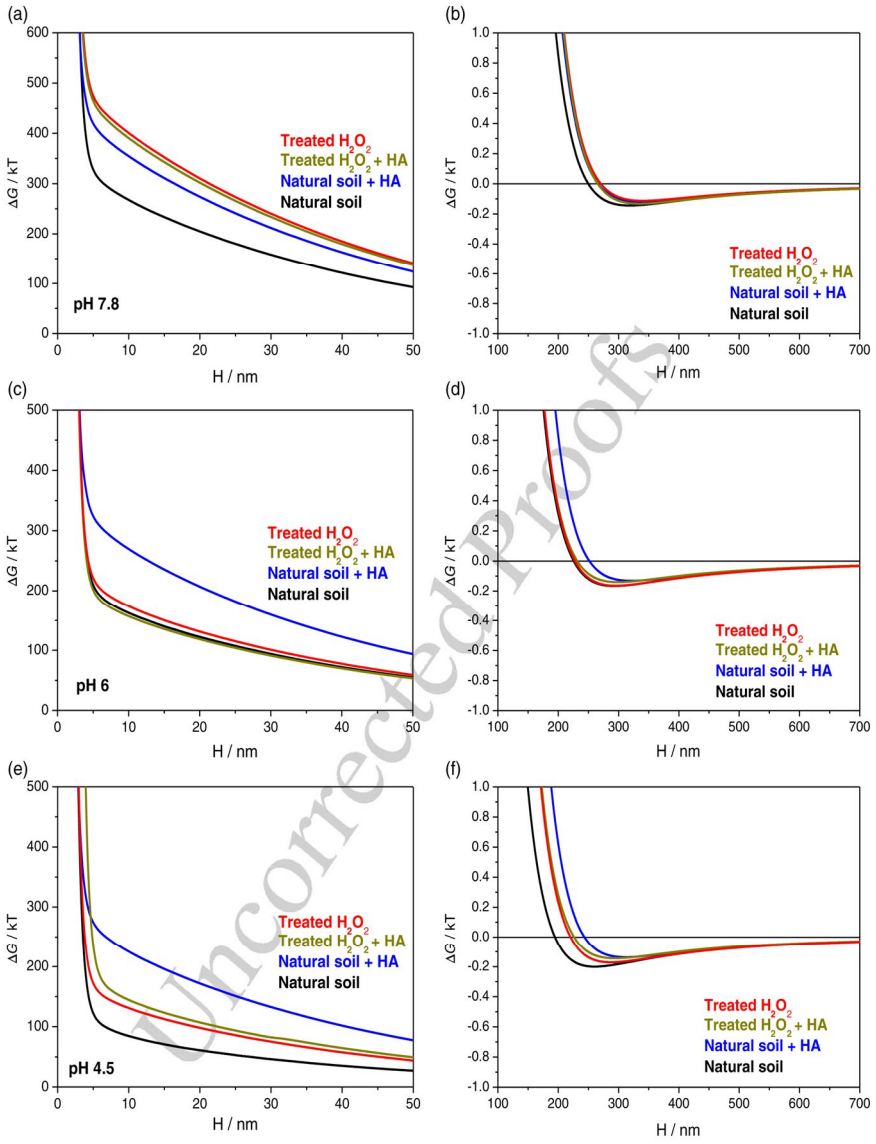


**Figure 6** Effects of hydrogen peroxide treatment and humic acid adsorption on the total interaction energy ($10^{-3}$ M, NaCl ionic strength). (a) Soil pH 7.8, (b) secondary energy minimum at soil pH 7.8, (c) pH 6, (d) secondary energy minimum at pH 6, (e) pH 4.5 and (f) secondary energy minimum at pH 4.5.

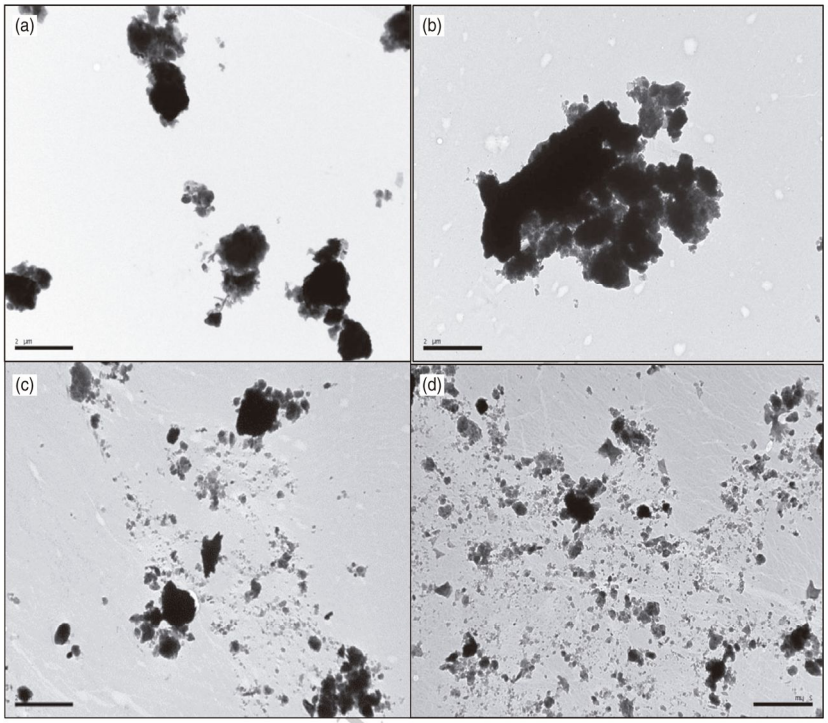


**Figure 7** The transmission electron microscopy (TEM) images of natural and peroxide-treated samples. (a) Natural sample, (b) natural sample plus humic acid, (c) peroxide-treated sample plus humic acids and (d) peroxide-treated sample. Scale bar represents 2 μm.

extensive dispersion, especially the one with no added HA. The natural plus HA sample appears to have the more flocculated fabric in the TEM images and differs from the prediction based on $\Delta G^{TOT}_{131}$ only.

Figure 8 shows HA adsorption isotherms at 283, 293 and 313 K (10, 20 and 40°C) and pH 7.8 that include the natural (Figure 8a) and $H_2O_2$-treated (Figure 8b) samples. Adsorption of C (mg $g^{-1}$) from humic acid in the natural soil is in the range for pure illite clay (Saidy *et al.*, 2013) and corresponds broadly with the adsorption identified by Kaiser *et al.* (1996) and Kothawala *et al.* (2008), but it was considerably larger than that determined by Vandenbruwane *et al.* (2007). Adsorption on the $H_2O_2$-treated surface was less than in the natural soil at any temperature tested, but particularly at the lower temperatures. There were no clear trends that related adsorption capacity and temperature in the natural soil. The surfaces adsorb the same amount of HA regardless of temperature. On the peroxide-treated surfaces, however, there was more adsorption at the higher temperatures. This indicates a predominance of chemisorption, whereas the absence of clear patterns of temperature dependence might indicate the dominance of weak physical mechanisms, such as hydrogen bonding or Van der Waals interactions. This accords with Kaiser *et al.* (1996), who found that small surface loadings of C, such as $H_2O_2$-treated surfaces, could indicate stronger binding mechanisms such as ligand exchange, whereas larger loads reduce their strength.

## Conclusions

The van Oss extended-DLVO model was applied for the first time to clay particle aggregation and humic acid (HA) adsorption in agricultural soils. Non-classical forces implemented in this model, such as acid–base (AB) interaction, helped to characterize HA adsorption and particle flocculation. The most favourable cation for aggregation was $Fe^{3+}$ followed by $Ca^{2+}$. In sodium samples, HA adsorption occurred only on surfaces from which natural organic matter had not been previously removed by hydrogen peroxide. Adsorption was verified by isotherms, which also showed the importance of weak interactions, such as the AB forces, in the

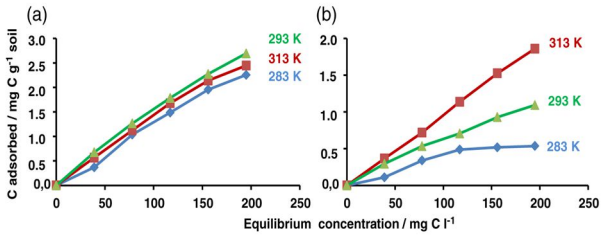


**Figure 8** Isotherms of the adsorption of carbon from humic acids at different temperatures. (a) Natural soil and (b) hydrogen peroxide-treated soil.

process. Humic acid adsorption produced a decrease in the total interaction energy, which slightly improved flocculation through a decrease in soil wettability. This was overcome, however, by the increase in repulsive electrostatic energy caused by humic acids and so the overall effect of the adsorbed HA was unfavourable for soil particle aggregation. Therefore, the type of soil organic matter used in soil amendments to increase soil carbon adsorption and storage should be chosen with care. In some cases, the possibility of interference between organic carbon adsorption on mineral surfaces and the stabilization of colloidal-scale soil structure should be considered.

## Acknowledgements

We thank Professor Margaret Oliver for her comments on the manuscript and valuable suggestions. This study was supported by the Institute of Jaen Studies ('Instituto de Estudios Giennenses') Project no RFC/IEG 2015.

## References

Aranda, V., Ayora, M., Domínguez, A., Martín, J., Calero, J., Delgado, R. *et al.* 2011. Effect of soli type and management (organic vs. conventional) on soil organic matter quality in olive groves in a semi-arid environment in Sierra Mágina Natural Park (S Spain). *Geoderma*, **164**, 54–63.

Aranda, V., Calero, J., Plaza, I. & Ontiveros-Ortega, A. 2016. Long-term effects of olive mil pomace co-compost on wettability and soil quality in olive groves. *Geoderma*, **267**, 185–195.

Barré, P., Fernandez-Ugalde, O., Virto, I., Velde, B. & Chenu, C. 2014. Impact of phyllosilicate mineralogy on organic carbon stabilization in soils: incomplete knowledge and exciting prospects. *Geoderma*, **235–236**, 382–395.

Baumgarten, W., Dörner, J. & Horn, R. 2013. Microstructural development in volcanic ash soils from South Chile. *Soil & Tillage Research*, **129**, 48–60.

Calero, J., Delgado, R., Delgado, G. & Martín-García, J.M. 2009. SEM image analysis in the study of a soil chronosequence on fluvial terraces of the middle Guadalquivir (southern Spain). *European Journal of Soil Science*, **60**, 465–480.

Calero, J., Cordovilla, M.P., Aranda, V., Borjas, R. & Aparicio, C. 2013a. Effect of organic agriculture and soil forming factors on soil quality and physiology of olive trees. *Agroecology and Sustainable Food Systems*, **37**, 193–214.

Calero, J., Martín-García, J.M., Delgado, G., Aranda, V. & Delgado, R. 2013b. A nano-scale study in a soil chronosequence from southern Spain. *European Journal of Soil Science*, **64**, 192–209.

Duman, O. & Tunc, S. 2008. Electrokinetic properties of vermiculite and expanded vermiculite: effects of pH, clay concentration and mono- and multivalent electrolytes. *Separation Science and Technology*, **43**, 3755–3776.

Duran, J.D.G., Ontiveros, A., Delgado, A.V. & González-Caballero, F. 1998. Kinetics and interfacial interactions in the adhesion of colloidal calcium carbonate to glass in a packed-bed. *Applied Surface Science*, **134**, 125–138.

FAO 2006. *World Reference Base for Soil Resources. A Framework for International Classification, Correlation and Communication*. World Soil Resources Report No 103, Food and Agriculture Organization of the United Nations, Rome.

Grasso, D., Subramanian, K., Butkus, M., Strevett, K. & Bergendahl, J. 2002. A review of non-DLVO interactions in environmental colloidal systems. *Reviews in Environmental Science and Biotechnology*, **1**, 17–38.

Hajnos, M., Calka, A. & Jozefaciuk, G. 2013. Wettability of mineral soils. *Geoderma*, **206**, 63–69.

Hussain, S.A., Demirci, S. & Özbayoglu, G. 1996. Zeta potential measurements on three clays from Turkey and effects of clays on coal flotation. *Journal of Colloid and Interface Science*, **184**, 535–541.

Kaiser, K., Guggenberger, G. & Zech, W. 1996. Sorption of DOM and DOM fractions to forest soils. *Geoderma*, **74**, 281–303.

Klute, A. 1986. *Methods of Soil Analysis. Part 1*, Agronomy Monographs, 9. ASA and SSSA, Madison, WI.

Kothawala, D.N., Moore, T.R. & Hendershot, W.H. 2008. Adsorption of dissolved organic carbon to mineral soils: a comparison of four isotherms approaches. *Geoderma*, **148**, 43–50.

Lagaly, G. 2006. Colloid clay science. In: *Handbook of Clay Science* (eds F. Bergaya, B.K.G. Theng & G. Lagaly), pp. 247–260. Elsevier, Amsterdam.

Lal, R. 2013. Soil carbon management and climate change. *Carbon Management*, **4**, 439–462.

Lanson, B. 1997. Decomposition of experimental X-ray diffraction profile (profile fitting): a convenient way to study clay minerals. *Clays and Clay Minerals*, **45**, 132–146.

Li, S., Li, H., Xu, C.Y., Huang, X.R., Xie, D.T. & Ni, J.P. 2013. Particle interaction forces induce soil particle transport during rainfall. *Soil Science Society of America Journal*, **77**, 1563–1571.

Lützow, M.V., Kögel-Knabner, I., Ekschmitt, K., Matzner, E., Guggenberger, G., Marschner, B. *et al.* 2006. Stabilization of organic matter in temperate soils: mechanisms and their relevance under different soil condition – a review. *European Journal of Soil Science*, **57**, 426–445.

Martínez, R.E., Sharma, P. & Kappler, A. 2010. Surface binding site analysis of $Ca^{2+}$ -homoionized clay humic acid complexes. *Journal of Colloid and Interface Science*, **352**, 526–534.

Nieto, O.M., Castro, J., Fernández, E. & Smith, P. 2010. Simulation of soil organic carbon stocks in a Mediterranean olive grove under different soil-management systems using the RothC model. *Soil Use and Management*, **26**, 118–125.

van Oss, C.J. 1994. *Interfacial Forces in Aqueous Media*. CRC Press, New York.

van Oss, C.J. & Giese, R.F. 1995. The hydrophilicity and hydrophobicity of clay minerals. *Clays and Clay Minerals*, **43**, 474–477.

van Oss, C.J., Chaudhury, M.K. & Good, R.J. 1988. Interfacial Lifshitz–van der Waals and polar interactions in macroscopic systems. *Chemical Reviews*, **88**, 927–941.

Page, A.L., Miller, R.H. & Keeny, D.R. 1982. *Methods of Soil Analysis. Part 2*, Agronomy Monographs, 9. ASA and SSSA, Madison, WI.

Plante, A.F., Conant, R.T., Paul, E.A., Paustian, K. & Six, J. 2006. Acid hydrolysis of easily dispersed and microaggregate-derived silt and clay-sized fractions to isolate resistant soil organic matter. *European Journal of Soil Science*, **57**, 456–467.

Plaza, I., Ontiveros-Ortega, A., Calero, J. & Aranda, V. 2015. Implication of zeta potential and surface free energy in the description of agricultural soil quality: effect of different cations and humic acids on degraded soils. *Soil & Tillage Research*, **146**, 148–158.

Ramos-Tejada, M.M., Ontiveros, A., Plaza, R.C., Delgado, A.V. & Durán, J.D.G. 2003. A rheological approach to the stability of humic acid/clay colloidal suspensions. *Rheologica Acta*, **42**, 148–157.

Saidy, A.R., Smernik, R.J., Baldock, J.A., Kaiser, K. & Sanderman, J. 2013. The sorption of organic carbon onto differing clay minerals in the presence and absence of hydrous iron oxide. *Geoderma*, **209–210**, 15–21.

Séquaris, J.M. 2010. Modeling the effects of $Ca^{2+}$ and clay-associated organic carbon on the stability of colloids from topsoils. *Journal of Colloid and Interface Science*, **343**, 408–414.

Somasundaran, P.B., Markovic, S., Krishnakumar, S. & Yu, X. 1997. *Handbook of Surface and Colloid Chemistry*. CRC Press, New York.

Sondi, I., Jasenka, B. & Velimir, P. 1996. Electrokinetics of pure clay minerals revisited. *Journal of Colloid and Interface Science*, **178**, 514–522.

Thomas, F., Michot, L., Vantelon, J., Montargès, D.E., Prélo, B., Cruchaudet, M. *et al.* 1999. Layer charge and electrophoretic mobility of smectites. *Colloids and Surfaces A: Physicochemical and Engineering Aspects*, **159**, 351–358.

Vandenbruwane, J., De Neve, S., Qualls, R.G., Sleutel, S. & Hofman, G. 2007. Comparison of different isotherm models for dissolved organic carbon (DOC) and nitrogen (DON) sorption to mineral soils. *Geoderma*, **139**, 144–153.

Wang, M. & Revil, A. 2010. Electrochemical charge of silica surface at high ionic strength in narrow channels. *Journal of Colloid and Interface Science*, **343**, 381–386.

Wiseman, C.L.S. & Puttmann, W. 2005. Soil organic carbon and its sorptive preservation in central Germany. *European Journal of Soil Science*, **56**, 65–76.

Xu, C.Y., Li, F.N., Hu, S., Li, X., Liu, M. & Li, Y. 2015. Non-classical polarization of cations increases the stability of clay aggregates: specific ion effects on the stability of aggregates. *European Journal of Soil Science*, **66**, 615–623.

Zhang, W., Morales, V., Cakmak, M.E., Salvucci, A.E., Geohring, L.D., Hay, A.G. *et al.* 2010. Colloids transport and retention in unsaturated porous media: effect of colloid input concentration. *Environmental Science & Technology*, **44**, 4965–4972.

### *5.3.3 Improvement of the structural stability at the colloidal scale in marginal olive grove soils by organic agriculture, characterized by the Extended-DLVO model.*

*Resumen*

Los suelos estudiados de Sierra Morena pueden considerarse como marginales desde el punto de vista agrícola por su pendiente, espesor y pedregosidad. Las muestras seleccionadas se denominan: BNG (Suelo con bosque mediterráneo o suelo forestal), CUG (suelo con manejo ecológico u orgánico y SCG (suelo con manejo convencional o tradicional).

En este trabajo se utilizó el modelo extendido-DLVO para calcular la energía total de interacción entre partículas de los tres suelos con el objetivo de comparar, primero, los efectos de la agricultura orgánica en suelos gestionados convencionalmente y, segundo, compararlos con un suelo no cultivado bajo bosque mediterráneo.

Los resultados muestran que cuando las energías totales son negativas o positivas pero cercanas a 0 kT para determinados iones, en este estado se produce la floculación de partículas, lo que se puede observar en la estructura a escala coloidal. La energía total fue menor en la muestra forestal y mayor en el suelo con manejo convencional, con un valor intermedio en el suelo ecológico. Esto indica una tendencia a la floculación de partículas y más estabilidad de la estructura a escala coloidal, lo que concuerda con los resultados obtenidos de otras propiedades físicas del

suelo como la macroporosidad o el índice de estabilidad estructural, que siguieron la misma tendencia.

De los tres componentes de la energía total de interacción, la fuerza ácido-base demostró ser clave. Este componente, relacionado con el componente donador de electrones de la energía libre superficial, $\gamma^-$, fue negativo (-150 kT a H=3 nm) cuando se analizaron las soluciones de calcio para el suelo forestal, lo que implica un claro carácter hidrofóbico de esta muestra. Creemos que esta hidrofobicidad podría explicarse por la alta cantidad y la naturaleza alifática de la materia orgánica del suelo en el suelo no cultivado.

Desde un punto mineralógico está formada principalmente por cuarzo (pico 0.425 nm) y filosilicatos (pico 0.445 nm), si bien es de destacar la aparición de un pico a 1.40 nm que demuestra la importante presencia de clorita o vermiculita, dentro de la fracción filosilicatos. En la fábrica SEM se observa una agregación de tipo biogénico (i.e. hifas de hongos) que predomina en los suelos de Sierra Morena. Dentro de un mismo tipo de suelo, los suelos convencionales son los que producen las estructuras menos estables.

# Articulo Científico

## IMPROVEMENT OF THE STRUCTURAL STABILITY AT THE COLLOIDAL SCALE IN MARGINAL OLIVE GROVE SOILS BY ORGANIC AGRICULTURE, CHARACTERIZED BY THE EXTENDED-DLVO MODEL.

# IMPROVEMENT OF STRUCTURAL STABILITY AT COLLOIDAL SCALE IN MARGINAL OLIVE GROVE SOILS BY ORGANIC AGRICULTURE, CHARACTERIZED BY EXTENDED DLVO MODEL

**I. Plaza[1], J. Calero[2], A. Ontiveros[1,3], Aranda[2], V., R. García-Ruiz[4], J.L. Vicente-Vicente[4]1**

**[1]Department of Physics. University of Jaén (Spain). Campus Universitario de las Lagunillas s/n, edificio A-3, 23071 Jaén (Spain).**

**[2]Department of Geology. University of Jaén (Spain). Campus Universitario de las Lagunillas s/n, edificio A-3, 23071 Jaén (Spain).**

**[3]Instituto Andaluz de Geofísica, University of Granada. Fuentenueva s/n, 18002 Granada (Spain).**

**[4,] Department of Animal Biology, Vegetal Biology and Ecology. Campus Universitario de las Lagunillas s/n, edificio A-3, 23071 Jaén (Spain).**

**Abstract**

In this work, we used the extended DLVO model to compute total energy of interaction between particles of three soils over granodiorites. The aim was to compare first the effects of organic farming on conventionally managed soils and, second, to compare these with a non-cultivated soil under Mediterranean forest. When total energies are negative or positive but near 0 kT, then particle flocculation occurs and the structure at colloidal scale can be determined. Total energy was less in the forest sample and greater in the soil of conventional groves, with an intermediate value in organic soil. This indicates a tendency toward particle flocculation and more stability of the structure at colloidal scale, agreeing with other soil physical properties such as the macroporosity or structural stability index, which followed the same trend. Of the three components of the total energy of interaction, the acid-base force was demonstrated to be a key factor. This component, related with the electron-donor component of surface free energy, $\gamma^-$, was negative (−150 kT at 3 nm) when calcium solutions were analyzed for the forest soil. This indicates a clear hydrophobic character of this sample. We believe that this hydrophobicity can be explained by the large amount and aliphatic nature of the soil organic matter in the non-cultivated soil.

**Keywords:** zeta potential, particle energy of interaction, SEM-fabric, organic soils, olive groves

* Corresponding author. Tel.: +953 21 28 30.
*E-mail address:* aontiver@ujaen.es

## 1. INTRODUCTION

Soil structure consists of the spatial arrangement of soil particles and aggregates through aggregation processes that operate at several scales, resulting in a complex network of pores of multiple sizes and shapes (Peng et al., 2015). Because it determines porosity, the structure is a fundamental property that largely determines all soil functions, such as $CO_2$ sequestration or water quality. Thus, soil structure should be considered a main indicator of soil quality. The structure deteriorates during traditional tillage, because of physical stress caused by the tillage itself and loss of organic matter from surface layers (Gomez et al., 2004, 2009). Karlen et al. (1997) indicated a close relationship between the loss of soil organic matter (SOM) and deterioration of the structure. Given this, normative frameworks of the European Union (EC, 2005; 2011) reflect a change of management recommendations from conventional agriculture to conservation and organic farming, based on the adoption of practices aimed at increasing soil organic matter, care of the structure, and erosion control.

The processes of aggregation of the primary soil particles result from both their spatial rearrangement caused by mechanical and biogenic stresses, and chemical and physical interactions between mineral surfaces (Bronick and Lal, 2005). Among the latter are flocculation and cementation, whose two processes are mediated by chemical composition of the soil solution, which includes both pH and balance between dissolved ions (Ca, Na, Al, etc.) and the nature of mineral surfaces. The electric charge and electrostatic interactions of these soil particles play a key role in the formation of soil structure. These can be characterized by the zeta potential ($\zeta$) and surface free energy SFE (Somasundaran et al., 1997; Aranda et al., 2016; Calero et al., 2017). According to Aranda et al. (2011), the electrical charges depend on the soil parent material and geological material. These interactions can be modeled through the Derjaguin, Landau, Verwey and Overbeek (extended DLVO) theory (Van Oss, 1998). Also, soil organic carbon (SOC) has a fundamental role as modulator of the processes of flocculation between particles. This function between the aggregation and SOC is reciprocal, because a sound structure is

related to a greater capacity of carbon retention in the soil (Six et al., 2002). The structure has a double aspect, spatial and functional. Thus, it has been studied by both morphological techniques of direct observation, among which the scanning electron microscope (SEM) stands out, and as a chemical and physical type, through the characterization of forces that join particles and aggregates to each other, as demonstrated in Moleon et al. (2015), Plaza et al. (2015); Aranda et al. (2015) and Calero et al. (2017).

The aim of the present work was to study the influence of organic agriculture on the soil structure at colloidal scale, characterized by the energy of interaction between particles and the SEM fabric of the soil.

**2. MATERIALS**

Andalusia (southern Spain) has the greatest production of olive oil in the world. Olive groves occupy 15,000 $km^2$, or 30% of the useable arable area. It is also the region with the largest production quota in the world, surpassing 21% (CAP, 2015). The historical extension of cultivation to mountain areas, mainly from the first decades of the 20th century (Amate-Infante, 2012), has meant in the current context of maximum competitiveness a substantial expansion of Andalusian olive groves into areas where topographic or soil conditions do not allow effective mechanization. This is especially relevant in Sierra Morena mountain range, whose olive groves are in gravelly soils with steep slopes and nutrient-poor acid soils (Alvarez et al., 2007).

Soil was sampled in the northeast of the province of Córdoba (Andalusia), in the municipality of Obejo, near road CP-165 that connects this town with Pozoblanco (38.37°–38.13°N, 4.88°–4.72°W). It is an area of moderate slopes (maximum 20%, average elevation 530 meters above sea level). The area is classified as “Pedroches Batolite” (granitoid complexes of post-kinematic origin) with granodiorite lithology. Regarding land use, the area has predominantly low-intensity conventional, rainfed olive groves, where soils are subjected to tillage and agrochemicals, and organic farms with no chemical fertilizer or pesticide addition and long-term (> 10 years) use of plant cover.

Three plots were selected as representative of the two types of olive groves (conventional and organic), and one of natural soils in the area: i) a conventional olive grove with no plant cover (SCG), which was under conventional tillage with frequent application of pre- and post-emergence herbicides; ii) an organic olive grove (CUG) with spontaneous plant cover, where organic fertilizer (compost) was applied about every five years; iii) natural soil (BNG), under small forest patches of oak and tall scrub (Quercus coccifera, Myrtus communis, Rhamnus sp., Viburnun Tinus, Arbutus Unedo) present in the sampling area. In each plot, five points were randomly sampled in the inter-canopy area of groves; cylindrical cores of 5 × 5 cm size and a known volume (98.17 $cm^3$) were taken at the soil surface to determine bulk density, and five samples from 0–5 cm depths for physical, chemical and mineralogical analyses.

## 3.THEORY AND METHODOLOGY

### *3.1Soil analysis and mineralogy*

Once in the laboratory, soil samples were spread and air-dried, then uniformly and carefully mixed to create a bulk sample per each plot. The bulk sample was sieved at 2 mm to obtain coarse fragments and the fine earth fraction (< 2 mm), which was submitted to the following analyses (Soil Conservation Service, 1972): texture by sieving and sedimentation (Robinson pipette); particle density with a pycnometer; organic carbon by dichromate oxidation; total nitrogen by the Kjeldahl method; $CaCO_3$ equivalent by Bernard calcimeter; cation exchange capacity (CEC) and exchangeable bases ($Ca^{2+}$, $Mg^{2+}$, $K^+$ and $Na^+$) by the ammonium acetate-sodium acetate method (pH 7) and measured by atomic absorption spectrometry; available phosphorus (P) extracted with sodium bicarbonate solution and determined by colorimetry (Olsen method), and pH by potentiometry in a 1:1 suspension of fine earth:water. Water retention at matric potential −10 kPa (field capacity) was done by pressure plate assembly with an Eijkelkamp 08.02 sand/kaolin box (Eijkelkamp Agrisearch Equipment, Giesbeek, The Netherlands). Total porosity was estimated from the particle and bulk density, and macroporosity from total porosity less microporosity. Macroporosity was measured as water content at field capacity. Finally, the aggregate stability index ASI of

Kemper and Rosenau (1986) was determined by means of a wet sieving apparatus (Eijkelkamp Agrisearch Equipment, Giesbeek, The Netherlands); ASI < 1 signifies fewer than 50% of 0.25-mm stable aggregates in the soil.

The clay fraction (< 2 μm) was isolated by sedimentation, after removing organic matter with a 15% $H_2O_2$ solution and dispersing it with a 10% sodium polyphosphate solution. Nitrogen ($N_2$) surface area was measured with a Micromeritics surface area analyzer (Model Gemini 2360, Micromeritics, Norcross, Georgia USA), which calculates specific surface area (SSA) according to the Brunauer–Emmett–Teller (BET) equation and by the ethylene glycol monoethyl ether (EGME) method. CEC of the clay fraction was measured by the ammonium acetate-sodium acetate method (pH 7).

Soil mineralogy of the fine earth and clay fractions was determined by X-ray diffraction using a Siemens D5000 diffractometer (Siemens AG, Karlsruhe, Germany) with Cu Kα radiation at 35 kV. Fine earth X-ray mineralogy in the 3–50 °2θ range was determined by the disoriented powder method and percentages of phyllosilicates and other minerals estimated by calculating relative peak areas and applying the intensity factors of Calero et al. (2009). Clay fraction mineralogy was examined by the oriented aggregate method, following the procedure described by Plaza et al. (2015) and Calero et al. (2017): i) the sample was dispersed in a 10% sodium polyphosphate solution and stirred overnight to extract the clay fraction (< 2 μm) by sedimentation; ii) Fe was removed from clay via the Mehra-Jackson procedure (Klute, 1986), and the resulting extract was measured by atomic absorption spectrometry; iii) two replicate samples of the clay were subjected to 1N $MgCl_2$ and 1N KCl saturation for 48 hours, respectively, and later air-dried over a glass plate; iv) the magnesium plate was solvated by ethylene-glycol vapor for 24 hours; v) the potassium plate was heated at 520 °C.

*3.2. Soil analysis and mineralogy*

Soil fabric was examined by an SEM with acceleration voltage 25 kV (S-510; Hitachi Ltd., Tokyo, Japan), equipped with an energy-dispersive X-ray detector (EDAX; Rontec

GmbH, Berlin, Germany). Fine earth was mounted on the sample holder with colloidal silver and metallized with carbon deposited in two orientations (20°–30°).

*3.3. Soil humus characterization*

Fractionation of SOM was done following the IHSS procedure (Swift, 1996). Total extractable carbon for humic and non-humic substances was extracted from soil by mechanically shaking the samples in a 0.1 M NaOH and $Na_4P2O_7$ solution at pH 14 for 24 h at 60 °C (1:10 w/v). The extracts were centrifuged and filtered (Millipore 0.45-μm). Separation of the total extractable carbon fraction into humic acids (HA) and fulvic acids (FA) was done by precipitation with $H_2SO_4$ and purification with polyvinylpolypyrrolidone to eliminate non-humic carbon, respectively. The FA fraction was considered the soluble carbon remaining from the humic extract, and the corresponding HA/FA ratio was found. Finally, any remaining carbon was considered the alkali-insoluble fraction of SOM (HUMIN). Amounts of carbon in the above fractions were quantified by wet combustion (Page et al., 1982). Visible spectra from 400 to 800 nm of 0.2 mg CmL −1 HA solutions (Kononova, 1966) in 0.1 M $NaHCO_3$ were recorded using a computer-controlled Varian Cary 50 spectrophotometer with Varian spectroscopy software WIN-UV. The samples were measured directly in a glass cuvette with 1-cm optical path. All spectra were smoothed using the Savitzky–Golay algorithm with order-2 polynomial. The ratio of absorbance at 465 and 665 nm (E 4 / E 6 ratio) and the second derivative were calculated from the smoothed visible spectra.

*3.4. Determination of zeta-potential (ζ)*

The determination of ζ used was previously described in Plaza et al. (2015), taking into account the following parameters:

i) Type of cation used to prepare the solution. This was the first parameter considered, setting a standard concentration of $10^{-3}$ M for the sodium, calcium, iron and aluminum solutions (Wang and Revil, 2010).

ii) Ionic strength of the solution. Subsequently, it was verified whether ζ underwent

variations according to the ionic strength, with the aim of establishing the most suitable concentration for the adsorption experiments. More concentrated and concentrated concentrations of $10^{-3}$ M ($10^{-2}$, $10^{-4}$ M) were used only for mono- and divalent ions (sodium and calcium, respectively).

iii) The fine earth was exposed to a commercial HA of Sigma-Aldrich brand with 39% C. Solutions were prepared with such humic salt at concentrations of 1 mM. For the determination of ζ, a Zetasizer 3000HS (Malvern Instruments, Worchestershire, UK) was used.

*3.5. Determination of surface free energy (SFE)*

Surface properties of the fine earth were determined using the method described by Plaza et al. (2015) and Moleon et al. (2015). In these works, the authors estimated the surface properties by contact angle measurement of three liquids (water, formamide and diodomethane) on the compressed soil. This was performed with the aid of a goniometer NRL C.A (ramé-hart Instrument Inc., New Jersey, USA). For this experiment, the soil samples were treated with solutions of sodium, calcium, iron and HA at $10^{-3}$ M. The samples were dried at 323 °K for 24 hours and subsequently held in a hydraulic press at 1.5 × $10^4$ kg $cm^{-2}$ for 10 min. According to Van Oss (1994) and Van Oss et al. (1988), we could obtain the dispersive components Lifshitz–van der Waals ($\gamma^{LW}$) and non-dispersive interaction of Lewis acid-base $\gamma^{AB}$ through this technique, as described in Plaza et al. (2015).

*3.6.Determination of energy of interaction through DLVO-EXT theory*

The extended DLVO model considers three interactions, AB (acid-base), LW (Lifshitz–van der Waals) and EL (electrical). This model is mentioned in Moleon et al. (2015), where it is explained that in any system composed of equal particles within an aqueous suspension, the total interaction energy is

$$\Delta G_{131}^{TOT} = \Delta G_{131}^{EL} + \Delta G_{131}^{LW} + \Delta G_{131}^{AB}, \qquad [1]$$

where the electrical component is determined using the equation of Durán et al. (1988), and the components LW and AB using the model proposed by Van Oss (1988).

*3.7. Determination of energy of interaction through DLVO-EXT theory*

The fine earth of our soils was subjected to an HA solution following the method of Moleon et al. (2015) and Plaza et al. (2015). We used three cations, $Na^{+}$, $Ca^{2+}$ and $Fe^{3+}$ to $10^{-3}$ M strength. The fine earth was subjected to various concentrations of HA (0.5 g/l) at three temperatures 283.15 K, 293.15 K and 313.15 K. Adsorption of HA by the soils was performed by differences in the initial and final concentrations. For this purpose, a Hitachi spectrometer (M Hitachi U2000; Hitachi Scientific Instruments, Mountain View, California USA) was used at 554 nm, following the instructions of Ramos-Tejada et al. (2013).

## 4. RESULTS AND DISCUSSION

*4.1. Physical and chemical analysis of soils*

Physical and chemical properties of the studied soils are listed in Tables 1 and 2. They showed very large amounts of coarse fragments (> 50%), reaching 80% in the non-cultivated soil, and medium-to-coarse textures (sandy loam and sandy clay loam). Bulk density in the cultivated soils (~1.50 g/cm$^3$) was in accord with these textures, but was remarkably low in the forest soil (1.27 g/cm$^3$). Soil properties related with structure quality (porosities and structural stability) had an increasing trend from the conventional to natural soil. However, poor macroporosity of the two cultivated soils (< 10%) should be highlighted, which might reveal some compaction process, even though their bulk densities were not high. Moreover, the ASI reached in the conventional soil was 0.66, a value characteristic of very degraded soils (Klute, 1986).

The forest soil had a total carbon content (10.51%) much higher than those of cultivated ones (0.81% and 1.56% for the organic and conventional samples, respectively), which are small or moderate values for Mediterranean soils. This high organic matter content may explain the low bulk density of the forest soil. Other indicators of chemical fertility

(nitrogen, potassium and exchange capacity) followed the same gradient as organic carbon; highest contents were in natural soils and the lowest in conventional groves. Values of total nitrogen (< 0.05), phosphorus (< 12 ppm), potassium (< 75 ppm) and cation exchange capacity (~10–15 $cmol_+ kg^{-1}$) for the cultivated soils were in accord with horizons of coarse to medium textures, and were large for the forest plot. pH values were relatively suitable (slightly acidic), although olive trees have more affinity for pHs in the basic range (Sys et al., 1992)

**Table 1.** Physical properties related to structure.

| | C. F (%) | Sand (%) | Clay (%) | Texture class | Bulk density (g $cm^{-3}$) | Total porosity (v/v) | Macroporosity (v/v) | ASI (p/p) |
|---|---|---|---|---|---|---|---|---|
| **SCG** | 77 | 49 | 27 | Sandy-clay-loam | 1,50 | 37 | 5 | 0.66 |
| **CUG** | 54 | 57 | 12 | Sandy-loam | 1,48 | 39 | 8 | 0.73 |
| **BNG** | 80 | 59 | 10 | Sandy-loam | 1,27 | 47 | 18 | 0.94 |

CF: coarse fragments; ASI: aggregate stability index = A/B x 100. A: weight of soil stable macroaggregates (≥ 0.25 mm), resisting wet sieving; B: weight of soil unstable macroaggregates (≥ 0.25 mm), passing through the 0.25 mm grid.

**Table 2.** Chemical properties of soil, change complex and colloidal fraction

| **Property** | **Sample** | **SCG** | **CUG** | **BNG** |
|---|---|---|---|---|
| Fine earth | O.C. (%) | 0.81 | 1.56 | 10.51 |
| | Total N (%) | 0.04 | 0.09 | 0.40 |
| | pH | 5.88 | 6,24 | 6,18 |
| | $CaCO_{3\ equiv.}$ (%) | 2 | 1 | 2 |
| | P.olsen (ppm) | 6 | 3 | 10 |
| Exchangeable complex | CEC ($cmol_+ kg^{-1}$) | 12.80 | 10.00 | 17.40 |
| | Exchangeable $Ca^{2+}$ ( $cmol_+ kg^{-1}$) | 15.71 | 12.70 | 58.93 |
| | Exchangeable $Mg^{2+}$ ( $cmol_+ kg^{-1}$) | 6.93 | 4.97 | 15.80 |
| | Exchangeable $K^+$ ( $cmol_+ kg^{-1}$) (ppm) | 0.99 (39) | 1.87 (73) | 5.37 (210) |
| | Exchangeable $Na^+$ ( $cmol_+ kg^{-1}$) | 1.58 | 1.52 | 4.83 |
| | Base Sat. (%) | 36 | 39 | 92 |
| | $Ca^{2+}$ Sat. (%) | 24 | 26 | 68 |
| Clay fraction | SSA-EGME($m^2 g^{-1}$) | 186.98 | 148.73 | 132.00 |
| | $Fe_2O_3$ clay (%) | 9.19 | 5.68 | 10.25 |
| | CEC clay ($cmol^+ kg^{-1}$) | 8.70 | 13.51 | 14.71 |
| | E4/E6 | 3.10 | 3.31 | 4.69 |

OC: total organic carbon; $Fe_2O_3$ clay: citrate-dithionite-bicarbonate iron of clay fraction; CEC: cation exchange capacity; *ASI: aggregate stability index = A/B x 100. A: weight of soil stable macroaggregates (≥ 0.25 mm), resisting wet sieving; B: weight of soil unstable macroaggregates (≥ 0.25 mm), passing through the 0.25 mm grid; SSA-EGME: specific surface area (ethylene glycol mono ethyl ether method); SSA-EGME: specific surface area ($N_2$ adsorption method).

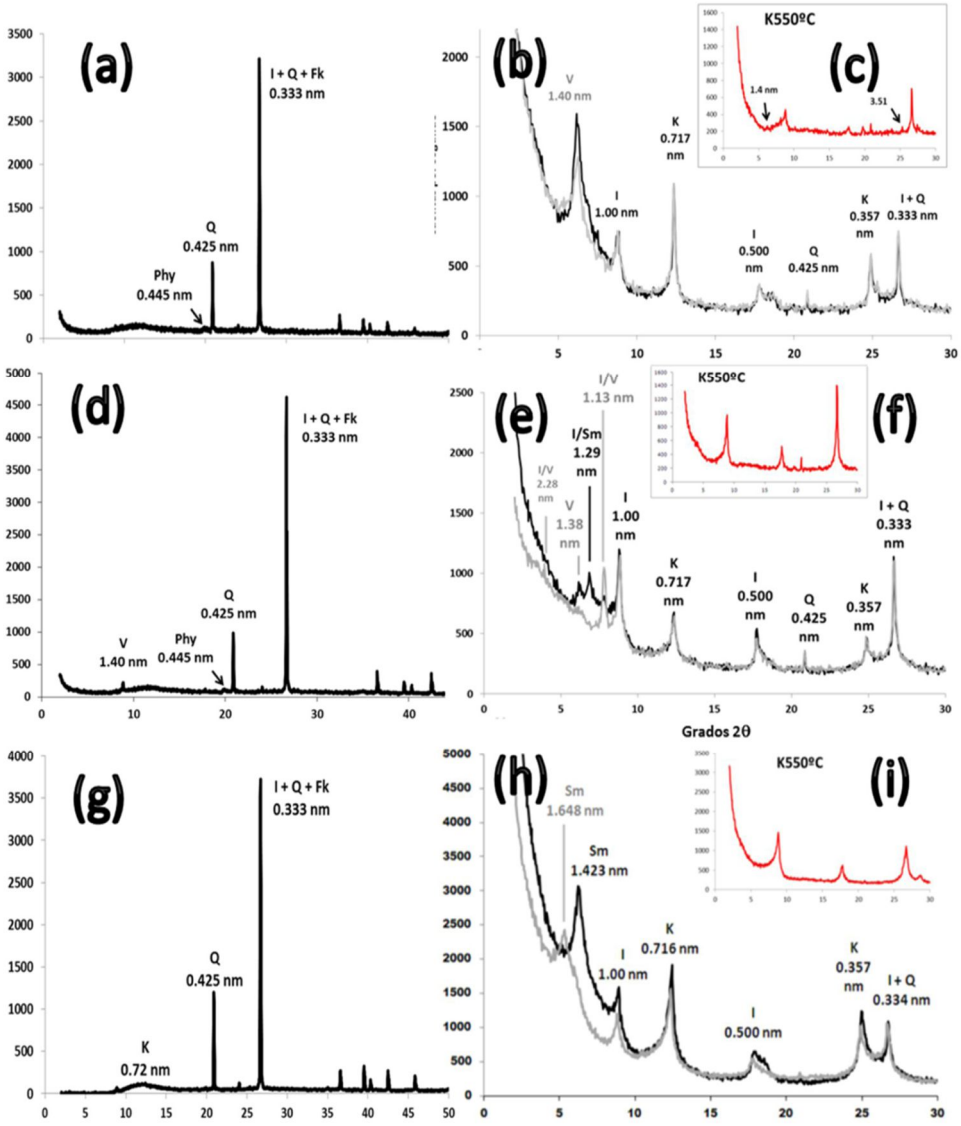


**Figure 1**. Total mineralogy of samples: BNG (a), CUG (d), SCG (g). Phy = phyllosilicates, Q = quartz, Fk = potassium feldspar, I = illite. Clay mineralogy (aggregate-oriented) of samples: BNG (b), CUG (e), and SCG (h). Black line = Mg dry air; gray line = Mg ethylene glycol. V = vermiculite, I = illite, K = kaolinite, Q = quartz, Chl = chlorite. Box: potassium treatment 550 °C. 4. Mineralogy of clays (oriented aggregate) in sample CUG. Black line = Mg dry air; gray line = Mg ethylene glycol. V = vermiculite, I / V = illite-vermiculite, I / Sm = illite-smectite, I = illite, K = kaolinite, Q = quartz. Box: potassium treatment 550 °C: BNG (c), CUG (f), SCG (i).

In general, the studied physical and chemical properties indicate a low agricultural potential, which together with the slope indicates theses soils would work better as pastures or forests.

*4.2 Mineralogy analysis of soils*

The disoriented powder mineralogy of the samples (Table 3) was similar and strongly influenced by the parent rock (granodiorite), with soils mainly formed by quartz (> 40%) and phyllosilicates (> 20%). Percentages of chlorite, goethite, and potassium and sodium feldspar were < 5% in all samples, and no carbonates were identified.

**Table 3.** X-ray mineralogy of fine earth fraction (< 2 mm) of soils (disoriented powder method). tr: traces (< 1%).

| Sample | Phyllosilicates | Quarz | Goethite | Hematites | Clorite | Feld.K | Feld.Na | Calcite | Dolomite |
|---|---|---|---|---|---|---|---|---|---|
| **BNG** | 21 | 73 | < 5 | tr. | < 5 | tr. | < 5 | tr. | tr. |
| **SCG** | 35 | 57 | < 5 | tr. | < 5 | < 5 | < 5 | tr. | tr. |
| **CUG** | 45 | 42 | < 5 | tr. | < 5 | < 5 | 5 | tr. | tr. |

The forest soil showed mainly quartz (0.425-nm peak) and phyllosilicates (0.445-nm peak) in the fine earth (Figure 1a). The most important phyllosilicate in the clay fraction (Figure 1b) was soil vermiculite, a non-swelling type of hydroxyl-interlayered mineral, so its diagnostic peak remained at 1.40 nm after glycol solvation. Other major phases in the clay fraction were illite (1.00 nm) and kaolinite (peak at 0.72 nm). The fine earth of the organic soil (Figure 1d) was similar to that of the forest soil, formed principally by quartz (peak 0.425 nm) and phyllosilicates (peak 0.445 nm), although the main phases in the clay fraction were illite (1.00 nm) and vermiculite-illite mixed layer (non-swelling peak at 1.13 nm in glycol; Figure 1e). Finally, the sample of conventional olive grove (SCG) (Figure 1g) was also formed mainly by quartz (peak 0.425 nm, 67%), but with a smaller percentage of phyllosilicates (32%) than the two previous soils. In contrast to them, the clay of SCG exhibited strong swelling, as evidenced by clear expansion of the 1.423-nm peak to 1.648 nm in glycol (Figure 1h). Based on this expansive capacity, we determined that the most important phase in this soil was smectite. This is supported by the higher SSA-EGME in

the SCG sample (Table 2), because the method to estimate SSA can measure not only the outer surface of phyllosilicates but also their inner (interlayer) surface. The most important phyllosilicate after the smectite phase was kaolinite (0.72 nm), followed by illite (1.00 nm), which is much more scarce than in forest or organic soils.

*4.3. Adsorption experiments: zeta potential (ζ), surface free energies (SFEs), and isotherms*

*4.3.1. Zeta potentials*

The following figures show ζ obtained from the samples for the $10^{-3}$ M solutions of sodium (Figure 2a), calcium (Figure 2b) and iron (Figure 2c).

In sodium solutions, we observed two groups of behaviors, one of natural soil and the other of organic and conventional soils; the latter was very similar across all treatments. ζ is always negative, which is explained by the predominance of 2:1 phyllosilicates in the soil colloidal fraction, whose main source of electric charge is pH-independent (isomorphic substitutions in the tetrahedral and octahedral layers of phyllosilicates) (Sondi et al., 1996). However, a decrease of soil ζ was observed with increasing pH, which can be attributed to both deprotonation of the pH-dependent loads of the clays ($OH^-$) and the acidic functional groups of SOM (-COOH, -OH, and others).

Figure 2b shows the effect of divalent ($CaCl_2$) ions produced in ζ of the sample, which was negative in all pH ranges tested. The results show that the calcium cation behaves like an indifferent ion. This effect in smectites has been described by Plaza et al. (2015), Thomas et al. (1999) and Lagaly (2006), by Duman and Tunc (2008) in vermiculites, and by Martínez et al. (2010) in illites. This behavior was attributed by Lagaly (2006) to a small ratio of pH-dependent charges in 2:1 phyllosilicates (illite, smectite, and vermiculite) and to strong particle aggregation caused by calcium.

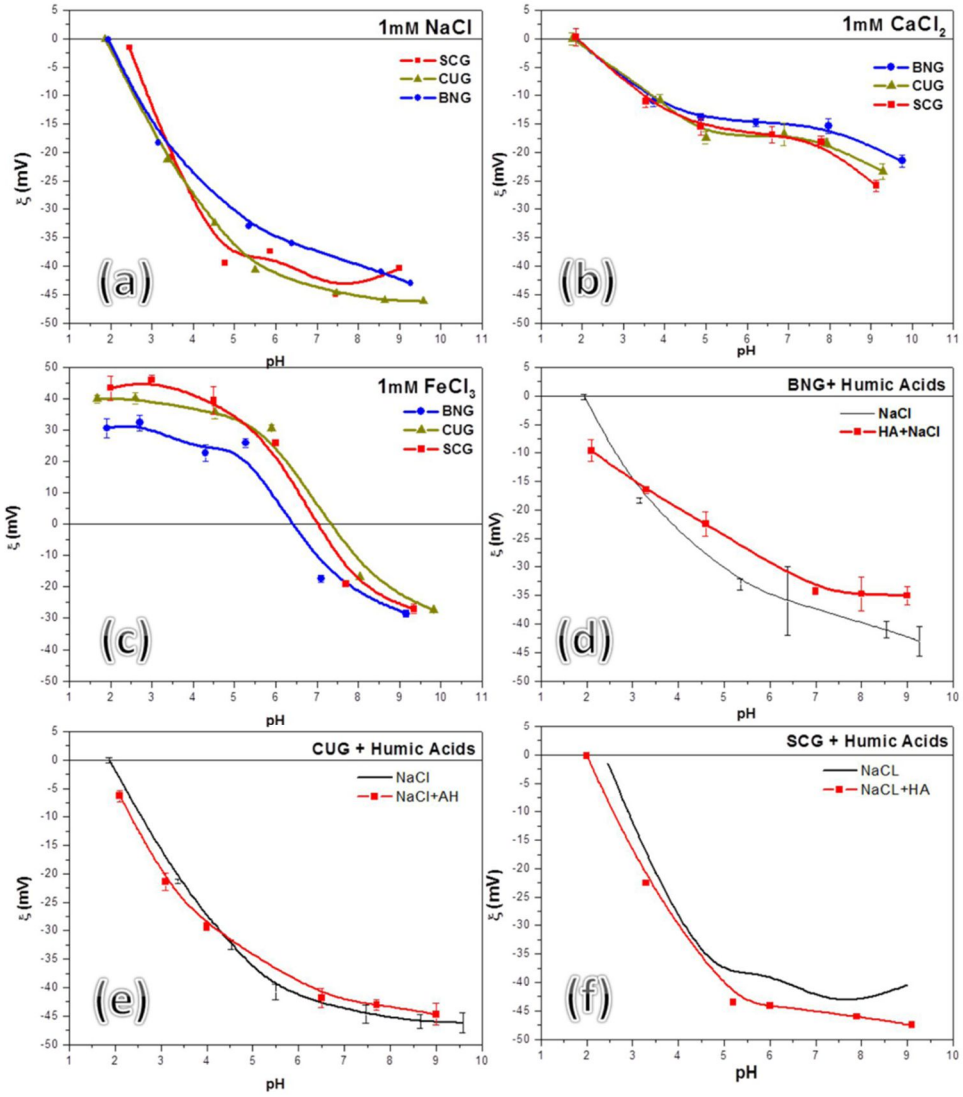


**Figure 2.** *(*A) Zeta-potentials for $10^{-3}$ M NaCl solution. Colored curves: siliceous samples (blue: BNG, red: SCG, green CUG). (B) Zeta-potentials for $10^{-3}$ M $CaCl_2$ solution. Colored curves: siliceous samples (blue: BNG, red: SCG, green CUG). (C) Zeta-potentials for $10^{-3}$ M solution $FeCl_3$. Colored curves: siliceous samples (blue: BNG, red: SCG, green CUG). (D, E and F). Effect of addition of 0.5 g/L of commercial humic acid (HA) on zeta-Potential ($10^{-3}$ M NaCl) of the siliceous soils (Sierra Morena).

The treatment with iron (Figure 2c) conditioned the samples treated with basic cations (calcium and sodium) so that ζ had positive values at acidic pH. This is because of the acidic nature of ferric salts, which is capable of protonating strongly at pH lower than its isoelectric or zero-charge point, indicating that these salts tend to precipitate on the colloidal phase in the form of iron oxides (given their low solubility) (Plaza et al., 2015).

*4.3.2 Effects of commercial HA addition on zeta potential of soils*

The adsorption was executed in solutions with ionic strength $10^{-3}$ M of NaCl (Figure 2d–f). The effects on ζ are shown when adding HA to soils of the Sierra Morena. The adsorption of humic acid can cause ζ variation of soil particles, owing to the action of ionizable groups of humic acid ($-COO^-$, $-NH_3^+$, and others). The samples for which ζ curves varied strongly (± 5 mV) showed a dependence on this behavior. The results show no effect of HA adsorption on the organic soil (Figure 2f), whereas there was an effect on the natural soil (Figure 2d), for which ζ decreased, and in the soil with traditional tillage (Figure 2e), for which ζ increased. The decrease of ζ in the natural soil may have been caused by saturation of their mineral surfaces, which simultaneously showed higher % OC and lower SSA-EGME of the three soils (Table 3). Eventually, an excess of humic acids may cause in the system the formation of micelles and consequent decrease of negative charge (Ontiveros-Ortega et al. 1998). In another case, an increase of negative charge is expected from the addition of HA carboxyl groups to the system, as stated by Plaza et al. (2015).

*4.3.3. Surface free energies*

The components of SFE for different ions and treatments with humic acid are shown in Table 4.

The soils had a monopolar character, with values of the basic component (electron donor) $\gamma^-$ much larger than those of the acid component (electron acceptor) $\gamma^+$, which tended toward zero. In Table 4 are also shown the dispersive component of Lifshitz–van der

Waals ($\gamma^{LW}$), whose values are common in inorganic soils and similar to those given by Hajnos et al. (2013). In addition, except for some values reached by the BNG sample, these are hydrophilic soils, given that $\gamma^{+} \approx 0$ and $\gamma^{-} > 28$ mJ/m$^2$, values typical of siliceous rock (Alfonso et al., 2014; Moleon et al. 2015) and established by van Oss and Giese (1995) as a hydrophobicity threshold for soils rich in phyllosilicates. The most variable component, considering the sample and the ionic treatment, was $\gamma^{-}$, from 15 mJ m$^{-2}$ (BNG, $CaCl_2$), a value substantially smaller than the hydrophobicity threshold, to 51 mJ m$^{-2}$ (SCG, $FeCl_3$). $\gamma^{LW}$ remained more constant, in a range between 40 and 49 mJ m$^{-2}$. About the electrolytes effect, we can state that $CaCl_2$ tended to produce a decrease in $\gamma^{-}$, while iron and sodium behaved in relatively similar ways.

It is also interesting to check the effect of HA addition on SFE. $\gamma^{-}$ did not show great variation for HA-added soil (> 5 mJ m$^{-2}$), so the adsorption did not substantially alter it.

Regarding soil management, the natural soil had a more hydrophobic character than the cultivated ones, which showed a similar wettability behavior. The hydrophobic character was present in all ionic treatments (near the aforementioned hydrophobicity threshold of 28 mJ m$^{-2}$), but was especially strong in calcium, reaching a value of highly water-repellent materials (15 mJ m$^{-2}$) (Ontiveros-Ortega et al. 1998). On the contrary, cultivated soils showed clear hydrophilicity, 45.6 and 48.6 mJ m$^{-2}$ for SCG and CUG, respectively.

*4.3.4. Total surface energies: extended DLVO model and interaction between soil particles as a function of ionic solution*

Figure 3 shows total interaction energies as a function of the various ions, at ionic strength $10^{-3}$ M. Figure 4 depicts total energy components (EL, AB and LW) for the calcium- and iron-treated soils.

Except for the BNG sample in calcium solution (Figure 3a), no primary energy minima can be discerned. However, there were secondary energy minima with kT < 0 (attractive force) at H > 100 nm for all cations studied (Figures 3 d, e and f). In spite of their small values (< 1 kT), these secondary minima may justify colloidal aggregation in samples with

moderate total interaction energies, even in the absence of primary minima when H approaches 0 nm (Zhang et al., 2010).

**Table 4**. Components of free surface energy of soils for different treatments.

| Sample | pH | Surface Free Energy (mJ $m^{-2}$) | $Na^+$ | $Ca^{2+}$ | $Fe^{3+}$ | $Na^+$ + HA |
|---|---|---|---|---|---|---|
| | | $\gamma^{LW}$ | 46.5 | 47.17 | 47.79 | 40.11 |
| **BNG** | 6,2 | $\gamma-$ | 29.75 | 15.14 | 30.28 | 30.97 |
| | | $\gamma^+$ | 0.65 | 0.43 | 0.7 | 0.811 |
| | | $\gamma^{LW}$ | 46.5 | 46.8 | 46.8 | 46.152 |
| **SCG** | 5,9 | $\gamma-$ | 45.6 | 46.8 | 51.04 | 47.45 |
| | | $\gamma^+$ | 0.39 | 0.39 | 0.26 | 0.237 |
| | | $\gamma^{LW}$ | 48.6 | 47.2 | 47.8 | 42.9 |
| **CUG** | 6,2 | $\gamma-$ | 48.6 | 41.9 | 45.2 | 44.8 |
| | | $\gamma^+$ | 0.18 | 0.56 | 0.27 | 0.32 |

Setting the interaction energy to 10 nm, which properly characterizes the tendency toward flocculation of particles in colloidal systems according to (Ontiveros-Ortega et al. 1998), the largest value in sodium solution was for the soil of conventional groves (1050 kT; Figure 3c), and the smallest value was for soil of the natural forest (700 kT; Figure 3a). The organic soil gave an intermediate value (900 kT; Figure 3b). In the behavior with HA treatment in sodium solution for the three samples, we observed variation of interaction energies in accord with the ζ data shown in Figure 2, i.e., a decrease in BNG from 700 to 540 kT (Figure 3a) and an increase in SCG from 1050 to 1175 kT (Figure 3c); the organic soil was unaffected by HA addition (Figure 3b). Because total energies were much greater than zero in all sodium samples, including the HA-added ones, a strongly repulsive force between particles can be presumed, so structural stability at colloidal scale should be weak in these systems. The negative effect of sodium on the structural stability of soils at colloidal scale is widely known (Baumgarten et al., 2012).

The behavior of samples in calcium and iron solution was noticeably different. They always produced a trend toward the precipitation of suspended colloids (< 350 kT), especially in the forest soil, where the total energy at 10 nm was < 100 kT. This latter value may be considered a threshold for energy barriers, where particles may have relatively high probabilities of flocculation (Ontiveros-Ortega et al. 1998). Furthermore, iron and calcium should be considered the most relevant cations for explaining colloidal behavior in field conditions. This is because calcium was the dominant exchangeable base in the three samples, and acid cations as iron were important in the cultivated soils, where base saturation was < 50% (Table 2).

Total energy in $CaCl_2$ had the same value for the two cultivated soils (150 kT, Figures 4a and c; however, there was an outstanding difference for the forest sample because the total energy of interaction became negative at small distance (H < 3 nm). Here, this primary minimum of energy was determined not by the cancellation of EL, but by the behavior of the AB component, which gave negative values (−150 kT at 3 nm; Figure 4a). A negative value of the AB component may be interpreted as an attractive force caused by a reduction in hydration pressure of water-repellent surfaces (Grasso et al., 2002). For cultivated soils, the AB component remained positive (Figure 4b and b). Hence, the strong tendency of colloids to flocculate predicted by the extended DLVO model was mainly conditioned by the hydrophobicity of this soil.

In $FeCl_3$, the forest sample also showed the smallest total energy values (~0 kT; Figure 4a) of all soils. Because this was determined by the ζ of iron solution (Figure 2c) and the isoelectric point was reached in it at around soil pH (6.18), the electrostatic repulsive force.

(EL) was canceled there (Figure 4d). Then, the total energy remained as a balance between the dispersive (LW) and AB components, which cancelled each other at small distances. This explains the virtually null value of total energy at H > 3 nm in $FeCl_3$ for the forest soil. The organic and conventional soils had relatively similar total energies of 350 and 250 kT in iron solution, respectively (Figure 4d and f).

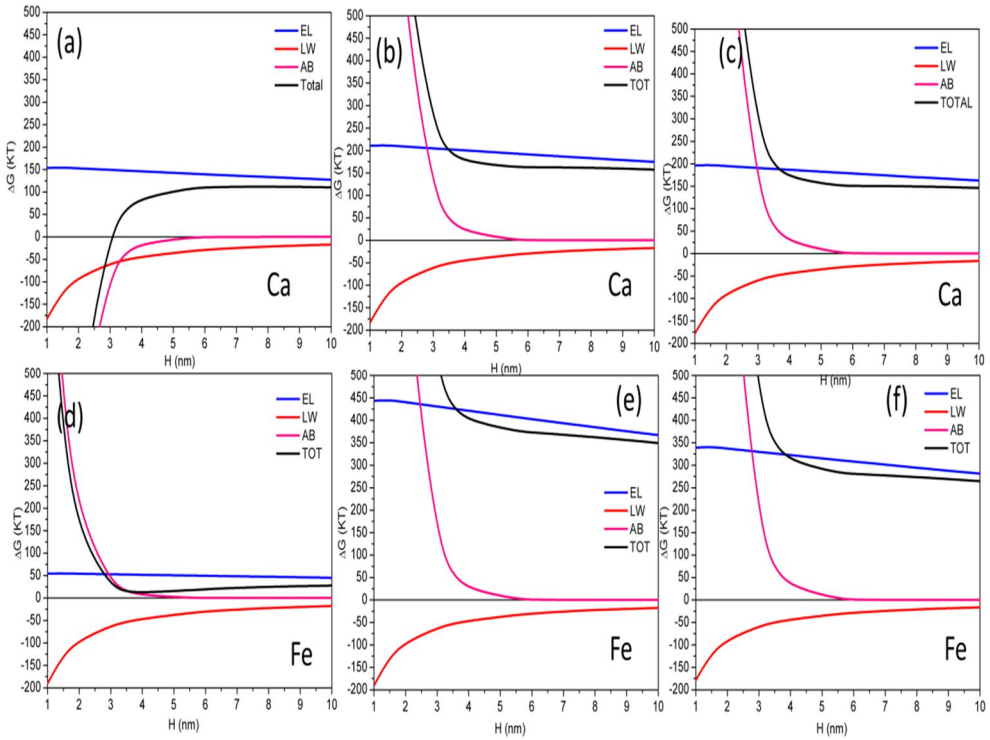


**Figure 3**. Total energies of interaction between particles according to different ionic solutions ($10^{-3}$ M): (a) Forest soil (pH 6.18); (b) organic soil (pH 6.24); (c) conventional soil $10^{-3}$ M (pH 5.88); (d) secondary energy minimum for forest soil; (e) secondary energy minimum for organic soil; (f) secondary energy minimum for conventional soil.

Hydrophobicity of forest soil may be in agreement with results of the SEM study (Figure 5), in which some biogenic activity, likely fungus hyphae, was recognized (Figure 5a). The relationship between acid pH, fungal activity and hydrophobicity has been advance by our research group in Aranda et al. (2016) and others (Kershaw et al., 2005, Maqbela et al., 2009, Fisher et al., 2010). Moreover, it is reasonable to establish a relationship between SOM quality and hydrophobicity in this sample. As indicated by the A4/A6 ratio in Table 2, humic molecules in BNG were less humified (larger A4/A6) than in cultivated soils. This implies a prevalence of aliphatic over aromatic compounds, which could be related to a stronger hydrophobic character for the forest soil. This might also be related with the potential saturation of colloidal surfaces in the BNG sample, explained above in view of the ζ behavior.

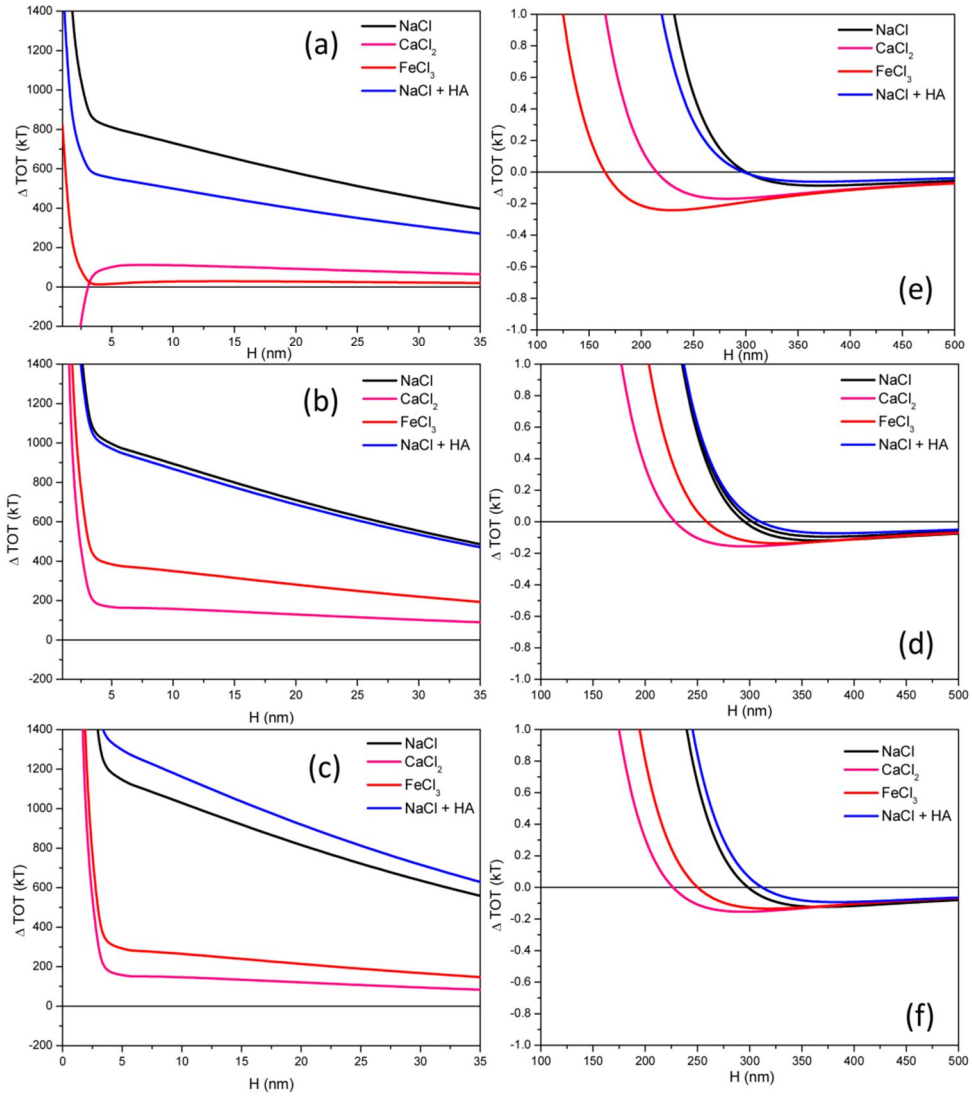


**Figure 4**. Components of total interaction energy at soil pH: (a) Forest soil, $10^{-3}$ M $CaCl_2$ solution (pH 6.18); (b) organic soil, $10^{-3}$ M $CaCl_2$ solution (pH 6.24); (c) conventional soil, $10^{-3}$ M $CaCl_2$ solution (pH 5.88); (d) forest soil, $10^{-3}$ M $FeCl_3$ solution (pH 6.18) (e) organic soil, $10^{-3}$ M $FeCl_3$ solution (pH 6.24); (f) conventional soil, $10^{-3}$ M $FeCl_3$ solution (pH 5.88). TOT, total energy; EL, electrostatic component; AB, acid–base component; LW, Lifshitz–van der Waals component

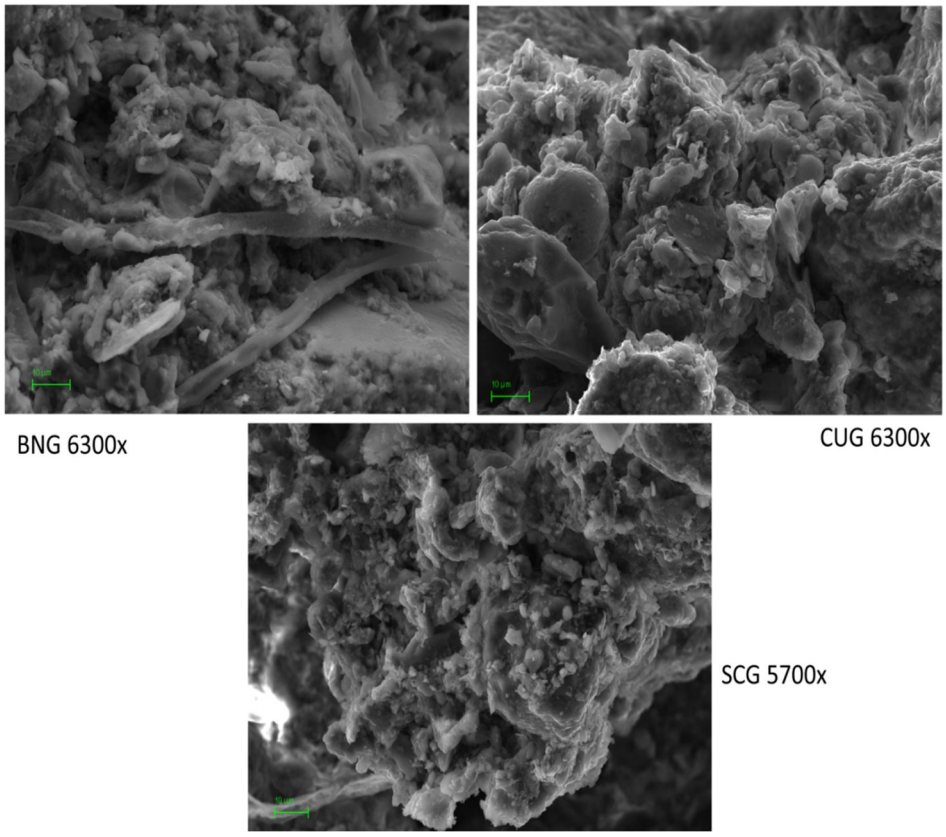


**Figure 5**. SEM images of soil structure at colloidal scale. (a) Forest soil (6300x): clay domains and clusters supported by filamentous structures of fungus hypha; (b) organic soil (6300x); (c) conventional soil (5700x).

*4.3.5 Adsorption isotherms*

Figure 6 shows adsorption isotherms 283.15 K, 293.15 K and 313.15 K of the soils studied. In general, the isotherms conform to the Langmuir model, yielding saturation values greater than 0.30–0.35 g of carbon added, although at higher concentrations there was a tendency toward some desorption and the curve decreases slightly. This desorption is attributed to the fact that after reaching the maximum value, it is caused by total coating of the surface by a monolayer of HA, which gives rise to reactions between the AH radicals

(Ontiveros-Ortega et al. 1998). The obtained C adsorption for the three soils had the order of the very acid (pH 4.37) podsol studied by Vandenbruwane et al. (2007), and was much less than that established by Saidy et al. (2013) for pure illite and smectite.

In general, the conventional soil (SCG) was the least adsorbent at any temperature. This may be explained by the lower contents of natural organic matter, which has been shown to be a contributing factor to adsorption (Plaza at. 2015). The soil with most adsorption at the three temperatures was the organic olive CUG, although it was very close to that of natural soil (BNG). This confirms in part the finding above on the basis of ζ curves.

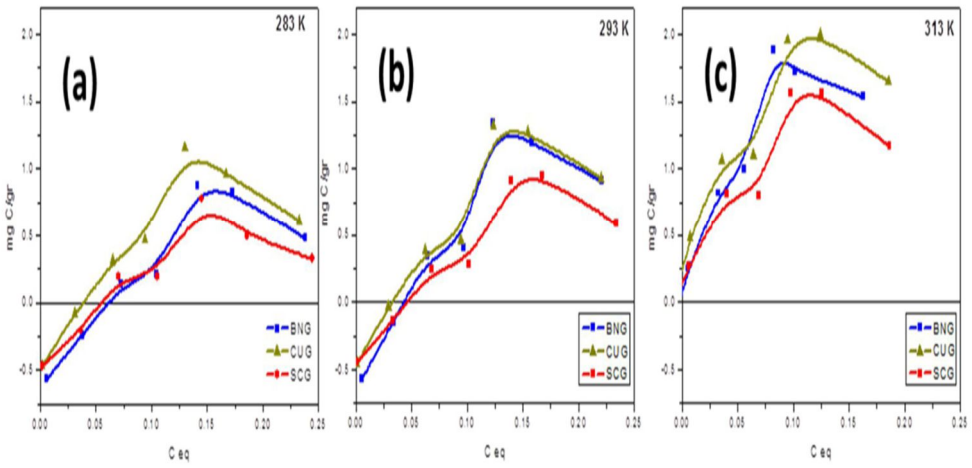


**Figure 6**. Absorption isotherms for studied soils: 283 K (a), 293 K (b) and 313 K (c). Colored curves: blue BNG, red SCG, green CUG

## 5. CONCLUSIONS

Soils of the Sierra Morena can be considered marginal for olive growth because of their slopes, thicknesses, stoniness and nutrient poverty. Here, we compared physical, chemical and colloidal properties of soil structure of a conventionally-managed olive grove with those of an organic olive farm, relating both to a natural soil under Mediterranean forest. The soil mineralogy matched the granodiorite parent rock, formed mainly by quartz (peak 0.425 nm) and phyllosilicates (peak 0.445 nm), but different 2:1 phases dominated the clay

fraction of each soil, i.e., smectite in the conventional, vermiculite in the forest, and a vermiculite-illite mixed layer in the organic soil. ζ curves of the fine earth fraction (< 2 mm) were negative (< 0 mV) in solutions of mono- (potassium) and divalent- (calcium) cation, corresponding to permanent charges of 2:1 phyllosilicates. However, in solutions of trivalent cations (iron), ζ attained positive values (> 0 mV) at acid pH. When commercial HA was added to the samples, ζ curves for the conventional and forest soil showed, respectively, a decrease and increase in mV, which was interpreted as surface adsorption of HA. Structural stability of the soil samples at colloidal scale where characterized by total interaction energies, calculated according the extended DLVO model. Total energies where lower in the natural sample than in the cultivated soils, so the first sample showed a greater tendency toward particle flocculation and greater stability. This matches the soil physical properties related to structural quality, such as soil macroporosity or the structural stability index, which were maximum in the forest soil. Specifically, in calcium solution, total energy of the forest sample was clearly attractive at close distance (< 0 kT at 10 nm). More than by the electrostatic force, this was determined by the negative value of the AB component, which was related to a small value of the electron-donor component of surface free energy $\gamma^-$ (15 mJ $m^{-2}$). The latter implies a clear hydrophobic character of the forest soil, which may have been caused by the high content and aliphatic composition of organic matter in this soil, as well as by biogenic activity shown by electron microscopy.

**References**

Álvarez, S., Soriano, M.A., Landa, B.B., Gómez, J.A., 2007. Soil properties in organic olive groves compared with that in natural areas in a mountainous landscape in southern Spain. Soil Use Manag. 23, 404–416.

Aranda, V., Ayora-Cañada, M. J., Domínguez-Vidal, A., Martín-García, J. M., Calero, J., Delgado, R., ... & González-Vila, F. J. (2011). Effect of soil type and management (organic vs. conventional) on soil organic matter quality in olive groves in a semi-arid environment in Sierra Mágina Natural Park (S Spain). Geoderma, 164(1), 54-63.

Aranda, V., Macci, C., Peruzzi, E., & Masciandaro, G. (2015). Biochemical activity and chemical-structural properties of soil organic matter after 17 years of amendments with olive-mill pomace co-compost. Journal of environmental management, 147, 278-285.

Aranda, V., Calero, J., Plaza, I., & Ontiveros-Ortega, A. (2016). Long-term effects of olive mill pomace co-compost on wettability and soil quality in olive groves. Geoderma, 267, 185-195.

Barré, P., Fernandez-Ugalde, O., Virto, I., Velde, B., & Chenu, C. (2014). Impact of phyllosilicate mineralogy on organic carbon stabilization in soils: incomplete knowledge and exciting prospects. Geoderma, 235, 382-395.

Baumgarten W, Neugebauer Th, Fuchs E, Horn R. Structural stability of Marshland soils of the riparian zone of the Tidal Elbe River. Soil and Tillage Research 2012;125:80e82012

Bronick, C. J., & Lal, R. (2005). Manuring and rotation effects on soil organic carbon concentration for different aggregate size fractions on two soils in northeastern Ohio, USA. Soil and Tillage Research, 81(2), 239-252.

Calero, J., Delgado, R., Delgado, G., & Martín-García, J. M. (2009). SEM image analysis in the study of a soil chronosequence on fluvial terraces of the middle Guadalquivir (southern Spain). European journal of soil science, 60(3), 465-480.

CAP, Consejería de Agricultura y Pesca. 2015. El sector del aceite de oliva y la aceituna de mesa en Andalucía, Consejería de Agricultura y Pesca - Junta de Andalucía, Sevilla.Giese (1995).

Duman, O., Tunc, S., 2008. Electrokinetic Properties of Vermiculite and Expanded Vermiculite: Effects of pH, Clay Concentration and Mono- and Multivalent Electrolytes. Separation Science and Technology 43, 3755-3776.

Duran, J. D. G., Ontiveros, A., Delgado, A. V., & Gonzalez-Caballero, F. (1998). Kinetics and interfacial interactions in the adhesion of colloidal calcium carbonate to glass in a packed-bed. Applied surface science, 134(1), 125-138.

EC, European Commission. 2005. Commission Regulation (EC) No. 2183/2005 of 22 December 2005 amending Council Regulation (EC) No. 1782/2003 establishing common rules for direct support schemes under the common agricultural policy and establishing certain support schemes for farmers and amending Regulation (EC) No. 795/2004 laying down detailed rules for the implementation of the single payment scheme provided for in Council Regulation (EC) No. 1782/2003.

EC, European Commission. 2011. Commission document COM(2011) 625/2, corrigendum Annule et remplace le document COM(2011) 625, establishing rules for direct payments to farmers under support schemes within the framework of the common agricultural policy (CAP). http://eur-lex.europa.eu/LexUriServ/LexUriServ.do?uri=COM:2011:0021:FIN:ES:PDF

Gómez, J.A. Battany, M., Renschler, C.S. and Fereres, E. 2003. Evaluating the impact of soil management on soil loss in olive orchards. Soil Use and Management 19, 127-134.

Fisher, T., Veste, M., Wiehe, W., Lange, P., 2010. Water repellency and pore clogging at early successional stages of microbiotic crust on inland dunes, Brandenburg, NE Germany. Catena 80, 47–52.

Giese, R.F., Costanzo, P.M., van Oss, C.J. (1995). The surface free energies of talc and pyrophyllite. Phys. Chem. Minerals 17, 611-616.

Gomez, J.A., Guzmán, M.J., Giráldez, J.V., Fereres, E. 2009. The influence of cover crops and tillage on water and sediment yield, and on nutrient, and organic matter losses in an olive orchard on sandy loam soil. Soil & Tillage Research 106, 137-144.

Grasso, D., Subramaniam, K., Butkus, M., Strevett, K., & Bergendahl, J. (2002). A review of non-DLVO interactions in environmental colloidal systems. Reviews in Environmental Science and Biotechnology, 1(1), 17-38.

Hajnos, M., Calka, A., & Jozefaciuk, G. (2013). Wettability of mineral soils. Geoderma, 206, 63-69.

Infante-Amate, J. (2012). The ecology and history of the Mediterranean olive grove: the Spanish great expansion, 1750-2000. Rural History, 23(02), 161-184.

J. Calero, A. Ontiveros-Ortega, V. Aranda and I. Plaza. Humic acid adsorption and its role in colloidal-scale aggregation determined with the zeta potential, surface free energy and the extended-DLVO theory. European Journal of Soil Science

Karlen, D. L., Mausbach, M. J., Doran, J. W., Cline, R. G., Harris, R. F., & Schuman, G. E. (1997). Soil quality: a concept, definition, and framework for evaluation (a guest editorial). Soil Science Society of America Journal, 61(1), 4-10.

Kemper, W.D., Rosenau, R.C., 1986. Aggregate stability and size distribution. In:Klute, A. (Ed.), Methods of Soil Analysis, Agronomy no. 9. American Society of Agronomy and Soil Science Society of America, Madison, WI, pp. 425–442.Kershaw et al., 2005,

Kononova, M.M., 1966. Soil Organic Matter, 2nd ed. Pergamon, Oxford.

Kothawala, D. N., Moore, T. R., & Hendershot, W. H. (2008). Adsorption of dissolved organic carbon to mineral soils: A comparison of four isotherm approaches. Geoderma, 148(1), 43-50.

Kute, A., 1986. Methods of Soil Analysis. Part 1. Agronomy Monographs, 9, ASA and SSSA, Madison, USA.

Lagaly, G. (2006). Colloid clay science. Developments in clay science, 1, 141-245.

Maqbela, M.P., Mnkeni, P.N.S., 2009. Nostoc cyanobacterial inoculation in South African agricultural soils enhances soil structure, fertility, and maize growth. Plant Soil 315, 79–92.

Martínez, R.E., Sharma, P., Kappler, A., 2010. Surface binding site analysis of Ca 2+ homoionized clay humic acid complexes. Journal of Colloid and Interface Science 352, 526-534

Moleon, J. A., Ontiveros-Ortega, A., Gimenez-Martin, E., & Plaza, I. (2015). Effect of N-cetylpyridinium chloride in adsorption of graphene oxide onto polyester. Dyes and Pigments, 122, 310-316.

Ontiveros A, Duran J, Delgado AV, Gonzalez-Caballero F, Chibowski E. A study on the adhesion of calcium carbonate to glass. Energy balance in the deposition process. Journal of Adhesion Science and Technology 1996a;10(9):847e68.

Ontiveros A, Duran JDG, Gonzalez-Caballero F, Chibowski E. Adhesion of colloidal ZnS on silicon. Effects of ionic strength and radio frequency electric field. Journal of Adhesion Science and Technology 1996b;10(10):999e1019.

Ontiveros-Ortega, A., Espinosa-Jiménez, M., Chibowski, E., & González-Caballero, F. (1998). Effect of tannic acid on the surface free energy of polyester dyed with a cationic dye. Journal of colloid and interface science, 199(1), 99-104.

Ontiveros-Ortega A, Vidal F, Giménez E, Ibañez JM. Effect of heavy metals on the surface free energy and zeta potential of volcanic glass: implication on the adhesion and growth of microorganism. Journal of Materials Science 2014;49(9):3550e9.

Page, A. L. (1982). Methods of soil analysis: chemical and microbiological proerpteis. Amen Society of Agronomy.

Plaza, I., Ontiveros-Ortega, A., Calero, J., & Aranda, V. (2015). Implication of zeta potential and surface free energy in the description of agricultural soil quality: Effect of different cations and humic acids on degraded soils. Soil and Tillage Research, 146, 148-158.

Ramos-Tejada, M. M., Ontiveros, A., Viota, J. L., & Durán, J. D. G. (2003). Interfacial and rheological properties of humic acid/hematite suspensions. Journal of colloid and interface science, 268(1), 85-95.

Saidy, A. R., Smernik, R. J., Baldock, J. A., Kaiser, K., & Sanderman, J. (2013). The sorption of organic carbon onto differing clay minerals in the presence and absence of hydrous iron oxide. Geoderma, 209, 15-21.

Soil Conservation Service, 1972. Soil Survey Laboratory Methods and Procedures for Collecting Soil Samples. U.S. Department of Agriculture, Washington.

Somasundaran, P., & Krishnakumar, S. (1997). Adsorption of surfactants and polymers at the solid-liquid interface. Colloids and Surfaces A: physicochemical and engineering aspects, 123, 491-513.

Sondi, I., Bišćan, J., & Pravdić, V. (1996). Electrokinetics of pure clay minerals revisited. Journal of Colloid and Interface Science, 178(2), 514-522.

Swift, R.S., 1996. Organic matter characterization (chap. 35). In: Sparks, D.L., et al. (Eds.), Methods of Soil Analysis, Part 3, Chemical MethodsSoil Sci. Soc. Am. Book Series n° 5. ASA/SSSA, Inc., Madison, WI, USA, pp. 1018–1021.

Sys, I.C., van Ranst, E., Debaeye,I.J., 1991. Land evaluation.AgriculturalPublications 7. University of Ghent, Belgium.

van Oss CJ, Chaudhury MK, Good RJ. Interfacial Lifshitzevan der Waals and polar interactions in macroscopic systems. Chemical Reviews 1988;88(6): 927e41.

van Oss CJ, Good RJ. Surface tension and the solubility of polymers and biopolymers: the role of polar and apolar interracial free energy. Journal of Macromolecular Science: Part A e Chemistry 1989;26(8):1183e203.

van Oss CJ. Interfacial forces in aqueous media. New York: Marcel Dekker Inc.; 1994

Van Oss, C. J. (1995). Hydrophobicity of biosurfaces—origin, quantitative determination and interaction energies. Colloids and Surfaces B: Biointerfaces, 5(3-4), 91-110.

Vandenbruwane, J., De Neve, S., Qualls, R. G., Salomez, J., & Hofman, G. (2007). Optimization of dissolved organic nitrogen (DON) measurements in aqueous samples with high inorganic nitrogen concentrations. Science of the total environment, 386(1), 103-113.

Wang M, Revil A., 2010. Electrochemical charge of silica surface at high ionic strength in narrow channels. Journal of Colloid and Interface Science 343, 381-386.

## 5.4 Estudio de hidrofobicidad del compost para añadir a suelos: Long-term effects of olive mill pomace co-compost on wettability and soil quality in olive groves.

*Resumen.*

Los suelos mediterráneos destinados al cultivo de olivos se caracterizan por el bajo contenido de materia orgánica, por el clima seco-semiárido en el que se desarrollan, y con un alto nivel de degradación provocado por las actividades humanas. En este contexto, el aumento de la materia orgánica del suelo se convierte en un requisito imprescindible para aumentar la producción agraria. La aplicación de abonos orgánicos, que contribuyen eficazmente al suministro de nutrientes para el crecimiento de las plantas es, por tanto, de interés, y también puede mejorar las propiedades físicas inherentes del suelo y preservar sus funciones alteradas por agronómica prácticas. Las implicaciones del uso de abono OMP (orujo molido de oliva) sobre la repelencia al agua en el suelo, no se han tratado con mucha extensión en el mundo científico, a pesar de su relevancia.

La humectabilidad del suelo y la repelencia al agua (hidrofobicidad) son características importantes del suelo. El régimen hídrico del suelo puede ser profundamente afectado por la hidrofobicidad debido a la relación de baja infiltración, conductividad hidráulica y el agua disponible. Por el contrario, la hidrofobicidad del suelo puede mejorar el desarrollo y la estabilidad de la estructura, la densidad aparente y la porosidad. La repelencia al agua ha sido ampliamente observada en zonas urbanas,

forestales y agrícolas en relación con la materia orgánica del suelo, la textura, mineralogía y el clima. Por lo tanto hay más estudios que relacionan la repelencia al agua con el tipo de suelo y la gestión del suelo específica.

Dada su importancia, la medida de repelencia del agua del suelo es importante. Hay varias técnicas para su estimación, yo he utilizado la técnica del ángulo de contacto (CA), que muestra un significado físico y me permite determinar las componentes de energía libre de superficie. Usar esta técnica tiene varias ventajas, por ejemplo, se puede explicar las superficies minerales en términos de componentes de ácido / base (la $\gamma^-$ donador de electrones y aceptores de electrones $\gamma^+$). El control de los fenómenos de floculación, adsorción, humectación y propiedades reológicas de la dispersión dependen de las interacciones entre partículas. La completa caracterización a través de las interacciones interfaciales nos proporciona una base para una definición natural y cuantitativa a través de la energía de interacción total entre las partículas en un medio acuoso. Tal definición puede revelar qué propiedades del materiales y del medio líquido son responsables de la su comportamiento interfacial y por lo tanto la cohesión del suelo.

El objetivo de este trabajo fue evaluar los efectos de compostado OMP sobre la humectabilidad y la hidrofobicidad de los suelos de olivar, la aplicación del modelo de van Oss para los componentes de energía libre de superficie.

Tras el estudio llegamos a la conclusión de que el factor determinante más decisivo de la capacidad de humectación del suelo parece ser el contenido en carbono orgánico, pero la presencia de carbonatos y otros parámetros relacionados con el área de superficie específica, así como la carga de la partícula, también podría influir fuertemente en esta propiedad del suelo.

De acuerdo con las pruebas, en todas las muestras existe una dependencias claras y fuertes relaciones entre energía libre de superficie (SFE), principalmente el componente γ-, y los indicadores de calidad del suelo (tales como el contenido de carbonatos y contenido de arena).

# Articulo científico:

# Long-term effects of olive mill pomace co-compost on wettability and soil quality in olive groves

# Revista científica:

# Geoderma

Geoderma 267 (2016) 185–195

Contents lists available at ScienceDirect

Geoderma

journal homepage: www.elsevier.com/locate/geoderma

# Long-term effects of olive mill pomace co-compost on wettability and soil quality in olive groves

V. Aranda [a,*], J. Calero [a], I. Plaza [b], A. Ontiveros-Ortega [b,c]

[a] Department of Geology, University of Jaén, B-3, 23071 Jaén, Spain
[b] Department of Physics, University of Jaén, A-3, 23071 Jaén, Spain
[c] Andalusian Institute of Geophysics, University of Granada, 18071 Granada, Spain

ARTICLE INFO

*Article history:*
Received 7 August 2015
Received in revised form 21 December 2015
Accepted 28 December 2015
Available online xxxx

*Keywords:*
Organic olive groves
Olive mill pomace
Soil hydrophobicity
Soil water repellency
Surface free energy

ABSTRACT

The importance of soil wettability and its relationship to many soil properties has been studied extensively. However, few studies have addressed it as a result of organic amendment in agricultural soils. Wettability (hydrophilicity) and soil quality in olive groves with olive mill pomace (OMP) compost amendment were compared to conventional groves with only mineral fertilization. In addition to soil management, soil parent material (carbonated vs. siliceous) and soil depth (surface 0–10 cm vs. subsurface 0–20 cm layers) were also studied by means of an unreplicated field experiment on the only appropriate farm available in Southern Spain. The aim of this work was to evaluate the effects of composted OMP on wettability and hydrophobicity of olive grove soils, using the van Oss model for surface free energy components. Other physical, chemical and mineralogical parameters were also analyzed. The electro-donor component $\gamma^-$ of surface free energy was found to be the most suitable parameter for assessing soil hydrophobicity over other current methods, such as WDPT tests or contact angle. All the soils analyzed were wettable, except the surface horizons of organic siliceous profiles, which were hydrophobic with a mean $\gamma^-$ of 27.57 mJ m$^{-2}$. The main factors that significantly increased soil hydrophobicity were depth and parent material. This implies, first, that the effects of compost only affect the soil surface, and second, the lack of carbonates in the siliceous quartzite contributes to further increases in soil hydrophobicity. The variables most correlated with hydrophobicity were organic carbon content (soil organic matter quality was not significantly related to soil hydrophobicity) and cation exchange capacity, but carbonates (the higher the carbonates, the lower hydrophobicity) and soil texture (the more sand, the higher hydrophobicity) also demonstrated their association. It may be concluded that, although moderate soil hydrophobicity seems to alter plant water availability and infiltration under unsaturated conditions, it could be positive for soil structure and soil quality in general.



## 1. Introduction

Soil wettability and water repellency (hydrophobicity) are important soil characteristics, mainly because they affect soil moisture. Soil water regimes can be profoundly affected by hydrophobicity due to lowered infiltration ratio, hydraulic conductivity and available water (Doerr et al., 2000). In contrast, soil hydrophobicity can improve structural development and stability (Goebel et al., 2005; Plaza et al., 2015) and bulk density and porosity (Doerr et al., 2000). Water repellency has been widely observed in urban (Diehl and Schaumann, 2007), forest (Mataix-Solera and Doerr, 2004) and agricultural soils (Diamantis et al., 2013; Peikert et al., 2015) related to soil organic matter, texture, mineralogy and climate (Doerr et al., 2000; Leelelamanie et al., 2010). Thus further studies relating the dynamics of water repellency to specific soil type and management seem desirable.

Given its significance, a suitable measure of soil water repellency (SWR) is important. There are several techniques for its estimation, from purely empirical to meaningful physical measures. Probably the most common method is the water drop penetration time (WDPT) test, which easily classifies soils into five water repellency classes (Bisdom et al., 1993). However, it has no linear quantitative scale for slight to moderately repellent soil (*e.g.*, <5 s), and could take a long time for repellent soils. Water/ethanol mixtures have been proposed as the liquid for the test, as the molarity of the ethanol droplet method reduces the WDPT test time, but has the same limitations as the WDPT test at low water repellency (Chau et al., 2014). Another widely used measure is the contact angle (CA) (Goebel et al., 2005; Woche et al., 2005; Diehl and Schaumann, 2007), which shows some physical meaning and enables SWR to be studied throughout the soil range (from wettable to extremely repellent). However, all the above tests estimate only the surface properties of solids in water, and do not provide a comprehensive thermodynamic characterization of the solid surface alone. Hence, a complete determination of surface free energy components

* Corresponding author.
*E-mail address:* varanda@ujaen.es (V. Aranda).

http://dx.doi.org/10.1016/j.geoderma.2015.12.027
0016-7061/

would be recommendable, particularly for mineral soils with low organic matter, where WDPT results are less useful (Hajnos et al., 2013). Few authors have applied this approach to soil wettability. Goebel et al. (2005) followed Fowkes's (1964) description of surface free energy in dispersive and non-dispersive interactions to characterize soil organic matter dynamics. But the van Oss et al. (1988) approach for acid–base and Lifshitz-van der Waals interactions has several advantages, e.g., it can explain mineral surfaces in terms of acid/base components (the electron-donor $\gamma^-$ and electron-acceptor $\gamma^+$). So the $\gamma^-$ component would delimit soil hydrophobicity better than Fowkes's non-dispersive component, because of the strong monopolarity of the main soil mineral surfaces, which typically show constant but very low $\gamma^+$ (Grasso et al., 2002). Hajnos et al. (2013) applied the van Oss model and found no dependencies between soil organic matter and wettability parameters.

Olive grove soils are typically Mediterranean, characterized by low organic matter content, by the semiarid climate in which they develop, and degradation by human activities (Nieto et al., 2010). Olive grove soils therefore typically show less than 1% in organic carbon. In this context, increasing soil organic matter becomes imperative. Application of organic amendments that contribute effectively to nutrient supply for plant growth is therefore of interest, and can also improve inherent physical soil properties and preserve soil functions altered by agronomic practices. In the south of Spain, the widely extended olive crop leads to a huge annual production (around four million tons) of OMP, the main byproduct of the two-phase olive oil extraction system (García-Ruiz et al., 2012). OMP recycling by composting and subsequent application returning it to the olive orchard could help to improve soil fertility and reduce the use of inorganic fertilizers in the olive-growing industry. While the implications of the use of untreated and composted OMP on soil fertility (López-Piñeiro et al., 2011; García-Ruiz et al., 2012; Lozano-García and Parras-Alcántara, 2013;) and soil microbiology/enzymatic activities (López-Pieñiro et al., 2011; García-Ruiz et al., 2012) have been reasonably-well studied, their effects on soil physical properties, and especially, on soil water repellency, have not been given much attention, in spite of their relevancy. To the knowledge of the authors, all other studies have been carried out only in olive groves on calcareous soil, which is the most common in the study area, so the effects of OMP compost amendment in siliceous orchards are not well known. Nevertheless, a location where the geology makes possible paired experimental designs for long-term OMP compost applications on calcareous/siliceous soils in replicated field plots is extremely uncommon.

The aim of this work was to evaluate the effects of composted OMP on wettability and hydrophobicity of olive grove soils, applying the van Oss model for surface free energy components. Results of this model are compared to the more widely used measures of water repellency, the WDPT and CA tests. Correlation of surface free energy parameters with soil chemical/physical variables is also analyzed, taking into account the three basic factors of variation in olive grove soils: management (organic vs. conventional), parent material (carbonated vs. siliceous) and soil depth (0–10 cm vs. 0–20 cm layers).

## 2. Material and methods

### 2.1. Site description and soil sampling

The olive groves studied are located in Andújar, Jaén Province (southern Spain). The climate is Mediterranean, with cool winters and hot, very dry summers and a mean annual temperature of 17.9 °C. All the olive groves (about 180 ha) under study had a density of 90–110, 35-to-45-year-old trees per hectare distributed regularly with a typical canopy cover of about 30% of the cultivated area. About half of these groves were fertilized with composted OMP (organic management) and the other half with mineral fertilizers (conventional management). Due to the low porosity of OMP, structuring agents, mainly olive tree leaves, are usually employed in composting. Several types of local manure, which act as a source of nitrogen to balance the C/N ratio and avoid nitrogen sequestration after addition to the soil, are also used. In fact, the compost used is considered a co-compost (50% OMP and 50% olive leaves and manure). 6–10 Mg ha$^{-1}$ of this co-compost had been applied annually in autumn to the organic groves for the last 17 years. It was always evenly spread over the soil in the intercanopy and followed by very superficial chisel passes to control plant cover. In the farms where the co-compost was applied, management was organic with no mineral fertilization or pesticides, and was characterized by no-till soils and maintenance of the spontaneous herbaceous cover. Fertilization of the conventional groves, which did not receive co-compost, consisted of the application of 50–70 kg N ha$^{-1}$ as urea or ammonium sulfate under the tree canopy in the early spring. Weeds were controlled by residual herbicides.

Four large homogeneous plots of soil (about 2500 m$^2$) which were near each other, two with calcareous soils developed over a Miocene calcarenite (with and without co-compost application) and two with siliceous soils over a Triassic quartzite (with and without co-compost application), were sampled. This field experiment was not replicated because no other suitable experimental conditions could be found in the study region (pairs of conventional and OMP-composted olive groves over siliceous and calcareous bedrock). Each plot which received co-compost was comparable to that which received no compost in terms of climate, slope, orientation, soil type, and tree density and age. Sampling in each plot consisted of a random selection of three locations in the intercanopy, and in each location, a soil sample composed of four subsamples (from the surface 0–10 cm layer and subsurface 10–20 cm) was taken at random within a 5-m radius.

### 2.2. Chemical, physical and mineralogical soil analyses

All analytical soil sample data refer to the fine-earth fraction (<2 mm). The procedures used in soil analyses were as outlined by the American Society of Agronomy and Soil Science Society of America (Page et al., 1982; Klute, 1986). The organic carbon (OC) content was determined by the Tyurin method with dichromate oxidation. Total N was measured with the Kjeldhal method. The pH (1:2.5) was found by potentiometry in distilled water. Electrical conductivity (EC) of water extracts had a soil/water ratio of 1:5, standardized at 25 °C. Equivalent $CaCO_3$ was found by volumetry with a Bernard calcimeter. Extractable phosphorus was extracted with sodium bicarbonate solution and determined by colorimetry (Olsen method). Exchangeable bases and cation exchange capacity (CEC) were found by the ammonium acetate method (pH 7) and the sodium chloride method, and then the concentrations were determined by atomic absorption spectrophotometry. Clay and sand contents were determined by the pipette method after elimination of organic matter with $H_2O_2$ and dispersion with sodium polyphosphate. Water retention at −33 kPa (field capacity) and −1500 kPa (permanent wilting point) was calculated by the Richards membrane method, and plant available water content (AWC) from the difference between water retention at −33 and −1500 kPa, employing the Cm coefficient for gravelly soils (Soil Conservation Service, 1972). Saturated hydraulic conductivity (Ks, cm h$^{-1}$) was measured by a constant-head permeameter (Eijkelkamp Agrisearch Equipment, Giesbeek, NL) in laboratory, using unaltered cores taken in the field. Unsaturated hydraulic conductivity was found at −10 kPa employing the pedotransfer functions given by Saxton and Rawls (2006). Soil bulk density was measured using the cylindrical core of known volume method and particle density with a pycnometer. Total porosity was estimated from the particle and bulk density, and macroporosity from total porosity less microporosity, the latter measured as water content at −33 kPa. The soil aggregate stability index (ASI) was determined with the method described by Kemper and Rosenau (1986), using a wet sieving apparatus (Eijkelkamp Agrisearch Equipment, Giesbeek, NL). The water drop penetration time test (WDPT) was performed following Bisdom et al. (1993) and employing

**Table 1**
Water repellency parameters for the 24 sampled horizons and the co-compost.

| Sample | Depth (cm) | WDPT (s) | CA (°) | Surface free energy components (mJ $m^{-2}$) | | | | |
|---|---|---|---|---|---|---|---|---|
| | | | | $\gamma^{LW}$ | $\gamma^{-}$ | $\gamma^{-}$ | $\gamma^{AB}$ | Total |
| CO1 | 0–10 | <1 | 37 | 46.84 | 0.19 | 38.47 | 5.41 | 52.24 |
| CO2 | 10–20 | <1 | 25 | 48.85 | 0.25 | 45.99 | 6.78 | 55.59 |
| CO3 | 0–10 | <1 | 34 | 46.84 | 0.72 | 36.12 | 10.20 | 57.02 |
| CO4 | 10–20 | <1 | 24 | 48.85 | 0.20 | 47.32 | 6.15 | 55.07 |
| CO5 | 0–10 | 16 | 43 | 46.15 | 0.81 | 28.10 | 9.54 | 55.67 |
| CO6 | 10–20 | <1 | 30 | 48.85 | 0.38 | 40.62 | 7.86 | 56.69 |
| CC1 | 0–10 | <1 | 27 | 47.48 | 0.43 | 43.58 | 8.66 | 56.17 |
| CC2 | 10–20 | <1 | 33 | 48.07 | 0.19 | 41.10 | 5.59 | 53.61 |
| CC3 | 0–10 | <1 | 33 | 47.17 | 0.68 | 36.95 | 10.03 | 57.20 |
| CC4 | 10–20 | <1 | 35 | 48.34 | 0.58 | 35.11 | 9.03 | 57.33 |
| CC5 | 0–10 | <1 | 29 | 47.17 | 0.25 | 44.44 | 6.67 | 53.78 |
| CC6 | 10–20 | <1 | 26 | 48.34 | 0.27 | 45.37 | 7.00 | 55.38 |
| SO1 | 0–10 | 1038 | 50 | 43.80 | 0.61 | 25.35 | 7.86 | 51.69 |
| SO2 | 10–20 | <1 | 16 | 48.85 | 0.10 | 54.19 | 4.66 | 53.47 |
| SO3 | 0–10 | 351 | 51 | 41.09 | 0.58 | 25.55 | 7.70 | 48.80 |
| SO4 | 10–20 | <1 | 28 | 47.48 | 0.21 | 45.53 | 6.18 | 53.61 |
| SO5 | 0–10 | 548 | 49 | 43.37 | 0.56 | 31.81 | 8.44 | 51.84 |
| SO6 | 10–20 | <1 | 25 | 47.48 | 0.19 | 48.06 | 6.04 | 53.55 |
| SC1 | 0–10 | <1 | 27 | 46.50 | 0.46 | 44.22 | 9.02 | 55.49 |
| SC2 | 10–20 | <1 | 35 | 45.03 | 0.55 | 38.01 | 9.14 | 54.19 |
| SC3 | 0–10 | <1 | 22 | 46.50 | 0.12 | 52.42 | 5.02 | 51.52 |
| SC4 | 10–20 | <1 | 23 | 48.61 | 0.14 | 49.96 | 5.29 | 53.94 |
| SC5 | 0–10 | <1 | 30 | 47.78 | 0.08 | 46.73 | 3.87 | 51.69 |
| SC6 | 10–20 | <1 | 32 | 46.50 | 0.37 | 41.09 | 7.80 | 54.27 |
| Compost | – | 2602 | 65 | 46.84 | 0.19 | 14.80 | 3.35 | 50.19 |

CA = contact angle ($H_2O$); CO = carbonated organic sample; CC = carbonated conventional sample; SO = siliceous organic sample; SC = siliceous conventional sample.

the repellency classes: wettable (WDPT ≤ 5 s), slightly water repellent (5–60 s), strongly water repellent (60–600 s), severely water repellent (600–3600 s), and extremely water repellent (>3600 s).

Fractionation of soil OM was done following the IHSS procedure (Swift, 1996): Total extractable carbon for humic and non-humic substances was extracted from soil by mechanically shaking the samples in a 0.1 M NaOH and $Na_4P_2O_7$ solution at pH 14 for 24 h at 60 °C (1:10 w/v). The extracts were centrifuged and filtered (Millipore 0.45 μm). Separation of the total extractable carbon fraction into humic acids (HA) and fulvic acids (FA) was done by precipitation with $H_2SO_4$ and purification with polyvinylpolypyrrolidone to eliminate non-humic carbon, respectively. The C content in HA and FA was determined by dry combustion with an RC-412 multiphase carbon (LECO Corp.), and the corresponding HA/FA ratio was found. Free lipids were extracted with petroleum ether (40–60 °C) in 250-mL Soxhlet extractors filled with 50 g of soil sample, and changing the extraction liquid every 4 h. The total extract was dehydrated with anhydrous $Na_2SO_4$, the solvent was evaporated under reduced pressure, and finally weighed. Mid-IR spectra between 500 and 4000 $cm^{-1}$ were recorded with a Varian 660 FTIR spectrometer with an attenuated total reflection accessory (ATR, Pike Technologies). The spectrometer was equipped with a three-reflection diamond crystal and a torque-limited pressure applicator to keep the sample in contact with the crystal, with a resolution of 2 $cm^{-1}$ and 128 accumulations. The AL/AR ratio (C–H aliphatic functional groups at 3000–2800 $cm^{-1}$/C=O aromatic functional groups at 1740–1600 $cm^{-1}$) were found from the IR spectra. Mineral content in the fine-earth fraction was determined by powder X-ray diffraction (XRD) using a Siemens D5000 diffractometer (Cu Kα radiation, 35 kV, 15 mA, scan speed 2°2θ $min^{-1}$, time constant 2 s). Mineral

**Table 2**
Mean values of soil quality indicators and surface free energy components for treatments in each source of variability (factor), and statistical tests for differences between means ($n = 24$).

| Variable | Parent material[a] | Management[a] | Depth[a] |
|---|---|---|---|
| | Carbonated/siliceous | Organic/conventional | 0–10 cm/10–20 cm |
| OC (%) | 1.00/1.55 n.s. | 2.17/0.39* | 2.20/0.36** |
| TN (%) | 0.08/0.13 n.s. | 0.18/0.04* | 0.18/0.04* |
| C/N | 10.90/11.54 n.s. | 11.70/10.74 n.s. | 12/10* |
| EC (dS $m^{-1}$) | 0.35/0.24*** | 0.32/0.28 n.s. | 0.29/0.31 |
| pH ($H_2O$) (1:2.5 w/v) | 8.14/5.65*** | 7.24/6.55 n.s. | 6.89/6.90 |
| Extractable P (mg $kg^{-1}$) | 11.17/24.67* | 25.92/9.92* | 24.08/11.75* |
| $CaCO_3$ eq (%) | 21.75/1.58*** | 6.58/16.75 n.s. | 8.92/14.42 |
| $Ca^{2+}$ exchan. ($cmol_c$ $Kg^{-1}$) | 9.87/4.88* | 9.83/4.92* | 9.37/5.38 |
| $Mg^{2+}$ exchan. ($cmol_c$ $kg^{-1}$) | 0.64/1.35* | 1.46/0.53** | 1.21/0.79 |
| $K^{+}$ exchan. ($cmol_c$ $Kg^{-1}$) | 0.26/0.30 n.s. | 0.43/0.14*** | 0.34/0.23 |
| $Na^{+}$ exchan. ($cmol_c$ $Kg^{-1}$) | 1.22/0.77*** | 0.87/1.24 n.s. | 0.98/1.01 |
| CEC ($cmol_c$ $Kg^{-1}$) | 14.67/11.67 n.s. | 15.42/10.42* | 14.92/10.92 |
| Sat. (%) | 82/57** | 81/59** | 74/65 |
| $\gamma^{LW}$ surface FE (mJ $m^{-2}$) | 47.75/46.08* | 46.54/47.29 n.s | 45.89/47.94** |
| $\gamma^{+}$ surface FE (mJ $m^{-2}$) | 0.41/0.33 n.s. | 0.40/0.34 n.s. | 0.46/0.29 n.s. |
| $\gamma^{-}$ Surface FE (mJ $m^{-2}$) | 40.26/41.91 n.s. | 38.93/43.25 n.s. | 37.81/44.36* |
| Total surface FE (mJ $m^{-2}$) | 54.48/52.84*** | 53.77/54.55 n.s. | 53.59/54.73 n.s. |
| Coarse fragments (%) | 14.0/58.0*** | 39.2/32.7 n.s. | 35/37 n.s. |
| Clay (%) | 16.4/10.7 n.s. | 10.4/16.7* | 10/17* |
| Sand (%) | 66.8/69.2 n.s. | 73.2/62.8*** | 72/74* |
| Silt (%) | 16.7/20.1 n.s. | 16/21* | 18/19 n.s. |
| WR − 33 kPa (%) | 15.0/14.4 n.s. | 16.7/12.8 n.s. | 15.8/13.7 n.s. |
| WR − 1500 kPa (%) | 6.8/9.5 n.s. | 11.3/4.9* | 10.7/5.5 n.s |
| AWC (mm $cm^{-1}$) | 1.1/0.5*** | 0.6/1.0* | 0.6/1.0 n.s. |
| Ks (cm $h^{-1}$) | 5.5/13.5 n.s. | 11.2/7.9 n.s. | 10.6/8.5 n.s. |
| K − 10 kPa (cm $h^{-1}$)[b] | 0.03/0.06 n.s. | 0.01/0.08* | 0.03/0.05 n.s. |
| Bulk density (g $cm^{-3}$) | 1.5/1.7 n.s. | 1.5/1.7 n.s. | 1.4/1.7** |
| Total porosity (%) | 29.5/33.6 n.s. | 42/35 n.s. | 44/33** |
| Macroporosity (%) | 26/21 n.s. | 25/22 n.s. | 28/19** |
| ASI | 0.62/0.47 n.s. | 0.66/0.43** | 0.62/0.48** |
| WDPT (s) | 2/162 n.s. | 163/1 n.s. | 163/1 n.s. |

OC = organic carbon; TN = total nitrogen; EC = electrical conductivity; CEC = cation exchange capacity; Sat. = base saturation; FE = free energy; WR = water retention; AWC = available water content; Ks = saturated hydraulic conductivity; ASI = aggregate stability index; WDPT = water drop penetration time.

[a] Student's t-test for two groups; significance: *<0.05, **<0.01, ***<0.001; n.s. = not significant differences among treatments.

[b] According to Saxton and Rawls (2006).

percentages were estimated measuring the relative area of peaks and applying the intensity factors method (Calero et al., 2009), for the following phases: phyllosilicates (including mica, smectite, vermiculite, kaolinite and mixed-layer) at 0.445 nm, chlorite at 0.710 nm, quartz at 0.425 nm, calcite at 0.303 nm, potassium feldspar at 0.324 nm, sodium–calcium feldspar at 0.320 nm and free iron oxides at 0.289 nm.

### 2.3. Surface free energy determination

The technique used to estimate the surface free energy of the soil samples entailed measurement of advancing contact angles of water, of known-surface-tension components, on dry soil pellets taken from the fine earth fraction (<2 mm) that had previously been ground in an agate mortar. A Rame-Hart Inc., NRL C.A. goniometer (USA) was used for this. Images of drops placed on the surface were captured with a video camera adapted to the goniometer, immediately after their deposition with a Gilmont (USA) micrometer syringe. Prior to contact angle measurements, the pellets were dried at 70 °C and kept in a desiccator. Only stable drops were used to compute the surface free energy components of the solids. The contact angles of water were measured on pellets of powder-soil, made by compressing dry powder under $1.5 \times 104\ kg\ cm^{-2}$ for 10 min. Only those pellets having a smooth, specular surface (optical microscope quality) were selected.

Detailed descriptions of this approach to surface free energy formulation are given in van Oss (1994) and van Oss et al. (1988). Thus the total surface free energy of a solid or a liquid is described as a sum of the Lifshitz-van der Waals component $\gamma^{LW}$ (including London dispersion, the main interaction, Debye polarization, and Keeson orientation) and the acid–base interaction $\gamma^{AB}$, in many cases due to hydrogen bonding. In general, the polar $\gamma^{AB}$ interaction is due to electron-donor, $\gamma^-$, and electron-acceptor, $\gamma^+$, contributions. The relationship of the contact angle θ, the Lifshitz-van der Waals (LW) and (Lewis) Acid–Base (AB) components of the surface free energy of the solid (Subscript 1) and the surface tension of the liquid (Subscript 3) can be written as:

$$2\sqrt{\gamma_1^{LW}\gamma_{Li}^{LW}} + 2\sqrt{\gamma_1^{+}\gamma_{Li}^{-}} + 2\sqrt{\gamma_1^{-}\gamma_{Li}^{+}} = \gamma_{Li}(1 + \cos\theta) \quad (1)$$

where $\gamma_{Li}$ is the surface tension of liquid i forming a contact angle θ on the solid and $\gamma^{LW}{}_{Li}$, $\gamma^{+}{}_{Li}$, and $\gamma^{-}{}_{Li}$ are the surface tension components of the liquid. The total, non-dispersive, Acid–Base (AB) component was obtained from the electro-donor and electro-acceptor components:

$$2\sqrt{\gamma^{+}\gamma^{-}} = \gamma^{AB}. \quad (2)$$

Thus by measuring the contact angles of the liquid, a Type (1) system of three-step equations can be solved to yield the three unknown variables, $\gamma_1^{LW}$, $\gamma_1^{+}$, and $\gamma_1^{-}$.

### 2.4. Scanning electron microscopy (SEM)

The microstructure of air-dried aggregates of selected soil surface samples was examined with a Hitachi S-510 scanning electron microscope (SEM; Hitachi Scientific Instruments, San Jose, CA) with an acceleration voltage of 25 kV. Soil fabric was described according to Calero et al. (2009) from images at 150′, 300′, 900′ and 1500′ magnifications.

### 2.5. Statistical analysis

A total of 24 samples comprised of three replicates from each of the four plots at two different depths, were subjected to statistical analysis, except for free lipids, HA/FA and AL/AR ratios and mineralogy, in which only the surface layers were analyzed ($n = 12$). A two-ways analysis of variance (ANOVA) was carried out to determine the importance of the three main factors: type of management (organic or conventional), soil parent material type (carbonated or siliceous) and sampling depth (surface or subsurface), and their interactions for each variable. A student's *t* test was also done to check for differences in means of the three main factors. Correlations between variables were analyzed with the Pearson´s correlation coefficient, assessing the partial correlations to examine any influence of organic carbon in the relationships of soil quality indicators to hydrophobicity parameters. A principal component analysis (PCA) was performed to reduce and explain the variability of the system and to represent samples in the PC scatterplot. The Bartlett's

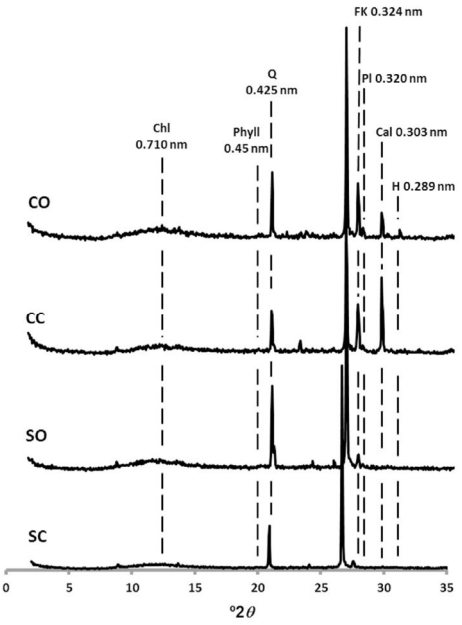


**Fig. 1.** DRX difractograms for the four plots. CC = conventional carbonated; CO = organic carbonated; SC = conventional siliceous; SO = organic siliceous. C = calcite; Q = quartz; FK = potassium feldspar; Pl = sodium–calcium feldspar (plagioclase); Phy = phyllosilicates (including: mica, kaolinite, smectite, and interstratified phases); Chl = chlorite; Ox = free iron oxides (goethite and hematite).

**Table 3**
Mean values of DRX mineral contents and SOM parameters in each source of variability (factor) for 0–10 cm horizons, and statistical tests for differences between means ($n = 12$).

| Variable | Parent material[a] | Management[a] |
|---|---|---|
| | Carbonated/siliceous | Organic/conventional |
| Phyllosilicates (%) | 10/13 n.s. | 11/12 n.s. |
| Chlorite (%) | 1/2 n.s. | 2/1* |
| Quartz (%) | 52/75*** | 67/61 n.s. |
| Potassium feldspar (%) | 16/5** | 10/11 n.s. |
| Plagioclase[b] (%) | 4/1** | 2/2 n.s. |
| Oxides[c] (%) | 3/3 n.s. | 3/3 n.s. |
| Calcite (%) | 14/1** | 5/10 n.s. |
| Free lipids ($g\ Kg^{-1}$) | 0.35/0.46** | 0.44/0.37 n.s. |
| AL/AR ratio | 1.95/1.21 n.s. | 1.10/2.06** |
| HA/FA ratio | 1.53/2.47 n.s. | 3.04/0.95*** |

AL = aliphatic compounds; AR = aromatic compounds; HA = humic acids; FA = fulvic acids.
[a] Student's t-test for two groups; significance: *<0.05, **<0.01, ***<0.001; n.s. = not significant differences among treatments.
[b] Includes potassium feldspar and sodium–calcium feldspar.
[c] Includes goethite and hematites.

test and Kaiser–Meyer–Olkin (KMO) measure of sample adequacy were applied to check whether the variables could be used with PCA. Only eigenvalues over 1 were retained in the correlation matrix and a Varimax rotation was employed. Analyses were carried out using Microsoft Excel and IBM SPSS Statistic 19.

## 3. Results

### 3.1. Soil water repellency and hydrophobicity of samples

According to the WDPT test (Table 1) soils were fairly wettable, having penetration times of <1 s, except four amended surface samples. CO5 from the organic carbonated soil was slightly repellent (16 s), and SO1, SO3 and SO5 from amended siliceous soils was strongly (60 to 600 s) to severely repellent (600 to 3600 s). Wettable samples always had contact angles in water of less than 40°, and the slightly repellent samples less than 45°, while strongly and severely repellent samples had contact angles of around 50°. Thus, the water contact angles for soil samples were coherent with classes found in the WDPT test, over 0°, but lower than the subcritical repellency angle of 90° given by Tillman et al. (1989). However, these subcritical angles do not prevent a certain amount of water resistance, which could impede infiltration and influence water uptake and other soil physical properties (Hallet, 2007). The most repellent material was the co-compost, with 2602 s penetration time (severely repellent) and a contact angle of >60°. Woche et al. (2005) found similar WDPT classes in agricultural profiles with the same texture (sandy loam). Wettable material prevailed in both organic and conventional soils, but water-soil contact angles were wider using the Wilhelmy plate methods. This shows that the complexity of the relationship between the contact angle and the WDPT classes, which may be dependent on measurement method or other factors.

Another approach to assessing water repellency is based on the surface free energy (SFE) components (Table 1), $\gamma^{LW}$, $\gamma^{+}$, and $\gamma^{-}$. In general, inorganic surfaces are relatively strong electron-donors, sense Van Oss et al. (1988) ($\gamma^{+} = 0$ and $\gamma^{-} \neq 0$). Both soils, carbonated and siliceous, regardless of depth, are observed to behavior as Lewis base, with much higher $\gamma^{-}$ than $\gamma^{+}$. This is typical of mineral surfaces dominated by silicate phases (Grasso et al., 2002). However, this behavior could be modified in the amended horizons due to acid–base neutralization between the mineral soil surfaces and the co-compost, which showed a relatively Lewis-acid character (the lowest electro-donor component, $\gamma^{-} = 14.8$ mJ m$^{-2}$). Thus the electron-donor component is seen to decrease in some amended siliceous soils (SO1 and SO3, and to a lesser extent SO5) and the surfaces becomes severely hydrophobic ($\gamma^{+} = 0$ and $\gamma^{-} \leq 28.2$; Van Oss et al., 1988), remaining higher when the soil has not been treated with co-compost (SC1, SC3 and SC5). This could have important implications for the soil structure. The soil dispersive component $\gamma^{LW}$, here found by the contact angle technique, ranged from 41.1 mJ m$^{-2}$ (SO3) to 48.9 mJ m$^{-2}$ (subsurface samples $CO_2$, $CO_4$, $CO_6$ and $SO_2$), which are almost the same as those found by previous authors (Hajnos et al., 2013; Plaza et al., 2015) for other siliceous and carbonated materials. The effect of co-compost slightly decreases the van der Waals component. This is probably because the co-compost causes the water molecules structure at the solid-liquid interface to be less well-ordered.

Surface free energies are in agreement with the other SWR measures. Wettable samples with contact angles <40° were hydrophilic, but repellent samples with contact angles >40° were around the threshold of hydrophobicity (28.2 mJ m$^{-2}$), also showing the lowest $\gamma^{-}$. Moreover, the co-compost was highly hydrophobic due to its $\gamma^{-}$ component (14.80 mJ m$^{-2}$), and had the highest penetration time and contact angle. SFE components ranges were short, less than 10 mJ m$^{-2}$, except for the $\gamma^{-}$ component, which was almost 30 mJ m$^{-2}$ (Table 1). This

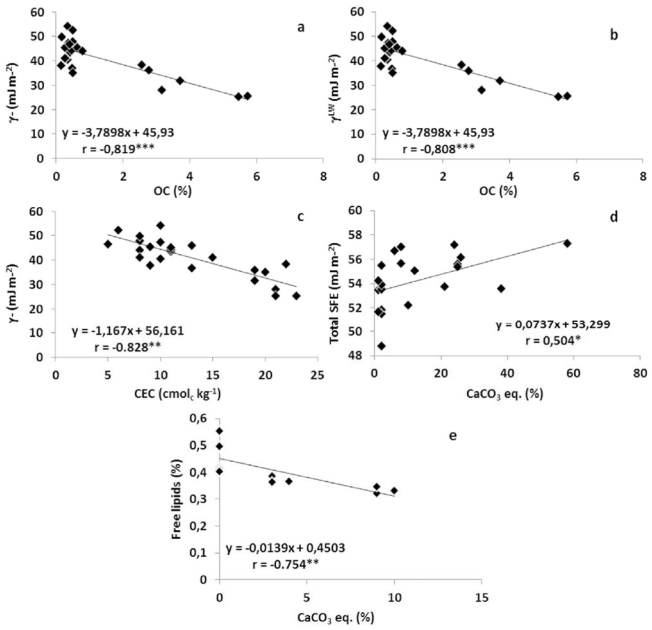


**Fig. 2.** Relationships between soil chemical indicators and surface free energy components.

suggests that this component would be more suitable for evaluating soil hydrophobicity than the non-dispersive total component $\gamma^{AB}$, at least in this kind of wettable mineral soils.

### 3.2. Effects of factors on chemical soil properties

Soil amendment significantly improved chemical fertility (Table 2). Means for organic carbon, total nitrogen, extractable phosphorus, exchangeable K, Ca and Mg, cation exchange capacity (CEC) and base saturation (% Sat) were significantly higher in organic than in conventional soils. These results were in agreement with García-Ruiz et al. (2012) for olive groves fertilized with OMP co-compost. Soil parent material significantly influenced properties related to carbonate presence, such as total carbonates, pH and exchangeable Ca, which were higher in soils over Miocene calcarenite regarding Triassic quartzite (Table 2). In contrast, more phosphorus was detected in siliceous soils, likely because the strong basic pH of carbonated soils (mean: 8.14) could increase soil retention of this element. Electrical conductivity and exchangeable Na were also affected by parent material, and were slightly higher in calcarenite soils, but without causing salinization or sodicity. Sodium probably comes from the calcarenite plagioclase (Fig. 1, Table 3). DRX mineralogy was heavily dependent on parent material. Therefore, significant differences were noted for quartz in the quartzite soils, and feldspar, plagioclase and calcite in calcarenite. As expected, soil amendment did not change soil mineralogy significantly. SFE components were not significantly affected by organic management (Table 2), but by parent material and depth. Carbonated soils had higher $\gamma^{LW}$ ($p < 0.05$) and total SFE ($p < 0.001$), and $\gamma^-$ and $\gamma^{LW}$ were higher in surface layers ($p < 0.05$). Mean free lipids were so much higher in siliceous than in carbonated soils ($p < 0.01$; Table 3) that they showed a strong correlation with carbonates ($r = -0.754$, $p < 0.01$; Fig. 2e). Organic matter was also more evolved (higher AH/AF and lower AL/AR ratios) in amended than in conventional soils ($p < 0.01$, Table 3), probably related to increased biological activity and an intensification of humification.

The above trends were modified by factor interactions, which were studied by two-ways ANOVA. Table 4 shows factor interactions and the mean differences affecting parent material and sampling depth with soil management (P × M and S × M, respectively). Hence, there is a strong P × M ($p < 0.001$) negative interaction between pH and EC, which leads to a decrease in both properties in carbonated soils, but an increase in siliceous ($p < 0.05$), accounted for by organic management. The interaction with pH has important effects on soil fertility of siliceous soils, because it causes an increase of almost two pH units (from 4.83 to 6.47), which is very noticeable from its practical consequences in an acidity-sensitive crop like olive groves (Sys et al., 1991). Very interesting also was the strong negative S × M interaction ($p < 0.001$) in the SFE $\gamma^-$ component. In the 0–10 cm layer, the means of this component in organic soil were much lower than in conventional soil (30.90 mJ m$^{-2}$ *vs.* 44.72 mJ m$^{-2}$; $p < 0.05$), revealing a co-compost effect which was not significant when organic soil was taken at its full depth (0–20 cm). This relationship was reversed at 10–20 cm, with higher $\gamma^-$ in the organic profiles. The mean $\gamma^-$ of 27.57 mJ m$^{-2}$ in the surface layers of the three siliceous organic soils (SO1, SO3 and SO5, Table 1), should be highlighted as hydrophobic material. Moreover, this value, 47.79 mJ m$^{-2}$ ($T = -6.275$, $p = 0.003$, $N = 6$) was significantly lower than in the surface layers of the conventional siliceous soils (SC1, SC3 and SC5, Table 1). Therefore, co-compost amendments are more effective in decreasing the non-dispersive electro-donor nature of the siliceous soils, which is mainly limited to the surface layer.

Strong significant correlations between SFE components and soil variables should be underlined. Organic carbon was correlated ($p < 0.001$) with both $\gamma^-$ and $\gamma^{LW}$: $r = -0.819$ and $r = -0.808$, respectively (Fig. 2a, b). In addition, interesting correlations were found between CEC and $\gamma^-$, $r = -0.828$ ($p < 0.01$; Fig. 2c), and between total SFE and carbonates $r = 0.505$ ($p < 0.05$; Fig. 2d). No other simple correlations between any chemical or mineralogical variable could be found, showing that the main factors controlling surface properties were the organic matter and cation exchange capacity, followed by carbonates.

**Table 4**
Two-way factorial ANOVA (soil parent material, management, sample deep) for variables which showed interactions between factors (*F* indicates the significance level), and difference between means for treatments.

| Soil quality indicator | Soil parent material (P) — management (M) | | | | |
|---|---|---|---|---|---|
| | P × M | Carbonated[1] | | Siliceous[1] | |
| | | Organic | Conventional | Organic | Conventional |
| EC (dS m$^{-1}$) | 19.077*** | 0.33a | 0.38a | 0.30a | 0.19b |
| pH ($H_2O$) | 83.896*** | 8.02a | 8.27a | 6.47a | 4.83b |
| $CaCO_3$ eq (%) | 10.466** | 12b | 32a | 1.67a | 1.50a |
| $Mg^{2+}$ exchan. (cmol$_c$ kg$^{-1}$) | 17.349*** | 0.70a | 0.59a | 2.32a | 0.48b |
| Sat. (%) | 23.037*** | 85a | 79a | 76a | 39b |
| WR −33 kPa (%) | 5.669* | 14.67a | 15.50a | 18.67a | 10.17b |
| ASI (%) | 8.092* | 0.65a | 0.58a | 0.67a | 0.28b |
| Free lipids (g kg$^{-1}$) | 8.02* | 0.37a | 0.33b | 0.51a | 0.41b |
| AL/AR ratio | 28.53*** | 1.21a | 2.70b | 1.00 a | 1.42b |
| AH/AF ratio | 43.34**** | 2.07a | 0.99b | 4.02a | 0.91b |
| **Soil quality indicator** | **Management (M) — sampling depth (S)** | | | | |
| | S × M | 0–10 cm[1] | | 10–20 cm[1] | |
| | | Organic | Conventional | Organic | Conventional |
| OC (%) | 32.285*** | 3.90a | 0.50b | 0.44a | 0.27b |
| TN (%) | 25.603*** | 0.31a | 0.04b | 0.04a | 0.03b |
| $Ca^{2+}$ exchan. (cmol$_c$ kg$^{-1}$) | 8.334** | 14.14a | 4.59b | 5.52a | 5.25a |
| CEC (cmol$_c$ kg$^{-1}$) | 29.235*** | 20.83a | 9.00b | 10.00a | 11.83a |
| WR −33 kPa (%) | 16.215*** | 21a | 11b | 12a | 15a |
| WR −1500 kPa (%) | 18.894*** | 18a | 4b | 5a | 6a |
| Ks (cm h$^{-1}$) | 7.985* | 17.434a | 3.782b | 4.926a | 12.020a |
| Bulk density (g cm$^{-3}$) | 24.192*** | 1.22b | 1.69a | 1.79a | 1.69a |
| Total porosity (%) | 23.285*** | 53a | 35b | 31a | 35a |
| Macroporosity (%) | 5.113* | 32a | 25b | 19a | 20b |
| ASI | 5.197* | 0.80a | 0.43b | 0.52a | 0.43a |
| $\gamma^{LW}$ surface FE (mJ m$^{-2}$) | 8.153** | 44.68a | 47.10b | 48.39a | 47.48b |
| $\gamma^+$ surface FE (mJ m$^{-2}$) | 5.919* | 0.58a | 0.34a | 0.22a | 0.35a |
| $\gamma^-$ surface FE (mJ m$^{-2}$) | 21.069*** | 30.90b | 44.72a | 46.95a | 41.77a |

Parameter abbreviations from Tables 1, 2 and 3.
Significance: $p < 0.05$ (*), 0.01 (**) or 0.001 (***).
[1] Different letters in the same row show significance for the Student's t-test ($p < 0.05$).

### 3.3. Effects of factors on physical soil properties

Mean values for physical soil properties are shown in Table 2. A strong textural difference in sand content ($p < 0.001$) between organic and conventional profiles should be stressed, although it was difficult to attribute this to soil management. Physical properties were, in general, more favorable in amended soils: higher field capacity (FC), porosities and aggregate stability index (ASI), and lower bulk density. However, except for ASI, data were widely dispersed and their mean differences were not statistically significant. Poor ASI (0.43) in the conventional profiles typical of severely degraded soils (Kemper and Rosenau, 1986) was significantly enhanced ($p < 0.01$) to 0.66 in organic soil. Similar results were reported by Mahmoud et al. (2012) in samples treated with olive mill wastewater (OMW). In contrast to the abovementioned properties, the available water content (AWC) decreased from 0.100 mm mm$^{-1}$ in conventional soil to 0.061 mm mm$^{-1}$ in organic soils ($p < 0.05$). This could be partly explained by the high permanent wilting point (PWP) measured in the latter (11.29%). However, Killi et al. (2014) and Lozano-García et al. (2011) found the same trend in amended olive grove soils, and the latter attributed it to hydrophobicity caused by the added olive waste. The correlations between water storage parameters and the $\gamma^-$ component may also be stressed. $\gamma^-$ showed significantly ($p < 0.001$) negative correlations

with WR at −33 kPa and −1500 kPa (Fig. 3a, b). Total SFE also correlated positively with AWC ($p < 0.01$; Fig. 3c). Therefore, although soils with water-repellency seem to retain more water, it appears to be less available for plant growth. Surface free energy, especially its $\gamma^-$ component, may play a decisive role in the soil water balance, a considerable factor in Mediterranean soils, where the main limiting factor in agriculture becomes soil moisture.

Saturated hydraulic conductivity (Ks) was slightly higher than expected according to Rawls et al. (1982) and USDA (1999) for sandy loam soils, because the samples studied were so stony (36% of mean). Ks was higher in organic (11.80 cm/h) than in conventional profiles (7.90 cm/h), but without statistical significance (Table 2). In soils from conventional olive groves with similar texture and stoniness, Álvarez et al. (2007) found lower Ks using a simple ring infiltrometer. In a study of a deeply eroded Ultisol with sandy clay loam texture, Obi (1999) found equivalent conductivities with a constant-head permeameter, which draws attention to the degraded starting point of our conventional soils. Nevertheless, from an agronomical perspective, this Ks (*high class*) does not cause any important restraint on soil infiltration in either organic or conventional soils. Strong correlations were found between Ks and the $\gamma^{LW}$ component (Fig. 3d). Unsaturated hydraulic conductivity at relatively high matric potential (−10 kPa) yielded one thousandth of the Ks in the range predicted for sandy soils by Diamantopoulos et al. (2013). However, it was higher in conventional soils ($p < 0.05$), showing a trend opposite Ks (Table 2). Unsaturated conductivity was positively correlated with $\gamma^-$ at the surface (Fig. 3e), thus an inverse dependence with soil water repellency could be stated: the higher the hydrophobicity, the lower unsaturated hydraulic conductivity. Analogous results were found by Mohawesh et al. (2014) in profiles irrigated with OMW, and in general, by Diamantopoulos et al. (2013) and Beatty and Smith (2013) in laboratory experiments. Mahmoud et al. (2010) think reduction in unsaturated hydraulic conductivity implies a considerable loss of infiltration capacity in surface layers, and could therefore be a problematic feature that could disturb OMW-amended soils.

Bulk density of conventional profiles (mean: 1.67 g $cm^{-3}$; Table 2) was higher than in other olive grove soils with a sandy loam texture (Marzaioli et al., 2010; Álvarez et al., 2007), and slightly higher than recommended by USDA (1999). Total porosity (35%) and macroporosity (22%) were in the range of the strongly degraded soils from ski pistes studied by Delgado et al. (2007), revealing soil compaction. Although these indicators improved in organic profiles, they were weak and not significant, but the S × M interactions (Table 4) caused the effect of organic management to be significant in surface layers, where BD was reduced to 1.22 g $cm^{-3}$ and total porosity and macroporosity increased to 53% and 32%, respectively. This agrees with what was reported by Lozano-García et al. (2011), but refutes the results of Mahmoud et al. (2010), who found a loss of macroporosity in soils treated with OMW. As in the case of water parameters, several intense correlations were found between bulk density, porosities and structural stability with surface free energy components. Among all these correlations, we should highlight a close negative correlation between ASI and $\gamma^-$, which was exceptional in surface horizons (Fig. 3f). This would imply a relevant role of relative hydrophobicity in soil structural development and stabilization. This role was demonstrated and discussed in olive grove soils by Plaza et al. (2015) and Mahmoud et al. (2012), and more generally by Goebel et al. (2005) and Hallet (2007).

### 3.4. SEM morphology of samples

Fig. 4 shows SEM images of the horizons from the four plots at low magnification (150′). All the soils except for the organic siliceous sample are clearly granular. Predominance of sand grains over the fine matrix of silt and clay, which is not organized in macroaggregates, was

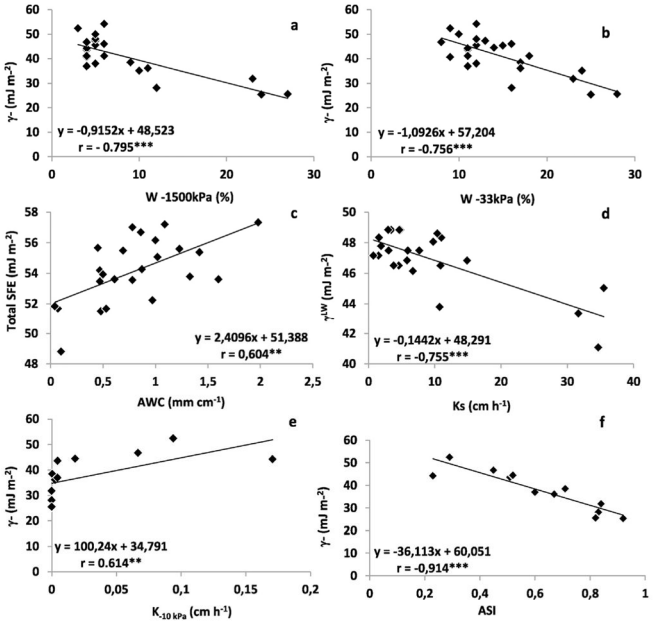


**Fig. 3.** Relationships between soil physical indicators and surface free energy components.

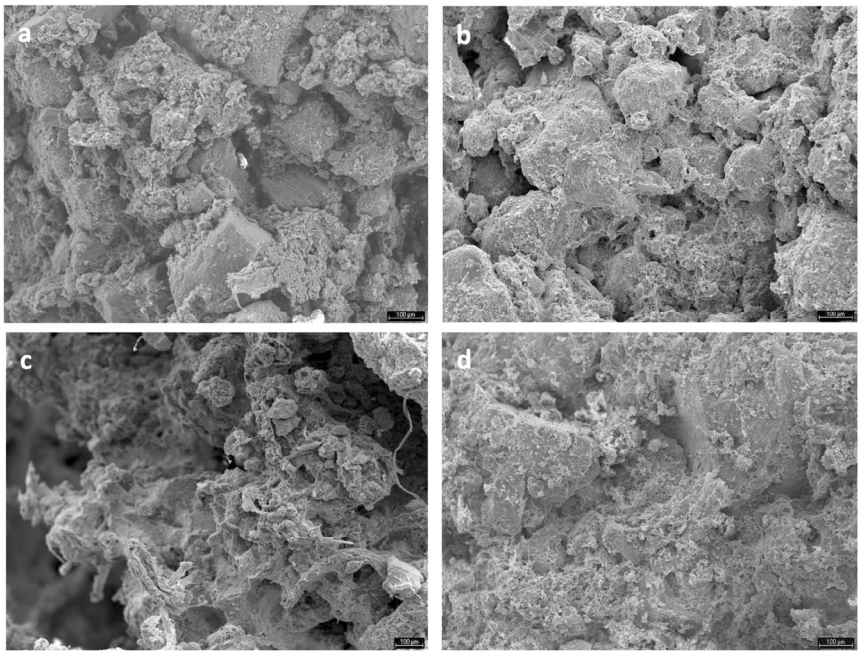


**Fig. 4.** SEM images of selected surface soil horizons at lower magnifications. a: Ah horizon from the organic carbonated plot (sample CO1). b: Ap horizons from the conventional carbonated plot (sample CC3). c: Ap horizon from the organic siliceous plot (sample SO1). d: Ap horizons from the conventional siliceous plot (sample SC3). Scale bar = 100 μm.

consistent with sample textures (>60% sand). Moreover, conventional quartzite sands (Fig. 4d) looked coarser than calcarenite sands (Fig. 4a, b), which is also consistent with its lithology. At higher magnifications (300'), the prevalence of sand grains over structural units as microaggregates (250–50 μm) or clusters (50–10 μm) was also observed (Fig. 5a, b and d). Due to lack of clay, these structural units were mainly formed by binding of fine silt particles (10–2 μm). Furthermore, there was very little cementation. The SEM fabric of conventional calcareous and siliceous samples was, therefore, skeletal (Calero et al., 2009), which explain its relatively high hydraulic conductivity and weak structural stability.

Unlike the other samples, and even though it had a similar coarse texture (sandy loam with > 80% sand), the organic siliceous horizon showed better structure at all magnifications: macroaggregates (Fig. 4c), microaggregates and clusters (Fig. 5c). Morphology of macroaggregates was irregular and elongated but microaggregates and clusters were more rounded. In any case, what stood out in this sample was the conspicuous biological activity, mainly fungal hyphae (Fig. 5e), and the massive organic cementation bonding mineral grains (Fig. 5f). These features mean a noteworthy morphological improvement in soil structure, which is supported by the aggregate stability index and other physical parameters. Thus the physical entanglement of soil particles by fungal hyphae observed may be an important way of increasing aggregate stability in siliceous sandy soils (Delgado et al., 2007). Moreover, the hyphae might be secreting the substance they were partially imbued with. From their morphological appearance, these coatings had a striated surface which could be from fungal hydrophobins (Kershaw et al., 2005), but could also be a bacterial extracellular polymeric substance (Maqbela and Mnkeni, 2009) or even other humic substances with no direct relationship with the hyphae. Anyway, it seems highly likely that hyphae and coatings were responsible for the SWR of siliceous organic samples, as reported by several other authors (Kershaw et al., 2005; Maqbela and Mnkeni, 2009; Fisher et al., 2010).

## 4. Discussion

In this work, we preferred to use the $\gamma^-$ component to measure hydrophobicity instead of the WDPT test or contact angle, because the soils under study were mineral soils with low to moderate organic carbon content (from 0.14 to 5.73%, with a mean of 1.29%). In this situation, typical water repellency measures might not be able to satisfactorily discriminate relative hydrophilicity/hydrophobicity and its effects on soil, as previously noted (Chau et al., 2014). Thus the WDPT test and CA test showed all samples under the subcritical repellency angle. However, clear dependencies and strong relationships between SFE, mainly the $\gamma^-$ component, and soil quality indicators have been revealed. Furthermore, the effect of amendment on hydrophobicity seems to be different depending on the treatment (carbonated/siliceous parent material or surface/subsurface layer), showing that processes generating or maintaining water repellency in agricultural soils are probably profoundly conditioned by soil properties or components.

According to several authors, one of the main factors in SWR is the organic matter chemistry, which may be characterized by ATR-FTIR. ATR-FTIR spectra were analyzed in two absorption bands, one showing the hydrophobic functional groups (C–H aliphatic at 3000–2800 $cm^{-1}$) and the other the hydrophilic functional groups (C═O aromatic at 1740–1600 $cm^{-1}$) (Ellerbrock et al., 2005). The AL/AR ratio found from these bands has traditionally been used to evaluate soil

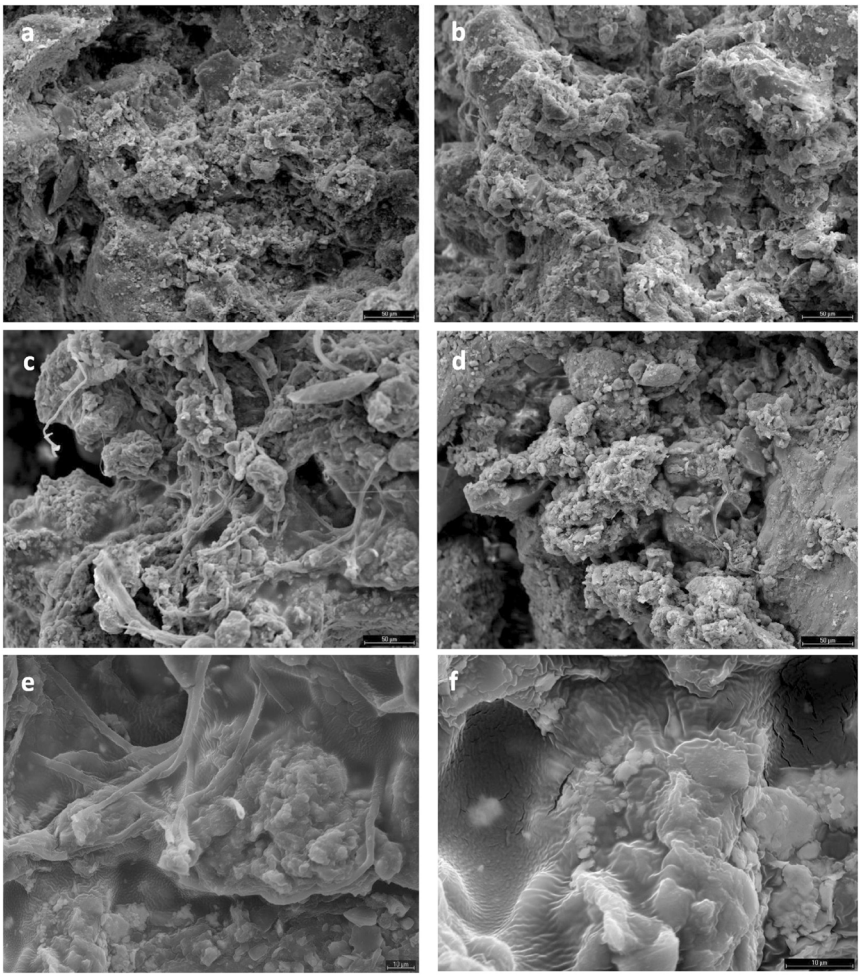


**Fig. 5.** SEM images of selected surface soil horizons at higher magnifications. a: Ah horizon from the organic carbonated plot (sample CO1). b: Ap horizons from the conventional carbonated plot (sample CC3). c: Ap horizon from the organic siliceous plot (sample SO1). d: Ap horizons from the conventional siliceous plot (sample SC3). e: Detail of image c (sample SO1). f: Detail of image c (sample SO1). a to d, scale bar = 100 μm; e and f, scale bar = 10 μm.

hydrophobicity (Leue et al., 2010; Matějková and Šimon, 2012). A decrease in the AL/AR ratio in the organic fraction would yield a loss in water repellency, but no correlation between the AL/AR ratio and the $\gamma^-$ component was identified (Table 5). In the case of the HA/FA ratio (polymerization degree of humic substances), where high correlation with the electro-donor component was found, no conclusive correlation between $\gamma^-$ and HA/FA could be established due to the strong controlling effect of the organic carbon (Table 5). To some extent, this lack of any relationship between organic matter chemistry and hydrophobicity may be due to the strong stability and humification degree of the co-compost added (García-Ruiz et al., 2012) over previously degraded soils, in which case, it would not be surprising.

**Table 5**
Pearson's correlation coefficients (r) between the electro-donor $\gamma^-$ component and soil quality indicators, controlling the effects of organic carbon.

| SFE | Variable | r | Partial r | p-Value |
|---|---|---|---|---|
| $\gamma^-$ | CEC | −0.828** | −0.522* | 0.011 |
| | $CaCO_3$ eq | −0.060 | −0.506* | 0.014 |
| | HA/FA | −0.865** | −0.111 | 0.745 |
| | AL/AR | 0.425 | −0.591 | 0.056 |
| | Free lipids | −0.470 | 0.504 | 0.114 |
| | Clay | 0.164 | −0.514* | 0.012 |
| | Sand | −0.097 | 0.454* | 0.03 |

Significance: *<0.05, **<0.01, ***<0.001.
Parameter abbreviations from Tables 1, 2 and 3.

There is some evidence that free lipids may change the water balance in soils under reforested vegetation (de Blas et al., 2010). The free lipids content was relatively high in the amended siliceous soils (mean: 0.51%, Table 4), also showing the highest contact angles and penetration times (Table 1). This could be explained by the good negative correlation between the free lipids and carbonates (Fig. 2e), which would involve some process by which the free lipids content is depleted in calcareous soils. It is also noteworthy that the mean free lipids content in siliceous soils (0.46%, Table 3) was higher than its concentration in the co-compost (0.38%), implying a relative enrichment of these compounds in this edaphic environment. Free lipids could also come from the fungal activity, as suggested by Zhao et al. (2004), which may be depressed in carbonated soils. Although the amount of free lipids in the amended siliceous soils is moderate, in absolute terms, some authors relate the hydrophobicity to the presence of residual oil in OMP. Niaounakis and Halvadakis (2006) mentioned that applied OMP increases soil hydrophobicity due to residual oil. This would also decrease water retention. In any case, no good correlations between free lipids and the $\gamma^-$ component have been revealed here (Table 5), which might show that this relationship, even in siliceous soils, might be too scarce to cause any measurable effect in surface energy.

Other soil properties repeatedly related with water repellency were the texture and acidity. Several authors (Woche et al., 2005; González-Peñaloza et al., 2013) have reported a relationship between coarse textures with small specific surface area, such as sand, and repellency. Here, it was interesting to note the strong influence of organic carbon on other soil parameters when they were related to the electron-donor component (Table 5). Hence, no simple correlations between sand or clay and $\gamma^-$ were found, but a relatively high significant r coefficient was when the organic carbon effect was controlled for. These partial correlations (positive with sand and negative with clay) agree and support the abovementioned good correlation with CEC (Fig. 2c), demonstrating the influence of coarser texture on increasing water repellency. With respect to acidity, calcareous soils would seem to be less prone to developing water repellency than acidic, which could be explained by the lower fungal activity registered at pH > 7 (Mataix-Solera and Doerr, 2004). This factor seems very likely in this case, due to the intense fungal activity observed with SEM in the amended siliceous soils, which are the most hydrophobic. As with the texture, no direct correlation was found with carbonates, but this was also an effect of the strong influence of organic carbon (Table 5). Thus a significant negative correlation between carbonates and $\gamma^-$ was revealed, and we may conclude that the most decisive factor determining SWR was not only the organic carbon content, but also the presence of carbonates and other parameters related to the specific surface area, as well as particle charges.

Since moderate hydrophobicity has been considered common in soil, its positive influence on soil structure and quality has begun to be recognized (Mataix-Solera and Doerr, 2004; Goebel et al., 2005; Mataix-Solera et al., 2011). Along with these positive effects, some undesirable impacts on soil infiltration and water storage in these soils should also be taken into account. A principal component analysis was performed (Table 6) to summarize the numerical analyses discussed above more easily. The 14 most explanatory soil variables were selected, highlighting organic carbon and CEC, with $PVAF_j$ of 6.8 and 6.7%, respectively. Two principal components were found from these indicators, explaining up to 85% of system variability. Thus, this model, with a KMO of 0.730, was highly suitable. The first component, explaining 55% of variance, was positive and strongly correlated with the chemical indicators organic carbon, CEC and exchangeable calcium, and the physical indicators logWDPT, W-33 y W-1500 kPa, total porosity and aggregate stability index, which showed component loading over 0.800. Furthermore, it was negatively related to bulk density and the $\gamma^-$ component. Hence, this component was closely related to soil physical and chemical fertility, increasing with component scores, and could be considered a proper soil quality component. Soil hydrophobicity estimated by both penetration time test and the electro-donor component, which indicates loss of wettability if it decreases, was also related to the component, and therefore, to soil quality. From this point of view, SWR also seems to be an important parameter of soil quality. The second component, explaining 27% of variance, was positive and strongly correlated with AWC, carbonates, $\gamma^{LW}$ and total free energy. This component was thus not only partially related to soil quality (AWC), but also strongly related to carbonates, and so also to the soil parent material.

**Table 6**
Principal component analysis of soil quality indicators: component loadings and variance explained by components and variables.

| Principal component | PC1 | PC2 | $VAF_j$ | $PVAF_j$ |
|---|---|---|---|---|
| Total surface FE (mJ $m^{-2}$) | −0.145 | 0.769 | 0.612 | 4.373 |
| $\gamma^-$ surface FE (mJ $m^{-2}$) | −0.870 | 0.206 | 0.800 | 5.714 |
| $\gamma^{LW}$ surface FE (mJ $m^{-2}$) | −0.567 | 0.716 | 0.833 | 5.952 |
| OC (%) | 0.818 | −0.538 | 0.959 | 6.848 |
| $CaCO_3$ eq (%) | 0.278 | 0.878 | 0.847 | 6.051 |
| Ca exchan. ($cmol_c$ $kg^{-1}$) | 0.930 | 0.144 | 0.885 | 6.324 |
| CEC ($cmol_c$ $kg^{-1}$) | 0.969 | 0.023 | 0.939 | 6.706 |
| logWDPT (s) | 0.844 | −0.375 | 0.854 | 6.098 |
| WR −33 kPa (%) | 0.900 | −0.093 | 0.819 | 5.849 |
| WR −1500 kPa (%) | 0.829 | −0.489 | 0.927 | 6.622 |
| AWC (mm $cm^{-1}$) | −0.060 | 0.942 | 0.890 | 6.359 |
| Bulk density (g $cm^{-3}$) | −0.921 | 0.053 | 0.852 | 6.085 |
| Total Porosity (%) | 0.921 | −0.057 | 0.851 | 6.079 |
| ASI | 0.901 | 0.030 | 0.813 | 5.811 |
| $VAF_s$ (eigenvalue) | 8.372 | 3.510 | 11.882 | 84.869 |
| $PVAF_s$ (percent) | 55.148 | 26.538 | | |

VAFs = variance accounted by the s-component.
Parameter abbreviations from Tables 1, 2 and 3.

## 5. Conclusions

The organic matter incorporated into the soil as OMP co-compost, due to its relationship with physical and physicochemical properties, may have a crucial role in conservation and improving soil quality in the agro-soil environment studied.

It should be mentioned with regard to chemical soil fertility that the use of an organic amendment with OMP co-compost increases OM, of vital importance in Mediterranean soils subjected to intensive, traditional, and not very sustainable cultivation, as well as essential nutrients such as nitrogen, phosphorus, potassium, and CEC. Soil physical properties are also generally favored, especially bulk density, total and macro porosity, and soil aggregate stability.

We conclude that the most decisive factor determining soil wettability seems to be OC content, but the presence of carbonates and other parameters related to the specific surface area, as well as particle charge could also strongly influence this soil property. According to the WDPT and CA tests, all samples were under the sub-critical repellency angle, but clear dependencies and strong relationships between SFE, mainly the $\gamma^-$ component, and soil quality indicators, such as CEC, carbonates and sand content have been demonstrated.

Although the experiment was unreplicated, which advises cautious interpretation, moderate soil hydrophobicity may have had a positive influence on soil structure and quality. In fact, in our study, this parameter was a positive factor for soil structure and quality through biological activity, mainly fungal, as observed in SEM images in organically amended siliceous samples. Nevertheless, along with these positive effects, some undesirable impacts on soil infiltration and water storage should also be taken into account in the soils studied. Hence, moderate soil hydrophobicity might somewhat alter plant water availability and infiltration under unsaturated conditions.

Our results show that the capacity for recovery after changing to organic management with olive mill pomace co-compost may depend on the type of soil. This information could contribute to improved soil management and protection in sustainable agriculture.

## References


Álvarez, S., Soriano, M.A., Landa, B.B., Gómez, J.A., 2007. Soil properties in organic olive groves compared with that in natural areas in a mountainous landscape in southern Spain. Soil Use Manag. 23, 404–416.

Beatty, S.M., Smith, J.E., 2013. Dynamic soil water repellency and infiltration in post-wildfire soils. Geoderma 192, 160–172.

Bisdom, E.B.A., Dekker, L.W., Schoute, J.F.T., 1993. Water repellency of sieve fractions from sandy soils and relationships with organic material and soil structure. Geoderma 56, 105–118.

Calero, J., Delgado, R., Delgado, G., Martín-García, J.M., 2009. SEM image analysis in the study of a soil chronosequence on fluvial terraces of the middle Guadalquivir (southern Spain). Eur. J. Soil Sci. 60, 465–480.

Chau, H.W., Biswas, A., Vujanovic, V., Si, B.C., 2014. Relationship between the severity, persistence of soil water repellency and the critical soil water content in water repellent soils. Geoderma 221-222, 113–120.

de Blas, E., Rodríguez-Alleres, M., Almendros, G., 2010. Speciation of lipid and humic fractions in soils under pine and eucalyptus forest in northwest Spain and its effect on water repellency. Geoderma 155, 242–248.

Delgado, R., Sánchez-Marañón, M., Martín-García, J.M., Aranda, V., Serrano-Bernardo, F., Rosúa, J.L., 2007. Impact of ski pistes on soil properties: a case study from a mountainous area in the Mediterranean region. Soil Use Manag. 23, 269–277.

Diamantis, V., Pagorogon, L., Gazani, E., Doerr, S.H., Pliakas, F., Ritsema, C.J., 2013. Use of olive mill wastewater to decrease hydrophobicity in sandy soil. Ecol. Eng. 58, 393–398.

Diamantopoulos, E., Durner, W., Reszkowska, A., Bachmann, J., 2013. Effect of soil water repellency on soil hydraulic properties estimated under dynamic conditions. J. Hydrol. 486, 175–186.

Diehl, D., Schaumann, G.E., 2007. The nature of wetting on urban soil samples: wetting kinetics and evaporation assessed from sessile drop shape. Hydrol. Process. 21, 2255–2265.

Doerr, S.H., Shakesby, R.A., Walsh, R.P.D., 2000. Soil water repellency: its causes, characteristics and hydro-geomorphological significance. Earth-Sci. Rev. 51, 33–65.

Ellerbrock, R.H., Gerke, H.H., Bachmann, J., Goebel, M.O., 2005. Composition of organic matter fractions for explaining wettability of three forest soils. Soil Sci. Soc. Am. J. 69, 57–66.

Fisher, T., Veste, M., Wiehe, W., Lange, P., 2010. Water repellency and pore clogging at early successional stages of microbiotic crust on inland dunes, Brandenburg, NE Germany. Catena 80, 47–52.

Fowkes, F., 1964. Attractive forces at interfaces. Ind. Eng. Chem. 56, 40–52.

García-Ruiz, R., Ochoa, M.V., Hinojosa, M.B., Gómez-Muñoz, B., 2012. Improved soil quality after 16 years of olive mill pomace application in olive oil groves. Agron. Sustain. Dev. 32, 803–810.

Goebel, M., Bachmann, J., Woche, S.K., Fischer, W.R., 2005. Soil wettability, aggregate stability, and the decomposition of soil organic matter. Geoderma 128, 80–93.

González-Peñaloza, F.A., Zavala, L.M., Jordán, A., Bellinfante, N., Bárcenas-Moreno, G., Mataix-Solera, J., Granged, A.J.P., Granja-Martins, F.M., Neto-Paixão, H.M., 2013. Water repellency as conditioned by particle size and drying in hydrophobized sand. Geoderma 209–210, 31–40.

Grasso, D., Subramanian, K., Butkus, M., Strevett, K., Bergendahl, J., 2002. A review of non-DLVO interactions in environmental colloidal systems. Rev. Environ. Sci. Biotechnol. 1, 17–38.

Hajnos, M., Calka, A., Jozefaciuk, G., 2013. Wettability of mineral soils. Geoderma 2006, 63–69.

Hallet, P.D., 2007. An introduction to soil water repellency. In: Gaskin, R.E. (Ed.), Proceedings of the 8th International Symposium on Adjuvants for Agrochemicals (ISAA2007). Hand Multimedia, Christchurch, NZ.

Kemper, W.D., Rosenau, R.C., 1986. Aggregate stability and size distribution. In: Klute, A. (Ed.), Methods of Soil Analysis, Agronomy Series, n° 9. ASA/SSSA, Inc., Madison, WI, pp. 425–442.

Kershaw, M., Thornton, R., Wakley, G.E., Talbot, J., 2005. Four conserved intramolecular disulphide linkages are required for secretion and cell localization of a hydrophobin during fungal morphogenesis. Mol. Microbiol. 56, 117–125.

Killi, D., Anlauf, R., Kavdir, Y., Haworth, M., 2014. Assesing the impact of agro-industrial olive-wastes in soil water retention: implications for remediation of degraded soils and water availability for plant growth. Int. Biodeterior. Biodegrad. 94, 48–56.

Klute, A., 1986. Methods of soil analysis, part 1, physical and mineralogical methods. Agronomy Series, n° 9, second ed. ASA/SSSA, Inc., Madison, WI, USA.

Leelelamanie, D.A.L., Karube, J., Yoshida, A., 2010. Clay effects on the contact angle an water drop penetration time of model soils. Soil Sci. Plant Nutr. 56, 371–375.

Leue, M., Ellerbrock, R.H., Gerke, H.H., 2010. DRIFT mapping of organic matter composition at intact soil aggregate surfaces. Vadose Zone J. 9, 317–324.

López-Pieñiro, A., Fernández, J., Rato-Nunes, J.M., García-Navarro, A., 2006. Response of soil and wheat crop to the application of two-phase olive mill waste to Mediterranean agricultural soils. Soil Sci. 171, 728–736.

López-Piñeiro, A., Albarrán, A., Rato, J.M., Peña, D., Cabrera, D., 2011. Long-term impacts of de-oiled two-phase olive mill waste on soil chemical properties, enzyme activities and productivity in an olive grove. Soil Tillage Res. 114, 175–182.

Lozano-García, B., Parras-Alcántara, L., 2013. Short-term effects of olive mill by-products on soil organic carbon, total N, C:N ratio and stratification ratios in a Mediterranean olive grove. Agric. Ecosyst. Environ. 165, 68–73.

Lozano-García, B., Parras-Alcántara, L., del Toro Carrillo, M., 2011. Effects of oil mill wastes on surface soil properties, runoff and soil losses in traditional olive groves in southern Spain. Catena 85, 187–193.

Mahmoud, M., Janssen, M., Haboub, N., Nassour, A., Lennartz, B., 2010. The impact of olive mill wastewater application on flow and transport properties in soils. Soil Tillage Res. 107, 36–41.

Mahmoud, M., Janssen, M., Peth, S., Horn, R., Lennartz, B., 2012. Long-term impact of irrigation with olive mill wastewater on aggregate properties in the top soil. Soil Tillage Res. 124, 24–31.

Maqbela, M.P., Mnkeni, P.N.S., 2009. Nostoc cyanobacterial inoculation in South African agricultural soils enhances soil structure, fertility, and maize growth. Plant Soil 315, 79–92.

Marzaioli, R., D´ascoli, R., De Pascale, R., Rutigliano, F., 2010. Soil quality in a Mediterranean area of Southern Italy as related to different land use type. Appl. Soil Ecol. 44, 205–212.

Mataix-Solera, J., Doerr, S.H., 2004. Hydrophobicity and aggregate stability in calcareous topsoils from fire-affected pine forest in southeastern Spain. Geoderma 118, 77–88.

Mataix-Solera, J., Cerdà, A., Arcenegui, V., Jordán, A., Zavala, L.M., 2011. Fire effects on soil aggregation: a review. Earth-Sci. Rev. 109, 44–60.

Matějková, Š., Šimon, T., 2012. Application of FTIR spectroscopy for evaluation of hydrophobic/hydrophilic organic components in arable soil. Plant Soil Environ. 58, 192–195.

Mohawesh, O., Mahmoud, M., Janssen, M., Lennartz, B., 2014. Effect of irrigation with olive mill wastewater on soil hydraulic and solute transport properties. Int. J. Environ. Sci. Technol. 11, 927–934.

Niaounakis, M., Halvadakis, C.P., 2006. Olive Processing Waste Management. second ed. Elsevier, London, UK, pp. 23–60.

Nieto, O.M., Castro, J., Fernández, E., Smith, P., 2010. Simulation of soil organic carbon stocks in a Mediterranean olive grove under different soil-management systems using the RothC model. Soil Use Manag. 26, 118–125.

Obi, M.E., 1999. The physical and chemical responses of a degraded sandy clay loam soil to cover crops in southern Nigeria. Plant Soil 211, 165–172.

Page, A.L., Miller, R.H., Keeney, D.R., 1982. Methods of soil analysis, part 2, chemical and microbiological properties. second ed. Agronomy Series n° 9. ASA/SSSA, Inc., Madison, WI, USA.

Peikert, B., Schaumann, G.E., Keren, Y., Bukhanovsky, N., Borisover, M., Garfha, M.A., Shoqeric, J.H., Dag, A., 2015. Characterization of topsoil subjected to poorly controlled olive oil mill waste water pollution in West Bank and Israel. Agric. Ecosyst. Environ. 199, 176–189.

Plaza, I., Ontiveros-Ortega, A., Calero, J., Aranda, V., 2015. Implication of zeta potential and surface free energy in the description of agricultural soil quality: effect of different cations and humic acids on degraded soils. Soil Tillage Res. 146, 148–158.

Rawls, W.J., Brakensiek, D.L., Saxton, K.E., 1982. Estimation of soil water properties. Trans. ASAE 25, 1316–1320.

Saxton, K.E., Rawls, W.J., 2006. Soil water characteristic estimated by texture and organic matter for hydrologic solutions. Soil Sci. Soc. Am. J. 70, 1569–1578.

Soil Conservation Service, 1972. Soil Survey Laboratory Methods and Procedures for Collecting Soil Samples. U.S. Department of Agriculture, Washington.

Swift, R.S., 1996. Organic matter characterization (chap. 35). In: Sparks, D.L., et al. (Eds.), Methods of Soil Analysis, Part 3, Chemical MethodsSoil Sci. Soc. Am. Book Series n° 5. ASA/SSSA, Inc., Madison, WI, USA, pp. 1018–1021.

Sys, I.C., van Ranst, E., Debaeye, I.J., 1991. Land evaluation. Agricultural Publications 7. University of Ghent, Belgium.

Tillman, R.W., Scotter, D.R., Wallis, M.G., Clothier, B.E., 1989. Water repellency and its measurements by using intrinsic sorptivity. Aust. J. Soil Res. 27, 637–644.

USDA (United States Department of Agriculture), 1999. The Soil Quality Test Kit Guide. USDA, Washington DC.

Van Oss, C.J., 1994. Interfacial Forces in Aqueous Media. Dekker, New York.

Van Oss, C.J., Chaudhury, M.K., Good, R.J., 1988. Interfacial Lifshitz-van der Waals and polar interactions in macroscopic systems. Chem. Rev. 88, 927–941.

Woche, S.K., Goebel, M.O., Kirkham, M.B., Horton, R., van der Ploeg, R.R., Bachmann, J., 2005. Contact angle of soils as affected by depth, texture, and land management. Eur. J. Soil Sci. 56, 239–251.

Zhao, X.R., Lin, Q., Brookes, P.C., 2004. Does soil ergosterol concentration provide a reliable estimate of soil fungal biomass? Soil Biol. Biochem. 37, 311–317.

# Capítulo 6
# Conclusiones Generales

A continuación se enumeran las conclusiones obtenidas durante el período de investigación de esta memoria:

1. El conocimiento de las propiedades eléctricas (potencial zeta) y termodinámicas (energía libre de superficie) es de gran interés, ya que condiciona el comportamiento microscópico y macroscópico del suelo respecto a aspectos tan importantes como la cohesión, la estabilidad de la estructura y la adsorción de carbono.

2. Se ha establecido una correspondencia entre la estructura microscópica del suelo, caracterizada mediante microscopía electrónica (SEM), y las propiedades interfaciales del material estudiado. De esta manera, fábricas dispersas correspondieron a muestras con mayor potencial zeta (en valor absoluto) y, en general, energías totales de interacción más repulsivas.

3. En general, los suelos con menores energías totales de interacción presentaron valores más idóneos de las propiedades físicas relacionadas con la estructura macroscópica (mayor calidad física): mayor índice de estabilidad estructural, macroporosidad y conductividad hidráulica saturada, así como menor densidad aparente.

4. Se ha puesto de manifiesto la relevancia de la atracción hidrófoba, estimada convenientemente mediante la componente $\gamma^-$, en la estructura de los suelos minerales, incluso aquellos que mostraron un carácter claramente hidrofílico ($\gamma^+ = 0\ \gamma^- > 28{,}2$ mJ $m^{-2}$). Su inclusión en el modelo DLVO-extendido de van Oss ha permitido cuantificar de forma precisa su efecto respecto a la energía total de interacción y la estabilidad de la estructura, que ha sido siempre beneficioso.

5. Se ha podido establecer una relación entre la hidrofobicidad y la cantidad y calidad de la materia orgánica del suelo, de manera que los suelos con mayor porcentaje y menor grado de evolución de la misma (*i.e.* mayor relación A4/A6) fueron los que manifestaron mayor hidrofobicidad. Este hecho debería ser tenido en cuenta a la hora de aplicar enmiendas orgánicas con el objetivo de fijar carbono o mejorar el suelo.

6. El tipo de material parental (silíceo o carbonatado) también influyó decisivamente en la hidrofobicidad del suelo, siendo los suelos silíceos los que, a igualdad de otros factores, desarrollaron mayor hidrofobicidad. Se recomienda tener en cuenta esta circunstancia a la hora de aplicar los

protocolos de agricultura ecológica a suelos sobre distintos materiales geológicos.

7. En general, la absorción de ácidos húmicos comerciales aumentó en valor absoluto el potencial zeta del suelo, incrementando la interacción repulsiva entre las partículas. Por esta razón, se recomienda precaución a la hora de seleccionar el material para enmiendas orgánicas.

8. La eliminación de la materia orgánica natural, incluso en suelos con bajos contenidos iniciales como los olivares convencionales, inhibió en todos los casos estudiados la adsorción de ácidos húmicos. Esto reafirma la importancia de la materia orgánica natural del suelo, por escasa que sea, en los procesos de fijación de carbono.

9. Las isotermas de adsorción de ácidos húmicos indicaron una menor adsorción de carbono en suelos ácidos que en básicos, aspecto que sería conveniente tomar en cuenta en los modelos de fijación de carbono en agrosistemas y cambio climático.

10. Si bien, de forma general, la teoría clásica propone que un aumento de fuerza iónica prevé una disminución de la carga superficial, nuestros resultados no se ajustan a este comportamiento, encontrando que la movilidad electrofónica para concentración 0.1 mM es mayor que 1 mM.

11. Los suelos mostraron carga negativa en todo el rango de pH para disoluciones mono y divalentes. La carga negativa aumentó con el pH del suelo, siendo significativamente más alta para los iones monovalentes (*i.e.* sodio) que para los divalentes (*i.e.* calcio). En el caso de iones trivalentes, se invirtió la carga de las partículas para pH ácidos, pasando de negativa a positiva. En base a lo anterior, los estados más favorables para el desarrollo de la estructura a escala coloidal fueron las soluciones cálcicas y férricas a pH ácidos.

# Capítulo 7
# Investigaciones futuras

En esta memoria se ha introducido la caracterización de la superficie de un material tan complejo como es el material edáfico. Debido a la gran importancia de estos materiales para la economía mundial, es de gran importancia llegar a conocer el complicado mundo de la formación de los complejos orgánicos-minerales del suelo y las variables que le afectan.

En primer lugar, las investigaciones futuras irán destinadas al estudio de la adsorción de compuestos orgánicos artificiales (pesticidas, herbicidas...) en suelos agrícolas. En este nuevo capítulo de la investigación se estudiará la energía de interacción total entre y como se modifican al interaccionar con los compuestos orgánicos artificiales. Estos compuestos de gran utilidad en el medio agrícola, están siendo muy estudiados por sus

efectos nocivos sobre la salud humana; por lo que sería interesante ver el tiempo de permanencia y descomposición de los mismos en el suelo.

En segundo lugar, el estudio de la cohesión de depósitos volcánicos ha puesto de manifiesto la gran dependencia de la estabilidad geotécnica de estos depósitos con los electrolitos presentes, así como, con el pH del medio, siendo un factor de estudio clave en la comprensión de deslizamientos de tierra. En este ámbito de investigación se deben intentar establecer una relación empírica entre la energía de interacción total y la cohesión del depósito. Siendo sin duda de gran interés la relación entre ambos para el estudio geotécnico de materiales edafológicos no consolidados.

# Capítulo 8
# Referencias


Abdel-Monem, A., Watkins, N. D., & Gast, P. W. (1971). *Potassium-argon ages, volcanic stratigraphy, and geomagnetic polarity history of the Canary Islands; Lanzarote, Fuerteventura, Gran Canaria, and La Gomera.* American Journal of Science, 271(5), 490-521.

Adamsom, A.W. Physical Chemistry of surfaces, 4ª Ed. John Wiley and Sons. New York. (1982).

Álvarez, S., Soriano, M. A., Landa, B. B., & Gómez, J. A. (2007). *Soil properties in organic olive groves compared with that in natural areas in a mountainous landscape in southern Spain*. Soil use and management, 23(4), 404-416.

Ancochea, E. H. (1999). *Evolution of the Cañadas edifice and its implications for the origin of the Cañadas Caldera (Tenerife, Canary Islands).* Journal of Volcanology and Geothermal Research, 88(3), 177-199.

Ancochea, E., Brändle, J. L., Cubas, C. R., Hernán, F., & Huertas, M. J. (1996). *Volcanic complexes in the eastern ridge of the Canary Islands: the Miocene activity of the island of Fuerteventura*. Journal of Volcanology and Geothermal Research, 70(3), 183-204.

Aranda, V., Ayora, M., Domínguez, A., Martín, J., Calero, J., Delgado, R., Verdejo & T., González, F., 2011. *Effect of soli type and management (organic vs. conventional) on soil organic matter quality in olive groves in s semi-arid environment in Sierra Mágina Natural Park (S Spain).* Geoderma 164, 54-63.

Aranda, V., Calero, J., Plaza, I., & Ontiveros-Ortega, A. (2016). *Long-term effects of olive mill pomace co-compost on wettability and soil quality in olive groves.* Geoderma, 267, 185-195.

Astis, G., La Volpe, L., Peccerillo, A., & Civetta, L. (1997). *Volcanological and petrological evolution of Vulcano island (Aeolian Arc, southern Tyrrhenian Sea).* Journal of Geophysical Research: Solid Earth, 102(B4), 8021-8050.

Bagshaw EA, Cockel CS, Magan N et al (2011) *The microbial habitability of weathered volcanic glass inferred from continuous sensing techniques.* Astrobiology, 11:651–664

Balcells R, Gomez JA. *Memorias y mapas geológicos del Plan MAGNA. 1:25000.* El Hierro, Hoja de Valverde: Instituto Geológico y Minero de España, España; 1997a (in Spanish).

Balcells, R., & Gomez, J. A. (1997). *Memorias y mapas geológicos del Plan MAGNA a escala 1: 25.000 de las Hojas correspondientes a la isla de El Hierro.* Hoja de Frontera, Instituto Geológico y Minero de España, Spain.

Barberi, F., Buonasorte, G., Cioni, R., Fiordelisi, A., Foresi, L., Iaccarino, S., ... & Villa, I. M. (1994). *Plio-Pleistocene geological evolution of the geothermal area of Tuscany and Latium*. Mem. Descr. Carta Geol. Ital, 49, 77-134.

Barré, P., & Velde, B. (2010). *Clays developed under Sequoia Gigantia and prairie soils: 150 years of soil-plant interaction in the parks of French châteaux*. Clays and Clay Minerals, 58(6), 803-812.

Barré, P., Fernandez-Ugalde, O., Virto, I., Velde, B., Chenu, C., (2014). *Impact of phyllosilicate mineralogy on organic carbon stabilization in soils: incomplete knowledge and exciting prospects.* Geoderma 235-236, 382-395.

Barré, P., Velde, B., Fontaine, C., Catel, N., Abbadie, L., (2008). *Which 2:1 clay minerals are involved in the soil potassium reservoir? Insights from potassium addition or removal experiments on three temperate grassland soil clay assemblages*. Geoderma, 146, 216–223.

Ben-Avraham, Z., & Grasso, M. (1990). *Collisional zone segmentation in Sicily and surrounding areas in the Central Mediterranean*. Ann. Tectonicae, 4(2), 131-139.

Bernett, M. K., & Zisman, W. A. (1962). *Wetting properties of acrylic and methacrylic polymers containing fluorinated side chains*. The Journal of Physical Chemistry, 66(6), 1207-1208.

Bertagnini, A., Méltrich, N., Francalanci, L., Landi, P., Tommasini, S., & Conticelli, S. (2008). *Volcanology and magma geochemistry of the present-day activity: Constraints on the feeding system. The Stromboli Volcano*: An Integrated Study of the 2002-2003 Eruption, 19-37.

Branca, S., Coltelli, M., De Beni, E., & Wijbrans, J. (2008). *Geological evolution of Mount Etna volcano (Italy) from earliest products until the first central volcanism (between 500 and 100 ka ago) inferred from geochronological and stratigraphic data.* International Journal of Earth Sciences, 97(1), 135-152.

Bronick, C.J., Lal, R., (2005). *Soil structure and management: a review*. Geoderma 124, 3-22.

Calero J., Cordovilla M.P., Aranda V., Borjas R, Aparicio C., (2013). *Effect of Organic Agriculture and Soil Forming Factors on Soil Quality and Physiology of Olive Trees. Agroecology and Sustainable* Food Systems, 37: 193-214.

Calero, J., 2005. *Génesis de la fracción mineral y de la ultramicrofábrica en una cronosecuencia de suelos sobre terrazas del río Guadalquivir.* PhD thesis, Universidad de Granada, Granada, Spain.

Calero, J., Cordovilla M.P., Aranda V., Borjas R, Aparicio C., 2013a. *Effect of Organic Agriculture and Soil Forming Factors on Soil Quality and Physiology of Olive Trees. Agroecology and Sustainable* Food Systems 37, 193-214.

Calero, J., Delgado, R., Delgado, G. and Martín-García, J.M. (2009). *SEM image analysis in the study of a soil chronosequence on fluvial terraces of the middle Guadalquivir (southern Spain).* European Journal of Soil Science 60: 465–480..

Calero, J., Martín-García, J.M., Delgado, G., Aranda, V., Delgado, R. 2013b. *A nano-scale study in a soil chronosequence from southern Spain.* European Journal of Soil Science, 64, 192-2009.

Carracedo JC, Badiola ER, Guillou H, de la Nuez J, Pérez Torrado FJ. *Geology and volcanology of La Palma and El Hierro, Western Canaries.* Estudios Geológicos 2001;57:175e273.

Carracedo JC, F.-T. J.-T.-B.-G. (2011a). *Comment on ''The distribution of basaltic volcanism on Tenerife,Canary Islands: implications on the origin anddynamics of the rift systems''.* Tectonophysics, 503:239–241.

Carracedo JC, R. B.-P. (2007). *Eruptive and structural history of Teide volcano and rift zones of Tenerife, Canary Islands.* Geol Soc Am Bull, 119:1027–1051.

Carracedo, J. C. (1975). *Estudio paleomagnetico de la isla de Tenerife.* Thesis, 265.

Carracedo, J. C., Paterne, M., Guillou, H., Torrado, F. P., Paris, R., Badiola, E. R., & Hansen, A. (2003). *Dataciones radiométricas (14 C y K/Ar) del Teide y el rift noroeste, Tenerife, Islas Canarias.* Estudios Geológicos, 59(1-4), 15-29.

Chaudhury, M. K. j colloid interface sci., 159, 174 (1987).

Chibowski *E. Solid surface free energy components determination by the thin-layer wicking technique.* Journal of Adhesion Science and Technology 1992;6(9): 1069e90.

Chibowski, E., Kerkeb, M. L., & González-Caballero, F. (1993). *Effect of inorganic ions on changes in the energetic heterogeneity of the cholesterol surface.* Langmuir, 9(10), 2491-2495.

Christensen BE, Kjosbakken J, Smidsrod OF (1985) *Partial chemical and physical characterization of two extracellular polysaccharides produced by Marine, Periphytic Pseudomonas sp.* Strain NCMB 2021. Appl Environ Microbiol, 50:837–845

Cockell CS, van Calsteren P, Mosselmans Jl et al (2010) *Microbial endolithic colonization and the geochemical environment in young seafloor basalts.* Chem Geol, 279:17–30

Cockell, C. S. (2010). *Geomicrobiology beyond Earth: microbe–mineral interactions in space exploration and settlement*. Trends in microbiology, 8(7), 308-314.

Courtney, R. C., & White, R. S. (1986). *Anomalous heat flow and geoid across the Cape Verde Rise: evidence for dynamic support from a thermal plume in the mantle*. Geophysical Journal International, 87(3), 815-867.

Cristofolini, R., Lentini, F., Patanè, G., & Rasà, R. (1979). *Intergrazione di dati geologici, geofisici e petrologici per la stesura di un profilo crostale in corrispondenza dell'Etna.* Bollettino della Società Geologica Italiana, 98(2), 239-247.

Debye, P. (1921). *Molecular forces and their electrical interpretation. Physikalische Zeitschrift*, 22, 302-308.

Derjaguin, ]3. V., Klissakov, (1939). M., Acta Physicochim. USSR 10, 25, 153

Dexter SC, Sullivan JD, Williams J, Watson SW (1975) *Influence of substrate wettability on the attachment of marine bacteria to various surfaces.* Appl Microbiol, 30:298–308

Directiva 2004/35/CE del Parlamento Europeo y del Consejo, de 21 de abril de 2004, sobre responsabilidad medioambiental en relación con la prevención y reparación de daños medioambientales.

Ducker, W. A., Senden, T. J., & Pashley, R. M. (1992). *Measurement of forces in liquids using a force microscope*. Langmuir, 8(7), 1831-1836.

Duran J. D. G., Ontiveros A, Delgado AV, Gonzalez-Caballero F, Chibowski E. (1996). J Adhes Sci Technol 10:847e68.

Duran JDG, Ontiveros A, Delgado AV, Gonzalez-Caballero F. *Kinetics and interfacial interactions in the adhesion of colloidal calcium carbonate to glass in a packed-bed*. Applied Surface Science 1998;134(1e4):125e38.

Duran, J. D. G., Guindo, M. C., Delgado, A. V., & Gonzalez-Caballero, F. (1995). *Stability of monodisperse zinc sulfide colloidal dispersions.* Langmuir, 11(10), 3648-3655.

Ellison, A. H., & Zisman, W. A. (1954). *Wettability studies on nylon, polyethylene terephthalate and polystyrene.* The Journal of Physical Chemistry, 58(6), 503-506.

Espinosa-Jiménez, M., Ontiveros-Ortega, A., Padilla-Weigand, R., Ramos-Tejada, M.M., Perea-Carpio, R, 2003. *Interpretation of Colloidal Dyeing of Polyester Fabrics Treated with N-Cetylpyridinium Chloride in Terms of Zeta Potential and Surface Free Energy Balance*. Macroml. Mater. Eng. 288, 954-950.

FAO, (2006). World Reference Base for Soil Resources. A Framework for International Classification, Correlation and Communication. World Soil Resources Reports, 103. Food nd Agriculture Organization of the United Nations, Rome, Italy

Fowkes, F., 1964. *Attractive forces at interfaces*. Ind. Eng. Chem. 56, 40–52.

Fox, H. W., & Zisman, W. A. (1952). *The spreading of liquids on low-energy surfaces.* III. Hydrocarbon surfaces. Journal of Colloid Science, 7(4), 428-442.

Francalanci, L., Tommasini, S., Conticelli, S., & Davies, G. R. (1999). *Sr isotope evidence for short magma residence time for the 20th century activity at Stromboli volcano, Italy*. Earth and Planetary Science Letters, 167(1), 61-69.

Fúster JM, A. V. (1968). *Geology and volcanology of the Canary Islands: Tenerife. Madrid: Instituto Lucas Mallada,* CSIC.

Galé, C., Ubide, T., Lago, M., Gil-Imaz, A., Gil-Peña, I., Galindo-Zaldívar, J., ... & López-Martínez, J. (2014). *Vulcanismo cuaternario de la Isla Decepción (Antártida): una signatura relacionada con la subducción de la Fosa de las Shetland del Sur en el dominio de tras-arco de la Cuenca de Bransfield.* Boletín Geológico y Minero, 125(1), 31-52.

Gillot, P. Y., Kieffer, G., & Romano, R. (1994). *The evolution of Mount Etna in the light of potassium-argon dating.* Acta Vulcanol, 5, 81-87.

*González-Ferrán, O. (1985). Volcanic and tectonic evolution of the northern Antarctic Peninsula—Late Cenozoic to Recent*. Tectonophysics, 114(1), 389-409.

Good, R. J. (1967). *Treatise on Adhesion and Adhesives*. Marcel Dekker, New York, 1(9), 21.

Good, R. J. (1993). *Contact angle, wetting, and adhesion: a critical review.* Contact angle, wettability and adhesion, 3-36.

Good, R. J., & Hope, C. J. (1970). *New combining rule for intermolecular distances in intermolecular potential functions.* The Journal of Chemical Physics, 53(2), 540-543.

Good, R. J., Hardy, E. E., Ellenburg, A. M., & Richards Jr, H. B. (1953). *The Solubility of p-Terphenyl in o-and m-Terphenyls and in Biphenyl1*. Journal of the American Chemical Society, 75(2), 436-442.

Gregory J. *Approximate expressions for retarded van der Waals interaction.* Journal of Colloid and Interface Science 1981;83(1):138e45.

Guillou H, Carracedo JC, Pérez Torrado F, Rodríguez Badiola E. K-Ar *ages and magnetic stratigraphy of a hotspot induced, fast grown oceanic island: El Hierro, Canary Islands.* Journal of Volcanology and Geothermal Research 1996;73(1e2):141e55.

Hamaker, H. C. (1936). *A general theory of lyophobic colloïds*. I. Recueil des travaux chimiques des pays-bas, 55(12), 1015-1026.

Hamaker, H. C. (1937). *The London—van der Waals attraction between spherical particles*. Physica, 4(10), 1058-1072.

Han, M. W., & Suess, E. (1987). *Lateral migration of pore fluids through sediments of an active back-arc basin, Bransfield Strait, Antarctica.* EOS Trans. AGU, 68, 1769.

Hausen, H. (1955). *Algunos aspectos geológicos y geomorfológicos de la más antigua de las islas Canarias.* El museo canario, (16), 53-80.

Hausen. (1947–1951). *Contributions to the geology of Tenerife (Canary Islands), vol XVIII (1). Societas scientiarum fennica, commentationes physico-mathematicae, geologic results of the Finnish expedition to the Canary Islands. Centraltryckeriet,* Helsingfors.

Hawkes, D. D. (1961). *The geology of the South Shetland Islands: II. The geology and petrology of Deception Island*.

Hjertén, S., Jerstedt, S., & Tiselius, A. (1969). *Apparatus for large-scale preparative polyacrylamide gel electrophoresis.* Analytical biochemistry, 27(1), 108-129.

Hogg, R. T. W. D. W., Healy, T. W., & Fuerstenau, D. W. (1966). *Mutual coagulation of colloidal dispersions.* Transactions of the Faraday Society, 62, 1638-1651.

Holtz, R. D. (1981). *An introduction to geotechnical engineering* (No. Monograph).

Huang, B., Babcock, H., & Zhuang, X. (2010). *Breaking the diffraction barrier: super-resolution imaging of cells.* Cell, 143(7), 1047-1058.

Hunter, R. J. (1966). *The interpretation of electrokinetic potentials.* Journal of Colloid and Interface Science, 22(3), 231-239.

Hwang, G., Lee, C. H., Ahn, I. S., & Mhin, B. J. (2010). *Analysis of the adhesion of Pseudomonas putida NCIB 9816-4 to a silica gel as a model soil using extended DLVO theory.* Journal of hazardous materials, 179(1), 983-988.

Ilustre Ayuntamiento de Villa de Arico. (2011). *Plan general de ordenación de Arico.*

Ip, S. W., & Toguri, J. M. (1994). *The equivalency of surface tension, surface energy and surface free energy.* Journal of materials science, 29(3), 688-692.

Israelachvili, J. N., & Berman, A. D. (1995). *Surface forces and microrheology of molecularly thin liquid films.* Handbook of micro/nano tribology, 267-319.

Israelachvili, J. N., & Wennerstroem, H. (1992). *Entropic forces between amphiphilic surfaces in liquids.* The Journal of Physical Chemistry, 96(2), 520-531.

Israelachvili, J., & Pashley, R. (1982). *The hydrophobic interaction is long range, decaying exponentially with distance.*

James, A. M. (1979). *Electrophoresis of particles in suspension.* In Surface and colloid science (pp. 121-185). Springer US.

Jirgensons, B., & Straumanis, M. E. (1965). *Compendio de química coloidal.* CECSA.

Junta de Andalucía, 2005. Mapa de Suelos de Andalucía, escala 1:400.000. Consejería de Medio Ambiente y Ordenación del Territorio, Sevilla. (http://www.juntadeandalucia.es/medioambiente/mapwms/REDIAM_Suelos_Andalucia?)

Kadar E, F. A.-J. (2014). *Colloidal stability of nanoparticles derived from simulated cloud-processed mineral dusts*. Science of the Total Environment, 466–467: 864–70.

Kaelbe, D. H. y Cirlin, E.H., J. Polym. Sci., 9, 363 (1971).

Kaelbe, D.H. y UY, C., J. Adhesion, 2, 50 (1970).

Kaelbe, D.H., J. Adhesion, 2, 66 (1970).

Kaiser, K., Guggenberger, G., Zech, W., 1996. *Sorption of DOM and DOM fractions to forest soils.* Geoderma 74, 281-303.

Kay B. D. (1990). *Rates of change of soil structure under different cropping systems.* Advances in Soil Science 12, 1-52.

Keesom, W. M. (1921). *Van der Waals attractive force.* Physikalische Zeitschrift, 22, 129-141.

Kemper, W.D., Rosenau, R.C., (1986). *Aggregate stability and size distribution*. In: Klute, A. (Ed.) Methods of Soil Analysis. Part 1. 2nd ed. ASA and SSSA, Madison, USA.

Kihira, H., Ryde, N., & Matijević, E. (1992). *Kinetics of heterocoagulation.* Part. 2—The effect of the discreteness of surface charge. J. Chem. Soc., Faraday Trans., 88(16), 2379-2386.

Kinsey, W. H., & Sharma, D. (2004). *Regionalized calcium signaling in zebrafish fertilization*. International Journal of Developmental Biology, 52(5-6), 561-570.

Klute, A., 1986. *Methods of Soil Analysis. Part 1*. Agronomy Monographs, 9, ASA and SSSA, Madison, USA.

Kumahor, S. K., Hron, P., Metreveli, G., Schaumann, G. E., & Vogel, H. J. (2015). *Transport of citrate-coated silver nanoparticles in unsaturated sand*. Science of the Total Environment, 535, 113-121.

Kunze, G.W., Dixon, J.B., (1986). *Pretreatment for Mineralogical* Analysis. In: Methods of Soil Analysis (ed. A. Klute), Agronomy nº 9. American Society of Agronomy and Soil Science Society of America, Madison, WI., pp. 91-99.

Lagaly, G., (2006). *Colloid clay science.* In: Bergaya, F., Theng, B.K.G, Lagaly, G. (Eds.), Handbook of Clay Science. Elsevier, Amsterdam, pp. 247-260.

Lal, R., & Shukla, M. K. (2004). *Principles of soil physics*. CRC Press.

Lal, R., (2007). *Soil Science and the Carbon Civilization*. Soil Sci. Soc. Am. J. 71, 1425–1437.

Lal, R., (2015). *Soil Carbon Management and Climate Change*. Carbon Management, 4, 439-462.

Lanson, B., (1997). *Decomposition of experimental X-ray diffraction profile (profile fitting):* A convenient way to study clay minerals. Clays and Clay Minerals, 45, 132-146.

Lentini, F. (1982). *The geology of the Mt. Etna basement,* Mem. Soc. Geol. Ital, 23, 7-25.

Li Z, Giese RF, Wu W, Sheridan MF, van Oss CJ. *The surface thermodynamic properties of some volcanic ash colloids.* Journal of Dispersion Science and Technology 1997;18(3):223e41.

Li, S., Li, H., Xu, C.Y., Huang, X-R., Xie, D.T., Ni., J.P., (2013). *Particle interaction forces induce soil particle transport during rainfall.* Soil Sci. Soc. Am. J., 77, 1563-1571.

Liébanas, G. M., Delgado, G., Delgado, R., Calero, J., Peña, R., García, J. M., & Aranda, V. (2002). *Análisis multivariante de los horizontes orgánico-minerales de los suelos del Parque Natural de Sierra Mágina (Jaén).* Journal of Iberian Geology, 28, 143-156.

London, F. (1930). On the theory and system of molecular forces. Quantum, 10, 9789812795762_0023.

Longpre M, Chadwick JP, Wijbrans J, Iping R. *Age of the El Golfo debris avalanche, El Hierro (Canary Islands): new constraints from laser and furnace 40Ar/39Ar dating.* Journal of Volcanology and Geothermal Research 2011;203(1e2):76e80.

Longpré MA, T. V. (2009). *Volcanic and geochemical evolution of the Teno massif, Tenerife, Canary Islands: some repercussions of giant landslides on ocean island magmatism.* Geochem Geophys Geosyst, 10:Q12017.

López-Sangil, L., Rovira, P., (2013). *Sequential chemical extractions of the mineral-associated soil organic matter: An integrated approach for the fractionation of organo-mineral complexes*. Soil Biology and Biochemistry, 62, 57-67.

Lützow, M.V., Kögel-Knabner, I., Ekschmitt, K., Matzner, E., Guggenberger, G., Marschner, B., Flessa, H., (2006). *Stabilization of organic matter in temperate soils: mechanisms and their relevance under different soil condition –a review*. European Journal of Soil Science, 57, 426-445.

Lyklema, J. (Ed.). (1995). *Solid-liquid interfaces*. Academic Press.

Martí, J. H. (1997). *Vertical and lateral collapses on Tenerife (Canary Islands) and other volcanic ocean islands.* . Geology, , 25(10), 879-882.

Martí, J., Geyer, A., & Aguirre-Diaz, G. (2013). *Origin and evolution of the Deception island caldera (South Shetland Islands, Antarctica).* Bulletin of volcanology, 75(6), 1-18.

Matijevic, J. V. E. (1976). Surface and Colloids Science, Vol. 8.

Merha, O.P., Jackson, M.L. (1960). *Iron oxide removal from soils and clays by a dithionite-citrate system buffered by sodium bicarbonate.* Clays and Clay Minerals, 7, 317-327.

Moleon, J. A., Ontiveros-Ortega, A., Gimenez-Martin, E., & Plaza, I. (2015). *Effect of N-cetylpyridinium chloride in adsorption of graphene oxide onto polyester.* Dyes and Pigments, 122, 310-316.

Nelligan, J. D., Kallay, N., & Matijević, E. (1982). *Particle adhesion and removal in model systems: V. Interpretation of the kinetics of particle detachment.* Journal of Colloid and Interface Science, 89(1), 9-15.

Neumann, A. W., Good, R. J., Hope, C. J., & Sejpal, M. (1974). *An equation-of-state approach to determine surface tensions of low-energy solids from contact angles.* Journal of Colloid and Interface Science, 49(2), 291-304.

Nieto, O. M., Castro, J., Fernández, E. and Smith, P. (2010). *Simulation of soil organic carbon stocks in a Mediterranean olive grove under different soil-management systems using the RothC model*. Soil Use and Management 26, 118–125.

Nieto, O. M., Fernández-Ondoño, E., & Castro, J. (2012). *Uso sostenible de suelos de olivar. Efecto del manejo del suelo en sus propiedades.* Spanish Journal of Soil Science, 2(1).

Nir, A., & Acrivos, A. (1976). *The effective thermal conductivity of sheared suspensions.* Journal of Fluid Mechanics, 78(01), 33-48.

O'Brien, R. W., & Hunter, R. J. (1981). *The electrophoretic mobility of large colloidal particles.* Canadian Journal of Chemistry, 59(13), 1878-1887.

Ochs, M., Ćosović, B., & Stumm, W. (1994). *Coordinative and hydrophobic interaction of humic substances with hydrophilic Al2O3 and hydrophobic mercury surfaces.* Geochimica et Cosmochimica Acta, 58(2), 639-650.

Ontiveros A, Duran J, Delgado AV, Gonzalez-Caballero F, Chibowski E. *A study on the adhesion of calcium carbonate to glass. Energy balance in the deposition process*. Journal of Adhesion Science and Technology 1996a;10(9):847e68.

Ontiveros A, Duran JDG, Gonzalez-Caballero F, Chibowski E. Adhesion of colloidal. *ZnS on silicon. Effects of ionic strength and radio frequency electric field.* Journal of Adhesion Science and Technology 1996b;10(10):999e1019.

Ontiveros-Ortega, A. V. (2014). *Effect of heavy metals on the surface free energy and zeta potential of volcanic glass: implications on the adhesion and growth of microorganisms.* . Journal of Materials Science, 49(9), 3550-3559.

Ontiveros-Ortega, A., Moleon, J. A., Plaza, I., & Guillén, C. (2015). *Effect of interfacial properties on mechanical stability of ash deposit.* Journal of Rock Mechanics and Geotechnical Engineering, 187-197.

Overbeek, J. T. G. (1952). *Electrochemistry of the double layer.* Colloid science, 1, 115-193.

Owens, D. K., & Wendt, R. C. (1969). *Estimation of the surface free energy of polymers.* Journal of applied polymer science, 13(8), 1741-1747.

Page, A.L., Miller, R.H., Keeny, D.R., (1982). Methods of Soil Analysis. Part 2. Agronomy Monographs, 9, ASA and SSSA, Madison, USA.

Paris, R., Giachetti, T., Chevalier, J., Guillou, H., & Frank, N. (2011). *Tsunami deposits in Santiago Island (Cape Verde archipelago) as possible evidence of a massive flank failure of Fogos volcano.* Sedimentary Geology, 239(3), 129-145.

Parsegian VA, Rand RP, and Rau DC: Chemica Scripta (1985), 25:28.

Paul JH, Jeffrey WJ (1985) *Potential importance of fish predation and zooplankton grazing on natural populations of freshwater bacteria.* Appl Environ Microbiol 50:431–437.

Peng, X., Horn, R., Hallett, P., 2008. *Soil Structure and its functions in ecosystems: Phase matter & scale matter*. Soil & Tillage Research 164, 1-3.

Pérez Torrado FJ, Rodríguez González A, Carracedo JC, Fernández Turiel JL, Guillou H, Hansen A, Rodríguez Badiola E. Edades C-14 del rift ONO de El Hierro (Islas Canarias). In: Resums XIII Reunió Nacional de Quaternari. Andorra; 2011. p. 101e4 (in Spanish).

Perez-Torrado, F. J., Carracedo, J. C., Rodríguez-González, A., Soler, V., Troll, V. R., & Wiesmaier, S. (2012). *La erupción submarina de La Restinga en la isla de El Hierro, Canarias: Octubre 2011-Marzo 2012.* Estudios geológicos, 68(1), 5-27.

Plaza, I., Ontiveros-Ortega, A., Calero, J., & Aranda, V. (2015). *Implication of zeta potential and surface free energy in the description of agricultural soil quality: Effect of different cations and humic acids on degraded soils.* Soil and Tillage Research, 146, 148-158.

Propuesta de Directiva del Parlamento Europeo y del Consejo, de 22 de septiembre de 2006, por la que se establece un marco para la protección del suelo y se modifica la Directiva 2004/35/CE.

Pugh, R. J., Matsunaga, T., & s, F. M. (1983). *The dispersibility and stability of carbon black in media of low dielectric constant. 1. Electrostatic and steric contributions to colloidal stability.* Colloids and Surfaces, 7(3), 183-207.

Rabinovich, Y. I., Derjaguin, B. V., & Churaev, N. V. (1982). *Direct measurements of long-range surface forces in gas and liquid media.* Advances in Colloid and Interface Science, 16(1), 63-78.

Ramos-Tejada, M. O. (2003). *Interfacial and rheological properties of humic acid/hematite suspensions.* Journal of Colloid and Interface Science , 268, 85–95.

Rao SM. *Mechanistic approach to the shear strength behaviour of allophanic soils.* Engineering Geology 1995;40(3e4):215e21.

Rasà, R., & Villari, L. (1991). *Geomorphological and morpho-structural investigations on the Fossa cone (Vulcano, Aeolian Islands): a first outline.* Acta Vulcanologica, 1, 127-133.

Riddle Jr, F. L., & Fowkes, F. M. (1990). *Spectral shifts in acid-base chemistry. 1. van der Waals contributions to acceptor numbers.* Journal of the American Chemical Society, 112(9), 3259-3264.

Ridley, W. I. (1970). *The petrology of the Las Canadas volcanoes, Tenerife, Canary Islands.* Contributions to Mineralogy and Petrology, 26(2), 124-160.

Romagnoli, C., Casalbore, D., & Chiocci, F. L. (2012). *La Fossa Caldera breaching and submarine erosion (Vulcano island, Italy).* Marine Geology, 303, 87-98.

Rošic, R. P.-R. (2012). *The role of rheology of polymer solutions in predicting nanofiber formation by electrospinning.* European Polymer Journal, 48(8), 1374-1384.

Schmincke, H. U. (1982). *Volcanic and chemical evolution of the Canary Islands. In Geology of the Northwest African continental margin (pp. 273-306).* Springer Berlin Heidelberg.

Schoeneberger, M., Bentrup, G., de Gooijer, H., Soolanayakanahally, R., Sauer, T., Brandle, J., ... & Current, D. (2012). *Branching out: agroforestry as a climate change mitigation and adaptation tool for agriculture*. Journal of Soil and Water Conservation, 67(5), 128A-136A.

Séquaris, J-M. (2010). *Modeling the effects of Ca2+ and clay-associated organic carbon on the stability of colloids from topsoils.* Journal of Colloid and Interface Science, 343, 408-414.

Shafrin, E. G., & Zisman, W. A. (1962). *Effect of progressive fluorination of a fatty acid on the wettability of its adsorbed monolayer.* The Journal of Physical Chemistry, 66(4), 740-748.

Sheludko.A.; Colloid Chemistry. Elsevier, Amsterdam (1966), pp. 211–213.

Six, J., Conant, R.T., Paul, E.A., Paustian, K. (2002). *Stabilization mechanisms of soil organic matter: implications for C-saturation of soils.* Plant Soil., 241, 155-176.

Skavarla, J., Kmet, S., Int. J. Min. Processing, 32, 111 (1991).

Smellie, J. L. (2001). *Lithostratigraphy and volcanic evolution of Deception Island, South Shetland Islands.* Antarctic Science, 13(02), 188-209.

Smoluchowksi, M. (1921). Stationäre Ströme. Handbuch: Graetz, L.

Tejada, M. H. (2009). O*il restoration using composted plant residues: Effects on soil properties.* Soil and Tillage Research, 102(1), 109-117.

Van Olphen, H. (1977). *Introduction to clay colloid* chemistry. Wiley.

Van Oss C.J., C. M. (1988). *Interfacial Lifshitz-van der Waals and Polar Interactions in Macroscopic Systems.* Chemical Reviews, 88, 927.

Van Oss CJ. (1994). *Interfacial forces in aqueous media.* Marcel Dekker, New York. Journal of colloid and Interface Science, 111(2), 378-390.

Van Oss, C. G. (1989). *Surface tension and the solubility of polymers and biopo-lymers: the role of polar and apolar interracial free energy,.* Journal of Macromolecular Science: Pure and Applied Chemistry , 26, 1183-1203.

Van Oss, C. J. (1993). *Acid—base interfacial interactions in aqueous media.* Colloids and Surfaces A: Physicochemical and Engineering Aspects, 78, 1-49.

Van Oss, C. J., Chaudhury, M. K., & Good, R. J. (1987). *Monopolar surfaces.* Advances in colloid and interface science, 28, 35-64.

Van Oss, C. J., Giese, R. F., & Costanzo, P. M. (1990). *DLVO and non-DLVO interactions in hectorite.* Clays Clay Miner, 38(2), 151-159.

Van Oss, C.J., Giese, R.F., (1995). *The hydrophilicity and hydrophobicity of clay minerals. Clays and Clay Minerals*, 43, 474-477.

Ventura, G. (1994). *Tectonics, structural evolution and caldera formation on Vulcano Island (Aeolian Archipelago, southern Tyrrhenian Sea)*. Journal of Volcanology and Geothermal Research, 60(3-4), 207-224.

Verwey, E. J. W., & Overbeek, J. T. G. (1948). *Theory of Stability of Colloids.*

Visser, J. (1972). *On Hamaker constants: A comparison between Hamaker constants and Lifshitz-van der Waals constants.* Advances in Colloid and Interface Science, 3(4), 331-363.

Wallenstein, N., Duncan, A., Chester, D., & Marques, R. (2007). *Fogo volcano (Sao Miguel, Azores): a hazardous edifice*. Géomorphologie: relief, processus, environnement, (3/2007), 259-270

Ward, C. A., & Neumann, A. W. (1974). *On the surface thermodynamics of a two—component liquid-vapor-ideal solid system.* Journal of colloid and interface science, 49(2), 286-290.

Washburn, E. W. (1921). *The dynamics of capillary flow. Physical review*,17(3), 273.

Whitting, L.D., Allardice., W.R. (1986). *X-Ray Diffraction Techniques.* In: Methods of Soil Analysis (ed. A. Klute). Agronomy nº 9. American Society of Agronomy and Soil Science Society of America, Madison, WI., pp. 331–359.

Wolff, J. A., & Storey, M. (1983). *The volatile component of some pumice-forming alkaline magmas from the Azores and Canary Islands.* Contributions to Mineralogy and Petrology, 82(1), 66-74.

Wu, S. (1970). *Surface and interfacial tensions of polymer melts. II. Poly (methyl methacrylate), poly (n-butyl methacrylate), and polystyrene.* The Journal of Physical Chemistry, 74(3), 632-638.

Wu, S. (1971). *Calculation of interaction in adhesion: recent advances in adhesion.* J Polym Sci C, 34, 19-30.

Yong, R. N., Warkentin, B. P., Phadungchewit, Y., & Galvez, R. (1990). *Buffer capacity and lead retention in some clay materials. Water, Air, and Soil Pollution*, *53*(1-2), 53-67.

Zhao, X.R., Lin,Q., Brookes, P.C., 2004. *Does soil ergo sterol concentration provide a reliable estimate of soil fungal biomass?* Soil Biol. Biochem. 37, 311–317.

# Apéndices

## Apéndice I. Listado de figuras.

***I.1.Derechos de autor.***

Las fotos recogidas en este documento, poseen derechos de copyright Creative Commons Attribution-Share Alike 3.0 Unported license.

> This file is licensed under the Creative Commons Attribution-Share Alike 3.0 Unported license.
>
> You are free:
>
> - to share – to copy, distribute and transmit the work
> - to remix – to adapt the work
>
> Under the following conditions:
>
> - attribution – You must attribute the work in the manner specified by the author or licensor (but not in any way that suggests that they endorse you or your use of the work).

- share alike – If you alter, transform, or build upon this work, you may distribute the resulting work only under the same or similar license to this one.

En cada figura de este documento vienen recogidos los diferentes autores de las fotografías utilizadas con el fin de cumplir con la licencia Creative Commons Attribution Share Alike 3.0.

Las fotos de portada y contraportada han sido realizadas por Toni Perez Fernández, Julio Calero González, Víctor Aranda SanJuan, R. García-Ruiz, J.L. Vicente-Vicente y Alfonso Ontiveros Ortega.

***I.2.Listado de figuras.***

Figura 2.6. Fuerza de solvatación monótona. Suelen aparecer en disoluciones acuosas donde existen enlaces de hidrogeno, lo que produce la aparición de una fuerza de "hidratación" adicional, que disminuye exponencialmente. para superficies hidrofílicas la componente monótona es repulsiva (curva superior numero 1)p mientras que para superficies hidrofóbicas es atractiva (curva inferior numero 2). Para liquido más simple no existe tal componente monótoma y tanto teoría como experimentos muestran que disminuyen en torno a la línea base de la fuerza de van der Waals (curva numero 3).

Figura 2.8. Descripción de diferentes clases de sistemas solido-liquido.

Figura 3.1. Composición fotográfica donde se pueden observar una panorámica de volcanes seleccionados en la península de Italia.

Figura 3.2. Composición fotográfica donde se pueden observar las muestras estudias de los diferentes volcanes: Vulcano (a), Estromboli (b) y Etna (c). cenizas antes de pretamientos (fotografía de la izquierda) y después del tratamiento con el mortero de ágata (fotografía de la derecha). De arriba a abajo encontramos las cenizas de Vulcano, Estromboli y Etna respectivamente.

Figura 3.3. Composición fotográfica donde se pueden observar fotografías de los volcanes: Tenerife (a), el Hierro (b) y Pico de Fogo (c).

Figura 3.4. Composición fotográfica donde se pueden observar fotografías de los volcanes: Tenerife (a), el Hierro (b) y Pico de Fogo (c) y Decepción (d). Cenizas antes (fotografía de la izquierda) y después del tratamiento con el mortero de ágata (fotografía de la derecha). De arriba a abajo encontramos las cenizas de Tenerife (a), el Hierro (b), Pico de Fogo ( c) y Decepción (d).

Figura 3.5. Composición fotográfica donde se pueden observar panorámicas de la isla Decepción (Antártida)

Figura 3.6. Localización geográfica de los suelos en la provincia de Jaén y Córdoba. En orden descendiente tenemos: mapa de Andalucía: ubicación de los suelos en sierra morena (a), ubicación de los suelos de Andújar (b), ubicación de los suelos en la Sierra de Magina (c). A sus izquierdas encontramos una ampliación de las zonas estudiadas a escala 1:20000.

Figura 3.7. Las dos imágenes superiores corresponden al suelo carbonatado (a su izquierda sus fotos del perfil de correspondientes a la zona de extracción) y las dos inferiores al suelo silíceo (a su izquierda sus fotos del perfil de correspondientes a la zona de extracción).

Figura 3.8. Composición fotográfica donde se puede ver los distintos suelos estudiados en Sierra Magina. De arriba a abajo tenemos suelos margosos (convencional derecha y ecológico izquierda), suelos coluviales (convencional derecha y ecológico izquierda y suelo en estado natural.

Figura 3.9. Composición fotográfica donde se puede ver los distintos suelos estudiados en Sierra Morena. De arriba a abajo tenemos olivar ecologico CUG1 y2 (ladera norte 1 y ladera sur 2), olivar convencional SCG y suelo en estado natural BNG.

Figura 4.1. En esta figura se muestran los aparatos de medición empleados para elaborar este documento. Imagen 1. The Boeco s-220 (uv/vis) and s-200 (vis) are high quality, compact, low cost measurement systems for daily analysis in education, QC and basic research imagen 2. Used sigma 2k15 refrigerated heated laboratory Benchtop centrifuge W/ ROTOR 12145. Imagen 3. Balanza analítica AE 240 balanza de dos campos imagen 4. Baño Memmert WNB7 TERMORREGULADO 7 LTS. PDF. BASIC WNB 7 /7 lts/amb+5ºc a 95ºc. Imagen 5. The model 30 and model 40 feature the same patented lightweight and ergonomic unibody design as the 12 ton and 20 ton models. Imagen 6. London Company PHM 62 - PHM62 - standard pH meter in business & industrial, healthcare, lab & life science, lab equipment.

Figura 4.2. Continuación de la figura 4.1. Imagen 7. Malvern Instruments ZETASIZER 3000 TITRATOR UNIT HSA PARTICLE SIZE 09636, for sale surplus used equipment from Hitechtrader price mt holly nj. Imagen 8. Anton paar instrument EKA (electro kinetic analyer). Imagen 9. Imagen obtenida de la cámara video del goniometro. Imagen 10. Gonimetro. Imagen 11. Hitachi U200 spectrophotometer

## Apéndice II. Listado de tablas.